Exploring Fresnel Holography for Optically Guided Atom Interferometry with Bose-Einstein Condensates

Victoria Anne Henderson

Experimental Quantum Optics and Photonics Group
Department of Physics and SUPA
University of Strathclyde

A thesis presented in the fulfilment of the requirements for the degree of

Doctor of Philosophy

2018

This thesis is the result of the author's original research. It has been composed by the author and has not been previously submitted for examination which has led to the award of a degree.

Signed:

Date:

Abstract

The progress and practicality of quantum technologies, such as rotation sensing, are contingent on the portability of existing ultracold atom technologies and the exploration of new alternative techniques. In response to this, we integrate existing knowledge with new Fresnel zone plate (FZP) holograms to begin the development of a compact Bose-Einstein condensate (BEC) interferometry device. Utilising high precision microfabrication, FZPs are exciting candidates for the production of static trapping potentials useful to atomtronics, interferometry, and fundamental physics. They are particularly useful for quantum technologies due to their simplicity and the potential for low cost mass-production.

We detail the build status of a new ^{87}Rb BEC experiment, designed for prototyping new waveguide technologies for atom interferometry. The experiment is deliberately modular to enable smooth upgrades. This is complemented by brief reporting of results from an existing BEC experiment. Density fluctuations indicating underlying phase fluctuations were observed in an elongated cigar shaped BEC.

The suitability of FZPs has been demonstrated with computational simulations comparing FZPs to spatial light modulators. Experimental imaging of various manufactured ring patterns gives an average RMS error in the brightest 10% of 3% with respect to trap depth. Typical optical profiles have residual limitations due to the imaging system, beam shape and alignment. The axial propagation of the potentials is presented experimentally and through numerical simulations; weak axial trapping is expected, though this is insufficient to support against gravity. A novel method by

which the azimuthal optical potential at the FZP can be simply mapped into the imaged ring is also presented.

The outlook for a second generation of kinoforms has been studied, with a view to allow for sub-wavelength spatial resolution and larger kinoforms. We detail a dark ring potential suitable for production with an FZP kinoform and map the parameter space possible for rings produced using FZPs.

Acknowledgements

I would like express a huge amount of gratitude to my supervisors, Aidan Arnold and Erling Riis. Without all your help and support I would never have got this far. Aidan, thank you especially for being so patient and inspiring. Paul Griffin, you may not have been my supervisor on paper, but on the ground you've always been around to answer my questions, be a listening ear and an excellent mentor.

The EQOP group at Strathclyde has been a wonderful place to work – I hope that my next group is nearly as warm and supportive as this community has become. I'd particularly like to thank the 'best office ever': Rachel E., Billy, Andrew, Jim, Gregg and all the other members over the years. Thank you for filling my work days with your pish and always putting a smile on my face. Carolyn and Rachel O., thank you for being excellent flat-mates as well as work mates. Jen, thanks for giving me some outside-the-lab physics perspective, for being such a caring friend, and for accompanying me on the West Highland Halfway.

Outside of Strathclyde, there are a huge number of people who have helped me get to where I am today. From school teachers who pushed me to follow my dreams (especially Mr. Cameron) to my Masters supervisor and mentor Matthew Jones, who introduced me to Atomic Physics and research.

Girl Guiding has played a huge part in my life, and I'm indebted to all of the volunteer leaders who ran my childhood units and to the leaders that I work with now, especially Olivia, Suzanne, Amanda, and Helen. The girls at Hyndland and Shincliffe Brownies are inspiring and I'm so proud of them. Plus I have them to thank for my 'Tawny Owl' super powers.

I am so lucky to have wonderful support structures through my Churches (St. Margaret of Antioch in Durham, St. Margaret of Scotland in Glasgow, and the students @ St. Mary's), you've all been like family when I'm away from my own. The Yarn

Cake knit nighters and ‘The Enablers’ have kept me sane, full of tea, and surrounded by wool; without these wonderful women, I would have lost my marbles instead of gaining lots and lots of wool.

Thank you Dan for clambering over those pews one Sunday at St. Mary’s and introducing yourself. Thank you for being my cheerleader all day and everyday, for your love and understanding, and for knowing me better than I do. Here’s to many more years of being an academic power couple.

Finally (and most importantly), I’d like to thank my family for making me me, for always believing in me, and for your amazing support. Mam and Dad, I couldn’t have done this without you, I hope I grow up to be like you. Ben and James, as your big sister I’m not really meant to say anything nice here, but thank you for making me smile, winding me up, and putting up with me bossing you about. My grandparents might not be here to see this, but it means the world to know how proud they would be of me finishing my PhD Thesis.

Contents

List of Figures

Chapter 1

Introduction

1.1 Rotation and Inertial Sensing

Inertial and rotation sensing are ubiquitous and important parts of our everyday lives, from MEMs based sensors in our mobile phones, to ring laser gyroscopes in aeroplanes. High precision and accuracy devices with high stability are of particular interest for inertial navigation, geodesy, geophysics, and tests of general relativity [1, 2]. Georges Sagnac published, in 1913, the first observation of a phase shift in an interferometer fringe due to rotation [3], with many of today's interferometers being based on this crucial result. Interestingly, Sagnac was more motivated with attempting to measure the 'whirling of the ether' than the seminal result about rotation [4] (much like other scientists of his time).

The Sagnac phase shift for an interferometer enclosing area A, rotating with rate Ω, using particles of relativistic energy E, is given by:

$$\Phi_{\text{Sagnac}} = \frac{4\pi E}{hc^2}\vec{A}\cdot\vec{\Omega}\,. \tag{1.1}$$

Here the direction of the area vector $\vec{A}$ is normal to the plane of the interferometer. This equation applies both to photon and atom based interferometers. If we want to measure rotation more precisely, we need the ratio between the measured phase shift and the rotation rate ($\delta\phi/\delta\Omega$) to be as large as possible. Thus we can either increase the size of the interferometer or increase the energy of the particles interfering. Naïvely, this means that by swapping the photons ($E = \hbar\omega$) for atoms ($E = mc^2$) we can increase the sensitivity of an interferometer by $mc^2/\hbar\omega$. For alkali atoms and visible

photons this is a factor of approximately 10^{11} [2].

Unfortunately, as for most things in life and a physics lab, it isn't really as easy as simply using atoms instead. Firstly, the factor 10^{11} is a per particle increase in sensitivity, meaning that the reduced flux of an atom interferometer compared to a light interferometer erodes the advantages of using atoms when integrating over time (i.e. the number of measurements is much greater for light interferometers). Error of an interferometer measurement when integrated over time scales as $1/\sqrt{N\tau}$ for atom number N and integration time τ, thus the precision improves with increasing flux and integration time [5]. Secondly, atom interferometry is a hard problem and requires a large amount of space (with experiments typically being the size of a room or even being a 10 m atomic fountain!). Despite this, because of the potential sensitivity and stability gains, atomic inertial measurement is a technology that could revolutionise metrology.

Our long-term challenge is to develop a prototype atom interferometer that could be used to measure rotation either in isolation or in a hybrid system alongside a classical light interferometer. To build an atom interferometer, we need five components [6]:

1. State selection (equivalent to the single mode of a laser)
2. Coherent splitting (the beam splitter)
3. Propagation - with low decoherence (the mirrors or wave-guide/fibre)
4. Coherent recombination (second beam splitter)
5. Read-out method (measure interference fringes)

In this thesis, we are largely concerned with items one and three in the above list (i.e. preparation and propagation), with the other components being investigated in another experiment in the group [7–10]. The rest of the introduction will set the scene, presenting background information and the current state of the art experiments relating to ultra-cold atoms, interferometry and optical potentials; concluding with an outline of the thesis.

1.2 Ultra-cold Atoms as Matterwaves

Quantum mechanics and wave-particle duality are crucial to our ability to perform atom interferometry and in fact for most other quantum sensors.

Following on from Einstein's discovery of wave-particle duality between light and photons through the photoelectric effect [11], de Broglie suggested that the same duality should occur for ordinary matter as well. He described this duality with what is now known as the de Broglie wavelength (λ) [12],

$$\lambda = \frac{h}{p}\,, \tag{1.2}$$

where h is the Planck constant, and p is the momentum of the particle. Its counterpart for energy and frequency (f) is $E = hf$. The simplest experiments demonstrating wave-particle duality are 'Young's slit' type experiments. These examples start with the original light-based experiment by Young in 1801 [13], moving to electron diffraction [14], and more recently to ultra-cold atoms [15–20] and large molecules [21, 22].

As is evident from Eq. 1.2, the larger a particle's momentum, the smaller its de Broglie wavelength. This explains why our perceived experience is classical: everything is too massive and too hot.

As we can describe atoms using wave-functions and create superposition states, we are able to interfere atoms just like coherent light in a classical interferometer. By placing atoms (or photons) into a superposition state, it is impossible to know which of two paths it takes (in fact one could say it takes both paths) and so we observe interference, with fringes in time and/or space.

In order to create these superposition states, we first have to prepare them in such a way that we can observe wave-like behaviour. This initial state selection part of an interferometer (or indeed almost any quantum sensor) is probably the most important element, and the part that has taken the longest to perfect (and has won a lot of people Nobel prizes!).

In the preparation stage of an interferometer, we perform state or momentum selection (or both), putting the atoms into a particular energy level or selecting a small subset of the momentum distribution. This can be as simple as sending atoms through a slit to select atoms of a similar momentum, or as complicated as cooling to degeneracy so that almost every atom occupies the same energy level (and the same wave-function).

In cold-atom experiments, we cool atoms to reduce the momentum spread and improve coherence. The methods used to do this are explained in Chap. 2. Here we

consider the size of the atom as the thermal de Broglie wavelength (λ_{dB}), the extent of the atom's wave-packet. For an atom of mass m, and temperature T, this is given by

$$\lambda_{\mathrm{dB}} = \frac{h}{\sqrt{2\pi m k_B T}} , \tag{1.3}$$

where k_B is the Boltzmann constant. As we cool atoms and their thermal de Broglie wavelength increases, we can reach the point at which λ_{dB} is comparable to the mean separation of the atoms and the individual wave-packets begin to overlap. At this point we can begin calling the cloud of cold atoms a condensate.

To reach condensation, we need to reduce the temperature at the same time as maintaining or increasing the atomic density. The relevant relation between density and temperature is described by a handy parameter called phase space density (PSD):

$$PSD = n\lambda_{\mathrm{dB}}^3 = n\left(\frac{h}{\sqrt{2\pi m k_B T}}\right)^3 , \tag{1.4}$$

where n is the atomic density. We reach quantum degeneracy when $PSD > 2.62$ for a box-shaped potential or at the centre of harmonic trap [23] or an average 1.20 for a harmonic trap [24].

Bose-Einstein condensates (BEC) are frequently used to study of quantum phenomena. Condensation was first proposed for photons by Bose in a letter to Einstein (who then translated and published the work in 1924) [25]. Bose applied the uncertainty principle to the Maxwell-Boltzmann distribution in order to describe microscopic particles for which fluctuations due to uncertainty would be significant. Work between Einstein and Bose resulted in the inception of Bose-Einstein statistics [26] as a description of identical particles with integer spin – Bosons. One can use Bose-Einstein statistics to show that, for a Bosonic ensemble at low temperatures (and high densities), there will be macroscopic occupation of the ground state.

The first experimental observations of a BEC [27, 28] heralded a new era of quantum mechanical experiments.

1.3 Atom Interferometry

At Strathclyde, we have performed interferometry in two different BEC experiments, with a new experiment (the one described in this thesis) currently being built. The

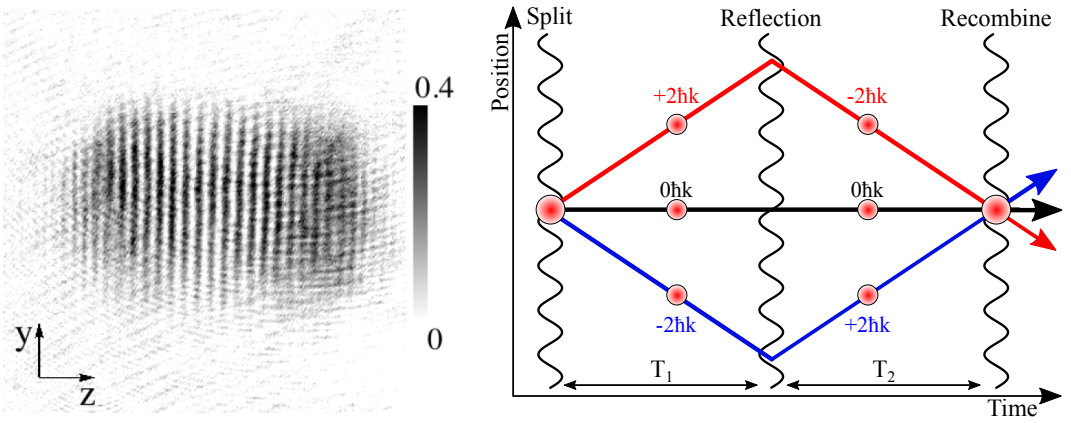

Figure 1.1: The fringes from the first Strathclyde interferometer, taken from Ref. [20], on the left, and a schematic of the second Strathclyde interferometer on the right, taken from Ref. [8].

first experiment performs Young's slits type interference by creating two BECs in a double well potential and allowing the two clouds to expand to overlap with one another and interfere [18–20, 29–31]. In this case the read-out is absorption imaging of spatial fringes in the final cloud. The second experiment is a three arm Mach-Zender interferometer using composite optical pulses (of a Kapitza-Dirac type) to split and recombine atoms in momentum space [7–10]. Here the read-out of phase is via momentum state populations which are measured using contrast interferometry. The two interferometers are shown in Fig. 1.1.

In general, there are many ways of doing interferometry. Superposition/splitting can be performed using the internal states of atoms [32, 33], the momentum states of atoms [9, 34], or by spatially separating parts of the cloud [35]. Each of these options are possible in the time or space domain (i.e. pulsed light beams versus spatially separate light beams). Between pulses, the atoms can either propagate freely in space, be confined in a trap (e.g. a double-well potential), or be guided (like light is guided in a fibre). Various configurations of such atom interferometers can be used to measure many other things apart from rotation. For example a gravimeter [36] using free-falling atoms, or a gravity gradiometer [37] using two clouds of atoms falling in a common laser beam. Constants such as Newton's constant G [38] and the fine structure constant [39–41] can be measured to high precision and cosmological phenomena can be investigated [42]. They can also be used to test the equivalence principle, and so test general relativity – a function which motivates putting cold atom experiments into

space [43–45].

Although BECs seem like the holy grail for atom interferometry as they have a very small momentum spread and have a large coherence length (compared to uncondensed cold atoms), mean field interactions can cause problems. These mean field interactions cause a BEC to expand after release from a trap, regardless of how little momentum the atoms had when in the trap. This increase in momentum can 'wash out' fringe contrast.

1.3.1 Inertial Sensor Sensitivity

In this thesis we are concerned with trying to build an inertial sensor, so we should understand existing state of the art technologies, for both quantum and classical interferometers. We compare these technologies in table 1.1. The first thing we notice in this table is that the best light interferometer [46, 47] has a better sensitivity than the best atom interferometer [33, 48]. We also see that results from the best atom interferometer were first published in 2000 [48] and improved upon in 2006 [33]. This time scale demonstrates how difficult the problem of rotation sensing is. We note that only one of the atom interferometers presented in the table uses a BEC, with this being a proof of concept experiment rather than demonstrating competitive sensitivity.

For navigation applications, it is estimated that short term stabilities of $< 0.1\,^\circ\,\mathrm{h}^{-1}$ ($480\,\mathrm{nrad\,s}^{-1}$) are required but demands increase greatly with $< 0.0005\,^\circ\,\mathrm{h}^{-1}$ ($2.42\,\mathrm{nrad\,s}^{-1}$) needed for strategic military applications [55]. In comparison, for tests of relativity (such as the Lense-Thirring effect), one would need to measure rotation rates of the order of $5 \times 10^{-3}\,\mathrm{prad\,s}^{-1}$ [48]. For geophysical studies, one needs to measure

Type	Experiment	Sensitivity $\mathrm{nrad/s/\sqrt{Hz}}$	Details	Size
Commercial ring laser gyro	Typical [1]	500	Drift: $0.0001\,^\circ\,\mathrm{h}^{-1}$	
	Honeywell GG1320AN [49]		Bias Stability: $0.0035\,^\circ\,\mathrm{h}^{-1}$	$454\,\mathrm{g}$; $4.4 \times 8.8\,\mathrm{cm}$
	Strategic (L-3 Space) [1, 50]	72	Bias Stability: $0.0001\,^\circ\,\mathrm{h}^{-1}$	$8.2\,\mathrm{kg}$; $12\,600\,\mathrm{cm}^3$
Large ring laser gyro	G-ring [46, 47]	12×10^{-3}	Drift: $0.164\,\mathrm{prad/s/day}$	$16\,\mathrm{m}^2$
Atom Interferometry	Thermal beam [33, 48]	0.6	Stimulated Raman Transitions Drift $< 96\,\mu^\circ\,\mathrm{h}^{-1}$	$2\,\mathrm{m}$
	Atomic Fountain [51]	140	Point-Source AI	$10\,\mathrm{m}$
	Exchanged MOTs [52]	1100	Stimulated Raman Transitions	$5000\,\mathrm{cm}^3$ head
	Continuous Atomic Fountain [53]	100	Stimulated Raman Transitions Drift: $1\,\mathrm{nrad\,s}^{-1}$ ($t_{int} = 10^4$)	$11\,\mathrm{cm}^2$ enclosed
	Toroidal BEC [54]	10^9	Collective Excitations	$16\,\mu\mathrm{m}$ radius ring

Table 1.1: A summary of interferometer sensitivities

the Earth's rotation rate of $\Omega_E = 72.92\,\mu\text{rad}\,\text{s}^{-1}$ to record variation of order $10^{-8}\ \Omega_E$ ($0.7\,\text{prad}\,\text{s}^{-1}$) [48].

One can estimate the shot-noise-limited resolution ($\Delta\Omega$) of a interferometer using the following Eq. [6, 56]:

$$\Delta\Omega = SNR_{\text{shot}}^{-1}\frac{\eta}{2\pi MA} = \frac{1}{2\pi MA\sqrt{N}}\,, \tag{1.5}$$

where the shot-noise-limited signal-to-noise is $SNR_{\text{shot}} = \eta\sqrt{2N}$, η is the contrast of the interferometry fringes, N is the number of atoms, A is the area of the interferometer, and M is the atomic mass. For a 100 µm radius ring, as proposed in Chaps. 5 and 6, one would anticipate a short term sensitivity of 9.1 µrad/s/Hz$^{1/2}$ [56] for a 26 ms interrogation time. This is not competitive with the state of the art listed in Tab. 1.1, however this is limited by the small enclosed area and is acceptable as a proof of concept experiment.

1.4 Waveguides for Atomtronics and Interferometry

One of the limiting factors for atom interferometers compared to light interferometers is the difference in area enclosed [46]. A light interferometer such as a ring laser gyro can enclose an area of many orders of magnitude larger than existing atom interferometers (16 m^2 in Refs. [46, 47] compared to 30 mm^2 in Refs. [33, 48] and 11 cm^2 in Ref. [53]). Atom interferometers are limited due to experiment size, the practicalities of optical beam sizes, and by atoms falling under gravity, all of which are problems due to requiring ultra-high vacuum. We can avoid some of these problems by confining or guiding the BEC or atoms, allowing much longer experiment times and potentially, if a ring guide is used, multiple revolutions that could be exploited to increase the area enclosed [57]. However, we note that when splitting confined BECs, uncertainty between atom number and relative phase resulting in unequal mean-field interactions can cause the superposition states to evolve at different rates and so dephasing would occur. This dephasing can limit the coherence time, for example in Ref. [6] it was limited to 50 ms.

The guiding of atoms and BECs for interferometry has been studied in detail [58, 59]. It was first demonstrated in Refs. [35, 60] and has been used in many experiments since then [30, 54, 61]. There are many uses for atom waveguides apart from interfer-

ometry [62]. For example, ring shaped potentials can be used to study various properties of BECs, from persistent currents [63–71] and non-equilibrium dynamics [72] to low dimensional atom systems [73]. Ring shaped traps can even be used to model effects such as the inflation of the universe [74]. Throughout the physics community there is also great interest in atomtronics – the ability to guide atoms in an analogue of a circuit (as can be done with light in optical waveguide arrangements known at integrated photonic circuits [75]). This would be a step change for interferometry, quantum computing and many other fields [62, 76].

1.4.1 Waveguides at Strathclyde

There are a great many ways to produce waveguides and ring potentials for atoms, in fact it has been a consistent focus of the Experimental Quantum Optics and Photonics (EQOP) group in Strathclyde, with each of the BEC experiments being conceived as a prototype ring system before changing focus.

In the first BEC experiment, a large diameter (10 cm) magnetic ring was created in combination with a Ioffe-Pritchard trap [18, 19, 29, 30]. The coils used to create this potential are shown on the left of Fig. 1.2. In this experiment atoms were successfully guided around the ring [30], however, interference fringes were not seen on recombination. The experiment has since changed to perform interferometry using two BECs in a double-well potential created by a Ioffe-Pritchard magnetic harmonic potential

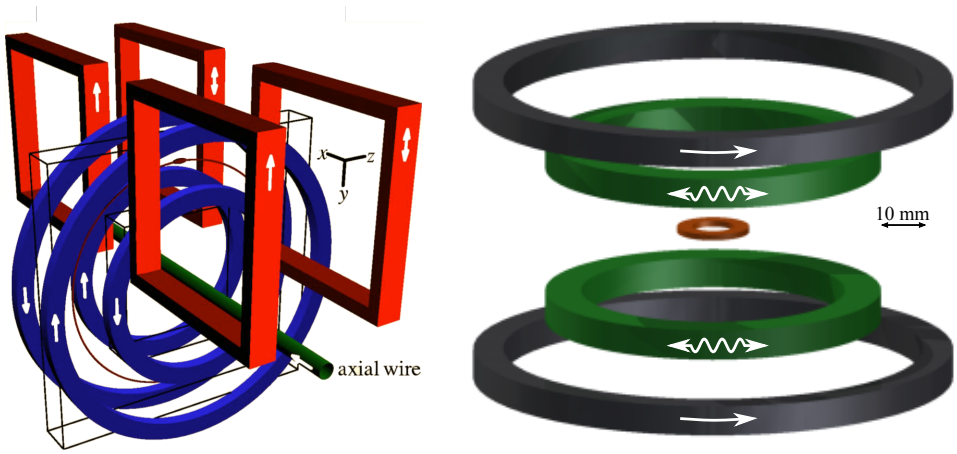

Figure 1.2: The coils for the two existing ring experiments at Strathclyde. The left image shows the 10 cm diameter ring (from Ref. [30]), and the right shows the AC coupled ring (from Ref. [8]).

and an optical dipole beam (which splits the trap into two wells) [18–20, 31]. In this arrangement, we perform a Young's slits type experiment allowing the atoms to expand into one another and interfere to produce fringes. Some of the results from this experiment are discussed in Sec. 4.2.

The second BEC experiment proposed the use of an AC coupled ring in which an induced current generates the trapping magnetic field (this coil structure is shown on the right of Fig. 1.2). Here, the use of induction removes 'edge effects' seen in conventional coils. This ring was proposed in Ref. [77] and realised in Refs. [7, 8, 61]. Since the AC ring work, the experiment has developed into a contrast interferometer with recent results published in Refs. [8–10], and further publications planned.

1.4.2 Waveguide Creation Methods

In the rest of the physics community, a variety of experiments have created or proposed waveguides for atoms and BECs, using a mixture of optical dipole or magnetic based traps. The three basic elements or building blocks needed to create a circuit are a planar waveguide, a toroidal (ring) trap, and a beam splitter; with these three components one could in principle create an arbitrary circuit. There a few general approaches taken to create these components: either magnetic or optical and either static or time-averaged (also known as painted potentials) with hybrid systems of these being possible.

We first consider the use of magnetic field based potentials (as used in the two existing BEC experiments at Strathclyde). The Zeeman interactions described in Sec. 2.2.2 create this form of potential. For linear waveguides or beam splitters, these potentials tend to be created using shaped conductors, i.e. wires or micro-wires on an atom chip or another substrate. Examples of this form of guiding for thermal atoms appear in Refs. [78, 79]. Electromagnetic coils have also been used to successfully guide BECs, for example the static 10 cm ring in Ref. [30], the few-mm diameter time-averaged ring in Ref. [80], and the linear, two armed interferometer in Refs. [35, 57, 81]. Other similar approaches use rf-dressed time-averaged traps to create ring potentials Refs. [82–86], and induction (or rf-induction) based traps have been proposed in Refs. [77, 87–90] and implemented in Refs. [7, 61]. Out of these examples, only one system has been successfully used for interferometry [35, 57], in which optical pulses were used to perform coherent splitting rather than the waveguide itself.

For the case of optical traps, early attempts to guide atoms using the dipole force steered atoms through the centre of hollow-core optical fibres [91,92], a method which limits some applications due to the atoms being inside a fibre. Development since then can be roughly split into three approximate, informal categories: composite potentials which are built from several component fields; painted potentials, which are the time-average of a moving dipole beam; and holographic traps which use an optical element or an array of elements to tailor the propagating electric field.

Examples of composite potentials include crossed dipole beams used to make a beam splitter [93, 94], planar waveguides using magneto-optical surface traps [95], and guiding with a collimated laser beam (working like the push beam in the magneto-optical trap discussed later) [96, 97]. These techniques have been particularly successful for the creation of rings used for studying persistent currents in BECs [64, 98]. For example, optical ring traps in the group of Gretchen Campbell are produced using a combination of a Laguerre-Gauss beam (for radial confinement) produced using a DMD and light sheets (for axial confinement) [65–69, 74]. Boxes and other interesting potentials have also been created in a similar way [99–101].

Painted potentials are generally made using a rapidly scanned laser beam which is deflected by either two 1D acousto-optical deflectors (AODs) or one 2D AOD. This approach is typically combined with at least one light sheet to provide axial confinement. It has been successfully used to produce ring-traps in the group of Halina Rubinsztein-Dunlop [102, 103], various atomtronic circuit elements in Refs. [104, 105] and other optical potentials such as boxes [106, 107]. Painted potentials are typically used in combination with other potentials such as a light sheet or a patterns derived using holography.

Finally, we have holographic and beam shaping traps, in which the whole electric field is shaped such that the required potential comes to a focus in the desired plane. This technique has the possible capability of being able to produce an optical trap using only a single laser beam [100]. For holography, we have four main options: composite micro-optical arrays [108], spatial light modulators (SLMs) [99, 109], digital mirror devices (DMDs), and diffractive optical elements like Fresnel zone plates. The final three of these provide beam shaping through holography, where phase (or intensity) modulation modifies an electric field such that the desired pattern is reproduced down-stream. Examples of experiments using holographic techniques include Refs. [110–120].

Group	Status	Type	Radius μm	ν_r Hz	ν_z Hz	Trap Depth nK
Strathclyde [29, 90]	BEC	Magnetic Coils	50 000			
Strathclyde [61, 77]	Cold atoms	Induced Magnetic	2600	16	60	10 000
Garraway/Perrin/Arnold [87]	Proposed	Inductive dressed	300	750	180	31 000
Foot [83]	BEC	Time-Averaged RF	50 to 262	90 to 120	50 to 80	
Mompart [101]	BEC	Conically refracted ring + light sheet	170	300	170	280
Perrin/Garraway [84] (Realized in Refs. [121, 122])	Proposed BEC	RF-dressed Magnetic Trap + Standing Wave	100 Adjustable	1100	43 000	
Rubinsztein-Dunlop [103]	BEC	Time-Averaged Dipole (bi-directional scan)	82	50	140	
Rubinsztein-Dunlop [102]	BEC	Time-Averaged Dipole	70	47	110	190
Campbell [67]	BEC	Composite Optical	40	110	550	700
Stamper-Kurn [54]	BEC	Composite Optical	16	86	260	

Table 1.2: A summary of parameters for rings discussed in the literature. $\nu_{r,z}$ refer to the radial and axial trap frequency of the rings. This list is by no means exhaustive and is ordered by ring radius, from largest to smallest.

As discussed above, there is a wealth of literature comprising proposals and demonstrations of ring/toroidal potentials for various different purposes. The parameters of a selection of these rings are summarised in Tab. 1.2. We are particularly interested in the radius and radial and axial trap frequencies ($\nu_{r,z}$), as these parameters will help inform design choices later in this thesis.

1.5 Thesis Outline

In this thesis I will begin by describing the techniques used to trap and manipulate atoms in Chapter 2, beginning with optics (Section 2.1), before moving on to trapping and cooling techniques (Section 2.2), followed by absorption imaging (Section 2.3).

Following this, in Chapter 3, the design and build process for a new BEC experiment will be detailed. At the time of writing this thesis, a 3D magneto-optical trap has been obtained in the experiment.

Chapter 4 explains the theory of BECs, beginning with general theory before discussing ring geometries in Section 4.1.3 (as preparation for later chapters) and phase and coherence in Sections 4.1.4 and 4.1.5. After this the chapter moves on to discuss some results obtained using the older Strathclyde BEC experiment in Section 4.2.

At this point in the thesis, the subject turns to the use of Fresnel zone plates (FZPs)

for creating ring shaped potentials to confine BECs during interferometry. Chapter 5 covers the theory surrounding FZPs, numerical simulations to compare them to existing technology (SLMs), designs for manufacture, and finally simulations pertaining to a hybrid FZP-SLM system. This chapter is based on our paper published in 2016: 'Comparative simulations of Fresnel holography methods for atomic waveguides' [123].

Following on from this, Chapter 6 discusses testing the manufactured zone plates through optical imaging of the potentials (without loading atoms into the trap).

Finally, Chapter 7 covers the theory necessary to design a second generation of zone plates. We first discuss alternative ring potentials in Section 7.3, then describe improvements to our simulation algorithm in Section 7.2.2, before finally completing numerical simulations to help chose ring parameters for the next generation of zone plates.

1.6 Research Outputs

1.6.1 Publications

- Y. Zhai, C. H. Carson, **V. A. Henderson**, P. F. Griffin, E. Riis, and A. S. Arnold, "Talbot-enhanced, maximum-visibility imaging of condensate interference," *Optica* **5**, 80-85 (2018)
- **V. A. Henderson**, P. F. Griffin, E. Riis, and A. S. Arnold, "Comparative simulations of Fresnel holography methods for atomic waveguides," *New J. Phys.* **18**, 025007 (2016)
- **V. A. Henderson**, M. Y. H. Johnson, Y. B. Kale, P. F. Griffin, E. Riis, and A. S. Arnold, "Optical Characterisation of Fresnel Holograms for Atomic Waveguides," In advanced prep.

1.6.2 Conferences and Presentations

- Talk title: "Fresnel Holography for Atomic Waveguides," (April, 2018)
  - Invited talk, Humboldt-Universität zu Berlin
- Poster title: "Fresnel Holography for Atomic Waveguides," (2017)

  - QuAMP, Glasgow. Awarded EPJ poster prize.
  - ICOLS, Arcachon, France.

- Poster title: "Fresnel Holography for Atomic Waveguides and Miniaturised Rotation Sensing," (2016)
  - Workshop on Many-body Dynamics and Open Quantum Systems (DOQS), Glasgow.
  - Multicomponent Atomic Condensates and Rotational Dynamics (MACRO), Newcastle.

- Poster title "Maximum Contrast Interferometry and Coherence in Bose-Einstein Condensates," (2015)
  - Non-Equilibrium Quantum Dynamics in Low Dimensions, Durham.
  - CLEO/EQEC, Munich, Germany.
  - Scottish Universities Summer Schools in Physics (SUSSP71): Frontiers in Quantum Dynamics and Quantum Optics, Glasgow.

Chapter 2

An Ultra-Cold Atom Recipe Book

Within this chapter, I will present the theory of techniques and tools used to trap, cool and manipulate atoms within our particular atom interferometry experiment, proceeding chronologically through the various stages that the atoms experience.

I like to think of the process of making a Bose-Einstein Condensate (BEC) as a recipe: you mix 'ingredients' (atoms, vacuum, light and magnetic fields) using certain 'methods' (following the example of groups that have come before you). By careful engineering of the vacuum chamber and precise control of magnetic fields, we can implement 'methods' for cooling and controlling atoms such as magneto-optical traps (MOT), dipole trapping, evaporative cooling; the list is almost endless.

The most common atom used in ultra-cold atom experiments is Rubidium (in either its 85 or 87 isotopes). It's an almost ideal atom for laser cooling due to its simple energy level structure - the transitions are easy to reach with cheap lasers and only two frequencies are required to produce a closed cooling cycle. Rubidium is also easy to vaporise without using an oven and extra pre-cooling steps (like the Zeeman slowers needed for atoms like Strontium [124–126] and Lithium [127]). For BEC creation Rubidium is particularly favourable due to its scattering length.

There are 2 main types of traps and cooling mechanisms for ultra-cold atoms: dissipative potentials or structures, such as molasses and magneto-optical traps, used for cooling; and conservative potentials, such as dipole potentials and purely magnetic traps, used for holding and guiding atoms.

2.1 Gaussian Optics

When creating trapping potentials and aligning optics, one needs to have strong understanding of Gaussian optics, from basic beams and Gaussian propagation, to higher-order solutions to wave-equations such as Laguerre-Gaussian (LG), Hermite-Gaussian (HG), or Bessel beams. In this section, I'll begin by defining the basic Gaussian beam equation, discuss its propagation and then define higher-order beams.

The electric field ($E(r,z)$) of a Gaussian beam at longitudinal position z and radial position r is given by,

$$E(r,z) = E_0 \frac{w_0}{w(z)} \exp\left(\frac{-r^2}{w(z)^2}\right) \exp\left[-i\left(kz + k\frac{r^2}{2R(z)} - \psi(z)\right)\right] , \tag{2.1}$$

where E_0 is the electric field magnitude at the origin, w_0 is the $1/e^2$ radius of the waist (the narrowest point of the beam), $w(z)$ is the waist at position z, k is the wave-vector as defined by $k = 2\pi/\lambda$ for a wavelength λ, $R(z) = z\left[1 + (z_\mathrm{R}/z)^2\right]$ is the radius of curvature of the wavefront at position z, $z_R = \pi w_0^2/\lambda$ is the Rayleigh length, and $\psi(z) = \arctan(z/z_\mathrm{R})$ is the Gouy phase at position z. The radius of curvature of a collimated beam tends to infinity but any real Gaussian beam with not be fully collimated and will still have a Rayleigh length.

When observing a cylindrically symmetric beam, we measure the intensity $I(r,z)$, as given by,

$$I(r,z) = \frac{\epsilon_0 c}{2} |E(r,z)|^2 = I_0 \left(\frac{w_0}{w(z)}\right)^2 \exp\left(\frac{-2r^2}{w(z)^2}\right) , \tag{2.2}$$

where, for a beam with power P_0, the peak intensity is given by $I_0 = 2P_0/\pi w_0^2$.

The width of a propagating beam ($w(z)$) evolves as,

$$w(z)^2 = w_0^2 \left(1 + \left(\frac{z}{z_R}\right)^2\right) . \tag{2.3}$$

The Rayleigh length (z_R) is the point at which $w(z_R) = \sqrt{2} w_0$. This equation only holds for a beam which is diffraction limited.

If a beam is diffraction limited, its beam parameter product, the product of the divergence angle (θ) and waist, is λ/π. The ratio between this ideal and the measured value gives the M^2 value, so $M^2 = \pi w_0 \theta/\lambda$. It is noted that the Rayleigh length

decreases with increasing M^2. The waist of a diffraction limited beam propagating in free space from a lens of diameter D and focal length f, and numerical aperture NA is,

$$w_0 = \frac{\lambda}{2NA} = \frac{\lambda}{2\sin\theta} = \frac{\lambda f}{D} \,. \tag{2.4}$$

2.1.1 Higher Order Modes

Although basic Gaussian beams are the most widely used beam shapes for atomic trapping, LG, HG and Bessel beams are of great interest for trapping schemes for many reasons including the presence of intensity zeros and thus the potential for dark traps [120] (dark traps are discussed in more detail in Secs. 2.2.8 and 7.3).

Laguerre-Gaussian and Hermite-Gaussian Beams

Upon propagation most beam profiles change due to diffraction, however certain modes of the electric field have a constant shape. The simplest of these modes is a Gaussian.

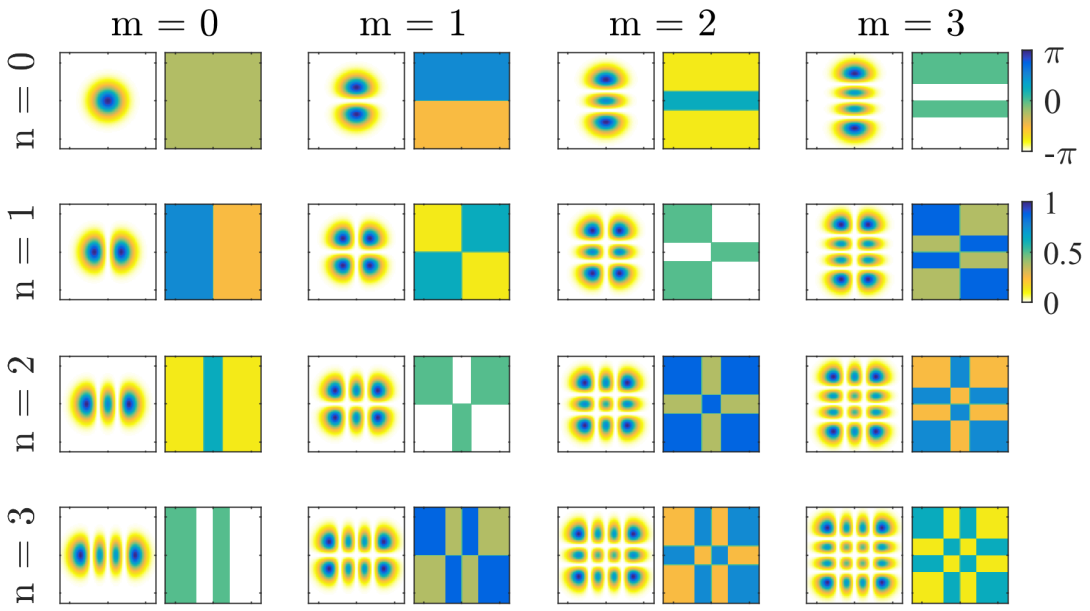

Figure 2.1: The electric fields corresponding to various Hermite-Gaussian modes as defined by Eq. 2.5, with the left of each column showing the normalised intensity ($|E|^2$) and the right showing the phase (plotted on a scale between $-\pi$ and π). The columns (rows) show different m (n). All plots show a 5×5 mm area with the waist of the beam being 1 mm.

This means that, for example in a cavity, one can decompose a beam into a series of these modes. LG and HG modes are two different, complete sets of these orthogonal modes, with LG beams providing circularly symmetric solutions and the HG modes being separable in Cartesian co-ordinates and so looking square.

The equation for a HG beam is shown below, with the first eight modes shown in Fig. 2.1,

$$E^H_{m,n}(r,z) = \frac{E_0}{w(z)} H_m\left(\frac{\sqrt{2}x}{w(z)}\right) H_n\left(\frac{\sqrt{2}y}{w(z)}\right) e^{-r^2/w(z)^2} \exp\left[-i\left(kz + k\frac{r^2}{2R(z)} - \psi_{m,n}(z)\right)\right], \tag{2.5}$$

where H_m and H_n are m^{th} and n^{th} Hermite polynomials, and the modified Gouy phase is $\psi_{m,n}(z) = (1+m+n)\ \arctan(z/z_R)$.

For an LG beam, the equation takes the following form, with the first eight modes

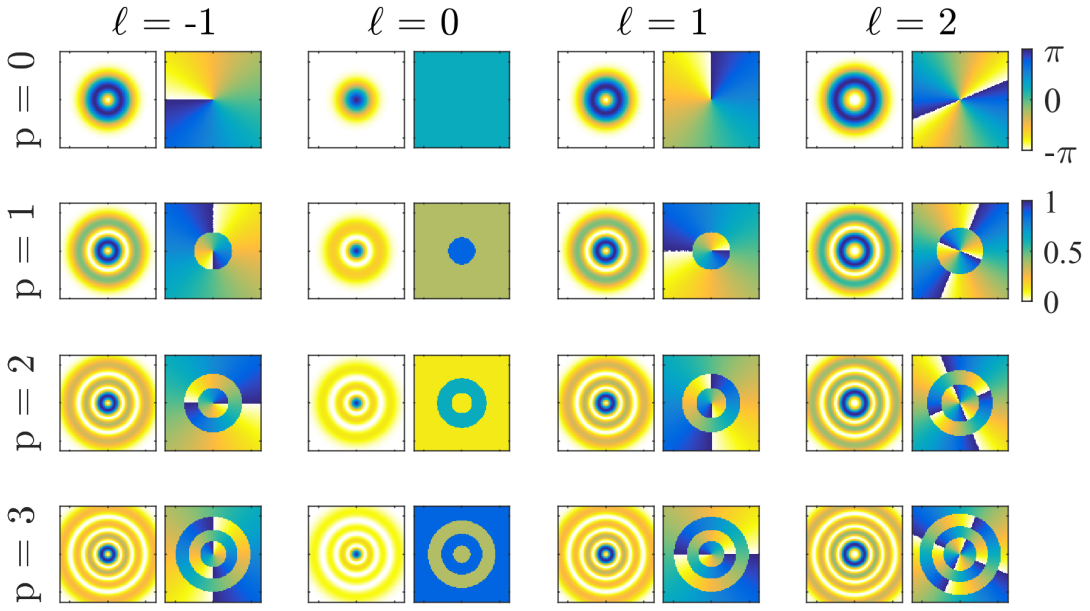

Figure 2.2: The electric fields corresponding to various Laguerre-Gaussian modes as defined by Eq. 2.6. The columns (rows) show different ℓ (p), with the left of each column showing the intensity and the right showing the phase (plotted on a scale between $-\pi$ and π). All plots show a 5×5 mm area with the waist of the beam being 1 mm.

shown in Fig. 2.2,

$$E^L_{\ell,p}(r,z) = E_0 \frac{e^{i\ell\phi}}{w(z)} \left(\frac{r}{w(z)}\right)^{|\ell|} L_p^{|\ell|}\left(\frac{2r^2}{w(z)^2}\right) e^{-r^2/w(z)^2} \exp\left[-i\left(kz + k\frac{r^2}{2R(z)} - \psi^L_{\ell,p}(z)\right)\right] , \tag{2.6}$$

where ℓ and p refer to the number of phase windings (integer multiples of $\hbar$ orbital angular momentum (OAM) per photon) and number of intensity rings (e.g. $p = 0$ is a Gaussian) respectively. L^ℓ_p is an associated Laguerre polynomial, and $\psi^L_{\ell,p}(z)$ is the the Gouy phase for such a beam: $\psi^L_{\ell,p}(z) = (|\ell| + 2p + 1)\ \arctan(z/z_R)$.

When we use LG beams in an atomtronic context, it's important that we note that the intensity maximum of a beam with $p = 0$ lies at radius [128]

$$r_\ell = w\sqrt{|\ell|/2}\,, \tag{2.7}$$

and the electric field in the radial direction has a full-width-half-maximum of $\sqrt{2\ln 2}w$ [120]. The relations for $p > 0$ are much more complicated as p corresponds to the number of radial intensity minima (for $|\ell| > 0$). Both these identities will be used in Sec. 5.2.

Bessel Beams

Although the overall profile of a LG and HG beam stays constant, its size changes due to diffraction. Bessel beams however, fall into a category of (theoretically) non-diffracting beams, and are self-healing [129, 130]. Bessel beams have an electric field proportional to a Bessel function of the first kind (J_0) and a Gaussian envelope. For example, we can describe a Bessel-Gauss beam with the following equation:

$$E(r, z = 0) \propto J_0(k_r r) \exp\left(-\frac{r^2}{w_0^2}\right) , \tag{2.8}$$

where $k_r = \sqrt{k^2 - k_z^2}$ is the size of the component of the wave-vector orthogonal to the z-axis [129]. A Bessel beam which is an exact solution of the Helmholtz equation has infinite energy, therefore it is impossible to reproduce one experimentally, but there are many ways to approximate them, such as using axicons [131, 132] and Spatial Light Modulators [133].

Within the investigations presented in this thesis, Bessel beams are of interest due to the zero crossing in the electric field equation. This makes them particularly interesting for producing dark rings [134] as the zero-crossing will always have a true intensity zero (rather than a minimum). The first four Bessel functions of the first kind are shown in Fig. 2.3, alongside the corresponding Bessel-Gauss (like Eq. 2.8) function.

2.2 Cooling and Trapping

With the advent of narrow line-width lasers one can exert significant forces on atoms [135] and use them for cooling [136–138]. Initially, such work was limited to Sodium atoms due to the availability of suitable (expensive dye) lasers, however, once cheap diode laser became accessible, other alkali atoms could be focused on.

Before considering the various potentials which can be used to trap, cool and manipulate atoms, it is useful to consider the (time-independent) Hamiltonian of an atom,

$$\hat{H}\left|\psi\right\rangle = E\left|\psi\right\rangle = \left(-\frac{\hbar^2}{2m}\nabla^2 + U\right)\left|\psi\right\rangle \ , \tag{2.9}$$

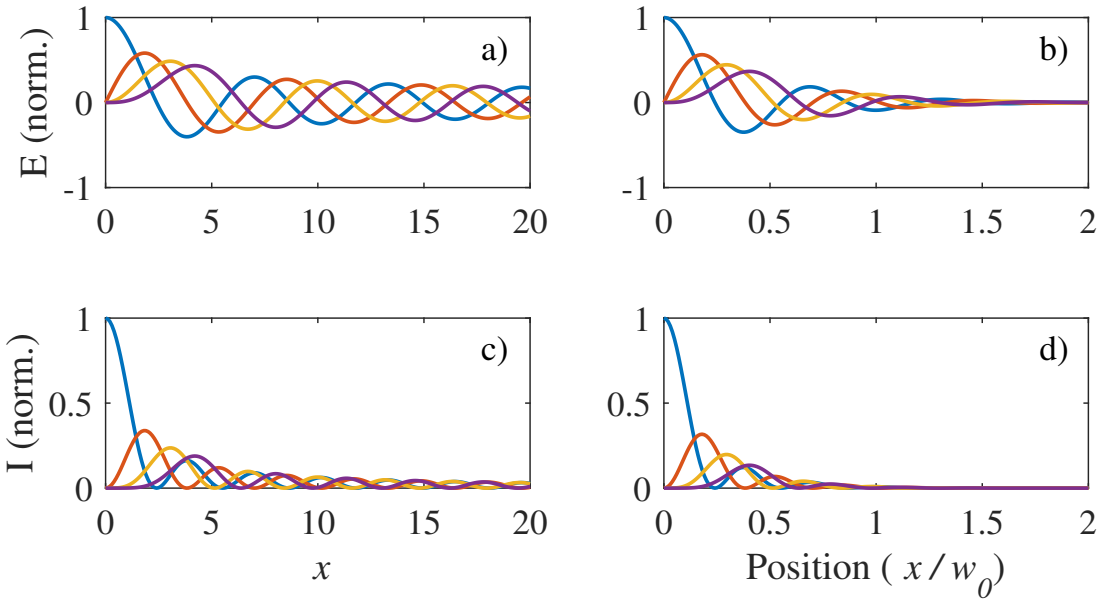

Figure 2.3: In a and b we show the electric field amplitude for a Bessel beam of the first kind ($J_\alpha(x)$) and a Bessel-Gauss beam (see Eq. 2.8) respectively, both with $k_r = 1$, for $\alpha = 0, 1, 2, 3$ (blue, red, yellow, purple). In c and d we show the intensity equivalent of a and b respectively.

which describes the atom's wavefunction (ψ) as the eigenvectors of the Hamiltonian with eigenvalues of the energy E. The basic Hamiltonian is split into contributions from kinetic energy (the $-\left(\hbar^2/2m\right)\nabla^2$ term) and the potential U (which in the context of our experiment is the contribution of the trapping potential). Additional terms can be added to describe the effects of field interactions (such as Zeeman splitting and Stark shifts), atom-atom interactions, and internal interactions (like hyperfine splitting). In Chap. 4, this formalism will be applied to introduce Bose-Einstein condensation.

2.2.1 Dissipative Light Forces

When a photon of angular frequency ω is absorbed by an atom, its momentum of $\hbar k$ is transferred to the atom. Conversely, when a photon is emitted by an atom, its momentum is transferred away from the atom, giving a recoil in the direction inverse to the photon direction. As the spontaneous emission of photons is inherently random (over the dipole radiation pattern of the atom), over many cycles of absorption and emission, emission recoils average to zero, and absorption recoil, resulting in an acceleration or force in the direction of the laser. Such scattering processes are the fundamental building blocks upon which all laser cooling techniques are built.

We can derive the force imparted by a laser beam to an atom by considering the rate of change of momentum, this means: $\vec{F}_{\text{scatt}} = photon\ momentum \times scattering\ rate$. We can describe the scattering rate using the optical Bloch equations for a two-level atom: the scattering rate is given by $R_{\text{scatt}} = \Gamma\rho_{22}$, where Γ is the decay rate of the state (the linewidth), and ρ_{22} is the excited state population, this means that we can represent the scattering force in term of the Rabi frequency Ω or the intensity and saturation intensity ($I/I_{\text{sat}} = 2\Omega^2/\Gamma^2$) [23, 139]:

$$\vec{F}_{\text{scatt}} = \hbar\vec{k}\frac{\Gamma}{2}\frac{\Omega^2/2}{\Delta^2 + \Omega^2/2 + \Gamma^2/4} = \hbar\vec{k}\frac{\Gamma}{2}\frac{I/I_{\text{sat}}}{1 + I/I_{\text{sat}} + 4\Delta^2/\Gamma^2}\ , \tag{2.10}$$

where $\Delta = \omega - \omega_0$ is the detuning of the laser from resonance.

When an atom is moving, we need to account for the Doppler shift in the frequency of light that the atom 'sees': $\omega' = \omega \pm \vec{k}\cdot\vec{v}$. The Doppler shift experienced by a moving atom leads us to introduce optical molasses, a damping or frictional force for atoms in light (if the detuning $\Delta < 0$). If an atom is placed in a pair of counter-propagating beams, it will experience light of a frequency shifted up (down) from the frequency of

the laser beam it is travelling towards (away from), this results in a molasses force:

$$F_{\text{molasses}} = F_{\text{scatt}}(\Delta - kv) - F_{\text{scatt}}(\Delta + kv) \approx -2\frac{\partial F}{\partial \omega}(\Delta)\, kv \,, \tag{2.11}$$

which means that we have a restoring force proportional to the velocity, just like friction or damping. Applying six counter-propagating beams (or three retroreflected beams) to a cloud of atoms, allows us to cool in 3D (as first demonstrated in [137]), assuming that the laser is red detuned ($\Delta < 0$). Although, to cool in N dimensions, one only strictly needs $N + 1$ beams rather than $2N$ [140]. We note that recently, blue-detuned MOTs have been demonstrated which cool using dark ground states and are anticipated to be used to produce molecular MOTs [141].

The temperatures reached by cooling with optical molasses are limited by the stochastic nature of the absorption-emission cycles used, leading us to the Doppler temperature T_{Doppler} which is typically of the order 0.1 mK [23], though lower temperatures are in practice reached through mechanisms described in Sec. 2.2.6.

When working with multi-level atoms, such as alkali atoms like ^{87}Rb, rather than the absorption-emission cycle operating between only two levels, it is generally possible for the atom to fall to a different hyperfine ground state. Thus it is necessary to 'close' the transition with an additional light of a different frequency, pumping the atoms out of the other ground state. This additional light is referred to as the 'repump' and can either be derived from a separate laser and overlapped with the cooling light or be introduced as a side-band on the cooling light. The energy level diagram of ^{87}Rb is shown in Fig. 3.1, which also includes the frequencies of light used for cooling and repumping in our experiment.

2.2.2 Atoms in Magnetic Fields

Neutral atoms with magnetic moments ($\vec{\mu}$) feel a force when in an inhomogeneous magnetic field ($\vec{B}$):

$$\vec{F} = \vec{\nabla}(\vec{\mu} \cdot \vec{B}) \,, \tag{2.12}$$

as was demonstrated in the Stern-Gerlach experiment [142–144]. The Zeeman effect results in an additional term in the atom's Hamiltonian of,

$$H_{ZE} = -\vec{\mu} \cdot \vec{B} \, . \tag{2.13}$$

The total magnetic moment of an atom is

$$\vec{\mu}_{\text{atom}} = -g_J \mu_B \vec{J} + g_I \mu_N \vec{I} = -g_F \mu_B \vec{F} \, , \tag{2.14}$$

where μ_B is the Bohr magneton, $\vec{J}$ is the total electron angular momentum, $\vec{I}$ is the nuclear spin, $\vec{F}$ is the total *atomic* angular momentum, $g_{J,I,F}$ is the Landé g-factor, and μ_N is the nuclear magneton, which is much smaller than the Bohr magneton. The total angular momentum of the electron is the sum of angular momentum $\vec{L}$ and spin $\vec{S}$, and equivalently, $\vec{F}$ is the sum of the nuclear spin and the electron angular momentum: $\vec{F} = \vec{L} + \vec{S} + \vec{I} = \vec{J} + \vec{I}$. This results in the Zeeman energy shift of

$$\Delta E_{ZE} = g_F \mu_B m_F |\vec{B}| \, . \tag{2.15}$$

Using this equation, we can start to talk about weak and strong field seeking atoms. If $g_F m_F > 0$, then ΔE_{ZE} is minimised when the field is minimised, i.e. the atoms experience a weak field. Conversely, if $g_F m_F < 0$ the opposite is true and we have a strong field seeking state.

2.2.3 Magnetic Field Creation

There are two basic coil combinations which are used in cold atom experiments - Helmholtz and Anti-Helmholtz coils, as shown in Fig. 2.4. Two sets of coils are placed co-axially with a separation between them, in the Helmholtz (anti-Helmholtz) orientation, current flows through the wires in the same (opposite) directions, and at the centre of the coils a line (point) of magnetic field minimum is produced. True Helmholtz coils, which minimise the non-uniformity of the field at the centre of the coils have a separation equal to the coil radius. Anti-Helmholtz coils are often called quadrupole coils, due to the quadrupole field close to the centre of the coils, that has the form:

$$\vec{B}(\vec{r}) = B_1 \left(-\frac{x}{2}, -\frac{y}{2}, z \right) \, , \tag{2.16}$$

with B_1 dependent on coil diameter, separation, number of turns, and current through the wire; it is derived using the Biot-Savart Law [145]. The resulting potential is:

$$U(x, y, z) = \mu_B g_F m_F B_1 \sqrt{\frac{x^2}{4} + \frac{y^2}{4} + z^2}\,. \tag{2.17}$$

The first demonstration of magnetic trapping used a quadrupole trap to collect atoms from a slowed atomic beam [146]. Although quadrupole coils are well suited for use within MOTs, at much lower temperatures (i.e. when evaporative cooling to BEC) the presence of a magnetic field zero means that spin flips can occur, causing atoms to be lost from the trap. These Majorana flips [147–150] occur when the thermal fluctuations are sufficient to 'flip' atoms from a confined to an unconfined hyperfine level. Close to a point of zero field, the Zeeman splitting on the hyperfine levels becomes small and so the rate of this flipping (i.e. losses) becomes higher. However in scenarios such as evaporative cooling, the losses prevent runaway evaporative cooling, so the point of zero field must be removed. There are various approaches to solve this problem in magnetic traps, from optically 'plugging' the hole [151], using a time-averaged, orbiting potential (TOP) [152], an adiabatic dressed potential [153], or using a Ioffe-

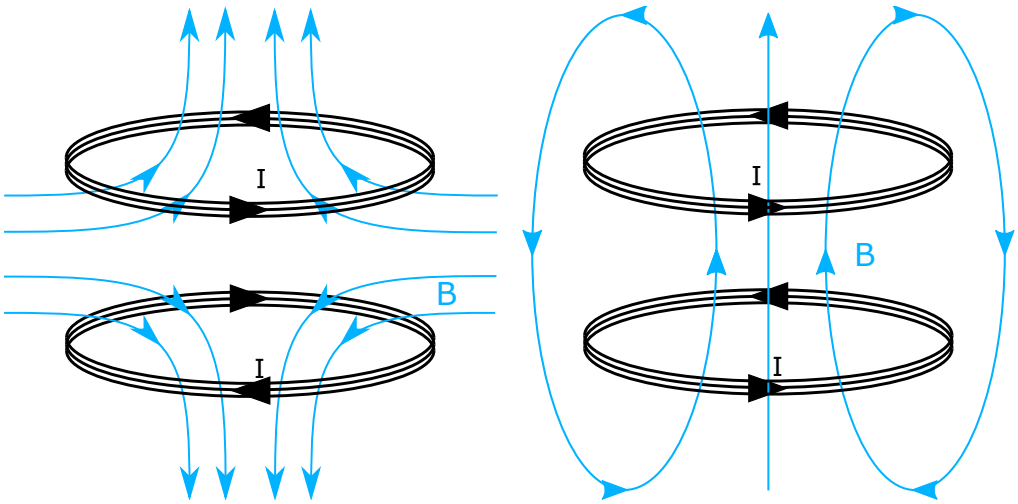

Figure 2.4: The left and right sets of coils show an anti-Helmholtz and Helmholtz arrangement respectively. The anti-Helmholtz coil forms a quadrupole field, as is used in MOTs; and Helmholtz coils are used to create bias fields or to shift the centre of a MOT.

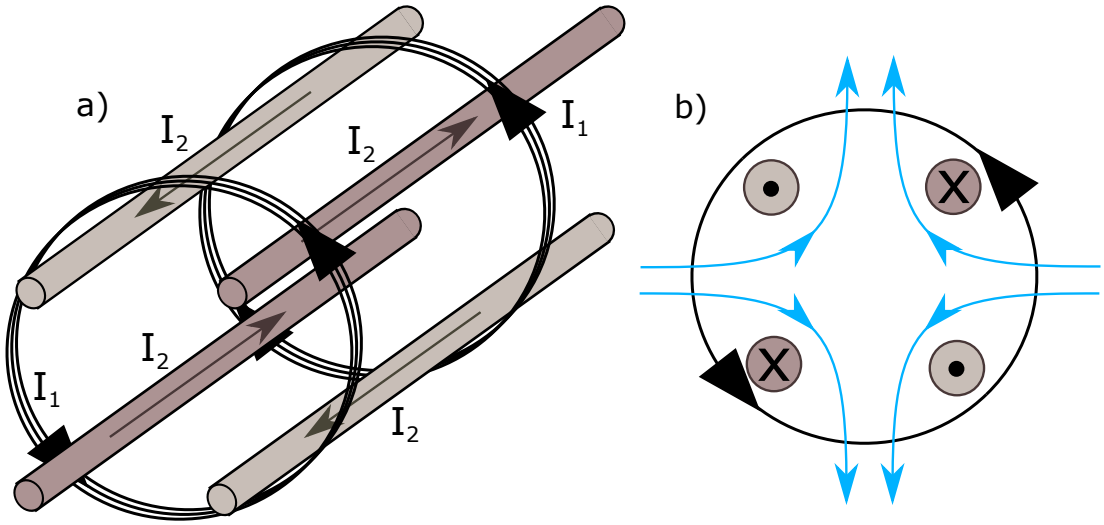

Figure 2.5: Ioffe-Pritchard coil configuration. The wires generate an elongated quadrupole field in the transverse direction (as shown by the blue field lines in b)). The Helmholtz coils at either end provide axial confinement.

Pritchard (IP) trap [154]. A typical form of IP coils are shown in Fig. 2.5, where four equidistant, straight wires produce a 2D, transverse, quadrupole magnetic field, and the Helmholtz coils at either end provide confinement in the axial direction. The resulting field is generally hyperbolic in the radial direction (parabolic (linear) close to (far from) the centre) [155].

2.2.4 Magneto-Optical Traps

Although molasses provides a cooling mechanism, eventually, atoms will diffuse out of the centre of the potential as the force is velocity dependent rather than position dependent. One can introduce a position dependence to the restoring force by adding a quadrupole magnetic field which provides this dependence through the Zeeman shifting of magnetic sub-levels [156].

We can begin describing a magneto-optic trap (MOT) by considering the Zeeman shifts of the (hypothetical) $F = 0 \rightarrow F' = 1$ transitions. In a quadrupole field, the magnetic field is approximately linear close to the centre of the trap, so that the hyperfine energy-levels of the $F' = 1$ state will be linearly dependent on position from the trap centre. Selection rules mean that left (right) circularly polarised light drive σ^- (σ^+) transitions with $\Delta m_F = -(+)1$. If we have counter-propagating beams of opposite circular polarisation, as in Fig. 2.6, atoms with a positive position will have

$m_F = -1$ closer to resonance than the $m_F = +1$ level and thus will absorb more photons from the σ^- beam than the σ^+ and feel a net force towards the centre of the trap. Likewise, atoms with negative position, will have the $m_F = +1$ shifted closer to resonance and so will absorb more light from the σ^+ beam (the beam travelling in the positive z direction), resulting in a net force towards the centre of the trap.

We can calculate the forces on atoms in the trap in the same way as we did for molasses in Eq. 2.11

$$F_{\mathrm{MOT}} \approx -2\frac{\partial F}{\partial \omega} kv + 2\frac{\partial F}{\partial \omega_0}\beta z \,, \tag{2.18}$$

where $\beta = \frac{g_F \mu_B}{\hbar}\frac{dB}{dz}$, and the equipartition theorem can be applied to deduce the size and temperature of the cloud of atoms in the MOT [157]:

$$k_B T = m v_{\mathrm{rms}}^2 = \beta z_{\mathrm{rms}}^2 \,. \tag{2.19}$$

Eq. 2.18 is an approximation which only holds for atoms close to the centre of the trap (i.e. where Doppler and Zeeman shifts are small compared to detuning). The size and temperature relation of Eq. 2.19 does not apply for large atom number MOTs where re-

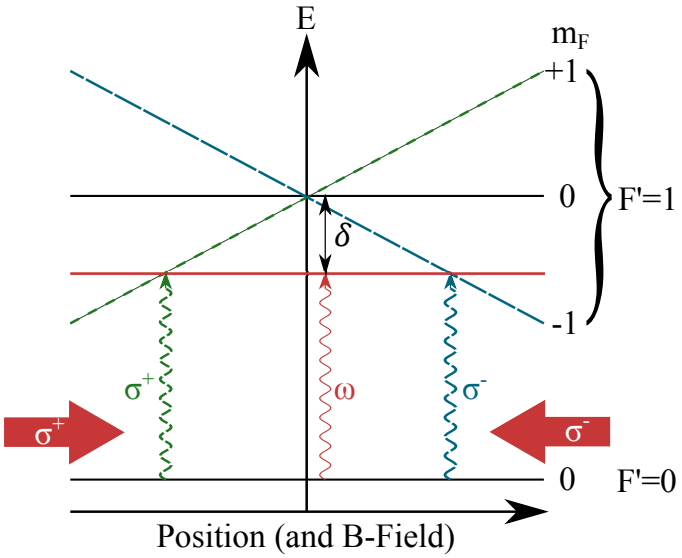

Figure 2.6: A schematic of atom-light interactions modified by a linear magnetic field in the centre of a MOT ($B \propto z$). The magnetic field causes a linear shift in the $m_F = \pm 1$, the green and blue line show the positive and negative sublevels respectively. This shift brings the sublevels into resonance with different cooling beams in different positions.

absorption of emitted photons results in an additional outward radiation pressure [23].

Properties of MOTs

Many of the properties of MOTs have been studied in detail, particularly with reference to loading rates and the dependence of atom number on trap parameters [158–162]. I will briefly summarise some of the results that are useful for the experiments discussed in this thesis, namely load rate, equilibrium atom number, and capture velocity, which will allow me to motivate the use of a double MOT arrangement. The loading rate (dN/dt) for a MOT is given by [23, 160, 161]

$$\frac{dN}{dt} = R - \gamma N(t) \,, \tag{2.20}$$

where R is the loading rate from the background vapour, $\gamma N(t)$ describes losses due to collisions with background gas, and we neglect losses due to two-body collisions. This is solved by

$$N(t) = \frac{R}{\gamma}\left(1 - e^{-\gamma t}\right) \,, \quad R = \frac{n_{\text{back}} V^{2/3} v_c^4}{2 v_{\text{back}}} \,, \tag{2.21}$$

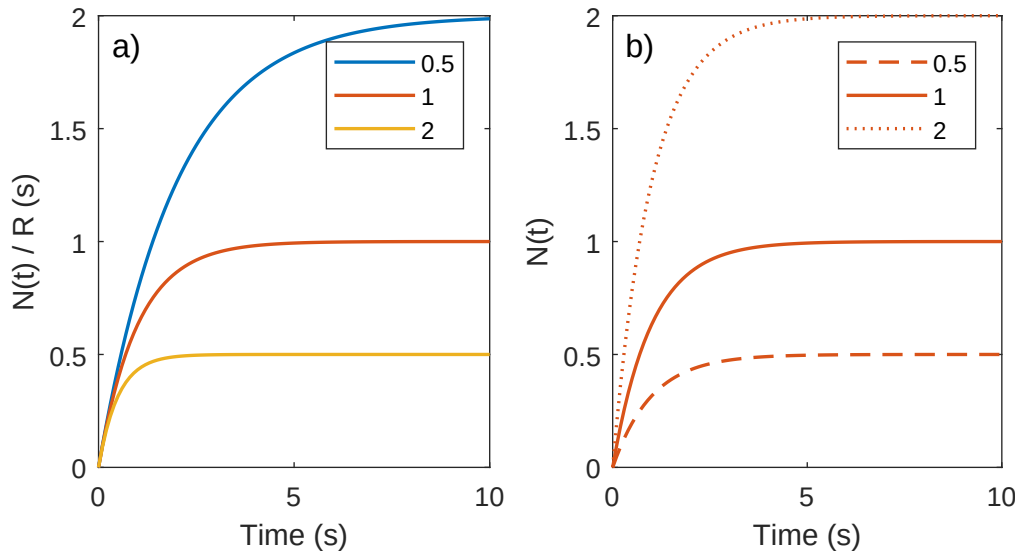

Figure 2.7: The loading of a MOT shown for 3 different loss rates γ (a) and 3 different loading rates R (b). In a), $N(t)/R$ is plotted to allow for comparison of behaviour caused by the loss rate rather than loading rate. In b), the loss rate is 1, as is given by the red line in a).

where n_{back} and v_{back}, are the density and average velocity of the background gas respectively, V is the trapping volume, and v_c is the capture velocity of the trap (which is related to the trap depth) [23, 160]. The filling of the trap is shown in Fig. 2.7. The dependence of capture rate on the density of the background gas means that MOTs can be used to measure background pressures [161].

In our experiment, we wish to operate with a high repetition rate (i.e. to have a high capture rate) and high atom number (as the evaporation techniques used to reach BEC are inherently lossy). However, we must balance increasing the loading rate R with background losses, both of which scale with n_{back} [160]. We also note, more importantly, that the lifetime of a BEC scales inversely with background gas density. This leads us to use a double-MOT set-up [163], meaning that we can have a high load rate MOT in a high pressure (HP) section of a vacuum chamber, which then feeds a 2nd MOT in a low pressure chamber (LP), striking a balance between load rate and loss rate in a way suitable for BEC production.

Double MOT Systems

At Strathclyde we have experiments which use the following three forms of double-MOT systems: 3D pushed to 3D, 2D (pushed) to 3D, and $2D^+$ to 3D. Each consists of a fast loading MOT in a high background pressure cell, atoms are then transferred through a differential pumping tube (DPT) into a low background pressure chamber

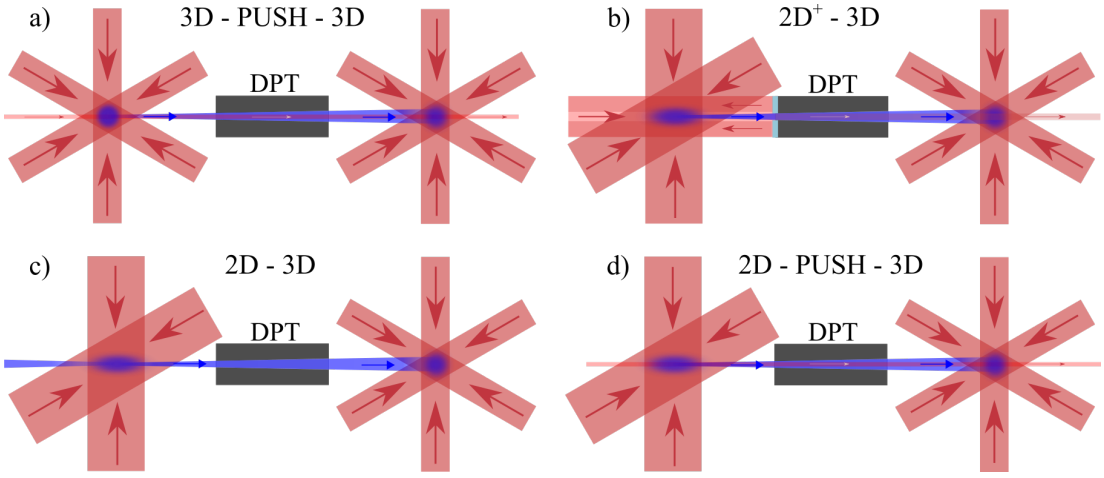

Figure 2.8: Four different double-MOT arrangements, with light being coloured red and atoms blue. Each of the two MOTs are separated by a differential pumping tube (labelled DPT). See text for descriptions.

Experiment Name	Double MOT Type	Load rate	Atom Number	Load Time
Big Ring (JA3.05b) [20]	3D - PUSH - 3D	$\approx 10^7\ s^{-1}$	10^9	20 s
Interferometer (JA3.07) [8]	2D - PUSH - 3D	$5 \times 10^7\ s^{-1}$	5×10^8	15 s
Boson Lattice (JA3.08) [168]	$2D^+$ - 3D	$5 \times 10^9\ s^{-1}$	1×10^{10}	5 s

Table 2.1: Double-MOT parameters in Strathclyde experiments

where they can be collected in a 3D-MOT. There are other methods of atom transfer and cold atom sources but they will not be discussed here (for example the LVIS scheme [164]). Schematics of 4 different double MOT set-ups are shown in Fig. 2.8. Fig. 2.8a) shows a 3D to 3D set-up, where a weak push beam is used to push atoms through the DPT to the LP MOT; the push beam and HP MOT are pulsed such that the HP MOT is turned off when the push beam is on to push atoms through the DPT. Fig. 2.8c) shows a 2D to 3D arrangement, in this case, in the HP cell, the atoms are only cooled in 2 dimensions so freely expand along the third axis through the DPT into the LP 3D MOT. Figs. 2.8b) and d) show modifications of the 2D to 3D arrangement, with a push beam being introduced in d) and a retro-reflecting mirror stuck to the end of the DPT in b) allowing for simultaneous pushing and cooling on the third axis (this retroreflection being the plus part of a $2D^+$ MOT). As one can see from the figures in table 2.1 and existing experiments [163, 165–167], loading an LP MOT from a $2D^+$ is more efficient than pushed 2D, which again is more efficient than a pushed 3D. Though we must note that the loading scheme is of secondary importance to the isolation of the HP and LP sides of the vacuum chamber.

Grating MOTs

Single input beam MOTs offer an obvious way to simplify a wide range of very complex ultra-cold atom experiments, alongside moving cold-atom based sensors closer to portability. Various methods have been demonstrated such as pyramid MOTs [169] and Tetrahedral mirror MOTs [170]. In a pyramid MOT, the capture volume is located inside the mirror structure (in the inverted pyramidal gap between mirrors) meaning that optical access is very poor. Tetrahedral mirror MOTs provided an obvious solution to this problem, with the reflected beams overlapping above the mirrors. The tetrahedral MOT demonstrated in [170] was extended from a mirror-based to diffraction grating based system in Ref. [171] before being integrated into a single microfabricated grating chip [172]. An example of one of the grating chips is shown in Fig. 2.9 (taken

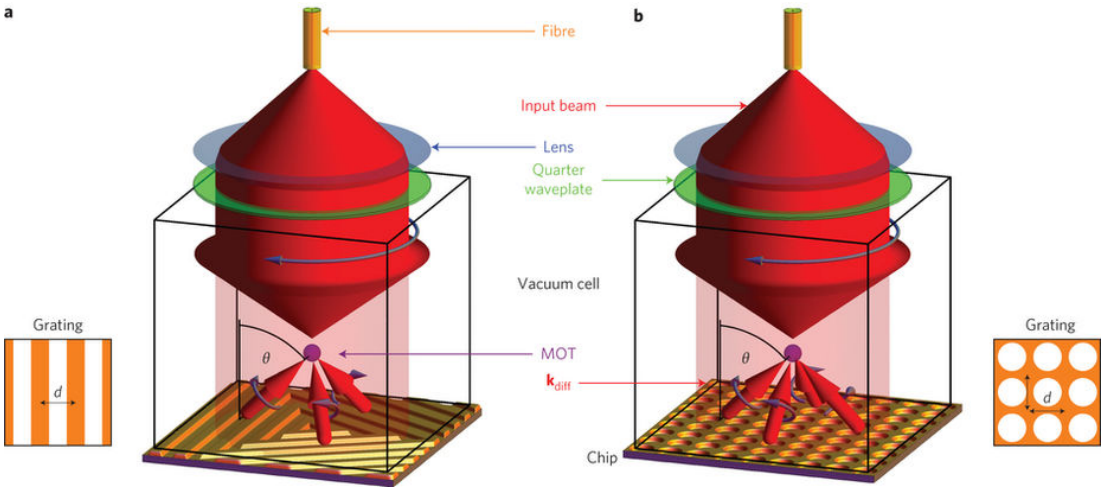

Figure 2.9: A schematic of two grating MOT set-ups detailed in Ref. [172] (a more detailed description can be found in the original paper). To summarise, a single input beam diffracts from the microfabricated grating chip into additional beams (shown by small red arrows) which overlap and create a trapping region. a) Shows a linear-tri grating which produces a 4 beam MOT; b) shows a grating formed of a square array of cylindrical indentations, this produces a 5 beam MOT.

from Ref. [172]). Within the Strathclyde EQOP group, as pioneers of this technique, GMOTs have become a standard technology, with detailed characterisation and optimisation being performed [162, 173–176] with particular focus on their inclusion in clock experiments [177].

As the aim of the experiment discussed in this thesis is to build a relatively compact and scalable system, we originally intended to use GMOTs rather than traditional six-beam MOTs. At the beginning of the design process, an existing experiment in the group (prior results from which are discussed in Sec. 4.3) was being upgraded to incorporate a in-vacuum GMOT (with a drilled hole acting as a DPT), the atom loading rates, given the available laser power constraints, currently rule out this option (details will be included the thesis of Johnathan Conway). This meant that, for ease, it was decided that the new BEC experiment should use a traditional free-space MOT beam configuration (but should be designed in such a way that one could easily upgrade to use gratings). Since this decision, there have been several demonstrations of 3D GMOTs loaded from a 2D GMOT: Ref. [178] uses a composite grating arrangement to replace both a traditional $2D^+$ and 3D arrangement; within the EQOP group, the QUDOS II project has created a microfabrication based 3D GMOT loaded by a 2D

GMOT [179]. We note that the experiment detailed in Ref. [178] created a 3D GMOT of $(2.46 \pm 0.07) \times 10^8$ atoms, with a 3D loading rate of $(1.12 \pm 0.03) \times 10^8$ atoms/s and a flux from the $2D^+$ of $> 4 \times 10^8$ atoms/s.

2.2.5 Optical Pumping

In order to trap atoms in a solely magnetic trap, we need to use weak field seeking states. However, after cooling (either via a MOT or molasses) atoms are equally distributed between the magnetic sub-levels of the ground state. Thus, we use a process called optical pumping to redistribute atoms into a particular magnetic quantum state.

To explain how this works we will use the example of ^{87}Rb cooled on the D_2 line, where the weak field seeking state is $|F = 2, m_F = 2\rangle$. Circularly polarised light (σ^+) pumps atoms between the $|F = 2\rangle$ and $|F' = 2\rangle$ states through $\Delta m_F = +1$ transitions. Once in the excited state, atoms can decay back down to the ground state with $\Delta m_F = +1, 0, -1$, meaning that atoms will amass in the $|F = 2, m_F = 2\rangle$ state which is dark to the optical pumping light. This process is shown in Fig. 2.10. We note that there must be a magnetic field on during optical pumping in order to define the quantisation axis.

2.2.6 Sub-Doppler Cooling

The Doppler-based mechanisms for cooling listed above are limited by the Doppler temperature T_{Doppler} [180,181]. This is the temperature at which the heating and damp-

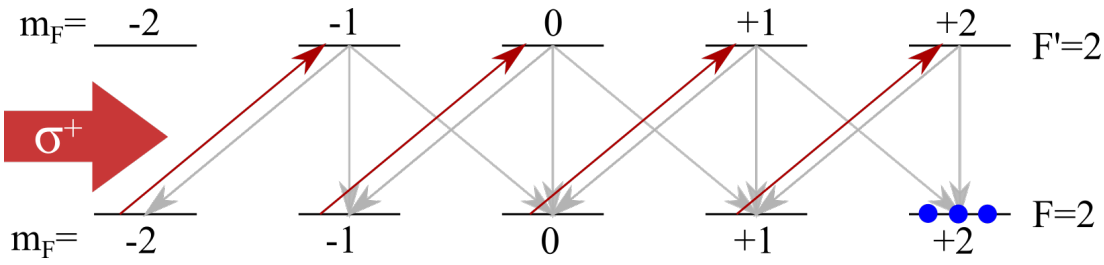

Figure 2.10: Optical pumping using circularly polarised light which drives $\Delta m_F = +1$ transitions (red arrows). Grey arrows show spontaneous emission. Atoms are pumped into the dark state $|F = 2, m_F = 2\rangle$.

ing of an atom in counter-propagating beams balance each other. It is given by

$$T_{\mathrm{D}} = \frac{\hbar\Gamma}{2k_B} \,. \tag{2.22}$$

For ^{87}Rb cooled on the $5^2\mathrm{S}_{1/2}\ F = 2 \rightarrow 5^2\mathrm{P}_{3/2}\ F' = 3$ transition, $T_{\mathrm{D}} = 146\,\mu\mathrm{K}$ [182]. Optical cooling is fundamentally limited by the recoil temperature T_{R} which corresponds to the recoil energy of one spontaneously emitted photon (with wavenumber k) [180, 181]

$$T_{\mathrm{R}} = \frac{\hbar^2 k^2}{2k_B M} \,, \tag{2.23}$$

which for the same transition as above is $T_{\mathrm{recoil}} = 181\mathrm{nK}$ [182].

In some of the first demonstrations of Doppler cooling, it was found that temperatures below the Doppler limit and close to the recoil limit were being reached [183, 184]. This led to polarisation gradient cooling being proposed by Dalibard and Cohen-Tannoudji in 1989 [181], verified independently in the same journal issue by Chu et. al. [185], and confirmed experimentally by the same experimental teams that found the temperature discrepancy [186, 187]. In this section we will explain two forms of polarisation gradient cooling and then move on to other dissipative methods for reaching lower temperatures than standard MOTs.

Polarisation Gradient Cooling

Polarisation gradient cooling mechanisms arise due to changes in optical pumping between the hyperfine levels of alkali atoms due to spatially varying light shifts. In a 1D system with two counter-propagating beams of orthogonal polarisation, the beams will interfere to create a polarisation gradient. To understand this in more detail, we will consider the case of linear polarisation and circular polarisation separately, following the formalisms detailed in [139, 157, 181].

Linear-linear configuration: When the counter-propagating beams are orthogonal and linear, they interfere to create a standing wave of polarisation that varies over half a wavelength as: linear (45° to the input) $\rightarrow$ right hand circular (σ^+) $\rightarrow$ linear (perpendicular to 1st direction) $\rightarrow$ left hand circular (σ^-) $\rightarrow$ linear (45° to the input), this occurs cyclically. The standing wave of polarisation induces an oscillating (in position) a.c Stark shift in the ground state energies. This is analogous to an atom in a

standing wave of intensity. The a.c. Stark shift is an energy level change induced by the presence of an electric field (with detuning Δ); the frequency shift of energy levels is of the form [139]:

$$\Delta\omega_{\text{stark}} = \frac{\Omega^2}{4\Delta} = \frac{\Gamma^2}{8\Delta}\frac{I}{I_{\text{sat}}} \,. \tag{2.24}$$

This is shown in Fig. 2.11, where the a.c. Stark shift of the $m_F = \pm\frac{1}{2}$ ground states is shown for a $J = \frac{1}{2} \rightarrow J = \frac{3}{2}$ transition. If we follow an atom in the $m_F = -\frac{1}{2}$ ground state, it will travel up that Stark shifted potential gradient to position $\frac{\lambda}{8}$ at which point the light will have σ^+ polarisation, which will (on average) pump it into the $m_F = +\frac{1}{2}$ ground state. This optical pumping results in, on average, a change in the ground state m_F of $\Delta m_F = +1$ because the σ^+ selects a $\Delta m_F = +1$ absorption and the spontaneous emission can occur with $\Delta m_F = 0, \ \pm 1$, thus averaging to a total $\Delta m_F = +1$ over the pumping cycle. The equivalent happens for an atom in the $m_F = +\frac{1}{2}$ ground state, which 'travels uphill' until it is optically pumped by σ^- light back to the $m_F = -\frac{1}{2}$ state.

As the atom travels uphill, kinetic energy is transferred to potential energy, which is then in turn transferred to the spontaneously emitted photon as it is optically pumped to the other ground state level. This process is commonly known as Sisyphus cooling due to its similarity to the Greek legend of the same name.

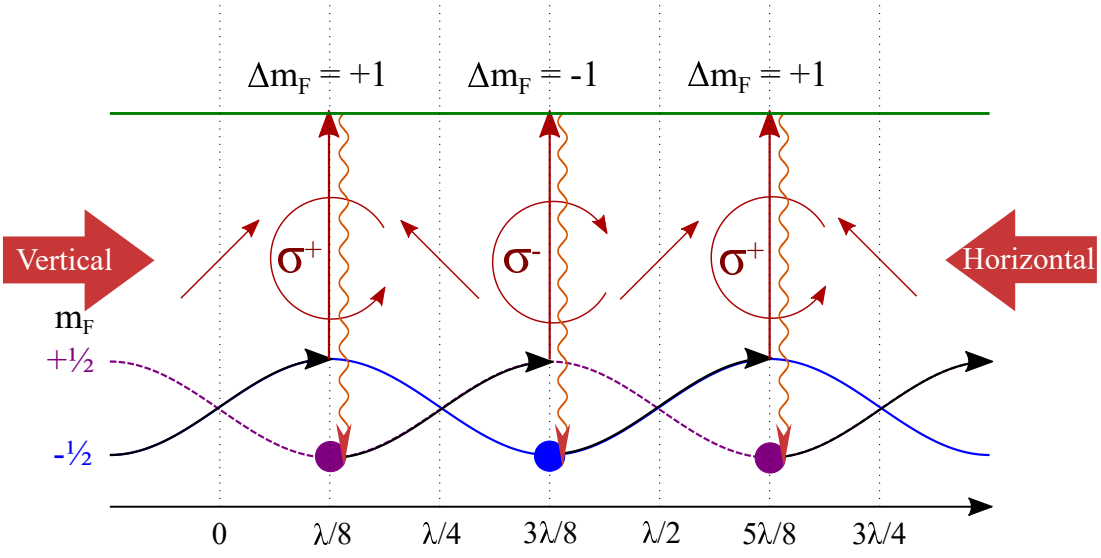

Figure 2.11: Linear-linear polarisation gradient cooling (Sisyphus). Atoms lose kinetic energy as they travel up the stark shifted hill, they are then pumped to the other ground state level, before travelling uphill again.

Sisyphus cooling is most efficient for atoms with a velocity equivalent to travelling a distance of $\lambda/2$ per optical pumping cycle (hotter atoms would begin to travel down hill before optical pumping occurs, and colder atoms would not reach top of the hill in time). This dependence on velocity is the source of the damping force generated by the polarisation gradient.

Circular (σ^+) - circular (σ^-) configuration: When the counter-propagating beams are both circularly polarized (but again orthogonal to one another), the electric field magnitude is constant and the polarisation is linear everywhere, rotating through 2π once per half optical wavelength [157]. Obviously, since there isn't a variation in electric field magnitude, Sisyphus cooling cannot occur in the same way as detailed above. Instead, damping occurs due to the atoms' motion through a region of rotating quantisation axis. As an atom is moving through a laser field with rotating polarisation, its dipole will try to orient along the polarisation (or quantisation axis). This rotation induces a light shift, changing the transition probabilities according to the direction and speed of travel [181].

The lower half of Fig. 2.12 shows the rotating polarisation, with the upper half showing the light shifts caused by the rotating field, as experienced by a stationary

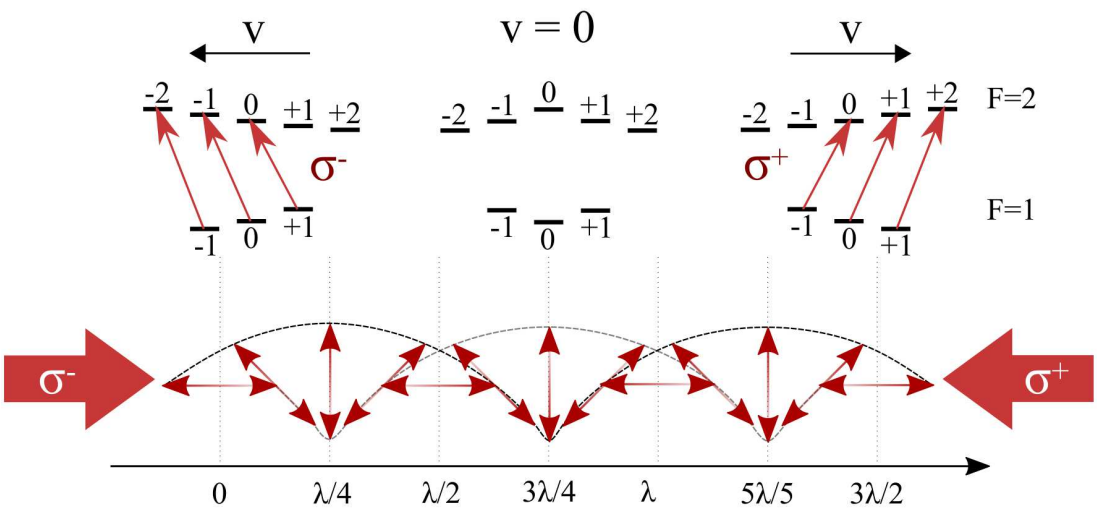

Figure 2.12: Circular-circular polarisation gradient cooling. Interfering propagating beams create a field of rotating linear polarisation, which induces a light shift in moving atoms as their dipoles try align with the polarisation direction of the light.

atom and moving atoms (in both directions). As one can see, for an atom moving towards the σ^+ (σ^-), the light shifts mean that there is an asymmetric ground state population, with more atoms in the positive (negative) m_F levels, this is because optical pumping preferentially pumps atoms towards states with larger light shift [157]. Even a small population imbalance can result in a large damping force as the $m_F = +1(-1)$ level scatters light from the σ^+ (σ^-) several times more efficiently than the light from the σ^- (σ^+) (15 times more for the $m_f = 2$ level in Na [23]). This means that there is a velocity dependent radiation pressure imbalance between the two beams - a damping force.

The final temperature (T_{molasses}) achieved in polarisation gradient cooling is proportional to the light shift, for both polarisation scenarios described above [157]. In both cases, the light shift scales in a similar way (for large detuning) [23], such that,

$$k_B T_{\text{molasses}} \propto \Delta E_{\text{light}} \propto \frac{\hbar \Gamma^2}{|\Delta|} \frac{I}{I_{\text{sat}}} \, . \tag{2.25}$$

This means that, in an experiment, one can reduce the molasses temperature by increasing the detuning and/or reducing the intensity of the cooling beams ($T_{\text{molasses}} \propto I/|\Delta|$). Semi-classical analysis breaks down for temperatures where the atomic de Broglie wavelength is of the order of the wavelength of the light, with a fully quantum model predicting a minimum momentum of $\approx 6\hbar k$ [23].

We note that at high atom number, polarisation gradient cooling is only effective over a central volume of radius $r_i \propto I_{\text{beam}}/\Delta\dot{B}$, outside which Doppler cooling dominates [188, 189], this leads to the a two-component structure with a diffuse Gaussian ball at large radii and smaller, denser component at the centre.

For Rubidium, this sub-Doppler cooling works well. However for a range of species (particularly fermionic species), such as potassium (^{40}K) and lithium (^{6}Li), the smaller excited state hyperfine-splittings lead to less efficient sub-Doppler cooling as transitions other than those used for cooling are more probable. Gray molasses is another sub-Doppler cooling technique which has been successfully used on a wide range of atoms. It involves a Sisyphus-like mechanism between light and dark states, where the coupling between light and dark states are velocity selective such that colder atoms are trapped in dark states where they interact less with light. Some recent exam-

ples of this technique can be found in [190–195].

2.2.7 Compression Techniques

As the goal of laser cooling in our experiment is to both reduce temperature and increase phase space density (so as to get closer to degeneracy), one not only needs to reach cold temperatures, but also to increase phase space density as much as possible before using evaporative cooling [188]. By reducing temperature and increasing phase space density, we can increase the 'useful' collision rate, and so improve evaporative cooling (see Sec. 2.2.9).

There are several ways in which one can quickly increase phase space density, the most common of which is to compress the MOT, as is done in some existing experiments in the group, though the increase in density comes at the cost of higher temperatures [8] (collision rate is a balancing act between high density and low temperature). The density of a MOT is dependent on the spring constant of the trap (directly proportional in the limit of high atom number) and thus is dependent on the magnetic field gradient [196]. There is a lower MOT loading rate with higher magnetic field gradient, so in a typical experiment, one would load a low gradient MOT before compressing it to achieve the fastest load rates possible. In [189, 196] and many other experiments, transient (i.e. rapidly peaking before decay) compression has been achieved by suddenly increasing detuning, ramping up magnetic field gradient and (in the case of [189]) reducing beam intensity, resulting in an increase in atom density of over an order of magnitude.

Dark SPOT Traps

At higher atom density, the contribution of re-absorption becomes more significant. Scattered photons, which are then absorbed by other atoms, are not coherent with the cooling light (i.e. they have a spread of wave-vectors rather than having the same value as the cooling light) and so they act to lower the spring constant (i.e. restoring force) of the trap [189]. One can minimise this re-scattering process by using a technique such as dark SPOT (spontaneous force optical trap) [197–201], or by using a form of laser cooling without spontaneous emission [202].

In dark SPOT traps, atoms are pumped into off-resonant states, thus avoiding re-scattering and allowing higher densities to be achieved. In an ^{87}Rb dark SPOT, the

same laser transitions as in a standard MOT are used, but when the repump light is switched off, atoms accumulate in the $F = 1$ ground state, which does not interact with the trapping light (tuned to the $F = 2 \rightarrow F' = 3$ transition). Early experiments spatially separated areas with and without repump light such that an outer annulus was repumped and an inner region was not pumped out of $F = 1$ (or was even depumped). However this was technically challenging. With beam shaping techniques such as SLMs becoming commonplace in labs, the experimental set-up required for a dark SPOT trap has been simplified significantly, with these technologies giving the added benefit of dynamic transfer from MOT to dark SPOT [201]. Such a technique recorded densities of up to $1.3 \times 10^{-12}\,\mathrm{cm}^{-3}$ and phase space densities of up to 8.5×10^{-6}, compared to $(1.5 \pm 0.5) \times 10^{-5}$ achieved transiently in [188].

2.2.8 Dipole Trapping

Unlike the other optical traps described above, optical dipole traps can be independent of the internal (electrical) states and charge of an atom (or a particle), so long as the trap is operated far from an atomic resonance. This means that they are a conservative potential and can reach lower temperatures compared to the other optical traps discussed above. The first optical dipole trap for neutral atoms was demonstrated in [138].

The optical dipole force is derived from dispersive interactions between the induced atomic dipole moment and the intensity gradient of light, resulting in a conservative potential with a minimum (and thus trapping) at the point of maximum intensity. The dipole potential and force is typically derived [203] using the oscillator model of an atom placed in an electric field ($\vec{E}$) which drives the atomic dipole moment ($\vec{d}$) at frequency ω, giving,

$$U_{\text{dip}} = -\frac{1}{2}\left\langle \vec{d} \cdot \vec{E} \right\rangle = -\frac{1}{2\epsilon_0 c}\mathrm{Re}(\alpha) I \,, \tag{2.26}$$

where α is the complex polarisability and is related to $\vec{d}$ and $\vec{E}$ by $\vec{d} = \alpha \vec{E}$. As force is the gradient of a potential, we can write it as,

$$F_{\text{dip}}(\vec{r}) = -\nabla U_{\text{dip}}(\vec{r}) = \frac{1}{2\epsilon_0 c}\mathrm{Re}(\alpha)\nabla I(\vec{r}) \,. \tag{2.27}$$

The residual photon scattering in the trap is calculated from the power absorbed (P_{abs})

from the electric field,

$$\Gamma_{\text{sc}}(\vec{r}) = \frac{P_{\text{abs}}}{\hbar\omega} = \frac{1}{\hbar\epsilon_0 c}\text{Im}(\alpha)I(\vec{r}) \ . \tag{2.28}$$

In the rotating wave approximation (detuning obeys $|\Delta| \ll \omega_0$ and Rabi frequency obeys $\Omega \ll \omega_0$) the above expressions can be approximated as

$$U_{\text{dip}}(\vec{r}) = \frac{3\pi c^2}{2\omega_0^3}\frac{\Gamma}{\Delta}I(\vec{r}) \ , \quad \Gamma_{\text{sc}}(\vec{r}) = \frac{3\pi c^2}{2\hbar\omega_0^3}\left(\frac{\Gamma}{\Delta}\right)^2 I(\vec{r}) \ . \tag{2.29}$$

Although these equations describe the situation for an atom or particle which can be approximated to be a two-level atom, due to the more complex state structure of ^{87}Rb, one must consider potentials which are state-dependent as laid out in Refs. [203, 204], i.e. the states are dressed by the a.c. Stark shift caused by the light. In this case, if one had an atom with total angular momentum F and magnetic quantum number m_F, the dipole potential becomes,

$$U_{\text{dip}}(\vec{r}) = \frac{\pi c^2\Gamma}{2\omega_0^3}\left(\frac{2+\mathcal{P}g_F m_F}{\Delta_{2,F}} + \frac{1-\mathcal{P}g_F m_F}{\Delta_{1,F}}\right)I(\vec{r}) \ , \tag{2.30}$$

where $\mathcal{P}$ is the laser polarisation ($= 0$ (linear), ± 1 ($\sigma^{\pm}$ circular)), g_F is the Landé g-factor, and $\Delta_{1(2),F}$ refers to the energy splitting between the ground state $^2S_{1/2}, F$ and the centre of the hyperfine levels $^2P_{1/2}$ ($^2P_{3/2}$), i.e. the D_1 (D_2) lines.

Placing these equations for dipole trapping in the context of atomtronics, it is useful to consider the heating rates of a trap or waveguide (noting that the temperature of atoms in the trap is limited by the trap depth and their temperature upon loading). The heating rates for a red or blue detuned dipole traps are given by $\dot{T}_{red}$ and $\dot{T}_{blue}$ respectively [203]:

$$\dot{T}_{red} = \frac{2/3}{1+\kappa}T_{rec}\frac{\Gamma}{\hbar|\Delta|}\hat{U} \ , \quad \dot{T}_{blue} = \frac{\kappa}{1+\kappa}T_{rec}\frac{\Gamma}{\hbar\Delta}k_B T \ , \tag{2.31}$$

where κ is the ratio between potential and kinetic energy, and $\hat{U}$ is the trap depth. From this we see that heating rates in blue-detuned traps are lower than the red-detuned equivalent, with a substantial advantage occurring for very deep potentials [203].

Potential Parameters

When putting atoms into a dipole potential, in order to model their behaviour (particularly that of a BEC) we need to know several parameters of the potential - the trap depth and the trap frequency.

For a tightly focussing Gaussian, we can combine Eq. 2.2 and Eq. 2.30 to give:

$$\begin{aligned} U_{\text{dip}}(r) &= \frac{\pi c^2 \Gamma}{2\omega_0^3}\left(\frac{2+\mathcal{P}g_F m_F}{\Delta_{2,F}}+\frac{1-\mathcal{P}g_F m_F}{\Delta_{1,F}}\right)\frac{2P_0}{\pi w_0^2}\exp\left(\frac{-2r^2}{w_0^2}\right) \\ &= U_0 \exp\left(\frac{-2r^2}{w_0^2}\right), \end{aligned} \tag{2.32}$$

at the focus of the beam. The depth of the potential is given by the prefactors before the exponential and can be expressed as a temperature by equating it to $k_B T$.

To calculate the trap frequency of the potential for $\Delta < 0$, we can use a Taylor expansion of $U(r)$ around the trap minimum and equating the 2nd-order term (in r^2) to a parabolic potential:

$$\omega_r = \sqrt{\frac{1}{m}\frac{\mathrm{d}^2 U(r)}{\mathrm{d}r^2}\Big|_{r=r_{min}}}\,. \tag{2.33}$$

For a simple focused Gaussian, this gives:

$$\omega_r = \sqrt{4\left|U_0\right|/m w_0^2}\,, \tag{2.34}$$

in the radial direction. In the direction of propagation, the trap is shallower and less tight.

2.2.9 Evaporation Cooling

Although one can reach impressively low temperatures with the laser cooling techniques described above, the phase space density reached is still many orders of magnitude below the quantum degeneracy limit of $n\lambda_{dB}^3 > 2.62$ for a box potential or 1.2 for the centre of a harmonic trap [24]. Evaporative cooling allows us to beat the recoil limit but at the cost of high atom losses.

Evaporative cooling constantly removes the high-energy atoms from a distribution, then allows the cloud to re-thermalise before repeating the process; just as evaporation occurs in everyday life with cups of tea and sweaty people. A schematic of this is

shown in Fig. 2.13.

There are several ways to perform evaporation cooling, and I will outline the basics of two of these techniques here: radio frequency (rf) evaporation and optical (dipole) evaporation, which are both used within experiments in the EQOP group of Strathclyde. Further information can be found in many review articles including [205, 206].

Radio Frequency Evaporation

Radio frequency evaporation uses an oscillating AC magnetic field to drive atomic transitions, performing both state and position selective removal of atoms from a cloud.

For magnetically trapped atoms, we can describe this process by considering the rf magnetic field (applied perpendicularly to the magnetic trap field vector) as a superposition of σ^+ and σ^- polarised magnetic fields which can drive $\Delta m_F = \pm 1$ ground state transitions, thus the transitions between weak and strong field seeking states. By using the equation for energy splitting in a magnetic field (Eq. 2.15) we find that state transfer occurs when the frequency of the oscillating magnetic field (ν_{rf}) is equal to:

$$h\nu_{rf} = |g_F|\,\mu_B B(r)\ . \tag{2.35}$$

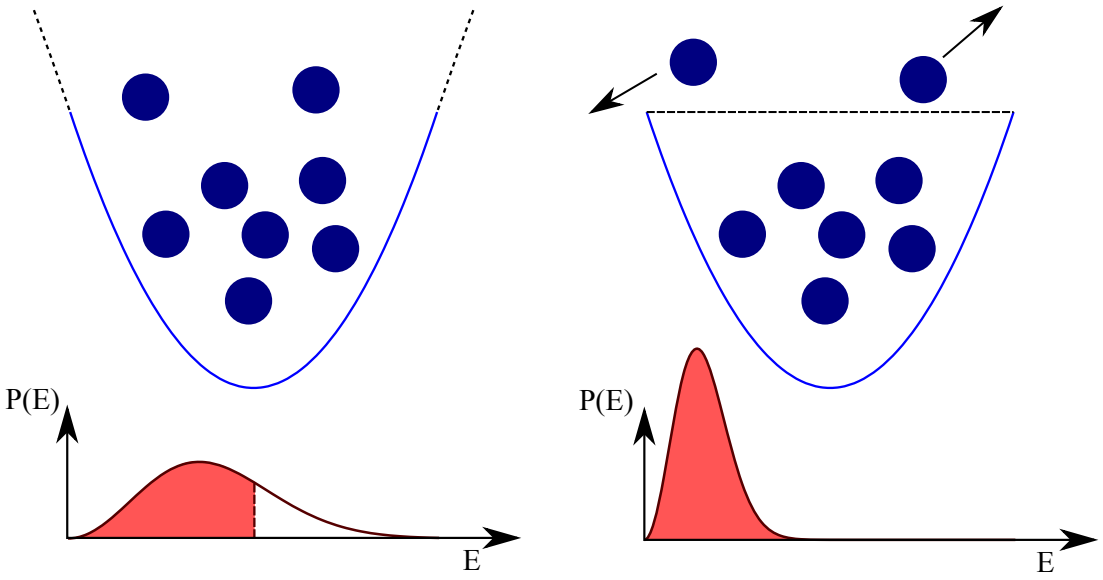

Figure 2.13: Evaporation cooling removes hot atoms from a trap (as shown in the top images). The remaining atoms (shown in the population graph in the bottom left) rethermalise to a lower average temperature (bottom right population distribution)

From this we can see that the spin-flips caused by the magnetic field are position dependent, creating an 'evaporation surface' at high (trap) magnetic field. As only the hotter atoms have enough energy to reach the evaporation surface, this makes the field interactions energy dependent as well as position dependent. In summary, the atoms which are hot enough to reach the evaporation surface are removed to an anti-trapping (high-field-seeking) state, leaving behind cooler atoms which can then re-thermalise. This means that we are effectively cutting the hot atoms off with an 'rf knife' - by slowly ramping the frequency of the rf knife down, we can reduce the energy cutoff, systematically lowering the temperature. It is worth noting that since the evaporation surface is not necessarily the equipotential surface, gravitational sag can cause asymmetric evaporation.

Optical Evaporation

In optical evaporation, the trap depth of the potential which traps the atom is gradually lowered allowing the hotter atoms to escape.

Following from the description of dipole potentials in Sec. 2.2.8 and Gaussian optics in Sec. 2.1, a tightly focused beam creates a Gaussian potential, with tight confinement perpendicular to the direction of propagation and a wider potential in the direction of propagation. Crossing two such traps gives us a crossed-dipole trap which was first demonstrated in Ref. [207], it was used in the first all-optical route to BEC [208], and there has been a wide variety of other demonstrations since [209–212].

In a crossed dipole trap, as one lowers the trap depth by reducing the beam power, the trap frequency (the confinement) also reduces. This decreases the density and the collision rate of the trapped atoms [211]. This means that, unlike in rf evaporation, one cannot typically (without system changes) reach 'runaway' evaporation, where rethermalisation occurs quickly. It is important to note, that the two dipole beams should be detuned with respect to each other (for example by 80 MHz in Ref. [208]) or the polarisations crossed in order to avoid interference effects.

There are several ways to achieve runaway evaporation using optical evaporation, thus alleviating the need for either long evaporation times or very high atom losses. For example, one can add a magnetic field to create a hybrid trap [8, 213, 214], use a misaligned cross-beam far off-resonant dipole trap (MACRO-FORT) [211] in which one dipole beam is tightly focused, while the other stays relatively wide, or opt for a more complex compression system [210]. In Sec. 3.6 we will discuss the relative

benefits some of these systems with reference to the design of the new experiment.

We note that recent developments in laser cooling has given rise to other all-optical methods of reaching degeneracy which avoid the need for evaporation. For example in Ref. [215] a strontium BEC is reached through a combination of Doppler cooling, light-shift induced transparency and a dipole dimple trap. In Ref. [216] a Rb BEC is created through compression in an optical lattice and Raman side-band cooling.

Evaporation Efficiency

It is important to be able to quantify a figure of merit for evaporative cooling: we want to be able to increase the phase space density of an ensemble without losing too many atoms. Thus this figure of merit (the evaporation efficiency γ) can be defined as the ratio between the change in phase space density (PSD) and the change in atom number [206, 217]:

$$\gamma = -\frac{dln(PSD)}{dln(N)} \,. \tag{2.36}$$

In a system where the truncation parameter (which for example describes the evaporation surface (or cut-off energy) in r.f. evaporation) can be chosen, the efficiency (γ) can be reduced to a ratio between different types of collisions. Good collisions are those which contribute to rethermalisation, such as elastic collisions (with rate Γ_{el}). Bad or unwanted collisions are those that cause atom losses, which are inelastic collisions: collisions with the background gas (Γ_{bg}), and three body collisions ($\Gamma_{3-\mathrm{body}}$) [218]. This gives:

$$\gamma \propto \frac{\Gamma_{\mathrm{elastic}}}{\Gamma_{\mathrm{inelastic}}} = \frac{\Gamma_{\mathrm{el}}}{\Gamma_{\mathrm{bg}} + \Gamma_{3-\mathrm{body}}} \,. \tag{2.37}$$

Practically, this relation means that, to achieve good evaporative cooling, one should have as high an elastic collision rate as possible whilst maintaining a dilute enough ensemble for three-body collisions to be minimised. It also means that the lower the vacuum pressure (and so the lower the background collision rate) the better the evaporative cooling efficiency.

2.3 Imaging

There are two main (destructive) imaging techniques used in atomic physics experiments: fluorescence and absorption imaging. There are also a variety of non-destructive imaging techniques such as Faraday imaging [219, 220] and phase contrast imaging [221] which can be used to image BECs. In our experiment, we initially plan to use absorption imaging to image the BEC and fluorescence imaging to monitor the loading of the MOTs, following the example of imaging systems in previous experiments in the group.

2.3.1 Absorption Imaging

Absorption imaging effectively images the shadow of an atomic cloud - its name originates from the absorption of light by atoms which yields this shadow [206]. The absorption of light passing through the cloud is proportional to the density of the atoms via the optical depth (OD). We can use the Beer-Lambert law to relate the OD of the cloud to the intensity distribution:

$$I = I_0 e^{-OD} \propto e^{-\sigma \int n(x,y,z)dz} , \tag{2.38}$$

where I_0 is the incident intensity, σ is the optical absorption cross-section (at the frequency of the incident probe light), and $n(x, y, z)$ is the density of atoms. The integral $\int n(x, y, z)dz$ represents the column density of cloud, that is the density integrated along the imaging axis.

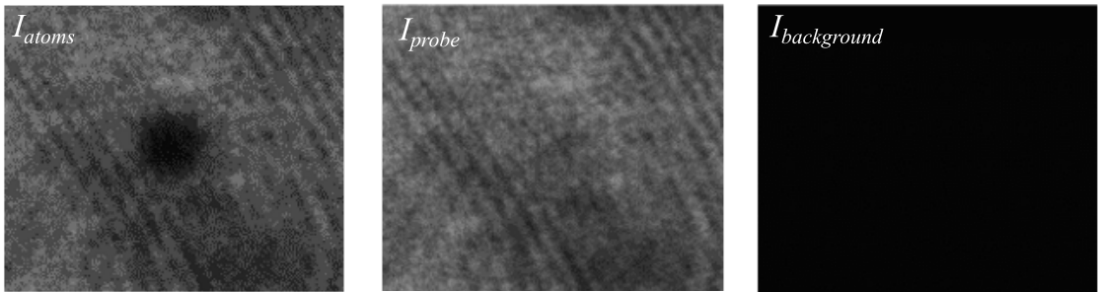

Figure 2.14: The three images needed for absorption imaging. From left to right: I_{atoms} is the probe light travelling through the atoms (showing the shadow of the atoms); I_{probe} is purely the probe light; $I_{\text{background}}$ is taken without any light or atoms present.

Since OD is proportional to atom density, it is this that we want to calculate from our imaging routine. This requires the taking of three separate images using a CCD camera, as shown in Fig. 2.14. The three images give us the atomic cloud shadow I_{atoms}, the raw imaging beam I_{probe}, and a background image $I_{\mathrm{background}}$. As each of these images are taken under identical conditions, before being combined using the following equation:

$$OD = ln\left(\frac{I_{\mathrm{probe}} - I_{\mathrm{background}}}{I_{\mathrm{atoms}} - I_{\mathrm{background}}}\right) . \tag{2.39}$$

This holds as long as the intensity is below the saturation intensity.

Chapter 3

Building a New BEC

In the following section, the experimental set-up of the new BEC experiment will be outlined; starting from the lasers and frequency control, moving towards the vacuum chamber, before discussing the trapping layouts and procedures. In each of the individual sections, the design process will be discussed before detailing the relevant experimental procedures. We note that at the stage of writing this thesis, the experiment has been implemented up to the point of a temporary 3D-MOT.

3.1 Laser and Atom Frequencies

As laid out in chapter 2, to be able to trap, cool and image atoms we need to accurately and precisely produce and control light at specific frequencies. To address particular transitions, one needs a small laser linewidth (far less than the splitting between levels) locked to the relevant transition. In our system we cool on the D_2 line of ^{87}Rb, the structure of which is shown in Fig. 3.1. In this figure, we show each of the different frequencies required, the points at which the lasers are locked, and the detunings from the atom transitions that we expect to use.

Our initial requirements are light for cooling/trapping and imaging, with dipole lasers being used for evaporative cooling and dipole trapping later in the experiment.

For cooling/trapping, we need three different, independently controlled, light sources: cooling, push/plus, and repump. To create a basic MOT, we simply need the cooling and repump light. The cooling light is red-detuned (by approximately 18 MHz) from the $F = 2 \rightarrow F' = 3$ transition, and needs at least 140 mW (based on previous experimental experience) for the 2D and 3D MOTs combined. This light must

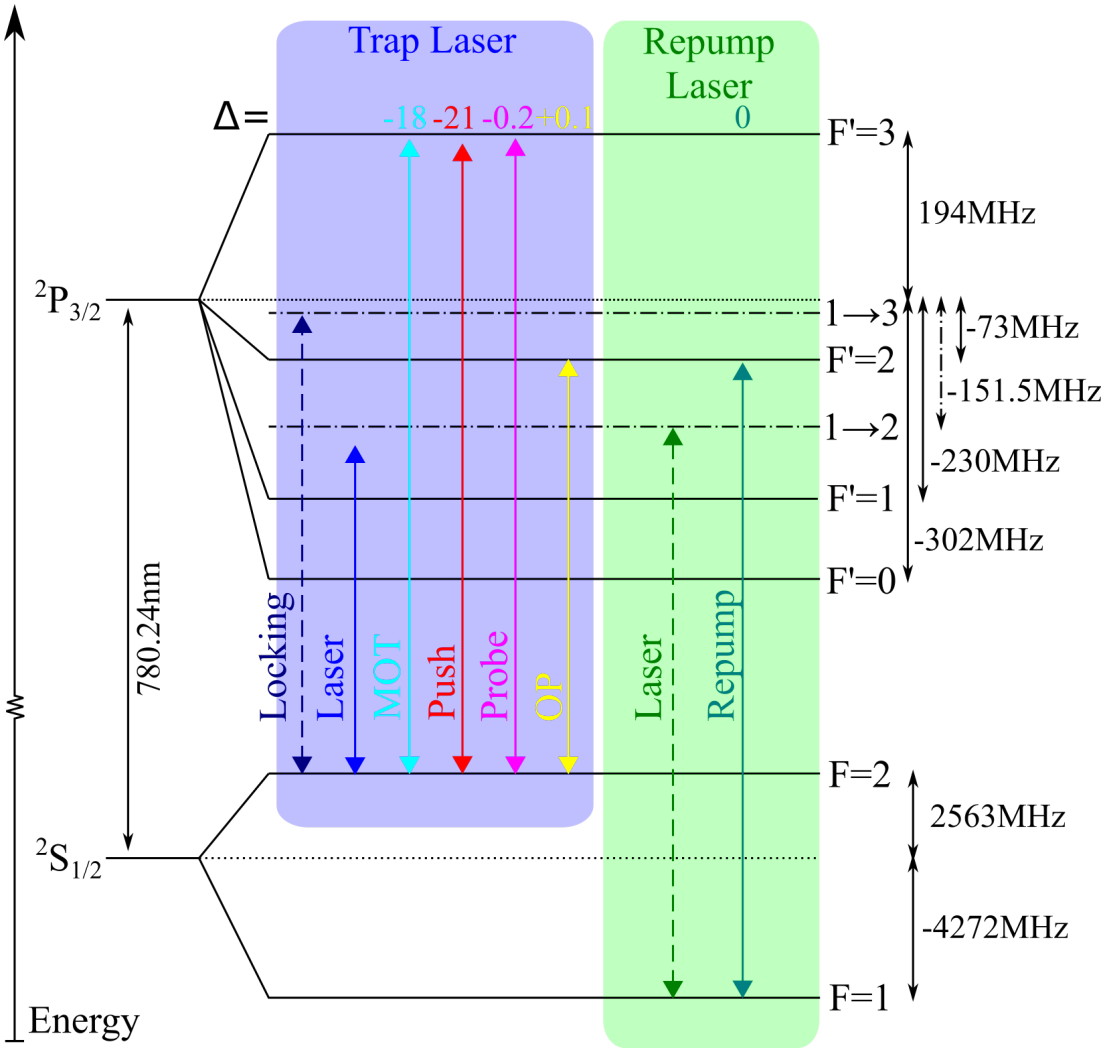

Figure 3.1: The energy level diagram for the D_2 line of ^{87}Rb, showing the laser frequencies used to trap, cool and image. On the diagram, the dot-dashed lines indicate cross-over peaks. We use two lasers, a trap (blue shading) and a repump (green shading) laser to achieve all the required frequencies. The lock point of each laser is shown with a dashed arrow (noting that the trap laser sits below the lock transition and is shown by the adjacent solid blue arrow). Frequency splitting values are taken from [182, 222, 223].

be circularly polarised when incident on the atoms. The repump light addresses the $F = 1 \rightarrow F' = 2$ transition and closes the cooling transition, such that an efficient cooling cycle exists. The repumper needs to be spatially overlapped with the cooling light, but much less power is required as it does not drive the cooling processes.

The push/plus light provides either a push from a 2D MOT through a differential pumping tube to a 3D MOT, or provides the 'plus' partial cooling beam to make a 2D MOT into a 2D+ MOT. These two arrangements were previously discussed in Sec. 2.2.4 and will be further discussed in Sec. 3.5.1. As it acts as a cooling beam, the plus/push light needs to be close to the same transition as the cooling light ($F = 2 \rightarrow F' = 3$) but needs much less power, for example, the push beam used in Ref. [8] is 500 µW. The plus beam can be either circularly or linearly polarised depending on which optimises the 3D MOT fill rate (in our experiment, linear light is used). In Fig. 3.1 the cooling/MOT, push and repump corresponds to the turquoise, red and teal arrows respectively.

For imaging or probing the atoms (assuming the use of absorption imaging), we need two different frequencies of light, spatially overlapped and with the same polarisation. We probe the atoms on the $F = 2 \rightarrow F' = 3$ (with minimal detuning), with the overlapped optical pumping light (labelled as OP in Fig. 3.1) serving to pump all of the atoms in the $F = 2$ state (as described in Sec. 2.2.5). This probe light allows us to do absorption imaging of our atoms (see Sec. 2.3.1), with the optical pumping increasing the optical depth (and atom number) of the cloud by ensuring all atoms are in the probe-able ($F = 2$) ground state.

3.2 Controlling Light

In our experiment, the objective is to build a modular system with a small footprint. This modularity will ensure that future upgrades are relatively easy to do, and will mean that the experiment can be reconfigured on the table with minimal realignment. To minimise the experimental footprint, we derive the frequencies detailed above using only two lasers - a trap laser (blue shading in Fig. 3.1), which is locked to the $2 \rightarrow 1-3$ crossover, and a repump laser (green shading in Fig. 3.1) which is locked to the $1 \rightarrow 1-2$ crossover. Fast switching and frequency control is provided by a series of acousto-optical modulators (AOMs) and amplification is done with a tampered amplifier (TA).

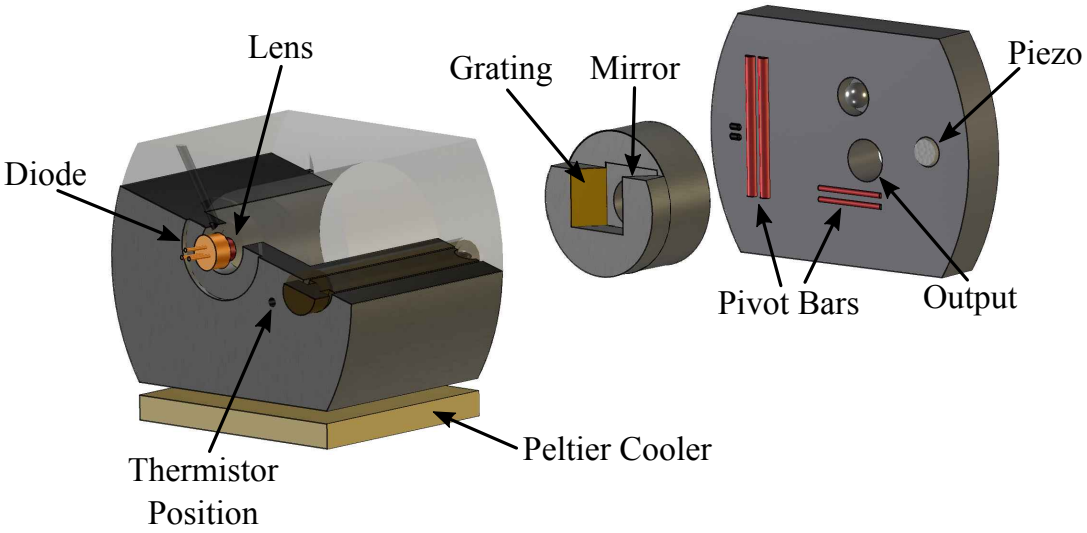

Figure 3.2: The Strathclyde ECDL design, adapted from [7, 8]. From left to right, the body segments referred to in the text are the main body, the feedback mount, and the front plate.

The frequency control, amplification and locking is done across three 450 × 450 mm optical bread boards which are mounted on a float-able optical table. We will describe the lasers and the optical layouts in following section.

3.2.1 The External Cavity Diode Laser

We use two home-built extended cavity diode lasers (ECDL), the design of which has been perfected over the course of many experiments in Strathclyde. ECDLs are a relatively inexpensive, compact and tunable way of producing light with a narrow linewidth at 780 nm suitable for an atomic physics experiment [224–226].

The home-built ECDLs follow the initial design detailed in [226] with further modifications and details described in [7]. The design is shown in Fig. 3.2 [7].

The bulk of the laser consists of a machined aluminium block which is mounted to a Peltier thermoelectric cooler creating a temperature stabilised environment, where the diode and optics are shielded from atmospheric turbulence. The main body holds the laser diode, a thermistor (for temperature feedback), and a collimating lens (mounted and adjusted using a gear arrangement). The remaining parts of the laser are the front plate and the feedback mount.

The feedback mount holds the silver mirror (Thorlabs ME055-P01) and grating (Thorlabs GH25-18V, 1800 lines/mm). The first order reflection of the grating forms a cavity with the laser diode (the external cavity of the ECDL name) and the zeroth order is coupled out of the laser with the mirror. The use of the mirror ensures that the direction of the output light does not change as frequency is tuned. The angle of the grating provides wavelength tunability as the angle of reflection/diffraction is determined by the wavelength of light incident upon it. The use of an external cavity creates the narrow linewidth as lasing is only possible on one of the cavity modes, which are narrow due to the relatively high finesse of the cavity.

The feedback mount is attached to the front plate via tensioned springs. The front plate is then itself attached to the main body via another set of tensioned springs. Rough tuning of the laser is done via two adjustment screws for which the pivot points are the 4 bars shown on the front plate. A screw on the front of the laser provides vertical angular adjustment (which optimises the cavity feedback, known as 'flashing' the laser), and a screw on the back provides horizontal angular control (which gives wavelength tunability). There is also a piezoelectric stack which provides fine adjustment for wavelength and allows us to the lock the lasers to a particular frequency via feedback.

Each laser is controlled by a commercial MOGLabs diode laser controller (MOGbox DLC-202 and MOGbox DLC-252) which provides temperature stabilisation through the Peltier element and frequency modulation to the laser via the diode drive current, which allows us to lock to the hyperfine structure of a saturated absorption signal. The noise spectrum and linewidth of lasers of this design are detailed in [7], with a linewidth of a locked laser being reported as 380 kHz. The lasers used in this experiment have comparable linewidths, with mode-hop free scanning ranges of over 5 GHz achievable. A section of the saturated absorption spectroscopy signal (and the corresponding error signal - the first derivative) obtained from one of our lasers is shown in Fig. 3.3.

3.2.2 Optical Layouts

Our optical layouts for cooling and probing light are split between three 450×450 mm bread boards and fibred to the experiment, making the system as modular and movable as possible. The three boards are: the trap laser board; the repump and tampered am-

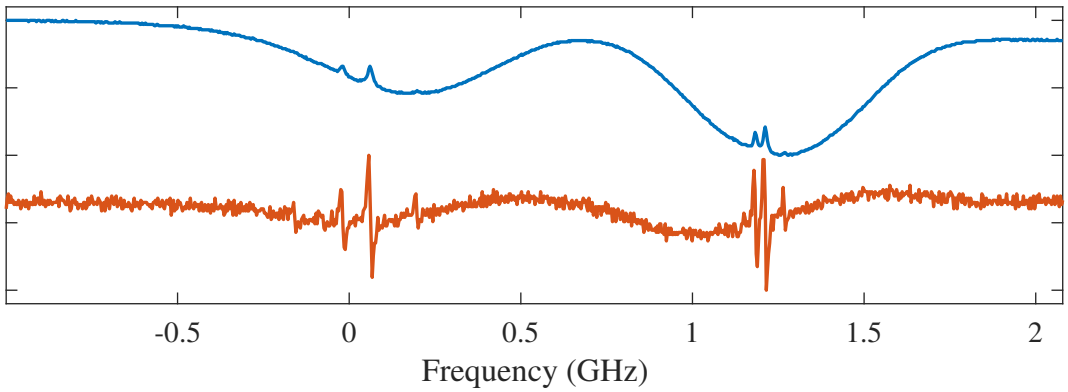

Figure 3.3: Saturated absorption spectroscopy signal (blue line) and the corresponding error signal (red line). Both signals are shown with an arbitrary vertical axis, with lines artificially offset from one another for clarity.

plifier (TA) board; and the push, optical pumping and push (POPP) board. They are shown in Fig. 3.4. For each laser, we have two mirrors close to the laser output which allow us to make the light completely horizontal and steer it through an optical isolator which prevents feedback affecting the laser outputs. Both lasers are locked using saturated absorption spectroscopy and shifted in frequency by AOMs.

Trap Laser: After transmission through an optical isolator, the laser is split into three parts using half waveplates and polarising beam splitters (PBS). The first PBS separates out light which is then sent to the 'POPP' board via a standard Thorlabs polarisation maintaining fibre. The input polarisation is corrected and adjusted with a quarter waveplate and a half waveplate. Fibre coupling is achieved using an aspheric lens (Thorlabs C560TME-B) mounted in lens tube such that its distance from the fibre can be easily adjusted. By fibre coupling in this way we are able to achieve efficiencies of approximately 80 %.

The second PBS splits off light which is directed to the tapered amplifier (TA). Here an additional isolator is used to ensure that back-reflections do not introduce additional noise to the spectroscopy set-up. After the isolator, polarisation is cleaned using a quarter waveplate, a half waveplate, and a PBS, and is precisely set for coupling into another optical fibre (using the same optics as before). Polarisation cleaning is necessary due to the sensitivity of the TA input to polarisation drifts.

The third PBS directs all the remaining light through a double-passed 110 MHz AOM which shifts the frequency of the light up before it is sent into the spectroscopy

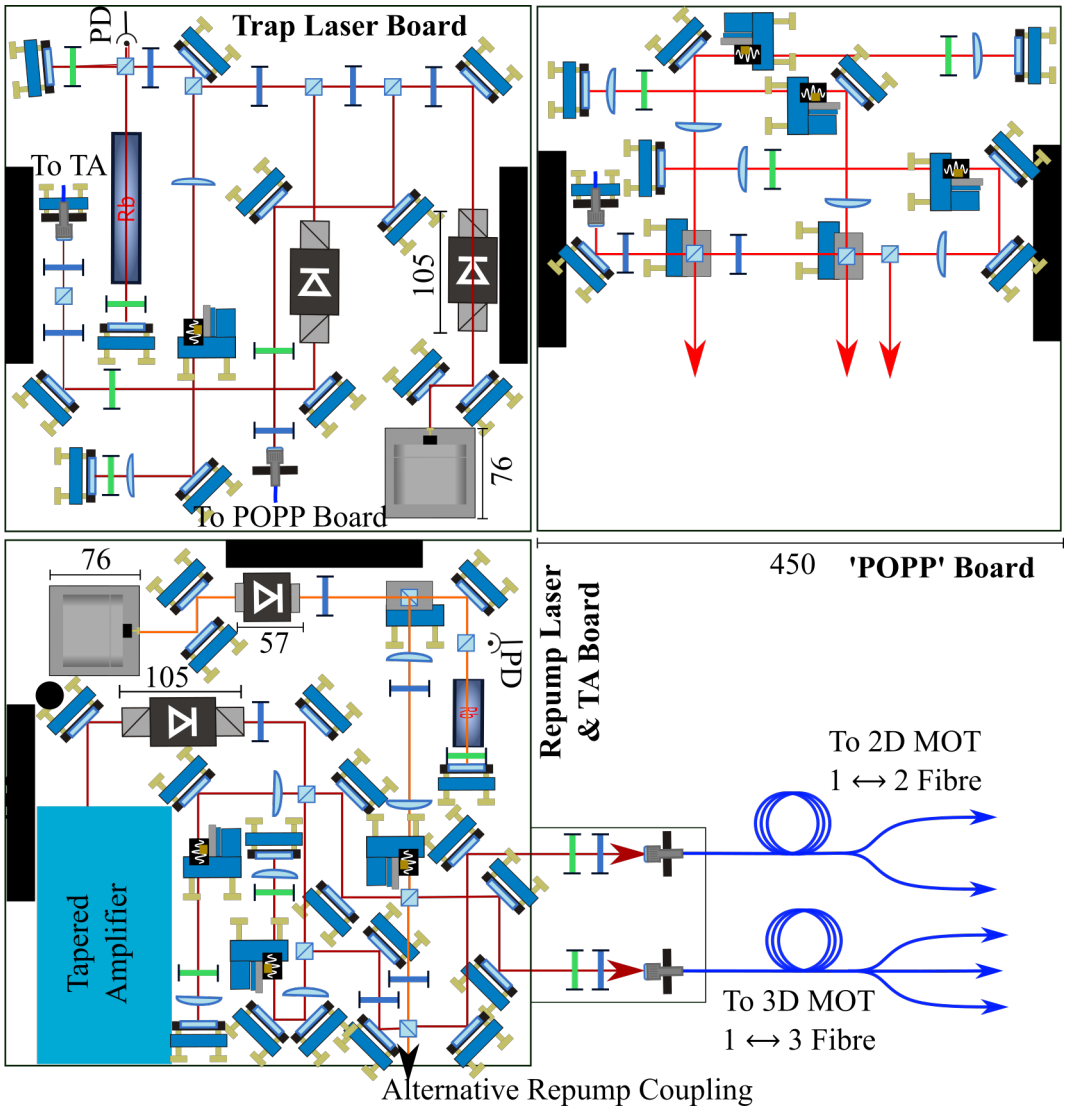

Figure 3.4: Optical layouts for cooling and probing light. Half wave-plates are shown in blue and quarter wave-plates in green.

cell. The AOM sits at the focus of a one-to-one telescope formed by two 150 mm focal length lenses. A pinhole blocks the unwanted diffracted orders (in this case we use the first positive order) before the light passes through a quarter waveplate and is retro-reflected back through the AOM. The use of the quarter waveplate means that output light is separated from the input by being orthogonally polarised. The output light then passes through the spectroscopy cell and is incident on a photodiode. Here we lock to the $2 \rightarrow 1-3$ crossover absorption peak. Having the AOM within the spectroscopy section of the optic layout means that the laser (and the light sent to other boards) is locked 200 MHz below the $2 \rightarrow 1-3$ crossover, and so is a total of 412 MHz below the cooling transition ($F = 2$ to $F' = 3$). The details of the frequency control is discussed in Sec. 3.2.3.

We note that this spectroscopy set-up includes an option to use a difference photodiode to minimise noise on the locking signal, though this is not currently necessary. To use this arrangement, one would direct half of the spectroscopy light through the cell, and half onto a mirror, these two signals would then be measured by two different photodiodes (on the same sensor head in the position labelled as PD in Fig. 3.4) and the signal subtracted.

Repump Laser: The repump laser follows a similar arrangement, with light being split between the spectroscopy and experiment set-ups with a PBS after the isolator. The spectroscopy arrangement is as before, but without the option for recording a difference signal. Here, as discussed previously, we lock to the $F = 1 \rightarrow 1-2$ crossover. Some magnetic shielding of the cell was required for the spectroscopy cell due to Zeeman shifts in transitions caused by the residual field of the isolator.

The light used for the experiment is passed through a reducing telescope (using lens of focal lengths $f = 100$ mm and $f = 35$ mm) which creates a beam of the correct size to be passed through a single-pass AOM. This AOM shifts the light by +78.5 MHz, bringing the frequency of the light close to the $F = 1 \rightarrow F' = 2$ repump transition.

After the AOM, the repump light is then overlapped with the trap light at two different PBSs and coupled into optical fibres to the experiment. We can also use repump light which is not overlapped with the trap light by coupling it out of the 'waste' port of the final PBS (this is shown with an arrow at the bottom of the optical layout in Fig. 3.4).

Amplified Trap Light: On the repump and TA board, in addition to creating and controlling the repump light we also amplify the trap light and control the frequency of light for each MOT separately. Light from the trap laser board is coupled into a fibre which acts as an input for the tapered amplifier (New Focus TA-7613, which has a maximum power output of 1 W at 780 nm). The technical specifications of the TA indicate that minimum seed power of 10 mW [227] is required. In our system this corresponds to a minimum input power of 19 mW before the input fibre, which in turn yields a seed of approximately 15 mW.

The TA output is raised to the correct beam height and made parallel to the table using a periscope, before being directed through an isolator which protects the TA from back reflections. The light is then split into two separate paths for the two MOTs with two PBSs. On the first PBS, the reflected light goes through a double-passed 200 MHz AOM at the centre of a one-to-one telescope formed of two 100 mm focal length lenses. The output beam is then transmitted through the PBS into the overlapping and fibre coupling section of the board. The light transmitted through the first PBS is transmitted through a second PBS into a separate double-passed AOM arrangement, which uses optics of the same specification. The output of this second AOM set-up is reflected from the PBS into the overlapping and fibre coupling section of the board.

After frequency controls each of the two MOT beams are overlapped with the repump light on their own PBS, before being coupled into optical fibres. There are two mirrors before and after each PBS (a total of four), allowing the trap and repump beams to be precisely (and separately) steered for coupling into the fibres. Rather than using off-the-shelf optical fibres for the MOT light, we use two different Laser2000 fused fibre splitters: a one input $\rightarrow$ two outputs fibre for the 2D MOT, and a one input $\rightarrow$ three outputs fibre for the 3D MOT. As before we couple into the fibres using position-adjustable aspheric lenses. However, due to the use of a fibre with a different mode-field-area, we use different lenses (Thorlabs C240TME-B). Due to the fusion method used to create the splitter fibres, it is more difficult to optimise the injection polarisation of the fibres as the polarisation axes are not perfectly aligned at the fuse point. This means that one has to minimise the overall drift in polarisation of the fibre outputs, rather than optimising a single output. We are also unable to couple light into the fibres as efficiently as desired due in part to poorer mode matching. The fibres are not perfectly balanced in intensity output, but this can be remedied later in the experiment. For example, through the $1 \rightarrow 3$ fibre we have a total efficiency of 52.8 % and

the three output ports contain 35.4 %, 31.7 % and 32.9 % of that output light.

'POPP' board: The 'POPP' board is seeded by light coupled out of the trap laser on the trap laser board. It is collimated using a fixed focus collimator. We split this light using PBSs to direct the light through three different double-passed AOMs, thus producing the push/plus beam, the probe (or imaging) light, and the optical pumping (OP) light (this ordering corresponds to the ordering of the relevant PBSs). In each of these cases, the AOM is at the centre of a one-to-one telescope formed by two $f = 150$ mm lenses. For the push beam we use a 200 MHz AOM set at 195.5 MHz, resulting in light which is 21 MHz below the $F = 2 \rightarrow F' = 3$ transition. Similarly, for the probe light, another 200 MHz AOM is used, which is set at 205.9 MHz, giving light which is 0.2 MHz below the $F = 2 \rightarrow F' = 3$ transition. Finally, the optical pumping light uses a 80 MHz AOM which is tuned to 72.55 MHz, giving a detuning of 0.1 MHz above the $F = 2 \rightarrow F' = 2$ transition.

The push/plus light is sent to the experiment using a standard Thorlabs optical fibre, coupled using a fixed focus collimator. The probe and optical pumping light will be overlapped on a non-polarising beam-splitter, to ensure that they have the same polarisation, before being coupled into another standard optical fibre.

3.2.3 Frequency Control

As discussed above, we use AOMs to provide precise and tunable frequency control as well as fast switching. We use AA Opto Electronic AOMs, with the MT80-B30A1-IR, MT110-B50A1-IR, and MT200-B100A0,5-800 models used to produce frequency shifts of the order of 80 MHz, 110 MHz and 200 MHz respectively. AOMs shift and angularly deflect beams through rf-induced Bragg diffraction in a crystal (in this case TeO_2). The frequency shift of the AOM is given by $\Delta\nu = nf$ where f is the frequency of the rf signal applied to the crystal and n is a positive or negative integer. We use the ±1 diffractive orders and block all unwanted modes. In addition to controlling the frequency shift of the light, the rf frequency determines the angular deflection of the diffractive orders (though this angular shift can be cancelled by operating in a double-passed arrangement). The diffraction efficiency depends on the power of the rf signal and the alignment of the crystal - the AOMs used here have a maximum rf input of 2 W.

We control our AOMs with two home-built driver boxes, which give us eight 2 W

radio frequency (rf) signals which are switchable and tunable both in power and frequency, with this controllability being mediated by LabView software. Following existing group knowledge we have implemented an adaptation of the controllers used in previous experiments [7,8,20,176] refined by Jonathan Pritchard into an easy to populate PCB set-up which controls (and limits) the voltages sent to the driver components.

The basic AOM driver (as used in [19, 20]) consists of a voltage-controlled oscillator (VCO), a mixer, an rf switch, and an amplifier attached in series. The VCO provides an oscillating signal, the frequency of which is controlled via a tuning voltage of 1 V–7 V. Its output is coupled into the local oscillator (LO) port of a double balanced mixer, providing amplitude control via a DC signal in the intermediate frequency (IF) port, with the resulting amplitude controlled signal being output through the rf-output port. We use Mini-Circuits VCOs ZX95-100-S+ and ZX95-200-S+, with frequency tuning over the ranges 50 MHz–100 MHz and 100 MHz–200 MHz respectively. Our mixers are again from Mini-Circuits and have model number ZX05-1-S+, they operate over a frequency range of 0.5 MHz–500 MHz. After frequency and amplitude control, switching is added with a high isolation rf-switch (Mini-circuits ZASWA-2-50DR+) which is controlled using a 5 V TTL signal. Finally, an AA Opto Electronics amplifier (AMPA-B-34-20.425) is used to amplify the signal to a maximum of 2 W.

3.3 Vacuum

Our vacuum chamber is an iteration on the design used in previous experiments [7, 8, 10].

Originally, as previously discussed (Sec. 2.2.4), we planned to use the grating MOT technology pioneered within the group [162,172,174–177], using a 2D GMOT pushed into a 3D GMOT. However, due to unforeseen problems during the upgrade of a the original BEC experiment at Strathclyde (see details in the thesis of Johnathan Conway), we returned to using the known technique of a standard 4 (6) beam 2D (3D) MOT in a glass cell. This change of tactic did not require significant changes to our laser system design. In fact we could simply use splitter fibres to create the extra beams needed.

In brief (and ignoring pumps etc.), the vacuum chamber consists of two glass cells separated by a differential pumping tube with a mirror attached to one end, a schematic of this is shown in Fig. 3.5. This gives us a high pressure chamber in which we can

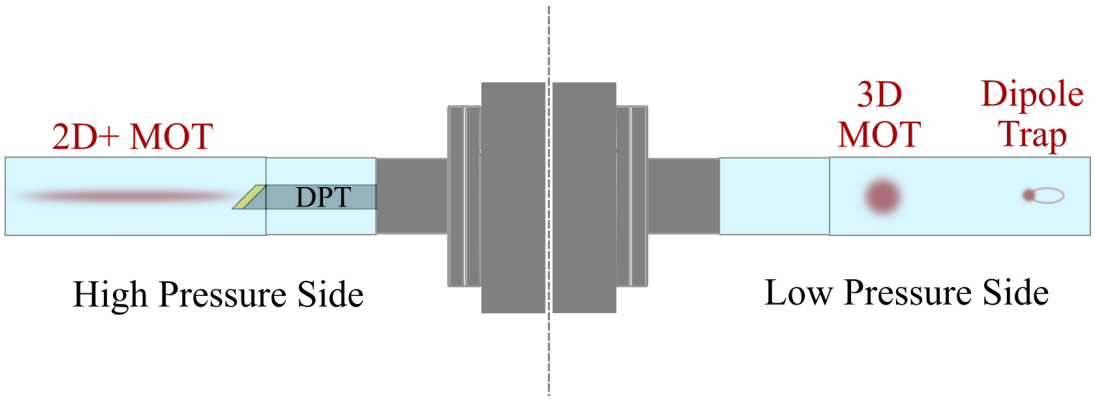

Figure 3.5: The basic schematic of the 'science' section of the vacuum chamber. Details are given in the text. The dashed line indicates a section of the body which is not shown. This is not to scale and is shown in more detail in later figures (Figs. 3.15 and 3.17).

collect atoms in a 2D+ MOT from a relatively rubidium rich atmosphere before the imbalance in intensity of the plus beam pushes atoms through a hole in the mirror, through differential pumping tube and into a low pressure cell at the other end. Here in the low pressure chamber, we can collect and further cool atoms in a 3D MOT with molasses, before magnetically transporting them to a crossed dipole trap for evaporation. The evaporative dipole trap will be overlapped with a dipole potential created by a Fresnel zone plate, allowing the zone plate trap to be loaded as easily as possible.

The vacuum chamber with magnetic field coils is shown in Fig. 3.6 from various view points.

The two glass cells used within our experiment were made by Precision Glass Blowing from Pyrex (also known as Schott glass or N-BK7). The cells have dimensions 30 mm $\times$ 30 mm and are 100 mm long; the glass has a thickness of 2.5 mm. The cell is attached to a 2-3/4" rotatable CF flange made of 316L/LN stainless steel, with the linking section having a 1.25" outer diameter (OD). The low pressure (a.k.a the 3D or science cell) is anti-reflection (AR) coated for 780 nm–795 nm. However the coating process had a low success rate resulting in Precision Glass Blowing being unable to supply a second coated cell. The two cells are shown attached the vacuum chamber in Fig. 3.7.

In order strike a balance between fast MOT load times (which requires a high

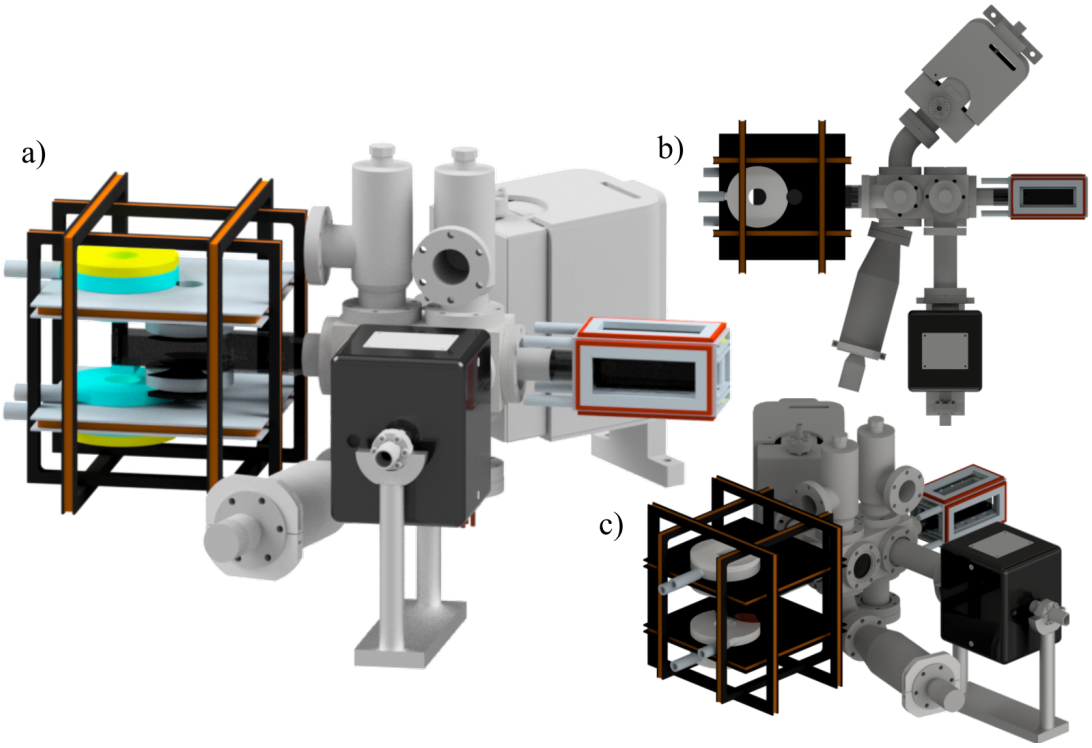

Figure 3.6: The vacuum chamber and coils. a) false colour view of the chamber (the false colour aids visibility), b,c) Alternative views.

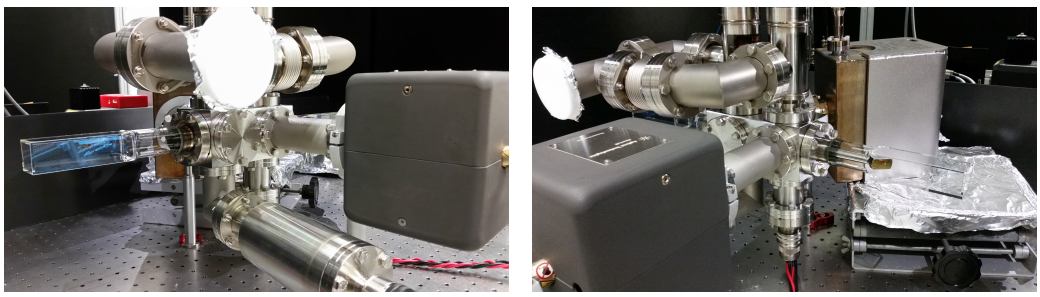

Figure 3.7: The two glasses cells. The low pressure (3D/science) cell is shown in the left image and the high pressure cell is shown on the right. We can see the gold mirror attached to the differential pumping tube in the high pressure cell.

background pressure of rubidium) and reaching temperatures and phase space densities compatible with BEC production (which requires a low background pressure), we need to separate the two halves of our vacuum chamber with a differential pumping tube. As suggested by its name, a differential pumping tube allows the two chambers it separates to have different pressures. This is done having a small diameter which restricts gas flow via its low conduction thus creating a situation where a lower pressure can be reached on one side. The tube also acts as an transverse velocity selector (that is for velocity perpendicular to the propagation of the push/plus beam) by virtue of its small aperture meaning that atoms with higher transverse velocity will collide with the sides of the tube, thus being lost between the two MOT stages. The design of the tube was informed by modelling of the expected velocity distribution of atoms in the MOT.

The design of the differential pumping tube is shown in Fig. 3.8, alongside a photo of the machined tube. Here we see that the tube initially has an inner 2 mm diameter, with this increasing in two steps along the length (156 mm) of the tube to 5.85 mm and 7.20 mm; the graduation in internal diameter, accounts for the thermal expansion of a jet of atoms travelling through the tube and the drop of the atoms under gravity. The tube was machined from 316L/LN stainless steel. Due to the tube's similarity to that used in [7], we expect it to have a similar conductance ($0.022\,\mathrm{L\,s^{-1}}$) and be able to maintain a pressure ratio of 10^{-4} between the two sides of the chamber.

At one end of the DPT, the tube is cut at a 45° angle. We attached a mirror to this surface using vacuum compatible epoxy. The mirror, a 25.4 mm diameter, protected-gold coated, aluminium substrate mirror from Edmund Optics (part number 47-114), was cut to size and a 2 mm hole drilled to match the end of the DPT.

All of the vacuum components were attached to a custom machine rectangular block of the same design as used in [7, 8, 10]. Its 316L/LN design has 10 2.75" CF ports and a plate in the centre onto which we mount the DPT. We use all but 2 ports for various vacuum components, with the unused ports sealed with blanks. The ports on the top of the chamber are home to two valves (MAV-150-V right angle valves), which allow us to attach a roughing pump to the chamber during the initial evacuation and baking process. The valves will also allow us to modify the chamber in the future (i.e. add additional dispensers) without breaking vacuum.

In order to achieve and maintain vacuum, we use three different vacuum pumps: a

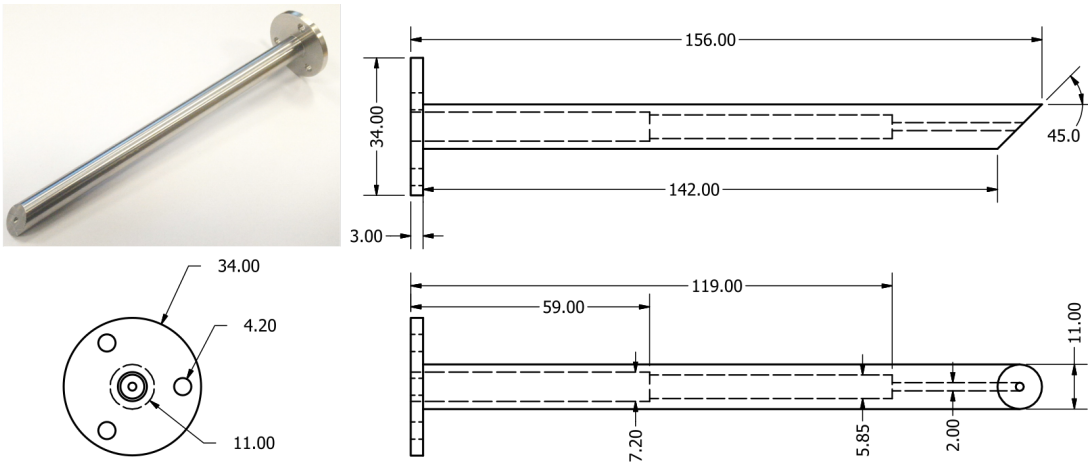

Figure 3.8: The differential pumping tube and its dimensions, with the technical drawing showing the shape and size of the inner tube.

45 L s^{-1} ion pump, a 20 L s^{-1} ion pump, and a non-evaporable getter (NEG). The lower rate pump is attached to the 2D cell side of the chamber (high pressure) and is an Agilent VacIon Plus 20. We use a custom-made mu-metal shield to reduce the influence of the pump's magnetic field on the experiment. The higher rate pump is attached to the 3D cell side (low pressure or science cell). In this case the pump is a Gamma Vacuum TiTan 45S ion pump, it has its own integrated magnetic shields. We control both these ion pumps with controllers from the corresponding manufactures (Agilent's MiniVac controller and Gamma Vacuum's SPC ion pump controller). The NEG is a SEAS CapaciTorr D 400-2 which is attached to the low pressure side of the vacuum chamber. Once activated this pump provides passive pumping, meaning that should low pressure chamber pump fail, we have back-up pumping. In Fig. 3.6 (a, c), the 45 L/s Gamma Vacuum pump is on the far side of the chamber, the 20 L/s Agilent pump is the black pump on the near side of the chamber, and the SEAS NEG is the tube on the near side of the chamber which is attached to the bottom of the vacuum block.

As an atom source, we attach four SEAS ^{87}Rb dispensers to copper feed-throughs in a ring layout. In Fig. 3.9, we show two of the four dispensers having been attached. Once all four dispensers are attached, they form a ring of dispensers. We can operate the dispensers in one of 3 arrangements (Fig. 3.9(b)), either using the dispensers individually (diagram A), or all together (B or C). If we wish to operate all dispensers simultaneously, schematic B requires a lower total operating current than C. The dis-

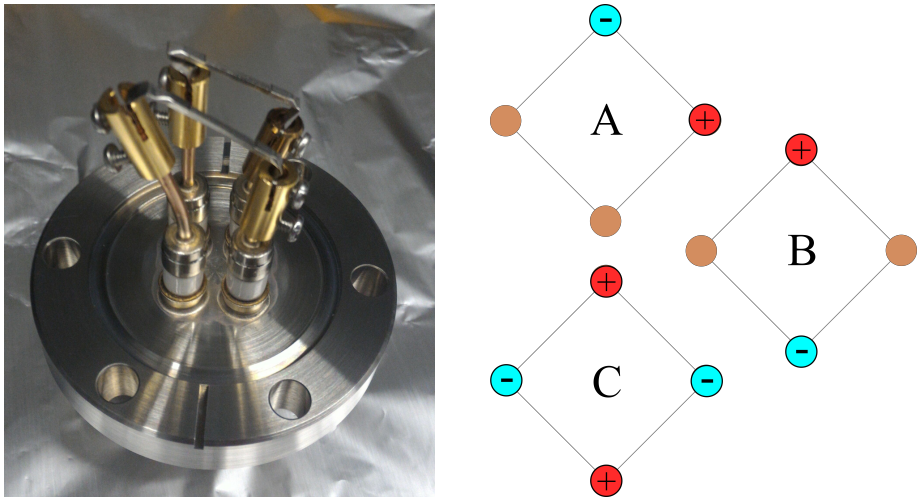

Figure 3.9: The attachment of dispensers in our system. The photo shows two of the four dispensers attached to feed-throughs. The right hand schematic shows three different arrangements for connecting the dispensers, allowing us to operate one dispenser at a time (A), or all at once (B and C).

pensers were activated while wired in the arrangement shown in B, but during normal operation, we utilise arrangement A so that we can use each dispenser in turn. The normal operating current for a single dispenser is 6.5 A.

We note that some compact high repetition rate BEC machines (namely the QUANTUS collaboration [218, 228]) have been unable to form a 2D+ MOT when using dispensers as their atom source due to contamination from other atomic species. They now use ovens instead (though still do not use a Zeeman or another precooler). Using an oven takes up a larger footprint but would operate in a similar manner (i.e. by heating the sample - here an ampoule). As we have been able to form a 2D+ MOT using dispenser, this is not a problem in our experiment.

3.3.1 Bake Out

In order to operate in ultra-high vacuum (UHV), we needed to bake the vacuum system. This out-gasses residual water in the vacuum components, and allows lower pressures to be reached. While the system is still hot, and before the ion pumps are fully turned on, we also need to activate the NEG, the ion pumps (known as 'burping' the ion pump), and the dispensers. This process allows any impurities in the components to be removed from the chamber by the roughing station pump rather than damaging the

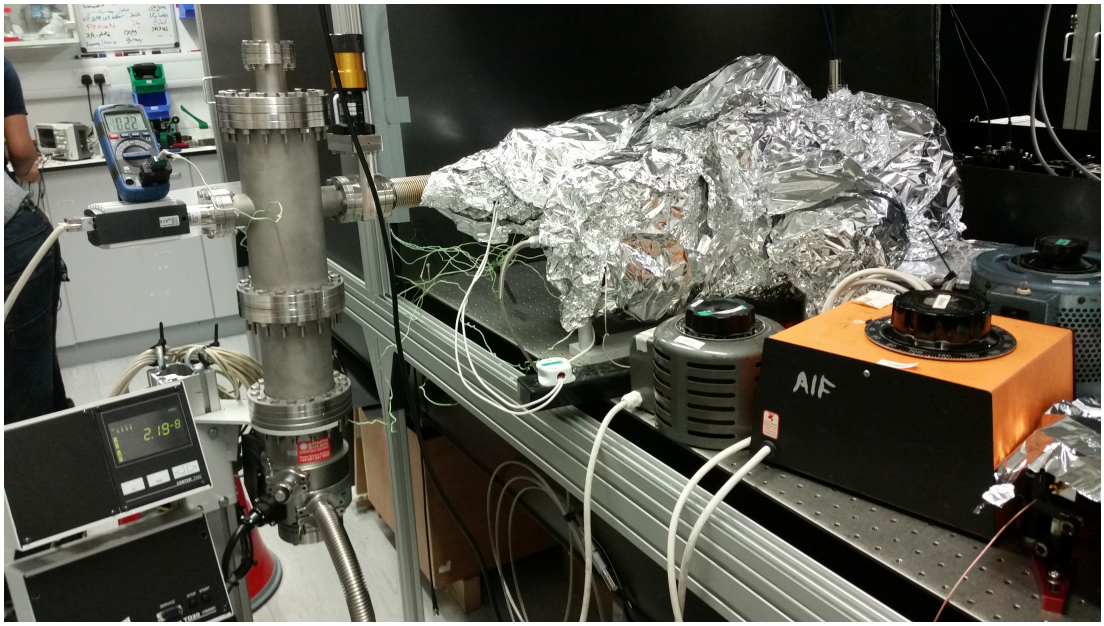

Figure 3.10: A photo of the chamber during the baking process. The chamber is insulated using foil, and heated using variac controlled heating tapes. The turbomolecular pump can also be seen.

ion pumps (such damage is known as poisoning). This is particularly important for the dispensers, as we need to coat the metal interior of the chamber with rubidium such that a useful vapour pressure is present, but this amount of rubidium may poison the ion pumps and reduce their life spans. A photo of the chamber during the baking process is shown in Fig. 3.10.

A time-line showing the temperature and pressure of the chamber during the baking process is shown in Fig. 3.11. We gradually heated the chamber up to 200 °C over a period of 6 days (with this period being determined by a bank holiday weekend), the chamber was kept at this temperature for 7 days, before being cooled gradually. We activated each component individually once the chamber had reached 40 °C. We record a pressure of 1×10^{-9} mbar in the high pressure side and 1×10^{-11} mbar in the low pressure side, with these values being at the lower limit of measurable range of the ion pump controllers.

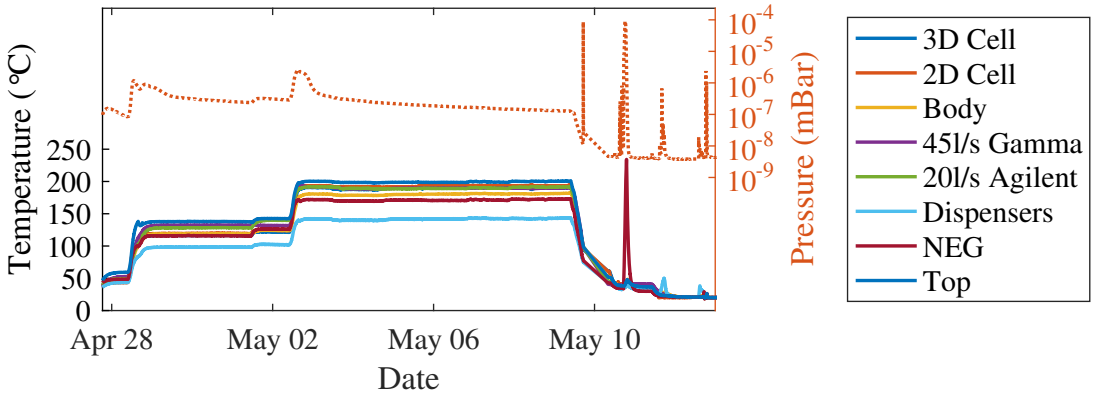

Figure 3.11: The baking process for our chamber. The solid lines correspond to temperature measurements at various positions around the chamber (their positions are shown in the legend). The orange dotted line (right axis) shows the pressure of the chamber throughout the bake, measured using an ion gauge on the roughing station.

3.4 Magnetic Fields

As discussed in Sec. 2.2, magnetic fields are a crucial part of any laser cooling set-up. In our experiment, we require three sets of trapping coils, plus two sets of compensation coils (also know as shim coils). The coils are designed to be easy to mount, with them being mounted on the vacuum chamber (by attachment to the flanges) as far as possible. This means that we can slip the coils on and off easily.

2D coils: For the 2D+ MOT, we require a 2D quadrupole field (i.e. a quadrupole field in the axes perpendicular to the MOT centre, such that a line of magnetic field minimum is present along the centre of the MOT, see Sec. 2.2.2 for details). A diagram and photo of the 2D coils are shown in Fig. 3.12. They are rectangular quadrupole coils in an anti-Helmholtz arrangement. The MOT coils yield the following gradients at their centre in the x, y, and z direction: 5.22 G/cm/A, 4.06 G/cm/A, and 1.17 G/cm/A. When operating at 4.5 A, the temperature increase of the coils is approximately 17 °C with continuous operation for over 1 h, with a negligible change in length of the coil wires. The shim coils (rectangular Helmholtz coils) give a suitably uniform magnetic field of 1.1 G/A at the centre.

3D MOT coils: For the 3D MOT we have a pair of circular coils in an anti-Helmholtz arrangement, giving us a 3D quadrupole field. Here the coils have an inner

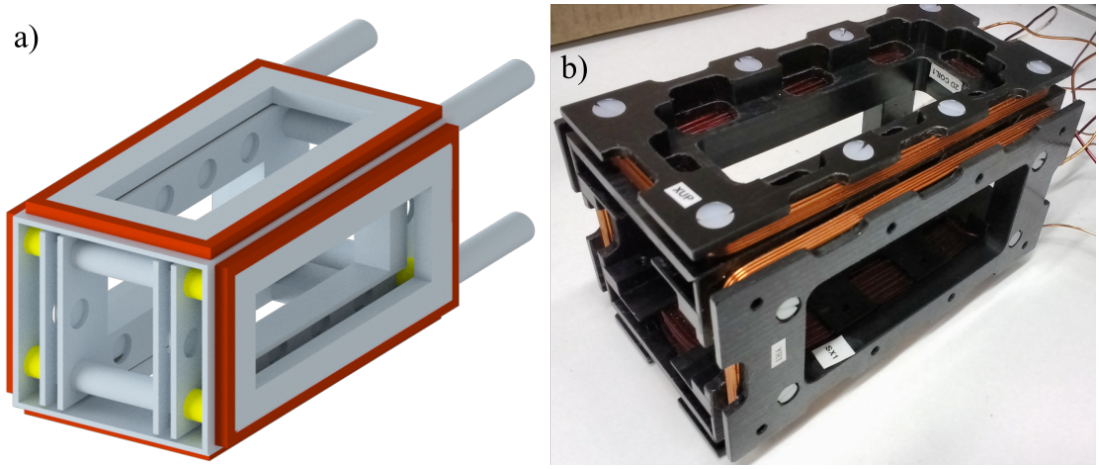

Figure 3.12: Magnetic field coils for the 2D+ MOT (2D quadrupole and shim coils). a) is a CAD drawing of the coils and b) shows the coils before being mounted on the chamber.

radius of 15 mm, a coil separation of 35 mm, and 180 turns. This yields an expected gradient of 18.6 G/cm/A and can be operated at a current of up to 3.5 A. The expected power dissipated by the coils during normal usage is less than 9.5 W, meaning that air cooling will be sufficient for their operation.

Magnetic quadrupole coils: We use a second set of circular coils in an anti-Helmholtz arrangement to create a quadrupole field which can be used for magnetic transport, hybrid evaporation cooling or as a levitation field. Due to the spatial constraints of the experiment (i.e. other coils and optical access), these coils must be further from the cell, and so require many more coil turns and run at a higher current (when compared to the MOT coils). In this case we have 289 turn coils with an inner radius of 18.5 mm and separation of 67 mm. This results in an expected gradient of 9.24 G/cm/A and required operating current of below 22 A. Due to this high current requirements, the coils dissipate a large amount of power (650 W) and so water cooling is needed. This cooling is provided by the white, 3D printed, Nylon (SLS Nylon PA2200) cups, which can be seen in Fig. 3.13, which hold the coils in turbulent flow of recirculating water.

3D shim coils: We use shim coils to cancel background magnetic fields in the lab. Being able to cancel magnetic fields is crucial for experiments with ultra-cold atoms

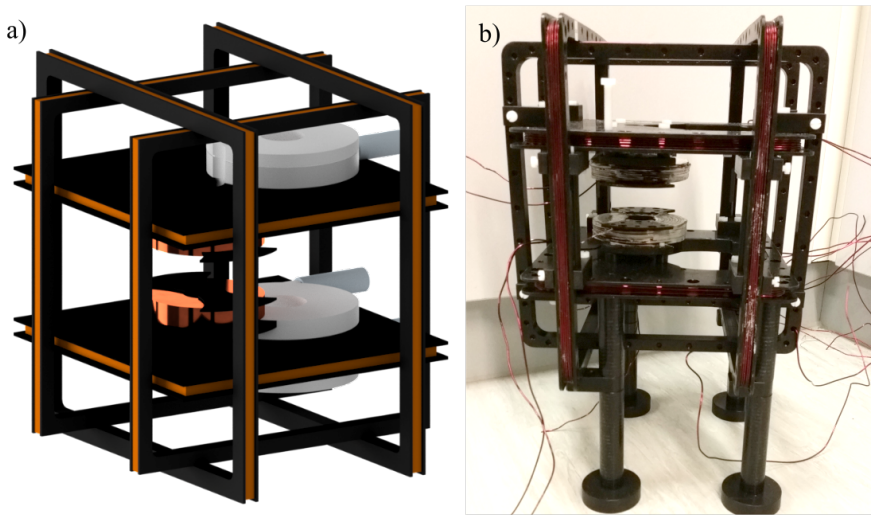

Figure 3.13: The magnetic field coils for the low pressure side of the chamber. In the CAD drawing (a), the square shim coils, 3D MOT coils (smaller circular coils), and the holder for the quadrupole coils (white mounts) can be seen. In the photo (b), the shim and 3D MOT coils have been attached, but the quadrupole coils are still being tested so are not present in the photo.

so as to avoid distortion of atom clouds, meaning that the shim coils on this side of the experiment are much more important than those used on the 2D side. On this side, we have three square pairs of coils, each in a Helmholtz-style configuration (i.e. with currents flowing in the same direction), allowing us to compensate for fields in all directions.

These square shim coils are designed to give similar magnetic fields at the centre of the coil: $(B_x, B_y, B_z) = (2.2, 2.2, 2.4)$ G/A. The coils have the following dimensions (where r is the coil side length, D is the coil separation, and N is the number turns): $(r_x, r_y, r_z) = (180, 210, 230)$ mm; $(D_x, D_y, D_z) = (180, 210, 230)$ mm; $(N_x, N_y, N_z) = (25, 30, 35)$. The x, y, and z directions correspond to the inner, middle and outer shim coils in Fig. 3.13.

3.5 Magneto-Optical Traps

Prior to creating a MOT in the new vacuum chamber, we tested the lasers in an existing atomic clock experiment [176], which we share a lab with. This experiment uses a grating to create a MOT (see Sec. 2.2.4), with the required light fibred to the

Figure 3.14: A fluorescence image of a GMOT created using our laser system.

vacuum chamber. This means we could simply replace their fibre input with ours and optimise polarisation to achieve a MOT. The MOT obtained is shown in Fig. 3.14. The frequency of the light was not optimised at this stage as the atomic clock experiment uses a different MOT scheme (GMOT) and experimental controls.

3.5.1 2D+ MOT

As is the repeated theme when designing this experiment, we have tried to make everything as compact and modular as possible. For the 2D+ MOT, this means that we have designed and created 'plug-and-play' output couplers where, once they're aligned, we can unplug or swap fibres without needing to realign the system.

Previous BEC experiments in the group have used either a standard 3D or 2D MOT with a push beam to load atoms through the differential pumping tube to the low pressure cell and a 3D MOT [7, 8, 10, 19, 20]. However, a 2D+ MOT can provide higher atom flux and lower temperatures without a more complex optical set-up [165, 167, 229–231]. In a 2D+ MOT, the push beam is larger than the DPT hole and is retro-reflected back through the MOT, giving molasses cooling along the axial direction and creating an intensity imbalance which gives atom flux through the DPT.

Typically, a 2D MOT will be produced using four elliptical beams, giving a long thin trapping volume. The elliptical beams are generally created with large cylindrical lenses, however, one can obtain similar results by using a series of smaller circular beams, which reduces the complexity and size of the optical set-up [229, 230, 232]. We use a similar arrangement to that used in Refs. [229, 232], using polarising beam-splitters to create a series of three individual circular beams.

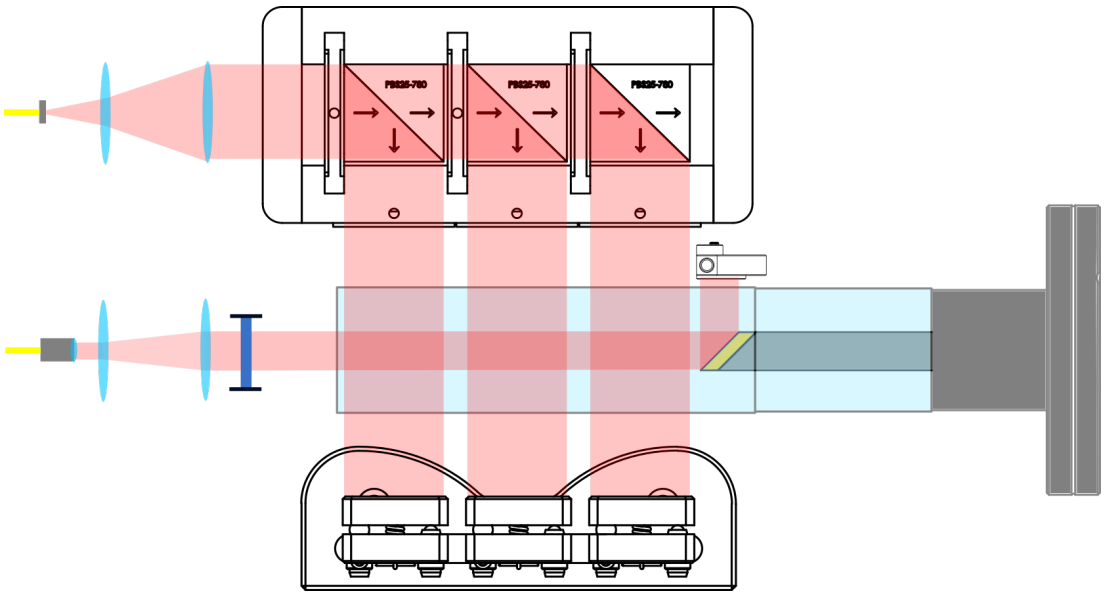

Figure 3.15: The optical layout of the 2D+ MOT (Not to scale). The layout is described in detail in the text.

A schematic of our 2D+ MOT optics is shown in Fig. 3.15. Here we show the glass vacuum cell (light blue) with the differential pumping tube and its mirror inside the cell (mirror is shown in yellow), the CAD line drawings above and below the cell show the designed couplers used to create the MOT - these are not to scale and are for illustration purposes rather than exact replicas of those actually manufactured (this is due to minor changes in the design occurring during manufacture).

2D MOT beams: To generate the MOT light, we use a cage-mounted telescope to expand and collimate each diverging fibre output. The telescopes use −50 mm and 75 mm lenses, with 30 mm between the fibre output and the first (−50 mm) lens, and 58 mm between the two lenses. This yields a collimated beam with 9.38 mm (9.13 mm) $1/e^2$ radius for the horizontal (vertical) coupler. The positions of the lenses are optimised for collimation and size using a shearing interferometer.

After the expanding telescope, the light is distributed through three PBSs using half-waveplates. The waveplates are set such that the three reflected beams have equal power (i.e. a third of the total power in this arm), and no light is transmitted through the final PBS. The half-waveplates are mounted in between the PBSs and are adjustable. After each PBS, the polarisation of each reflected beam is made circular using a quarter-waveplate. The quarter-waveplate positions are indicated by the small

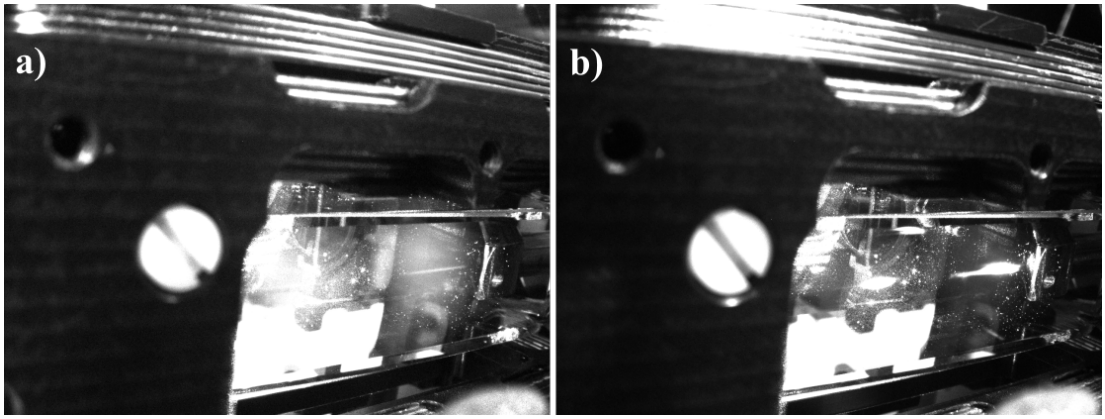

Figure 3.16: Images of the 2D+ MOT. a) Shows an optimised 2D+ MOT - the atoms are visible as a thin line in the centre of the chamber. In b) the MOT is optimised for florescence (maximum visibility) rather than for loading rate; here we can see two 2D MOTs forming at the overlap of two of the 2D beams.

circles at the output ports of the mount in the schematic. After the light passes through the cell, it is retro-reflected by mirrors with quarter-waveplates glued to them.

Plus beam: The plus beam is collimated out of its (standard Thorlabs) optical fibre with a fixed focus collimator (Thorlabs F280APC-780), giving a $1/e^2$ radius of 1.5 mm. This is then expanded using a telescope with lenses of focal length −50 mm and 100 mm, giving a final $1/e^2$ radius of 3.13 mm. The light then passes through a half-waveplate which allows the orientation of this linearly polarised light to be optimised. Light is then reflected out of the cell by the DPT mirror and retro-retroreflected back through the cell by a d-shaped mirror.

To align and optimise the 2D+ MOT, a temporary 3D MOT on the low pressure side was used to collect atoms. It is a temporary set-up used to optimise the 2D+ MOT in advance of the low pressure side coils being completed. The optics system used is the same as will be used in the final 3D MOT, though the exact positioning of the optics may be modified to enable optical access for later experimental stages.

Images of the 2D MOT are shown in Fig. 3.16, with (a) showing the optimised 2D+ MOT (a line of atoms can be seen in the centre of the cell and is particularly visible in the right half of the image). In (b) the MOT is optimised for fluorescence rather than loading rate, allowing us to see the positions of the individual 2D MOTs. Here we can only see two MOTs rather than the three expected, this is due to two

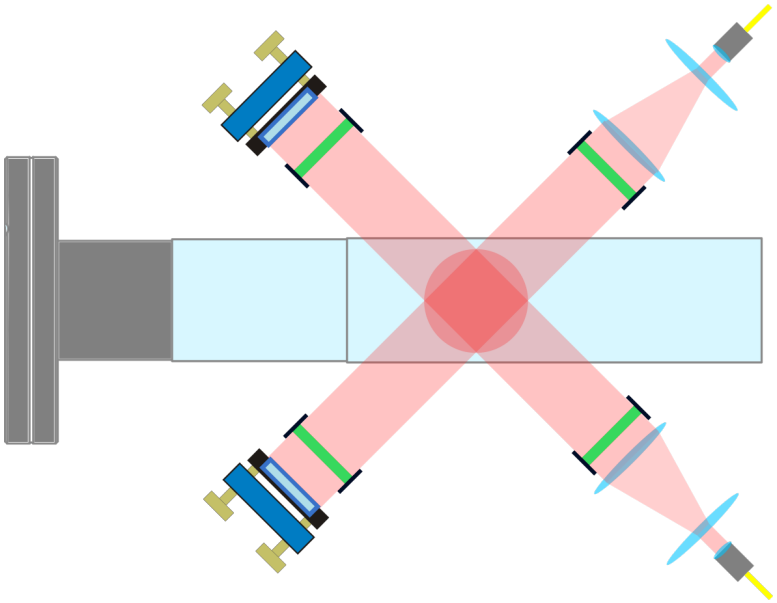

Figure 3.17: The optical layout of the temporary 3D MOT (Not to scale). The layout is described in detail within the text.

problems encountered when combining the designs of the beam splitter mount and the magnetic field coils. Firstly, during the manufacturing process, the width of the half-waveplate mounts between PBSs increased, meaning that the total length of the mount and the separation between successive MOTs would be larger. This meant that the beam furthest from the DPT is clipped by the coil former. Although the clipping means that a third MOT does not form, it should still result in extra cooling. However, the magnetic field at this end point is no longer shaped as a quadrupole due to edge effects from the coils and so a MOT cannot be formed in this region.

3.5.2 3D MOT

The 3D MOT consists of three retro-reflected MOT beams which give us a traditional six beam MOT. Light is sourced from the one-to-three splitter fibre, with each fibre having identical expansion telescopes and polarisation optics.

The light is expanded to the same beam radius as for the 2D MOT using the same telescope arrangement. It then passes through a quarter-waveplate to set the polarisation to circular. After passing through the cell and atoms, the light is retro-reflected from a mirror with a quarter-waveplate attached. This set-up is repeated for each of the three dimensions, with Fig. 3.17 showing the 2 horizontal beams (the circle in the

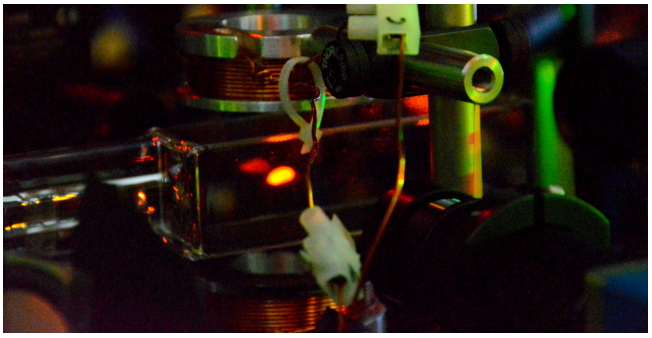

Figure 3.18: A photo of the temporary 3D MOT.

centre shows the vertical MOT beam).

We can use the 3D MOT to characterise and optimise the 2D+ MOT by recording and optimising loading rates. We see a maximum load rate of $(5.32 \pm 0.09) \times 10^8$ atoms/s which is comparable to the 2D-push MOT shown in table 2.1, but lower than the 2D+ loading rate shown. This loading rate is measured via pulsed loading of the MOT. With a 15 s load time, we achieve an atom number of $>5 \times 10^9$ in the 3D MOT, 10 times higher than in Ref. [8]. The optimisation and characterisation of the MOTs will be discussed in detail in future work. A picture of the 3D MOT is shown in Fig. 3.18.

3.6 Evaporation Cooling

A variety of evaporative cooling techniques were mentioned in Sec. 2.2.9. Here we will discuss which of these techniques are expected to be used with this experiment. We summarise a small subset of existing BEC experiments in Fig. 3.19, showing a range of atom chip, hybrid, all-optical and laser cooling based BEC machines, which (in general) are designed for fast BEC creation.

Here we see that the smallest and fastest BEC machines use atom chip traps with rf evaporation [218, 233–235]. Atom chips allow fast creation of BECs due to their size and proximity to the atoms, this means that tight, flexible magnetic traps can be made in a very small space.

All-optical evaporation is a relatively new technique (compared to rf evaporation) with fast evaporation being challenging due to the difficulties of reaching the runaway regime in a standard dipole trap. A variety of techniques have been used to mediate this problem, such as MACROFORT [211], compressible (or double-compressible)

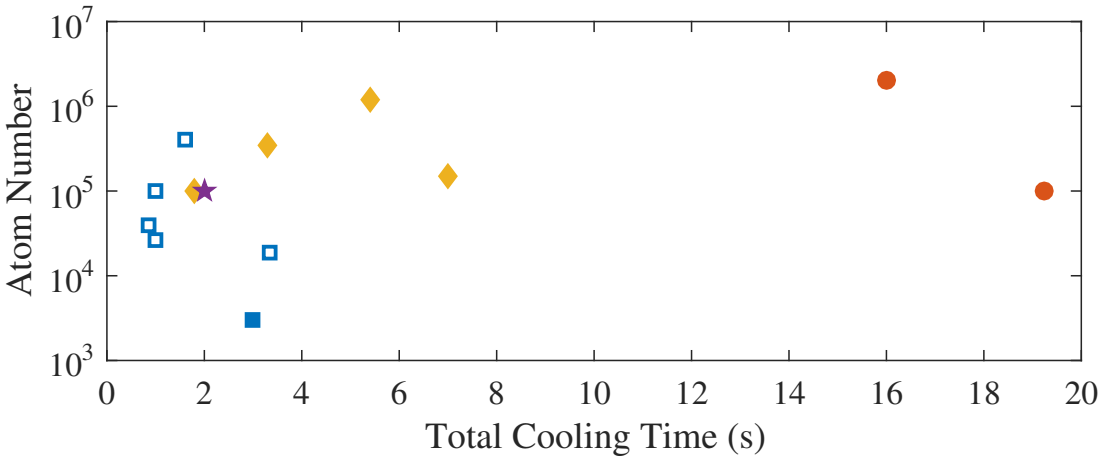

Figure 3.19: Comparison of a variety of evaporative cooling methods, with final BEC atom number being plotted against total cooling time (including precooling steps). Compact experiments are shown with unfilled symbols as opposed to filled markers. Atom chip [218, 233–235], hybrid (optical and magnetic) [8, 9, 213], all optical [210, 211, 236, 237], and laser cooling [215] techniques are shown by the blue square, orange circle, yellow diamond, and purple star respectively. We note that the all optical route with the smallest cooling time uses Yb rather than Rb in the other cases.

crossed-dipole traps [210, 236], or dynamically shaped optical traps [237]. These all-optical techniques can reach similar total cooling times and atom numbers as atom chips, though they are not yet commonly implemented in compact/portable set-ups.

An earlier optical evaporation technique is that of hybrid traps, where a crossed dipole beam and a quadrupole magnetic field are used. This is used in an existing experiment at Strathclyde [8, 9], which achieves 1×10^5 atoms in under 20 s, where the first 15 of those seconds are dedicated to MOT loading.

By comparing the optical access, footprint and complexity, we can assess the suitability of the above techniques for our experiment.

We need very good optical access in order to use the zone plates and we want to be able to easily overlap and load the zone-plate generated potential, so atom chips are not suitable for our experiment. An atom chip would block optical access from at least one direction, and we would not be able to overlap the trap centre with a zone plate easily due to the small distance from the trap to the chip. We also note that the zone plates are designed to produce a potential approximately in the centre of the chamber, a position which is not achievable with an atom chip.

This leaves either an all-optical trap (with its associated complexity) or a hybrid trap (which requires a magnetic field as well as dipole beams). As both scenarios require the use of two crossed dipole beams, it makes sense to make the experiment as flexible as possible, by creating a situation where either technique could be used. We also note, that if we wish to use a ring in vertical orientation (that is to place the zone-plate glass at the end face of the cell), we would need to be able to evaporate in this position as well as in an arbitrary position along the centre of the cell, requiring magnetic transport. We also know that hybrid evaporation works in a chamber very similar to ours as it has already been done in this group [8].

Therefore, since we need to use magnetic transport to allow for overlapping of potentials, we should initially build the experiment with the view of using hybrid evaporation, for which we already have a suitable quadrupole coil (as discussed in Sec. 3.4). We would then be able to possibly upgrade the experiment to use a simple all-optical evaporative process after magnetic transport to increase the repetition rate.

3.7 Imaging

Within the experiment, we will use a variety of imaging techniques to analyse the atomic ensemble. Mainly, we will use fluorescence imaging to achieve in-situ imaging of the MOTs during loading and optimisation phases, and use absorption imaging to image the BEC. In order to perform an interferometric read-out, we plan to use the contrast interferometry scheme used and outlined in [8–10]. The methods by which one can use absorption imaging to characterise a BEC are described in Sec. 4.2.1.

Chapter 4

Understanding and Analysing Ultra-cold Atoms and Bose-Einstein Condensates

In all the experiments discussed in this thesis we use or plan to use a BEC to perform precise measurements. A thorough understanding of how BECs behave is crucial to being able to use them for metrology and for predicting how BECs will behave in the ring traps covered later in the thesis (Chaps. 5, 6, and 7).

This chapter is split into two parts, in the first I will discuss some of the theoretical description of BECs which are most relevant to our experiments. This will start by explaining the Gross-Pitaevskii equation (a form of the non-linear Schrödinger used to describe BECs), then move on to discussing properties such as temperature, density, phase and coherence, and various excitations which can lead to phase fluctuations.

The second part will be concerned with the practicalities of making measurements using BECs. This will begin with introducing how BECs can be measured using absorption imaging, to find out atom numbers and temperatures. This will then be used to briefly discuss results pertaining to the existence of phase fluctuations in elongated, cigar-shaped condensates. The imaging system modifications and experimental results presented in this section were obtained early in my PhD. Further details of this experiment are covered in Refs. [18–20, 29–31].

4.1 Properties of Bose-Einstein Condensates

As presented in the introduction (Sec. 1.2) and the experimental theory chapter (Chap. 2.2.9), a Bose-Einstein condensate (BEC) is a quantum degenerate state in which an atomic cloud condenses such that the ground state is macroscopically occupied. This condensation occurs when the de Broglie wavelength of the atoms becomes larger than the interatomic spacing. At this point the atoms behave as a single, observable, quantum mechanical object.

As the ground state of a BEC has macroscopic occupation, it can be described by a single wavefunction. Naïvely, we can say that the cloud of atoms are completely coherent that so it provides a perfect analogue for a laser in an atom interferometer. However, this perfect behaviour only occurs at zero temperature, an ideal we cannot hope to reach. So we need to understand how typical experimental conditions, like finite temperature and various trapping geometries, affect a condensate.

4.1.1 The Gross-Pitaevskii Equation

To build a quantum mechanical description of BEC we can begin with the Hamiltonian for an atom in a potential in Eq. 2.9 and add in inter-atomic interactions as we're now looking at an ensemble of atoms, this approach follows that laid out in Refs. [238,239].

BECs are very dilute as well as being low temperature, this means that atoms interact via s-wave, 2-body collisions. In this scenario, the interaction potential (U) of a single pair-wise interaction between two atoms can be modelled by

$$U\left(\vec{r}-\vec{r'}\right) \approx g\,\delta\left(\vec{r}-\vec{r'}\right)\,, \tag{4.1}$$

where the interaction is completely described by the s-wave scattering length a_s:

$$g = \frac{4\pi a_s \hbar^2}{m}\,, \tag{4.2}$$

If one sums over all particles then this contact interaction becomes a mean field potential proportional to the atomic density ($n(\vec{r})$), $U_{\text{eff}}(\vec{r}) = g\,n(\vec{r})$, giving us an effective Schrödinger equation for an atom $\psi(\vec{r})$ with energy ϵ in a trapping potential V_{trap}

$$H_{\text{eff}}\psi(\vec{r}) = \left[-\frac{\hbar^2}{2m}\nabla^2 + U_{\text{trap}}(\vec{r}) + U_{\text{eff}}(\vec{r})\right]\psi(\vec{r}) = \epsilon\psi(\vec{r})\,. \tag{4.3}$$

In the thermodynamic limit (i.e. $N \to \infty$), at $T = 0$, this equation reduces to the equation below. This semi-classical approach is called the time-independent Gross-Pitaevskii Equation (GPE) [238, 239], which describes the ground state wave-function ($\psi_0(\vec{r})$) for N atoms with an eigenvalue of μ, the chemical potential:

$$\left[-\frac{\hbar^2}{2m}\nabla^2 + U_{\text{trap}}(\vec{r}) + gN\left|\psi_0(\vec{r})\right|^2\right]\psi_0(\vec{r}) = \mu\,\psi_0(\vec{r})\ . \tag{4.4}$$

The ground state wave-function can also be thought of an order parameter, which is a useful description when considering the coherence of a BEC (Sec. 4.1.4). In these descriptions it is important to note that $\left|\psi_0(\vec{r})\right|^2 = n(\vec{(}r))$.

Thomas-Fermi Limit

When analysing a BEC, we tend to operate under conditions that satisfy the Thomas-Fermi limit, the limit of large atom number. In this case, the interaction term dominates over the kinetic energy, so the GPE reduces to:

$$U_{\text{trap}}(\vec{r}) + gN\left|\psi_0(\vec{r})\right|^2 = \mu\ , \tag{4.5}$$

which, recalling that $n(\vec{r}) = N\left|\psi_0(\vec{r})\right|^2$, has the following solution [239]:

$$n(\vec{r}) = \begin{cases} \frac{\mu - U_{\text{trap}}(\vec{r})}{g} & : \mu > U_{\text{trap}}(\vec{r}) \\ 0 & : \mu < U_{\text{trap}}(\vec{r}) \end{cases} \tag{4.6}$$

This solution leads us to the concept of a Thomas-Fermi radius, which is the radial position in a harmonic trap at which the trapping potential and the chemical potential are equal. Outside of this radius, in the Thomas-Fermi approximation, the condensate density is zero.

Eq. 4.6 can be used to calculate the chemical potential of the condensate in a particular trapping potential through normalisation, that is by realising the condition $N = \int dV\ n(\vec{r})$ (an integral over all volume V).

In an anisotropic harmonic trap, as used in experiments presented at the end of this chapter, a potential of the form

$$U_{\text{trap}}(x, y, z) = \frac{1}{2}m\left(\omega_x^2 x^2 + \omega_y^2 y^2 + \omega_z^2 z^2\right)\ , \tag{4.7}$$

has a chemical potential of the form [239],

$$\mu = \frac{\hbar\bar{\omega}}{2}\left(15Na_s\sqrt{\frac{m\bar{\omega}}{\hbar}}\right)^{2/5}, \tag{4.8}$$

where $\bar{\omega} = (\omega_x\omega_y\omega_z)^{1/3}$, is the geometric mean of the trap angular frequencies in each direction ($\omega_{x,y,z}$). An equivalent chemical potential will be described in Sec. 4.1.3.

For a spherical harmonic trap with $\omega_r = \omega_{x,y,z}$ (i.e. $\bar{\omega} = \omega_r$) the Thomas-Fermi radius (R_{TF}) is given by,

$$R_{\mathrm{TF}} = \sqrt{\frac{\hbar}{\omega_r}}\left(15Na_s\sqrt{\frac{m\bar{\omega}}{\hbar}}\right)^{1/5}. \tag{4.9}$$

4.1.2 Temperature and Density

To understand condensation at finite temperature, i.e. that the ground state is macroscopically occupied but there is still finite occupation of the excited states, we can look to a statistical model of condensation.

By adopting the 2-fluid model of superfluidity, we can describe a condensate at non-zero temperature by the density decomposition $n = n_n + n_0$, where n_n is the normal thermal fraction which occupies the excited states of a trapping potential, and n_0 is the condensate (ground-state) fraction [238,239]. The condensate fraction is well described by the Thomas-Fermi limit of density (Eq. 4.6), whereas the normal fraction is well described by the Bose-Einstein distribution.

The Bose-Einstein distribution gives the mean occupation number of an energy state ϵ_i in terms of the chemical potential μ and the temperature T:

$$f(\epsilon_i) = \frac{1}{e^{(\epsilon_i-\mu)/k_BT} - 1}. \tag{4.10}$$

We can use this and the density of states (per unit volume) to write the particle density as a function of temperature and chemical potential, which in turn means that the chemical potential can be written in terms of the temperature and particle density. This is a standard derivation and is presented in Refs. [238, 239]. Condensation occurs at the transition temperature T_C, which is defined as the point at which the chemical potential of a non-interacting Bose gas is zero. At this point of condensation, the excited states are saturated and any particles added to the system must populate the ground

state rather than the excited states. For a harmonic trapping potential, the critical temperature is given by,

$$T_C = \left(\frac{N}{\zeta(3)}\right)^{\frac{1}{3}} \frac{\hbar\bar{\omega}}{k_B}\,, \tag{4.11}$$

where $\zeta(3) = 1.202$ is the Riemann zeta function evaluated at 3.

The derivations above give us a way to the write the relative ground state occupation (i.e. the condensate fraction) in terms of the ratio between the temperature and the critical temperature:

$$\frac{N_0}{N} = \frac{n_0}{n} = 1 - \left(\frac{T}{T_C}\right)^3\,, \tag{4.12}$$

though, as with all the statistical derivation mentioned above, this is approximate as it does not account for finite particle number and assumes a perfectly harmonic trap (the exponent 3 is dependent on the trap geometry so, for example, is 3/2 for a box in 3D).

When measuring a BEC or any cloud of atoms, our observable is the density distribution (as is discussed in Sec. 2.3.1), which for the normal, thermal, fraction is approximated by

$$n(\vec{r}) = \frac{N}{(2\pi)^{3/2}\sigma_x\sigma_y\sigma_z} \exp\left(-\left(\frac{x^2}{2\sigma_x^2} + \frac{y^2}{2\sigma_y^2} + \frac{z^2}{2\sigma_z^2}\right)\right)\,, \tag{4.13}$$

where $\sigma_i^2 = k_B T/(m\,\omega_i^2)$ are the widths of the cloud in each direction [239]. This assumes that thermal atoms mainly occupy the low-density, weakly interacting edges of the cloud and so the Bose-Einstein distribution is well approximated by the Maxwell-Boltzmann distribution [155]. The density distribution of thermal atoms and the condensate fraction are shown for a harmonic, cigar-shaped trap in Fig. 4.1.

The condensate fraction as written above, assumes that the condensate and the thermal atoms are well separated, whereas in reality the condensate acts to modify the potential in which the thermal atoms reside – raising the bottom of the effective potential felt by the thermal atoms [240]. This correction does not play a significant part in the analysis of data with our experiment as we do not operate close enough to $T = 0$ or the transition temperature. A first order correction (as derived in [240]) is shown in Fig. 4.1 in addition to the relation given by Eq. 4.12.

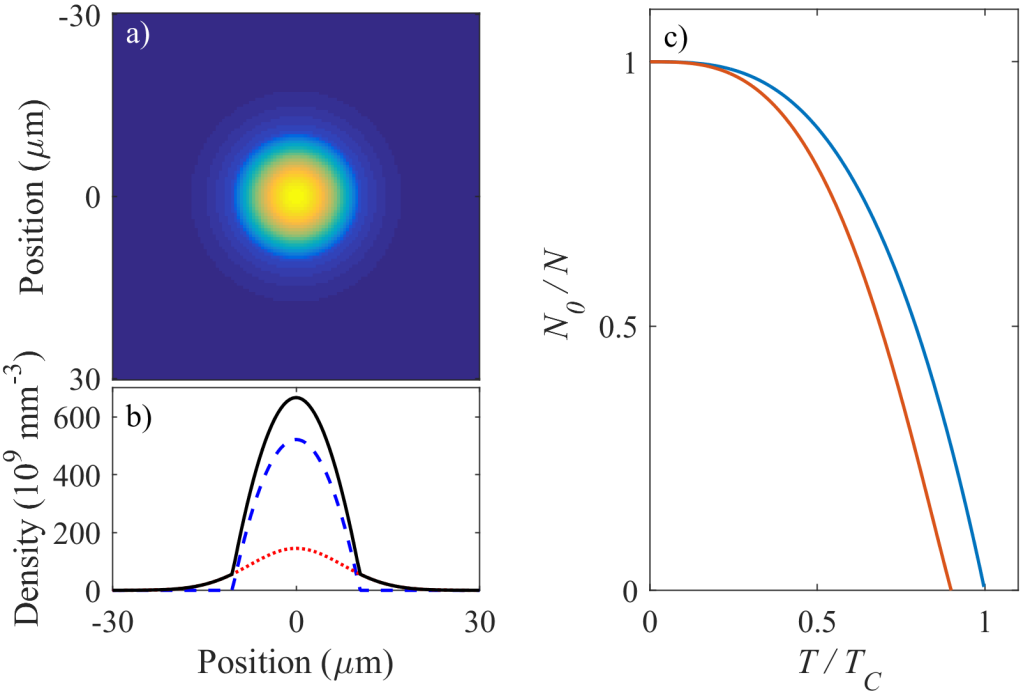

Figure 4.1: a) and b) show the theoretical particle density (radially) for a condensate with 10^7 atoms at 200 nK in a cigar shaped trap with frequencies $\omega_r/2\pi = 92.3$ Hz and $\omega_z/2\pi = 9.11$ Hz, as is used in the experiment discussed later in the chapter [20]. In b) the black solid line is the total atom density ($n = n_n + n_0$), the dotted red line is the thermal fraction (Eq. 4.13), and the blue dashed line is the condensate density (Eq. 4.6). c) shows the approximate relationship between the condensate fraction and temperature, with the blue curve showing Eq. 4.12 and the red curve showing a first order correction detailed in Ref. [240].

4.1.3 Ring Geometries

A wide variety of ring geometry BECs have been demonstrated for a wide range of experiments, with many groups theoretically modelling dynamics as discussed in Sec. 1.4 with further modelling in Refs. [241–243].

In Ref. [84], the density distribution and chemical potential for an equilibrium BEC in a ring trap is derived. This is done by first considering the trapping potential to be of the form:

$$U(r,z) = U_0 + \frac{1}{2}m\omega_r^2(r-r_0)^2 + \frac{1}{2}m\omega_z^2 z^2 \,, \tag{4.14}$$

where U_0 is a background potential, r_0 is the radius of the ring, and ω_r and ω_z are the radial and axial trapping frequencies respectively. By substituting this potential in

Eq. 4.6 and normalising this density, the following chemical potential is derived:

$$\mu = \hbar\bar{\omega}\sqrt{\frac{2Na_s}{\pi r_0}}\,, \tag{4.15}$$

where $\bar{\omega} = \sqrt{\omega_r\omega_z}$ is the geometric mean of the trap frequencies. This is only meaningful for a 3D system so $\mu > \hbar\omega_z$ (i.e. the chemical potential is bigger than the energy scales associated with axial harmonic potential) or equivalently $N > (\pi r_0/2a)\,(\omega_z/\omega_r)$.

The critical temperature of a ring (or any power-law potential) can be calculated following derivations detailed in Ref. [24], whereby,

$$\frac{N}{2\pi r_0}\lambda_{\mathrm{dB}} = g_{5/2}(1)\frac{k_BT_C}{\hbar\omega_\rho}\frac{k_BT_C}{\hbar\omega_z} = g_{5/2}(1)\left(\frac{k_BT_C}{\hbar\bar{\omega}}\right)^2\,, \tag{4.16}$$

where $g_{5/2}$ is a polylog function and $g_{5/2}(1) \simeq 1.3415$. This can then be expressed equivalently with the following relations [84, 102]

$$k_BT_C = \left(\frac{N}{2\pi r_0}\frac{\hbar^2\omega_\rho\omega_z}{g_{5/2}(1)}\frac{h}{\sqrt{2\pi m}}\right)^{2/5}\,, \tag{4.17}$$

$$\frac{N_0}{N} = 1 - \left(\frac{T}{T_C}\right)^{\frac{2}{5}}\,. \tag{4.18}$$

4.1.4 Coherence

In Eq. 4.4, the wave function or order parameter is a complex function with an amplitude Ψ_0 and phase θ [244]:

$$\psi_0(\vec{r}) = |\psi_0(\vec{r})|e^{i\theta(\vec{r})} = \sqrt{n_0(\vec{r})}e^{i\theta(\vec{r})}\,. \tag{4.19}$$

As, in normal circumstances, the phase of the condensate is global, it does not contribute to the density profile and in a normal BEC, the 'choice' of phase can be considered as spontaneous symmetry breaking – it doesn't matter what the phase is, but it needs to exist. In a hydrodynamic model of a BEC (that is considering it as a superfluid with flow – a description common when describing superfluid helium and superconductors) the phase fixes the velocity (field) of the fluid. BECs can be described by hydrodynamic equations of superfluids when the effects of the thermal background is small. We also note that this description is valid if physical quantities vary slowly over

distances longer than the healing length [244].

The healing length (ξ) is defined as the minimum distance over which the order parameter can heal [244]. It is derived by balancing the quantum pressure and interaction energy of a condensate when the density of a condensate grows from nothing to a density n [239, 244, 245]:

$$\xi = \frac{1}{\sqrt{8\pi n a_s}} \,. \tag{4.20}$$

The healing length is typically of the order of a fraction of a micrometer [246]. Typically in a BEC, the scattering length is smaller than the healing length which is in turn smaller than the size of the condensate ($a_s < \xi < L$).

4.1.5 Simple Excitations

Typically the first excitations we learn about in condensates are quantised vortices, which occur as a consequence of a net circulation in an irrotational field (which is a condition of superfluid flow) [238]. For vortices, the flow must by quantised, meaning that the phase of the order parameter must only change by an integer multiple of 2π, this integer is called the winding number. As vortices involve a change in order parameter phase, the size of their cores is determined by the healing length [244, 245]. Vortices have been observed using many experimental techniques, a review of which can be found in Ref. [246]. The concept of quantised superflow has also been demonstrated in ring geometries, where, in general, stirring is used to introduce a flow [63–65, 67–72, 247, 248].

Although the appearance of vortices is conceptually easy to understand, they aren't the most elementary excitations of a BEC. These are periodic solutions to the time-dependent GPE and can be described as travelling wave density fluctuations in a hydrodynamic formulation [239]. The energy spectrum of the travelling wave solutions consists of: phonons at low momentum (i.e. length scales (inverse of the wave number) longer than the healing length ξ) which means collective motion with sound-like properties; and high momentum free particles. At small phonon wavevector $\vec{q}$ the phonon energy ϵ_q is [239]

$$\epsilon_q \approx s\hbar q \,; \quad s = \sqrt{ng/m} \,, \tag{4.21}$$

where s is the velocity. Phonon based excitations are associated with phase fluctua-

tions [239].

Low-Dimensionality and Phase Fluctuations

The effective dimensionality of a BEC can be altered by modifying the shape of its trapping potential. If the trapping frequency in a particular direction is high enough that the excited level spacing is much greater than the thermal fluctuations (on the order $k_B T$), then excitations in this direction are in effect 'frozen' out. This can be formalised by considering the relative sizes of trapping frequencies and the chemical potential to define the dimensionality of the system [84]:

$$\begin{aligned} 3D: &\quad \hbar\omega_{z,r} < \mu \\ 2D: &\quad \hbar\omega_z < \mu < \hbar\omega_r \quad , \\ 1D: &\quad \mu < \hbar\omega_{z,r} \end{aligned} \tag{4.22}$$

One can in effect move between the 3D and a quasi-1D regime by modifying the trapping frequencies of an elongated, cigar-shaped BEC where the BEC is tightly confined in the radial direction (ω_r), but more loosely confined in a transverse direction (ω_z), with aspect ratio $\Lambda = \omega_r/\omega_z$. This also holds for a toroidal potential, though the relative ordering of ω_z and ω_r can be different.

The condensate has a range of length scales: the physical size (determined by trapping frequencies ω_i), the healing length (ξ, as detailed in Eq. 4.20), the thermal de Broglie wavelength (λ_{dB}, given by Eq. 1.2) and the coherence length (l_ϕ). The coherence length characterises the exponential decay of the single-particle correlation function $g_1(\vec{r}) = \left\langle \psi^\dagger(0)\psi(\vec{r}) \right\rangle$ [249]. When the coherence length is of similar size or shorter than the condensate itself then the condensate is said to be in a phase fluctuating regime [249].

Experimental Observations

Phase fluctuations have been observed in a variety of scenarios previously, in several geometries such as cigar-shaped and ring-shaped traps [102, 103, 250–252], all of which operate in a quasi-condensation regime.

In a system very similar to the experiment discussed in the next section of this chapter (Sec. 4.2), pronounced stripes were observed across a BEC, which appeared stronger at lower atom numbers and higher temperatures [250]. Following previ-

ous theoretical work [253–255], they were able to confirm that the density variations (σ_{BEC}) associated with random (thermal) phase fluctuations are strongly dependent on temperature, according to:

$$\left(\frac{\sigma_{\mathrm{BEC}}}{n_0}\right)^2 = \frac{T}{\Lambda T_\phi}\sqrt{\frac{\ln\tau}{\pi}}\left(\sqrt{1+\sqrt{1+\left(\frac{\hbar\omega_r\tau}{\mu\ln\tau}\right)^2}}-\sqrt{2}\right), \tag{4.23}$$

where τ is related to the droptime/evolution time t by $\tau = \omega_r t$, and T_ϕ is a characteristic temperature: $k_B T_\phi = 15\left(\hbar\omega_z\right)^2 N_0/32\mu$. This suggests that phase fluctuations could be used to determine the temperature of condensate at temperatures where the background thermal fraction is negligible [256, 257].

The momentum distribution of phase fluctuations is expected to be Lorentzian, a characteristic which was confirmed in Ref. [252], with the width of this momentum distribution determined by the temperature of the cloud.

Phase fluctuations are important for the non-equilibrium dynamics of elongated BECs, particularly for understanding how equilibrium states are formed [251]. The elongation of a cigar shaped atom ensemble means that the formation of a BEC occurs locally, meaning that oversized, oscillating BECs can form.

In contrast to the thermal fluctuation based (random) phase fluctuations presented above, it is possible to drive a BEC system to induce similar density fluctuations, such as Faraday waves [258]. In this paper, they modulate transverse confinement potential of a cigar shaped BEC (with the transverse direction referring to the tightly confined ω_r axis) and observe the resulting longitudinal Faraday waves. The periods of the excited waves decrease with increasing driving frequency. This dependence on driving frequency could yield a method to differentiate between driven and spontaneous (thermal) phase fluctuations, i.e. if one is able to change the period of the observed fluctuations by changing an experimental parameter, then this is likely to be the source of the fluctuations.

4.2 Measurements

A variety of interesting effects have been measured in the Strathclyde JA3.05B BEC experiment detailed in [18–20, 29, 31]. In the following section we will briefly present

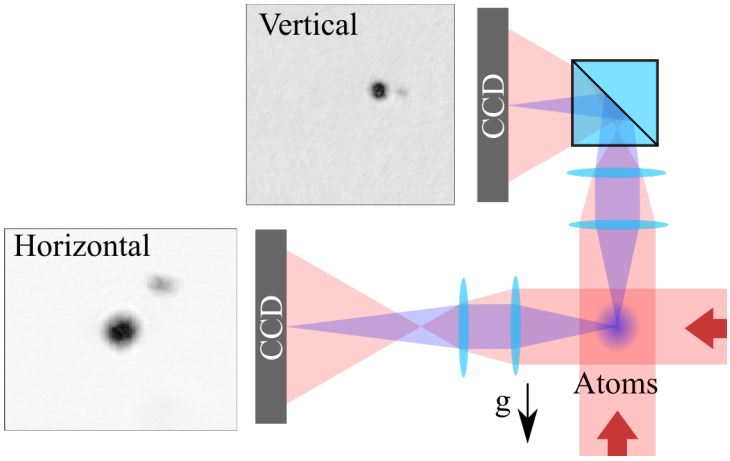

Figure 4.2: A schematic of absorption imaging. The incident light is shown in red, and the shadow of the atoms in blue.

some of the results which have been contributed to during the course of this thesis.

4.2.1 Imaging

In the BEC experiment described in [18–20, 29, 31], we can now image the BEC from 2 directions, giving 3D information about the cloud. The experimental set-up is shown in Fig. 4.2, with the vertical imaging system that I made whilst working on the experiment.

In Fig. 4.2, we show probe light incident on a BEC from two directions, it is then magnified by approximately 2×, before being imaged on a CCD – in the horizontal direction this is a Andor luca^{EM} DL658M with pixel size 10 µm, in the vertical direction a FLIR USB2.0 Chameleon camera is used (CMLN-13S2M-CS) which has a pixel size of 3.75 µm.

Images of the BEC taken from both directions are shown alongside the schematic, with these photos being taken separately as imaging on multiple axes simultaneously complicates the optical depth equations and requires modifications to optical pumping arrangements (due to quantisation axes). In the images we can see a 'lobe' containing atoms in a different m_F level which is split from the rest of the BEC by the magnetic field which acts as a quantisation axis for the optical pumping light which spatially overlaps with the probe light.

The vertical imaging system gave us the ability to monitor the motion of the BEC

parallel to the main imaging light. If a BEC is released away from the centre of a harmonic trap, then oscillations or 'sloshing' is observed. By monitoring BEC position over a range of drop times, this motion can be characterised and minimised. The minimisation of sloshing in the direction of the main probe beam was essential to the results shown in Ref. [31] which demonstrate the observation of the Talbot effect in light passing through a matter-wave grating created by two interfering BECs. This is because the Talbot effect means that the contrast of our interference fringes are strongly dependant on the distance between the camera and the atoms.

4.2.2 Time of Flight Expansion – Atom Number and Temperature

It is a common result to use Eq. 4.13 to describe the thermal fraction of a BEC (or a thermal cloud of atoms). But in time of flight expansion (used to calculate temperature) it is necessary to convolve this initial Gaussian (width σ_0) with the expanding one (the velocity distribution) such that the resulting width is given by $\sigma^2(t) = \sigma_0^2 + \sigma_0^2 t^2$. From this we can derive an expression for the temperature in terms of the width after a certain time of flight. In a cylindrically symmetric, cigar-shaped, harmonic trap with axial and radial frequencies ν_z and ν_r, the temperature (in direction $i = r, z$) is given by

$$T_i = \frac{m}{k_B} \frac{\sigma_i^2(t)}{t^2 + \frac{1}{(2\pi\nu_i)^2}} \,, \tag{4.24}$$

where $\sigma_i(t)$ is the thermal cloud width in the i^{th} direction at drop time t , and m is the mass of the cold atom used [155].

From a single image of a BEC, by fitting the thermal and condensate fraction, we can derive information about the BEC purity (i.e. the ratio between thermal and condensate fractions) the temperature and the critical temperature.

4.3 Observations of Phase Fluctuations

In our BEC experiment [20], by changing the shape of our trap between the condensate and quasi-condensate regime, we were able to observe the appearance of phase fluctuation in the cloud. A selection of images of the BEC exhibiting phase fluctuations are shown in Fig. 4.3.

Contrary to previous observations of phase fluctuations [250–252], rather than see-

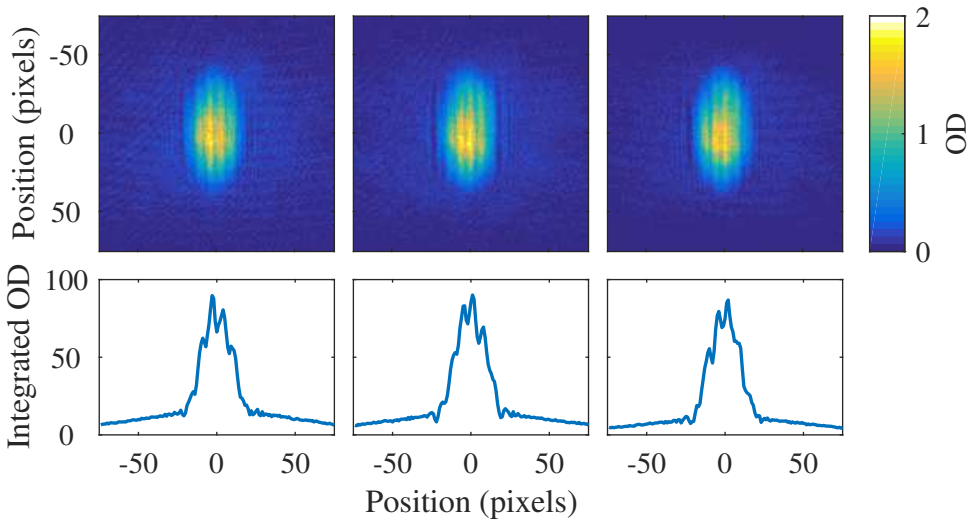

Figure 4.3: Three absorption images of BECs displaying phase fluctuations. The integrated profiles are shown below the images. All of these images are taken with the same droptime (58 ms) and the same aspect ratio (40).

ing the BEC phase fragment randomly, thus creating non-periodic density fluctuations in time-of-flight images, we see strongly periodic density fluctuations in our time-of-flight images. Regular phase fluctuations have only been observed prior to this in systems with deliberate modulation of the trap [258]. However we were not able to modify the periodicity of our phase fluctuations, suggesting we are not observing this particular phenomenon. The phase fluctuations in our experiment have been previously discussed in Ref. [20], with subsequent work being beyond the scope of this thesis.

Chapter 5

The Theory and Simulation of Fresnel Zone Plates

As discussed in the introduction (Sec. 1.4.2) there are many methods which can be used to produce tailored optical potentials, ranging from acousto-optic beam deflection techniques ('painted potentials') [106, 107] and composite potentials [65, 66, 68, 69, 98–101, 259] to holographic phase manipulation using a phase adjustable spatial light modulator (SLM) [99, 111, 112, 260] or micro-mirror devices (DMD) [261, 262].

All of these methods have yielded interesting results allowing for to study of phenomena such as persistent currents [63–71], non-equilibrium dynamics [72], and low dimensional atom systems [73]. The holographic method has proved to be very adaptable, paving the way for the production of novel optical lattices for quantum simulation [263], dark spontaneous-force optical traps [201] and exotic Laguerre-Gauss modes [120, 264, 265].

When discussing how to create traps, it is important that we consider the system requirements. Trapping ultra-cold atoms requires a very smooth trap, as the presence of very small perturbations in a potential can result in heating of a cold atom cloud or fragmentation of a trapped Bose-Einstein condensate [266]. Within previous demonstrations of all-optical ring trapped BECs, the azimuthal variation of the ring minimum was far below the chemical potential of the BEC. To successfully produce trapping potentials for BEC, we must aim to match or surpass the above limit on azimuthal variation, thus aiming to produce traps of μK depth with a roughness of below 1 %.

Much of the work contained within this chapter is an extension of previously published work [123]. In this chapter the work begins by introducing holography and zone plates with physical comparisons to other techniques. In Sec. 5.2 the creation and simulation methods are detailed, with this theory being used for numerical comparisons of Zone Plates and SLMs. We then apply the simulations to the problem of atom trapping in Sec. 5.3.1 and design prototype plates for manufacture in Sec. 5.4. The chapter finishes by considering the potential for creating exotic toroidal potentials in a FZP-SLM hybrid system. Secs. 5.4 and 5.5 contain work completed subsequent to the numerical comparison paper [123].

5.1 What is a Fresnel Zone Plate?

Fresnel Zone Plates (FZPs) and other holography techniques work by spatially modulating either the amplitude or phase of a light beam, resulting in interference of the optical field after propagation; by design of this modulated region one can in principle then produce an arbitrary optical pattern, or trapping potential for atomtronics.

The prototypical FZP is one that acts as a lens, resulting in a focused spot in the selected focal plane ($z = f$). While the operation of such an FZP is standard in the

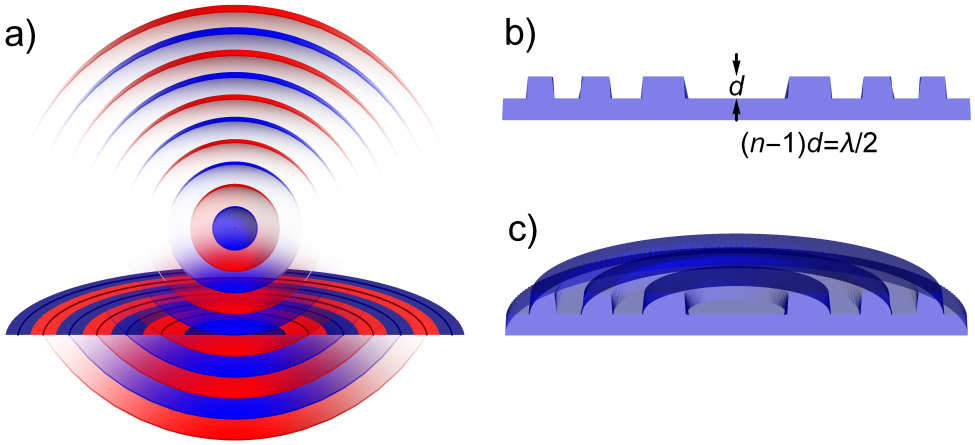

Figure 5.1: a) Spherical light wave phasefronts (separated in phase by steps of π) emanating from a focused light beam form a distinctive Fresnel phase pattern when intersecting a plane. b), c) Binary transmission holograms with equivalent phase characteristics are made from refractive index n material, with half-wavelength steps in optical depth $(n-1)d$. Higher bit-depths of phase resolution enable hologram blazing. Figure taken from Ref. [123].

teaching literature of diffraction [267], we find it intuitive to briefly consider the FZP required to generate a single focus, shown diagrammatically in Fig. 5.1 a). We make use of the time/direction symmetry of linear optics by starting from the desired result and finding the full electric field pattern at a defined plane. Our goal is now to create an optical element, the FZP, that matches an input beam, for example an idealised plane wave, to the field pattern that we produced in the plane. The FZP can then be considered the hologram generated by a plane wave and the backward-propagating field from the focus. For a binary FZP, we obtain a two–level map of the phases of the electric field in the plane of the FZP required to generate the desired focus.

This type of plate (Fig. 5.1) consists of alternating Fresnel zones forming concentric rings that alternate between the chosen binary heights at radii,

$$r_j = \sqrt{j\lambda f + \frac{j^2\lambda^2}{4}}\,, \tag{5.1}$$

where j can take any integer value, and λ is the wavelength of the incident light. Successive rings can be blocked, allowing only those that constructively interfere at the target plane to propagate. Alternatively, a phase shift of π can be added to otherwise 'destructive' zones, increasing the useful power at the focal plane. Figs. 5.1 b), c) demonstrate an envisaged transmissive binary FZP etched into a substrate, with consecutive zones that would be completely out of phase experiencing an increased optical path length.

A similar approach can be used to make straight waveguides with a linear (rather than circular) symmetric FZP pattern, or to create arbitrary FZP-like patterns by recording the phase of a near-field diffraction pattern. In the next section we discuss in detail the theory and numerical methods to implement this.

Physical Comparison of Zone Plates to other Holography Techniques

DMDs and SLMs are commonly used updatable holography techniques. DMDs are 2D arrays of micro-mirrors which can be programmed to apply binary (on/off) intensity modulation to an incident electric field. Rather than mechanically modulating light, SLMs are arrays of liquid crystal pixels which impart an adjustable (via an applied voltage) phase modulation on reflected light.

State of the art SLMs can have pixel sizes as small as 12 µm, effective areas of approximately 2 cm^2, typically operate with 8-bit precision and are updatable. To op-

erate an SLM, a computer with a suitable monitor port is needed, alongside the large controller. Relatively complex optical systems are required for optimised use [268], increasing the complexity of using such a technology. In comparison, DMDs are binary updatable systems with relatively small controllers. A typical off-the-shelf DMD (the Texas Instruments DLP4500NIR) has an array of 912 $\times$ 1140 7.6 µm mirrors. The FZPs discussed in this thesis can be manufactured with pixel size as small as 10 nm and with large total areas of up to 25 cm^2 [172]. Despite these obvious spatial advantages, FZPs are by their very nature static, with only two levels of phase control. These technologies are already being utilised for trapping, in the form of optical tweezers [269, 270].

Despite the successes outlined previously, SLM holography for atom trapping still remains an imperfect and computationally intensive technique, notwithstanding significant improvement in the iterative algorithms used [99, 260, 271]. This is due to a combination of system aberrations, low spatial resolution, dead space between pixels, and the difficulty of creating an algorithm that converges on a solution suitable for atom trapping (i.e. smooth and without background light which could cause low loading rates or tunnelling out of the trap [99]) without lowering light usage efficiency. Some of the spatial resolution disadvantages of SLMs compared to FZPs can be mitigated through appropriate demagnification. However additional optics introduce additional aberrations and immediately increase experimental complexity.

We anticipate that microfabricated FZPs will overcome many of the limitations posed by the use of SLMs in atom trapping experiments. The higher spatial resolution and sharper edges between pixels offer the ability to reach higher spatial frequency and thus produce a wider range of more accurate holograms. Additionally, due to their size and transmissive operation, we expect that FZPs could be placed inside a vacuum chamber (as with the grating MOTs shown in [162, 172]), thus immediately addressing the major system aberration of propagation through a vacuum chamber window. SLMs also have considerable size, weight and power (SWaP) overheads associated with their operation. Therefore, if we can sacrifice updatability, FZPs offer a passive, low SWaP alternative to other holography techniques.

5.1.1 Light Forces

In order to use a FZP-only system, we need to be able to produce potentials which will support against gravity without any additional applied potential. This requirement results in the condition that gravitational force ($F_{\text{grav}} = mg$) is less than the force resulting from the optical potential. As shown by Eq. 2.27, the dipole force is the negative gradient of the potential, thus we can apply this condition by calculating the maximum component of the light force in the direction of gravity at the same radial position as the focus (here we assume that propagation is aligned with gravity, and we call this direction z). For a Gaussian focus, we can calculate this condition to be:

$$mg < \frac{32}{9\sqrt{3}} \frac{U_0}{z_R} \,. \tag{5.2}$$

It also important for us to consider the requirements for the roughness of a trap. Various papers approach this in different manners for example, in Ref. [105] they state that "it is necessary to flatten the time-averaged potential to better than 10% of its depth". In in order to generalise this, we should consider the energy scales involved with a BEC propagating around a ring. We have a chemical potential, a kinetic energy, and the potential energy of the trap. Thus we should to aim to have variation in the potential energy less than the chemical potential and kinetic energy combined.

5.2 Designing Fresnel Zone Plates

Within our initial, comparative, work [123], we calculated and simulated phase plate patterns (known as kinoforms) for single foci, rings, and beamsplitters, as shown in Fig. 5.2. These target intensity distribution were chosen due to their applicability to cold-atom trapping and atomtronics. The single focus allows both the calculation and propagation methods to be evaluated and compared to the simplest FZP model, whereas the ring allows for comparison of this method to existing toroidal traps which are the simplest closed-loop circuits. In order to extend the simulations to consider complex elements for atom optics we finally considered a beam splitter, as such an element is essential as a building block to create a circuit type interferometer. Later in our investigations, prior to manufacture, we adopted a slightly different beam splitter model, emulating the y-shaped junctions demonstrated in Ref. [105] due to anticipated heating effects and the symmetry linked limitations of the zone plates.

5.2.1 Simulations

The phase patterns required for production of the optical traps shown in Fig. 5.2 are calculated using a Fourier–optics method of modelling the propagation of an initial electric field $\mathcal{E}^{(0)} = E(x', y', z = 0)$ to a distance z. This uses the angular spectrum of the field, ($\mathcal{A}^{(0)}$), and the Helmholtz propagator, $\mathcal{H}$, such that,

$$\mathcal{E}^{(z)} = \mathcal{F}^{-1}\left[\mathcal{H}(z)\mathcal{A}^{(0)}\right] = \mathcal{F}^{-1}\left[e^{ik_z z}\mathcal{F}\left[\mathcal{E}^{(0)}\right]\right] \ , \tag{5.3}$$

where $\mathcal{F}$ denotes the 2D Fourier transform [267] over x and y, the z-component of the wave vector is $k_z = \sqrt{k^2 - k_x^2 - k_y^2}$ for an electric field with wave vector $|k| = 2\pi/\lambda$ [272, 273]. We use this method, following the details in Ref. [272], and references therein, to complete the design algorithm shown in Fig. 5.3.

Firstly, a target intensity is calculated and then propagated backwards, using Eq. 5.3, by the focal length. The phase of the resulting electric field in this plane is rounded to the desired bit depth, as discussed later in the text. This routine acts to calculate the required kinoform, and the performance of the result is tested numerically by simulating a desired input beam (either a plane wave or a Gaussian beam with defined width) that is then propagated forward by the focal length. This is achieved using a MATLAB scripts written by me based on previous code written by Paul Griffin [272]. The code uses the fast Fourier transform algorithm to perform the propagation. It also uses

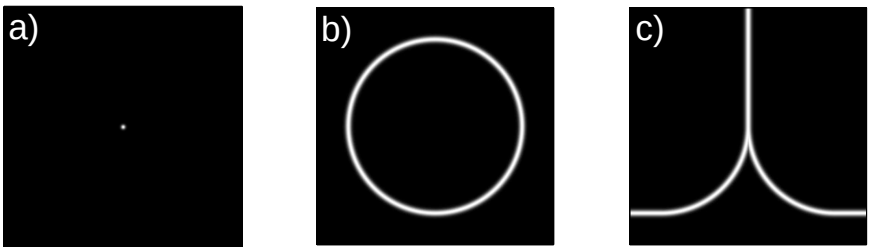

Figure 5.2: The target intensity distributions used to simulate a range of potentials useful for atomtronics and interferometry; a), b), and c) show a focused spot, a ring and a beam-splitter, respectively. These simulation distributions are formed of Gaussians with $1/e^2$ widths of 2 µm (or 5 µm for the focus) and ring radii of 200 µm. However, for visibility, the distributions shown above have a larger width and are cropped to show only the 600 µm × 600 µm area around the non-zero intensity. We note that these parameters are not necessarily used in the manufactured zone plates presented in Chap. 6. Figure taken from Ref. [123].

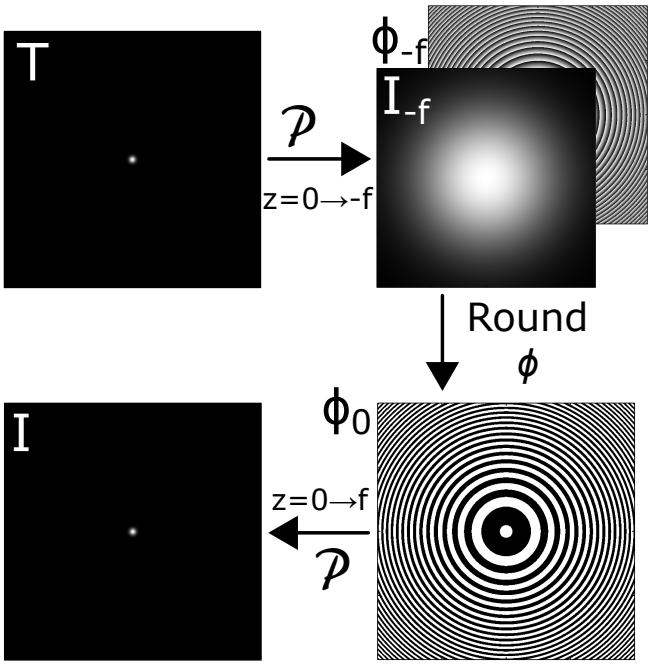

Figure 5.3: Schematic of the kinoform, or phase plate pattern, design process used. The target (T) electric field distribution is propagated (denoted by $\mathcal{P}$) backwards a distance f using Fourier techniques and maximum spatial resolution (4096 $\times$ 4096). The electric field is spatially averaged over a variable size grid of pixels, then separated into phase ($\phi_{-\mathrm{f}}$) and amplitude ($I_{-\mathrm{f}}$) components, with the phase rounded to 1-8 bit resolution. The kinoform is then illuminated to create an image. Figure taken from Ref. [123].

a nearest-neighbour interpolation algorithm to resize matrices in order to have lower pixel size optical element in a higher resolution simulation area. Simulation accuracy is limited in part by the accuracy of double-precision floats in the specific MATLAB distribution used (of the order 1×10^{-16}) and the propagation of this numerical noise.

Our method of simulation means that the pixel sizes of the kinoform and simulation (the electric field) are independent. Although we set the input beam and target plane to have flat phase fronts, we allow for phase freedom in the resultant distribution. As we are not utilising a feedback algorithm, our method intrinsically avoids the presence of optical vortices, which can be confirmed through observations of simulation results. We consider the case in which the kinoform acts as a transmissive element and the incident light only illuminates the patterned area. We extend the simulation in later work to consider a scenario closer to that achieved experimentally (see Chap. 7). It should also be noted that no optimisation is used to improve the kinoform. This full

Helmholtz propagation method is computationally efficient and accurate, reducing the possibility of fringing artefacts in comparison to the paraxial approximation utilised in many hologram calculations as also highlighted in Ref. [99].

To evaluate the success of each kinoform, we calculate the root mean squared (RMS) error for the normalised two dimensional final and target intensities,

$$\epsilon = \sqrt{\frac{1}{N}\sum\left(\tilde{I} - \tilde{T}\right)^2}, \tag{5.4}$$

where N is the number of pixels (in the simulation), $\tilde{I}$ is the final intensity, and $\tilde{T}$ is the target intensity distribution, both intensity distributions are normalised by the mean of the pixels in T that are brighter than 50% of the maximum value [112].

The target distributions we have chosen to simulate are shown in Fig. 5.2: a) a focus with $1/e^{-2}$ intensity radius of $w_0 = 5\,\mu\text{m}$; b) a ring of radius $r = 200\,\mu\text{m}$ and radial Gaussian waist $w_r = 2\,\mu\text{m}$; c) a beam splitter formed from straight segments and radii as given in b), again with waist $w_b = 2\,\mu\text{m}$.

In the simulations, we anticipated that laser powers of 2 mW for the focus and 30 mW for the ring/beam-splitter at a wavelength of 1070 nm would be used in order to give trap depths of a few μK, which would be comparable with potentials discussed in the literature. Moreover, this would yield trap frequencies of the order kHz in the direction of tightest confinement, which is higher than most existing ring shaped dipole potentials [54,65,66,70,104,247,248] and permits access to lower dimensional regimes. The ring radius is larger than these previous demonstrations to increase its applicability to interferometry where sensitivity scales with the area enclosed. We note that larger rings have been successfully used for interferometry, with the rings being rf-dressed time averaged adiabatic potentials rather than light-based dipole potentials [86].

Throughout the simulation process, the electric field propagation is calculated to a resolution of a wavelength with a simulation area of $4.38 \times 4.38\,\text{mm}^2$ ($2^{12}\,\lambda \times 2^{12}\,\lambda$), limited solely by the reverse propagation technique and computation memory requirements. For foci kinoforms illumination by Gaussian beams, the choice of input beam $1/e^2$ radius, $w(z)$, is determined by the desired focal length and the Gaussian width, w_0 of the desired features by $w(z) = w_0\sqrt{1 + (z/z_\text{R})^2}$, with Rayleigh length $z_\text{R} =$

$\pi\, w_0^2/\lambda$. However, for rings and beam splitters, an optimum $1/e^2$ radius is found to be 1 mm, determined through careful iterative simulations. We do note that these computation limitations mean that the active area is smaller than, if comparable to, typical SLM active areas of $\gtrsim 1\,\mathrm{cm}^2$.

Examples of the calculated kinoforms for FZPs illuminated by a Gaussian and producing a ring and beam splitter are shown in Fig. 5.4.

We are also able to simulate the electric fields which would result from more complex incident beams, thus simulating an effective hybrid FZP-SLM system in which potentials could be dynamic. This is discussed in further detail in Sec. 5.5.

5.3 Comparisons Between Zone Plates and Spatial Light Modulators

For the simulations shown in the paper, we executed the calculations for a wide range of kinoform pixel sizes and phase resolution (which is referred to here as bit depth).

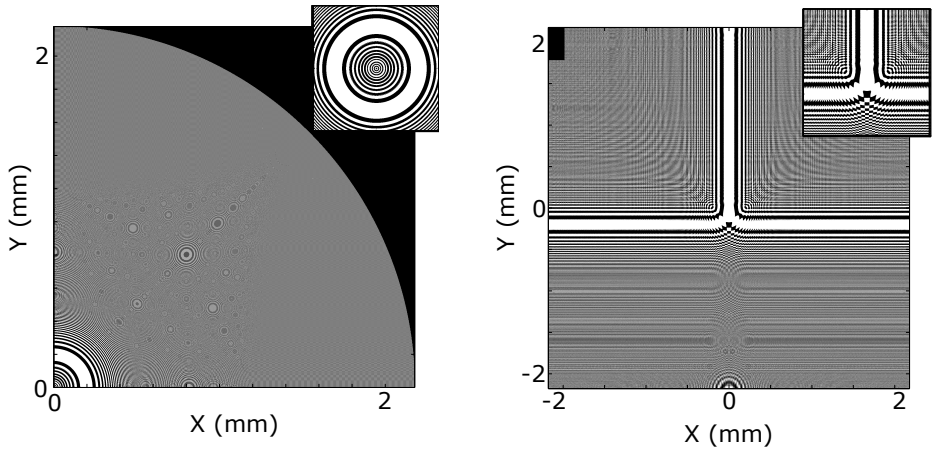

Figure 5.4: Fresnel Zone Plates calculated for producing a ring and a beam splitter using Gaussian beam illumination (as highlighted by the 5-point star in Fig. 5.6). The inset shows the central section of the kinoform, magnified to allow the zone plates features to be easily seen. Note that the outer regions of the zone plates appear grey due to pixel dithering where the Fresnel zones would be smaller than a pixel. The pure black area at the edges denotes the masked area, where the plate is non-transmissive or light is blocked (in the simulations). The off-centre appearance of rings in the ring kinoform are artefacts of the finite simulation pixel size. Figure taken from Ref. [123].

This allowed comparisons to be drawn between binary FZP-type kinoforms with a simulated pixel size of 1 µm and 8-bit SLM type kinoforms with simulated pixel sizes of 12 µm or more (with 12 µm corresponding to the state of the art for SLMs at the time of publication [274]). This effectively amounts to a comparison of whether better phase resolution (i.e. the higher bit depth of an SLM) or better spatial resolution (i.e. the smaller pixel sizes provided by a FZP) is more important for hologram generation. We assume that phase resolution ($\delta\phi$) is related to the bit depth (n) of a kinoform via $\delta\phi = 2\pi/2^n$. In a real SLM, the phase range may cover more than 2π resulting in some redundancy and reduction of phase resolution due to overlap of the high and low value pixels.

Maps of RMS error, calculated in the simulations using Eq. 5.4, are shown in Figs. 5.5 and 5.6. For all three target patterns and illumination beams (except the plane focus), there is a clear increase in RMS error with increasing pixel size and decreasing bit depth, as expected. The simulations also show that a two level FZP consistently has an RMS error lower than that of a kinoform comparable to an SLM. In addition, we can note that, at low pixel size, increasing the bit depth from 2 to 4 level phase resolution significantly reduces the RMS error, thus improvements in microfabrication techniques would significantly increase the accuracy of FZP-type kinoforms by allowing for non-binary phase. We also note that the ability to blaze the FZP kinoform would permit much higher hologram efficiency [275, 276].

When considering the RMS error maps, we expected RMS error to increase as more information about the ideal field in the kinoform plane ($E_{-\mathrm{f}}$, see Fig. 5.3) is lost. Our comparison between the two methods (FZP and SLM) is effectively a comparison of the magnitude and significance of phase information loss for differing spatial and depth resolution; couching the problem in these terms will help us to understand our findings.

The RMS error map, shown in Fig. 5.5, for a focus kinoform illuminated by a plane wave clearly shows an unexpected increase in RMS error at high phase (high bit depth) and spatial resolution (small pixel size), contrary to the expected result. In this area of higher RMS error, we observe that the optical power is concentrated in a tighter focus than the target 5 µm $1/e^2$ radius. This is shown in Fig. 5.7. We can understand this as each pixel of the kinoform is illuminated equally, unlike Gaussian optics where a concomitant Gaussian illumination of the optical element is required.

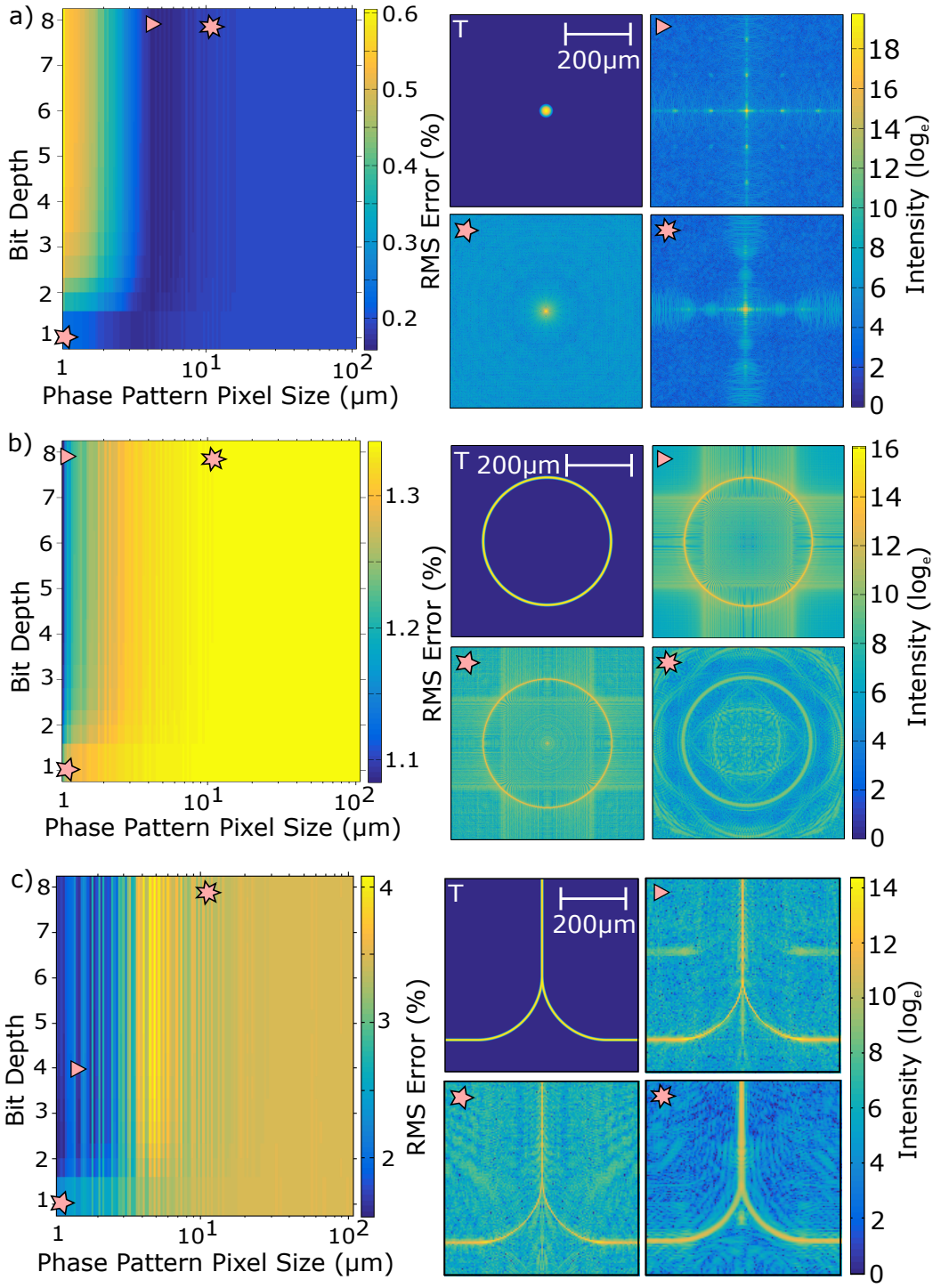

Figure 5.5: Plot of RMS error for kinoforms of varying spatial and phase resolution, illuminated by plane waves. The target intensity distributions, labelled T and with a scale bar, are to the right of the corresponding RMS error plot. The obtained intensity distributions for the lowest RMS error, typical FZP, and typical SLM are labelled by the triangle, 5-point star and 7-point star respectively. Figure taken from Ref. [123].

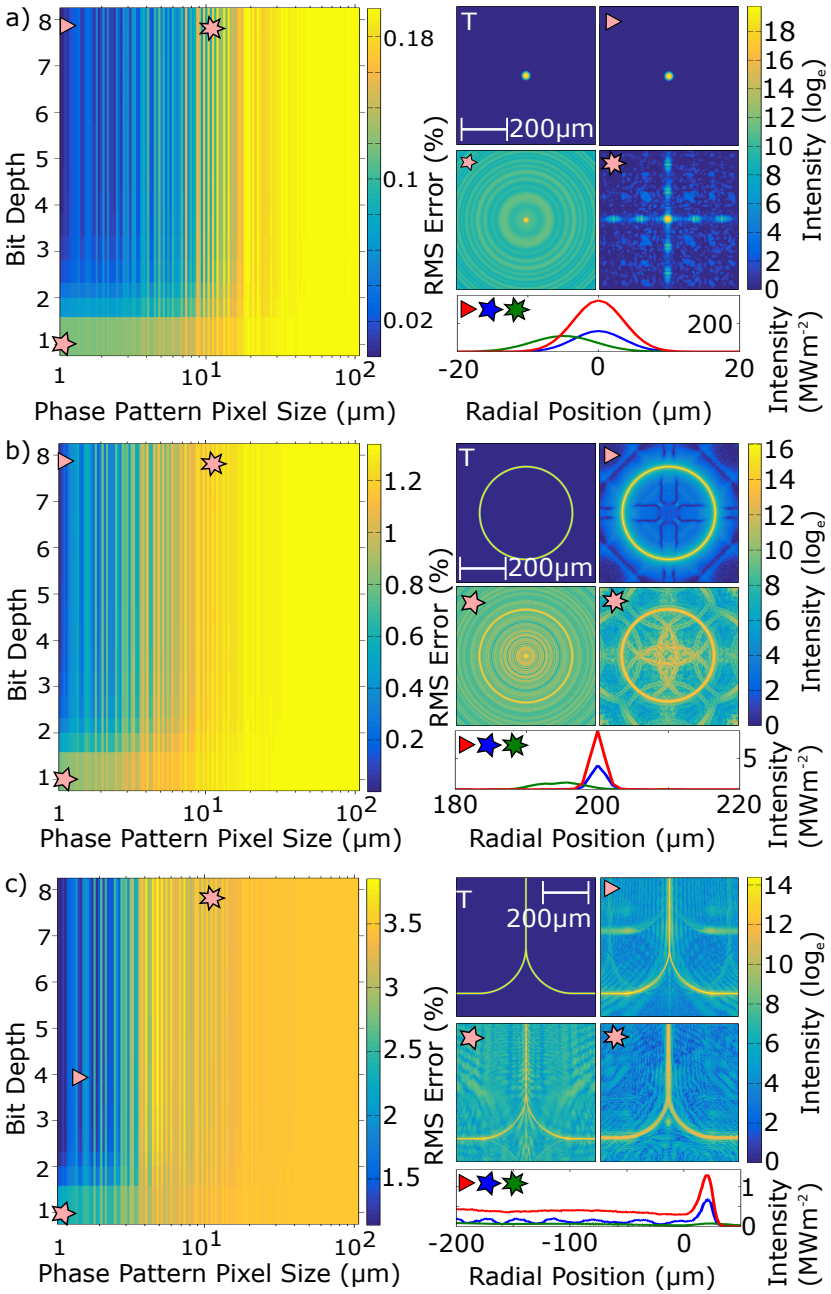

Figure 5.6: Plot of RMS error for kinoforms of varying spatial and phase resolution, illuminated by collimated Gaussian beams of optimised widths. The obtained intensity distributions for the lowest RMS error, typical FZP, and typical SLM are labelled by the triangle, 5-point star and 7-point star respectively, shown logarithmically. Line graphs of intensity versus radial position are shown below the full intensity plots. For the focus and ring, the area around the (symmetrical) brightest region is shown at an appropriate scale. The equivalent for the beam splitter shows the intensity distribution along the vertical line of symmetry, with the peak offset from the distribution centre indicating the position of split. Figure taken from Ref. [123].

The consequences of this observation can be explored by considering three of the contributors to the RMS error (two of which are introduced above): phase resolution error, (phase) spatial resolution error, and illumination error. In our routine (see Fig. 5.3) all spatial intensity information from back-propagation is lost and replaced by the intensity information of the illumination beam, whereas the phase information loss is only limited by the pixel size and phase resolution. At large pixel size and low phase resolution, these sources of error dominate over the intensity error, but at high resolutions, the lost intensity information becomes dominant. Thus we need to consider the clear mismatch between the illumination beam and its ideal profile. It is a standard result of diffraction in Gaussian optics that a smaller focus diverges more rapidly than a larger focus, meaning that the tighter the focus desired, the larger a kinoform or lens should be used (or, in the case of a large lens, a larger incident beam), such that the numerical aperture can be increased. Conversely, this means that the size of the illuminated area of the kinoform, as well as the phase across it, can affect the size of the focus produced. So, for the plane wave case, the illumination is more similar to that required for a smaller focus than 5 μm. We do not see this in the Gaussian illumination simulations, Fig. 5.6, due to the Gaussian weighting of the intensity at the kinoform, which more closely matches the ideal illumination.

As one can see from the RMS errors shown in Figs. 5.5 and 5.6, accuracy of intensity reproduction is reduced with pattern complexity and for distributions with less obvious symmetries. Reproduction of the beam splitter is much less accurate than for either the focus and the ring. We can understand the impact of symmetry on the suitability of patterns for this technique by considering the basic FZP for a focus shown in Fig. 5.1. In the description shown in the figure, the electric field is considered as a train of spherical wavefronts emanating from a focus which we can easily adapt as a thought experiment for other patterns. In the case of the focus, limited information is lost, as the phasefronts do not overlap, meaning that we can reproduce it very well. If we compare this to a ring, we can imagine the phasefronts emanating from the ring in a way analogous to field lines around a current carrying wire – now we imagine cylindrical phase fronts with the wave guide at the centre (i.e. concentric toroids). These cylindrical phase fronts retain the circular symmetry of the ring, like the Gaussian input beam. This symmetry matching creates a smooth ring.

Conversely, if we imagine this for the beam splitter shown in Fig. 5.2c, we en-

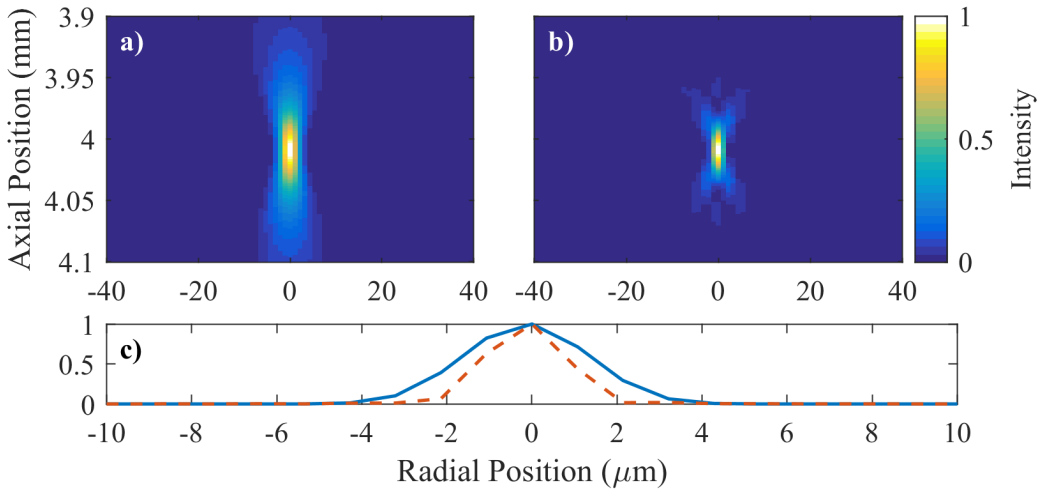

Figure 5.7: Foci produced by a 0.5 mm $1/e^2$ radius Gaussian (a) and a plane wave (b) incident on a binary zone plate designed to produce a 5 µm $1/e^2$ width at a focal length of 4 mm (with a pixel size of λ). Cross-sections at the foci are shown in c), the Gaussian (plane wave) illuminated focus has a $1/e^2$ width of 2.9 µm (1.8 µm) to 1 s.f.. Intensities are normalised.

counter difficulties due to the lack of symmetry. The phasefronts will overlap in such a way that more phase-information is lost for points along the waveguide that lie close to the split point, simply because they overlap sooner than for points far from the split. This means that for non-circularly-symmetric patterns, phase-information loss is not equal for every point along the waveguide, leading to much more aberration. We note that talking about phase information 'loss' is an oversimplification of the system, as interference means that information is still retained even when the imagined phasefronts overlap. However, the beam splitter remains rough due the lack of symmetry matching of the incident beam and because the phase pattern could become too complex to be resolved in our system (i.e. variation in phase could occur on smaller length-scales than the pixel size).

One way to take advantage of the inherent symmetry of some patterns is through using masking to modify the shape of the illuminated area simulated. Both the ring and the focus have been masked to form circularly symmetric kinoforms, meaning that artefacts caused by the square shape of the active area are reduced. However, the reduced symmetry of the beam splitter makes this process more complex. The masking makes pixels outside of a desired area completely dark, thus creating an active 'area' of illuminated pixels and excluding pixels which cause aberrations. In the beam-splitter

case, we were able to use the symmetry properties of a straight waveguide Fresnel zone plate to shape the active area appropriately, thus blocking light incident more than a certain distance from the centre of the intensity lines. This technique improved accuracy, but required further fine-tuning to allow the approach to be applied to an arbitrary intensity pattern. We also note that it would be difficult to implement it in a physical (rather than simulated) scenario.

Due to symmetry considerations, in further work (Chap. 5.4) we adopt a y-shaped junction as a more symmetric alternative to the curved beam splitter simulated here.

We can also discuss the suitability of targets for this holographic method by considering discontinuities in profiles. During the simulation work, we noted that the discontinuous nature of the example beam splitter was an additional source of error in its production, this led to us using a target that reached the edges of the simulation area to avoid such issues. In a useful intensity distribution for atomtronics, one would want to produce a target intensity with no discontinuities (i.e. a closed-loop circuit), such as a ring with a beam splitter at either end for use in interferometry; hence, the discontinuity based artefacts and errors are not critical to the success of these simulations.

In all the error maps, particularly for the Gaussian illumination, we see non-monotonic variations in the errors between consecutive pixel sizes. This is due to aliasing between the three length scales involved in the kinoform design calculations: the length scale of phase change, the simulation pixel size (λ), and the kinoform pixel size. Due to the involvement of three length scales we were not able to reduce this roughness with suitable choice of any of these values. It may be possible to reduce the aliasing with numerical techniques or filtering but this was not explored as important trends in the data are clearly visible without additional analysis. The roughness in RMS error is less pronounced for plane wave illumination as the overall RMS error is higher and so this aliasing is less prominent.

As an extension to the simulations above, we noted that if the appropriate spatial distribution of the incident field, with a flat phase front, can be produced at the kinoform, then the errors would rapidly tend to zero, as for the single focus in the upper plots of Fig. 5.6. Indeed, producing such a large scale pattern is well suited to the coarser resolution of an SLM, suggesting that SLMs and FZPs can be used together

synergistically. This will be further discussed in Sec. 5.5.

5.3.1 Expectations for Atom Trapping with FZPs

In order to demonstrate the applications of the hologram method of optical trap generation (particularly the potential for three dimensional trapping), we have demonstrated propagation through the focus of the ring distribution in Fig. 5.8. This is shown both for the best kinoform and for an FZP, with the average intensity of the ring minimum at each distance shown as a scatter plot alongside the full intensity distributions. Both cases demonstrate a full-width-half-maximum (FWHM) in the propagation direction of 20 µm, similar to that expected for a focussed Gaussian beam (for which the FWHM is equal to $2z_R \approx$ 24 µm). Radial plots of intensity are shown as line graphs in Fig. 5.6, allowing for intensity noise to be seen. We can note that the intensity distribution in the case of the focus and ring are too narrow to show any noise due to the pixel size of the simulation. However, we can see significant noise along the vertical waveguide section of the beam splitter. The beam splitter's noise is largely due to beating between the vertical and horizontal sections of the waveguides and could be reduced with more careful target distribution design.

In the simulations of RMS errors in Figs. 5.5 and 5.6, we adopted a compromise position whereby we compared both target and image distributions across the whole grid size. This means that even the background wings (i.e. non-target zone) of the intensity distribution - which could affect the atomtronic circuit loading efficiency - contribute to the error. However, for a given application one may be mainly interested in a subset

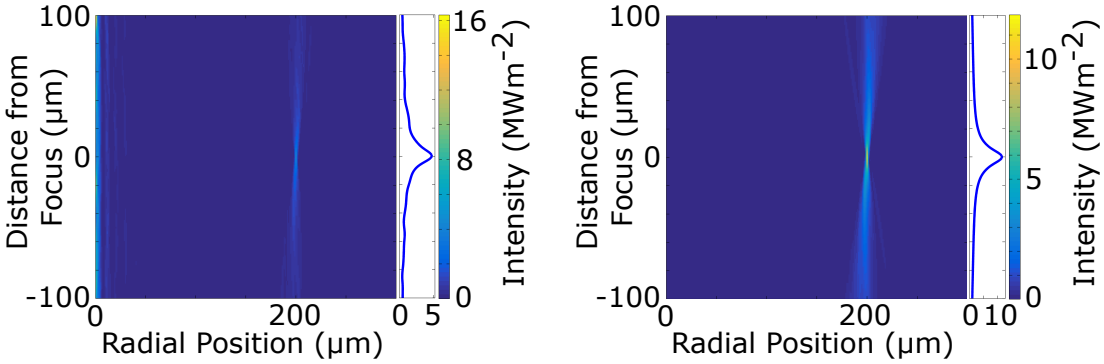

Figure 5.8: Propagation through the focus for a ring hologram generated using an FZP (left) and the best kinoform (right). The intensity at the ring radius (200 µm) is shown in the cross-section plots on the right of each image. Figure taken from Ref. [123].

of the image and target, e.g. the pixel region where the top 50 % of the target intensity distribution. This region is where the coldest atoms would be trapped and in this case it makes sense to modify Eq. 5.4 to only consider pixels in this zone. Moreover, one should then adapt $\tilde{I}$ the final intensity, and $\tilde{T}$ the target intensity distribution, so that the intensity distributions are independently normalised by their maximum value over the pixels in T which are brighter than 50 % of the maximum value. This gives a more realistic estimate of the in-situ trap roughness, which can be seen in Fig. 5.9. The left figure shows the results for a ring shaped potential and the right hand one shows the results for a complex target 'OR' gate which was used in [99, 260] and is included for

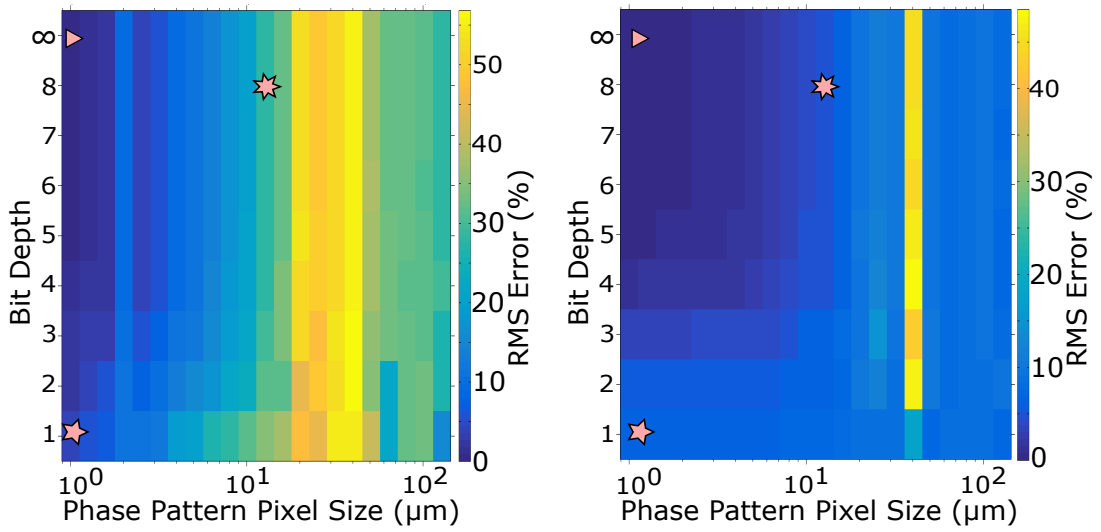

Figure 5.9: For the ring-shaped target, image (a) is a demonstration of how the rms error is modified if one considers only the grid points in which the target is within 50% of the maximum intensity. The target is normalised to its maximum value within this pixel range, and the image is scaled by a constant which minimises the rms error. Note the much higher overall error, as the large background content of the image can give a false impression of pattern smoothness. The lowest rms error, typical FZP, and typical SLM are labelled by a triangle, five-point star and seven-point star, with corresponding errors of 0.0%, 3.7%and 32.7%, respectively. In image (b), for benchmarking, we consider a complex target 'OR' gate which was used in [99, 260]. Note that in this case the lowest rms error, typical FZP, and typical SLM are labelled by a triangle, five-point star and seven-point star, with corresponding errors of 0.0%, 17.4% and 19.0%, respectively. Such values appear high, however it is important to consider the small target size, and that there is no additional hologram optimisation. The phase profile across the target is flat in all cases, with no observable vortices. The holograms are illuminated by its ideal spatial intensity distribution. Figure taken from Ref. [123].

benchmarking purposes. The lowest RMS error, typical FZP, and typical SLM have corresponding errors of 0.0 %, 3.3 % and 13 % respectively for a ring shaped target (rounded to two significant figures, hence the zero value). In this situation, rather than the plane wave/Gaussian illumination considered in Figs. 5.5 and 5.6, the hologram is illuminated by its ideal spatial intensity distribution.

5.4 Design of Kinoforms for Manufacture

After completing the simulations detailed above, we needed to choose a range of 24 different kinoforms to be manufactured as detailed in Sec. 6.1, which will allow us to map as large a range of parameter space as possible, whilst also being useful within our experimental system. In the following section we will discuss the range of parameters investigated, how each parameter should affect the potentials and finish by explaining how the final 24 patterns were chosen.

The first decision required is what shaped patterns should one use. Following on from our simulations shown above and in Ref. [123], it is obvious that we should test some foci and rings as they will allow us to confirm that the zone plates work as expected and will produce potentials that are useful for atom trapping. The beam splitters simulated, however, were not so successful, and so needed further development before the kinoforms were manufactured. As briefly mentioned above, an alternative beam splitter candidate is that of a y-shaped junction, it is demonstrated as a successful painted optical potential in Ref. [105]. We also note from the findings in Ref. [105] that propagation through bent waveguides can cause excitation of a BEC away from the ground state. The solution to this problem is to make careful choices about curve types or the use of discontinuities (such solutions are suggested in Ref. [277]). This makes curved waveguides impractical for production using a permanent kinoform like a zone plate. The y-junction type of beam splitter is a more promising candidate as it can be designed in a manner with a higher degree of rotational symmetry.

In summary, we chose to test potentials of the following shapes: Gaussian of various sizes; rings of various widths and radii; y-junctions with varying angles between output ports and different widths; a linear wave-guide; a ring with input and output ports (referred to as a ‘ring-track’) ; and the beam splitter shown in the above simulations, with a variety of different kinoform shapes.

As discussed in Sec. 3.3, our vacuum cell has interior dimensions 25 × 25 ×97.5 mm and the glass has a thickness of 2.5 mm, thus, one can calculate the effective optical path length to the centre of the cell to be 18.185 mm (assuming the zone plate is positioned approximately 2 mm from the outside edge of the cell). In order to investigate the impact of focal length (and hence numerical aperture) on the potentials, four prospective focal lengths were simulated, 4 mm, 7 mm, 10 mm and 18.185 mm, with the shortest focal length being for use inside the vacuum chamber as opposed to outside for the others. It is a standard result in Gaussian optics, that the minimum spot size ($1/e^2$ width w_0) of a beam focused by a lens of focal length f is given by this diffraction limited formula shown in Eq. 2.4. This equation should apply to the simple focus patterns simulated, but is unlikely to apply in the case of the rings due to subtle interference from all parts of the incident intensity profile. We also used this and typical trap frequencies in other experiments to inform our choices of $1/e^2$ intensity widths for the patterns, considering 5 µm, 10 µm and 15 µm.

In order to decide which of the 24 patterns to have etched, we simulated each shape of potential for a range of focal lengths and $1/e^2$ widths, then calculated the RMS error prediction for each simulated output field. From these RMS error measurements and examination of each of the resulting potentials, we were able to choose 24 patterns which would represent both the best candidates in terms of suitability and interest. A table of the parameters for the chosen patterns is shown in Tab. 5.1

5.5 Simulations of a Hybrid FZP-SLM System for Phase Winding

One of the exciting potential uses for Fresnel Zone Plates is to use them in combination with SLMs to create potentials that combine the benefits and mediate some of the disadvantages of both systems. In this set-up, the SLM acts to tailor an electric field profile incident on the zone plate, giving freedom to either improve the patterns generated or modify them dynamically.

We are able to propose and simulate two possible approaches to this system: the simplest is to predict what happens when known incident fields (like Laguerre-Gauss beams) are applied, and the more complex, but potentially more powerful is to cal-

Focus $f = 18.185$ mm $w_0 = 5$ µm	Focus $f = 10$ mm $w_0 = 5$ µm	Focus $f = 7$ mm $w_0 = 5$ µm	Focus $f = 4$ mm $w_0 = 5$ µm	Ring $r_0 = 100$ µm $f = 18.185$ mm $w_0 = 5$ µm	Ring $r_0 = 100$ µm $f = 18.185$ mm $w_0 = 10$ µm
Ring $r_0 = 100$ µm $f = 10$ mm $w_0 = 5$ µm	Ring $r_0 = 100$ µm $f = 7$ mm $w_0 = 5$ µm	Ring $r_0 = 200$ µm $f = 18.185$ mm $w_0 = 5$ µm	Ring $r_0 = 200$ µm $f = 18.185$ mm $w_0 = 10$ µm	Ring $r_0 = 200$ µm $f = 18.185$ mm $w_0 = 15$ µm	Ring $r_0 = 200$ µm $f = 10$ mm $w_0 = 5$ µm
Ring $r_0 = 200$ µm $f = 10$ mm $w_0 = 10$ µm	Ring $r_0 = 200$ µm $f = 7$ mm $w_0 = 5$ µm	Y-Junction $\theta = 2\pi/3$ $f = 18.185$ mm $w_0 = 5$ µm	Y-Junction $\theta = 2\pi/3$ $f = 18.185$ mm $w_0 = 10$ µm	Y-Junction $\theta = 2\pi/3$ $f = 10$ mm $w_0 = 5$ µm	Y-Junction $\theta = 15°$ $f = 18.185$ mm $w_0 = 5$ µm
Y-Junction $\theta = 15°$ $f = 10$ mm $w_0 = 10$ µm	Ring Track $r_0 = 200$ µm $f = 10$ mm $w_0 = 5$ µm	Line Circular Mask $f = 10$ mm $w_0 = 5$ µm	Curved BS Square Mask $f = 18.185$ mm $w_0 = 5$ µm	Curved BS Circular Mask $f = 18.185$ mm $w_0 = 5$ µm	Curved BS Loci Mask $f = 18.185$ mm $w_0 = 5$ µm

Table 5.1: Parameters corresponding to the selected for manufacture. In the table, r_0 is the radius of a ring, f is the focal length, w_0 is the $1/e^2$ intensity radius (or width), θ is the angle between output ports of a y-junction, and mask refers to the shape of the kinoform. If the mask shape is unspecified, it is circular with radius 1 mm.

culate the incident E-field requirements for a particular target E-field considering the zone plate used. Here we assume the use of zone plates manufactured for this thesis (Secs. 5.4 and 6.1).

Case 1 - Applying known incident fields: In the first case, one uses Eq. 5.3 so the resultant field is calculated by taking the chosen incident field, multiplying it by the phase imprinted by the zone plate (this is it propagating through the kinoform), before propagating forward by the required (focal) distance.

Case 2 - Tailoring the incident beam: In the second case, one begins with a target E-field and follows a similar routine to that shown in Fig. 5.3. Starting with the target, we propagate this to the plane of the zone plate, but rather than calculating the zone plate as before, the phase imprinted by the zone plate is divided from the E-field and the remaining field is the incident beam required to produce a pattern using the zone plate. A schematic for this design process is shown in Fig. 5.10 for a 100 µm radius ring (focal length 18.185 mm and $1/e^2$ width of 5 µm) with a 0 to 2π phase winding.

The use of both approaches described above can produce rings with phase winding, with varying levels of success. Here we will detail the simulations showing this potential, and this will then be experimentally investigated in Sec. 6.3.

In Fig. 5.11 we show example of case 1 where a range of Lageurre-Gauss beams are

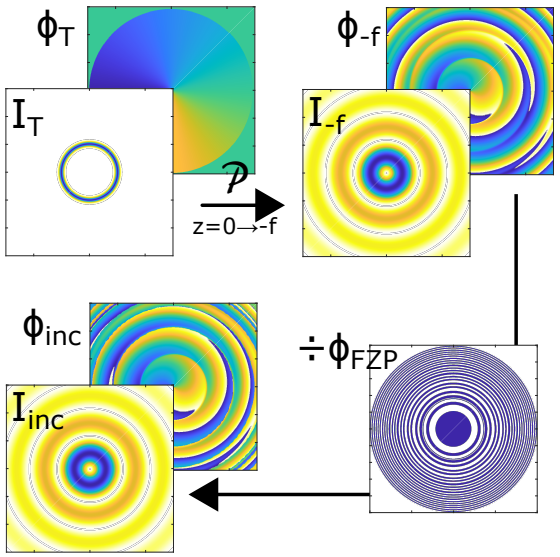

Figure 5.10: Schematic of the incident beam design process used. The target (T) electric field distribution is propagated backwards a distance f using Fourier techniques (giving phase $\phi_{-\mathrm{f}}$ and amplitude $I_{-\mathrm{f}}$). The phase shift of the zone plate (ϕ_{FZP}) is then removed via division to yield the required incident beam with phase (ϕ_{inc}) and amplitude (I_{inc}). In the plots shown, the field plots are 0.3mm×0.3mm, whereas the FZP is 2mm×2mm.

applied to several of our ring zone plates. Then in Fig. 5.12 we show examples of case 2 where we aim to produce rings with a variety of phase windings by calculating the appropriate incident beam. Here both the illumination fields required and the expected results are shown. In each of these cases, we show the results for three different rings to demonstrate how changing the radius, and focal length affect the results.

Case 1: Applying Known Incident Beams

Fig. 5.11 shows the simulated results of applying different LG beams to three different ring FZPs (case 1). Here we apply the LG beams to rings: (radius/width/focal length) 100 µm/5 µm/18.185 mm; 100 µm/5 µm/7 mm; 200 µm/5 µm/18.185 mm. The LG beams are applied with different phase windings ($p = 0$ and $\ell = 1$, 2 and 10) and different ratios between ring (r_0) and LG radius (R): r_0/R. We use the ratio between the two ring radii to allow accurate comparisons between the 100 µm and 200 µm radius rings.

The resultant fields shown in Fig. 5.11 show that the phase of an incident LG-beam is converted from winding into a spiral pattern (this is most easily seen in the $\ell = 10$

case for each ring), the radii and widths of the resultant rings are not independent of LG beam radius and a double (or even triple) ring structure (in intensity) is seen when the LG beam is larger than the ring radius. We can also note that the amount of light contained in the ring (rather than in background artefacts) increases with increasing LG-beam radius, but that this is limited by the size of the zone plate (i.e. if the LG-beam is too large it does not illuminate the centre of zone-plate sufficiently, as in the cases of high ℓ and r_0/R). The multi-ring structure is mainly seen for $r/R > 2$ in the first ring – this ring has the smallest numerical aperture (longest focal length, smallest radius and smallest width)

Comparing the rings of focal lengths 18.185 mm and 7 mm and the rings of radii 100 µm and 200 µm in Fig. 5.11 (i.e. comparing the first and second or first and third kinoforms) allows us to see the effects of changing numerical aperture. This shows that for a high numerical aperture (i.e. smaller focal length or larger radius) a tighter ring is produced, with more defined phase winding. This is particularly seen when comparing the $\ell = 2$, $r_0/R = 2$ of these three rings – for the first kinoform (lower NA), the resultant output field doesn't display a clear ring of phase winding, but the two higher NA kinoforms do.

Case 2: Calculating a Tailored Incident Beam

These results contrast with those demonstrated in Fig. 5.12 where we define the target field by adding phase winding to the original Gaussian target rings, then calculate the field that must be incident on the kinoform to produce these. Again this is done for $\ell = 1$, 2 and 10 and for rings: (radius/width/focal length) 100 µm/5 µm/18.185 mm; 100 µm/5 µm/7 mm; 200 µm/5 µm/18.185 mm.

The results seem to show that this method is more successful for narrow rings than wide ones (comparing $w_0 = 5$ µm and 10 µm) as a greater percentage of light is directed into the ring as opposed to the background area. We also see that the ring potentials seem to be better reproduced for higher ℓ. We note however, that creating the incident patterns calculated here would require very precise recreation of the beam, which may not be practically reproducible experimentally, particularly as these incident fields vary on the µm scale.

Experimental realisations of some of these simulations are presented in Sec. 6.3.

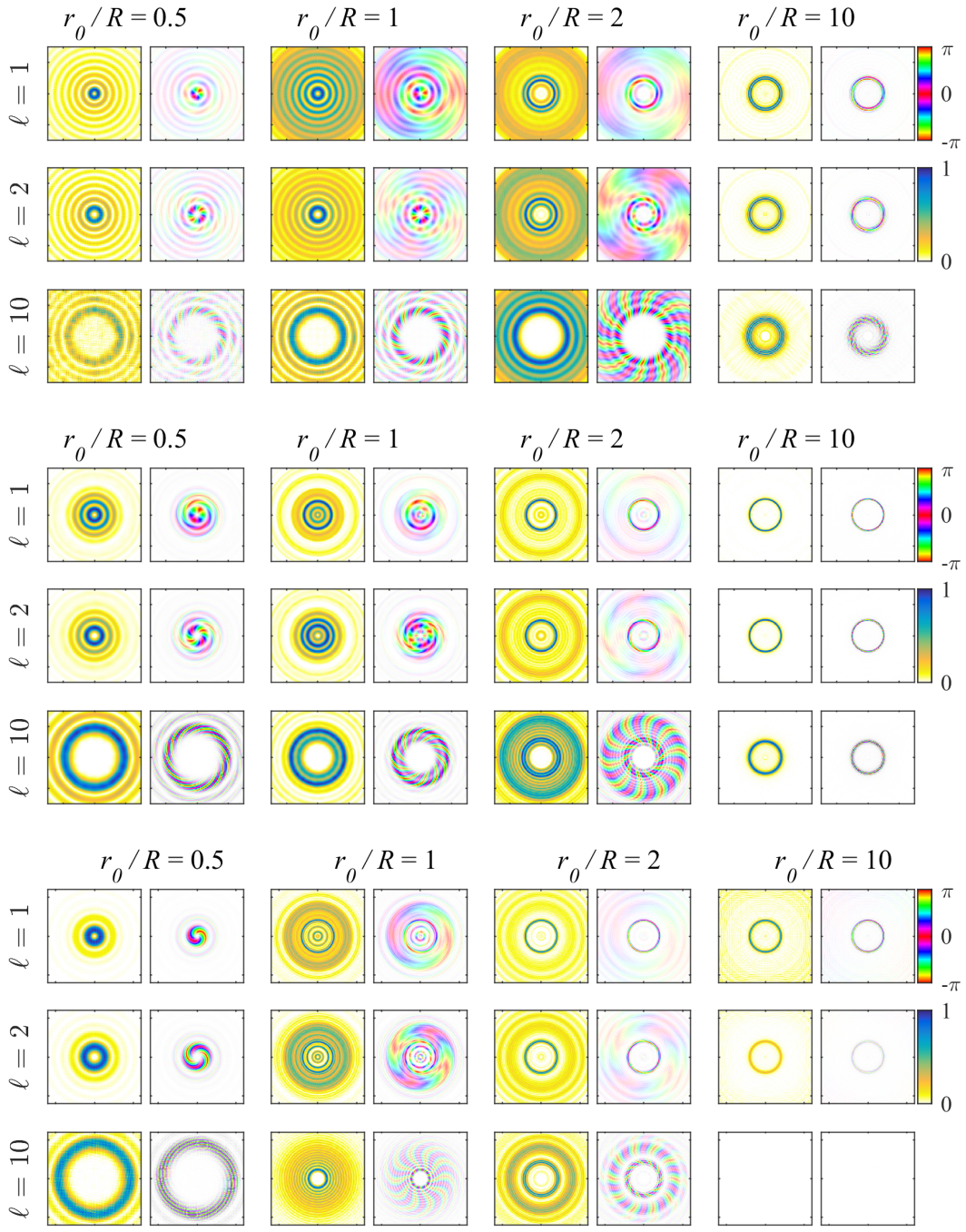

Figure 5.11: Resultant fields for kinoforms illuminated by Laguerre-Gauss beams. We illuminate with LG beams of $p = 0$, $\ell = 1, 2, 10$ and ring radii equal to $0.5, 1, 2,$ and 10 times the radius of the ring produced by a manufactured zone plates. Figures show an area of six times the radius along each axis, centred on the ring. Each intensity plot is normalised and the transparency of the phase plot is dependent on the intensity. The LG beams are applied to three different ring zone plates, from top to bottom: (radius/width/focal length) 100 µm/5 µm/18.185 mm; 100 µm/5 µm/7 mm; 200 µm/5 µm/18.185 mm.

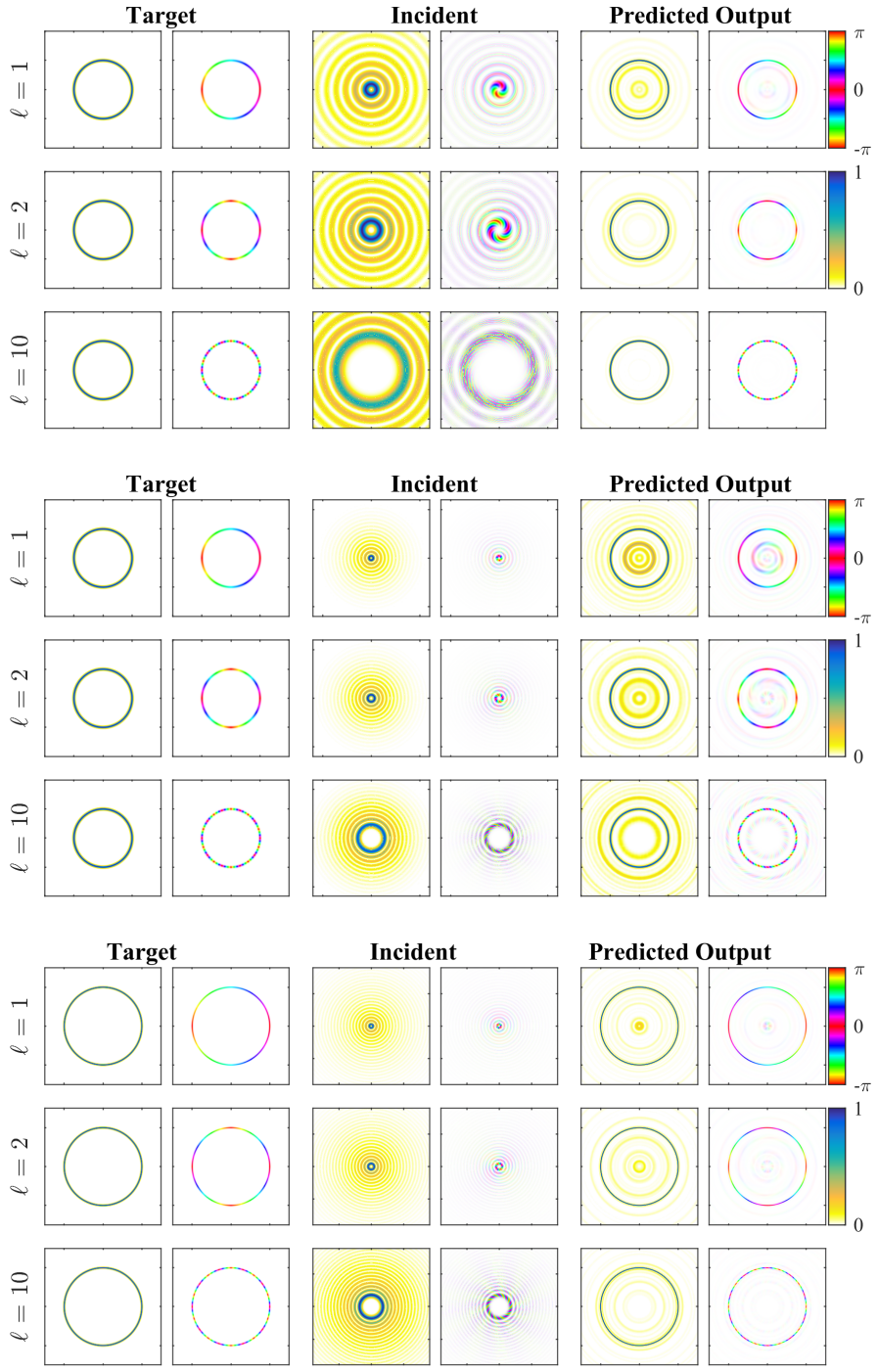

Figure 5.12: The modelling of rings with phase winding ($\ell = 1, 2, 10$). The target ring (on a square of $4r_0 + 200$µm), calculated require illumination field (on a square of $12r_0 + 600$µm) and resultant pattern (on a square of $4r_0 + 200$µm) are shown for three ring zone plates. From top to bottom: (radius/width/focal length) 100 µm/5 µm/18.185 mm; 100 µm/5 µm/7 mm; 200 µm/5 µm/18.185 mm.

Chapter 6

Testing of Fresnel Zone Plates

In this chapter, we present the optical testing of the manufactured Fresnel Zone Plates. Manufacturing is detailed in Sec. 6.1.

We image each of the potentials produced by the zone plates, with the methods detailed in Sec. 6.2.1 and preliminary results shown at the beginning of Sec. 6.2.2. We then analyse the ring potentials in detail. This begins with basic characterisation of the shapes, axial focusing, and efficiency in Sec. 6.2.3. The roughness of the rings is then analysed in more detail in Sec. 6.2.4, using an RMS error approach initially, followed by Fourier analysis of the potentials to determine the dominant lengths scales involved.

After converting the measured ring parameters into trapping parameters in Sec. 6.2.5, preliminary results from an FZP-SLM hybrid system are presented in Sec. 6.3. These results are a proof of principle demonstration of the creation of dynamic potentials and intensity correction.

6.1 Zone Plate Manufacture

A selection of 24 patterns have been etched onto a 18 $\times$ 26$\times$ 3 mm fused silica substrate by Holo/Or specified by a csv file detailing the digital depth patterns to be etched (an image of this csv file is shown in Fig. 6.1 a). The etching process is a combination of photolithography and then dry plasma etching steps [278]. We note that some of their etching techniques are listed in US patents [275, 276]. The substrate used is specified to have a surface flatness (before etching) of $\lambda/20$, with a tolerance depth of approximately $\pm 3\,\%$ on an etch depth of 1200 nm and wall slopes of better than 80° (resulting in sub-wavelength differences in feature size at the top and bottom of the

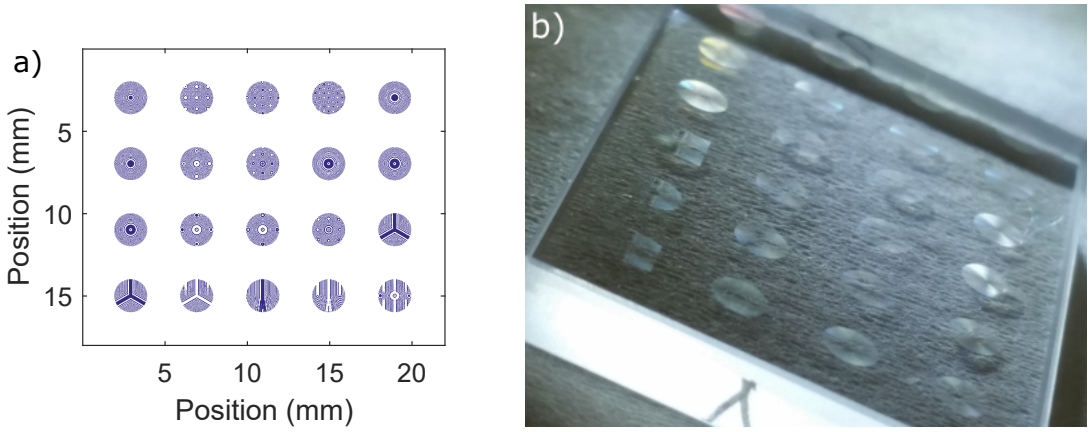

Figure 6.1: a) The csv file sent to be etched showing 24 different kinoforms. b) is a photograph of one of the three identical plates etched.

etch). The minimum feature achievable in the etching process is 0.7 µm. However, due to computing limitations files of pixel size 1 µm were used to design the etch pattern (this has subsequently improved within the work detailed in chapter 7). We note that the substrate is not coated in order to minimise complexity and cost. Only a single layer of anti-reflection coating would be possible and uniform coating would be very difficult to achieve. A photograph of one of the three etched plates is shown in Fig. 6.1 b.

6.2 Optical Testing

6.2.1 Testing Procedures

We have optically measured the patterns generated by the etched kinoforms using the imaging layout detailed in Fig. 6.2. This system consists of three main parts, incident beam preparation, mounting of the zone plate, and the imaging section.

Within the preparation section a fibre laser (NP-Photonics Rock$^{\mathrm{TM}}$ Module) is launched using a triplet collimation package (using Thorlabs: TC12APC-1064) which results in a beam of approximately 1 mm $1/e^2$ radius and an M^2 close to 1 (as shown in Figs. 6.3 and 6.4). This is followed by the option of inclusion of a Dove Prism (with flip mirrors allowing for its relatively seamless inclusion and removal from the system), which permits the incident beam to be rotated. A series of mirrors allow for the incident beam to be precisely aligned with the imaging system. We note that polar-

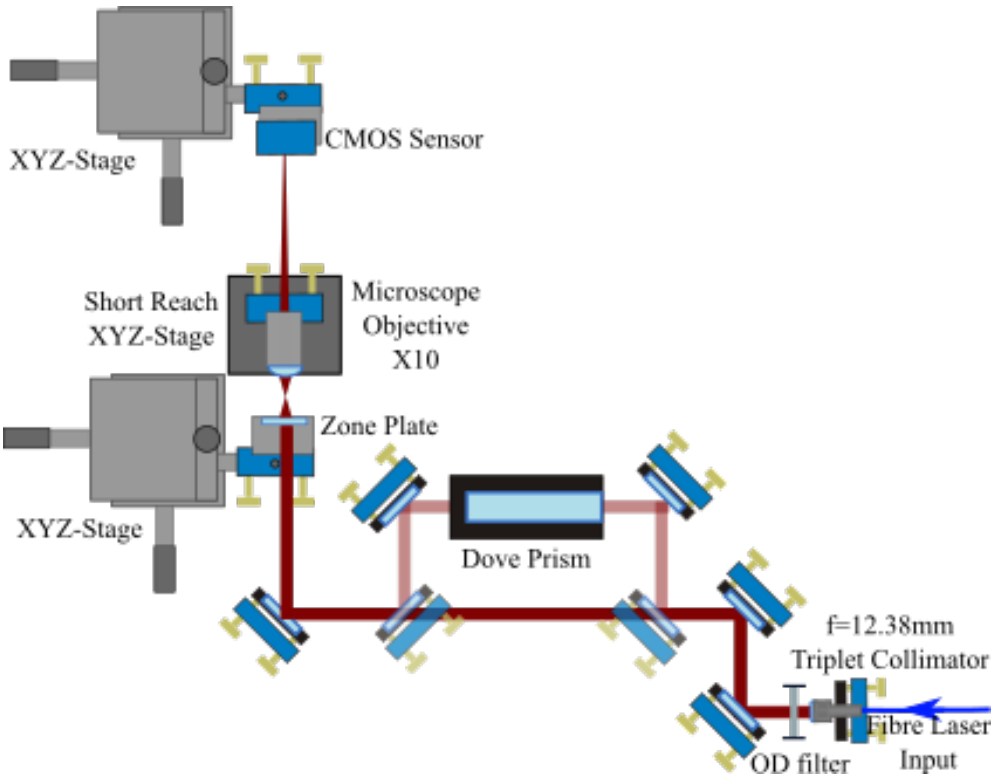

Figure 6.2: A schematic of the optical layout used to image the zone plates further information can be found in the text. The more transparent section is an optional path accessed via flip mirrors which allows the Dove prism to be used to rotate the incident beam.

isation optics are not necessary as the orientation or purity of polarisation do not affect the produced holograms.

The imaging section of the system consists of a $\times$ 10 microscope objective (with a numerical aperture of 0.25 and working distance of 160 mm) and a CMOS-sensor camera. Both of these components are mounted on translation stages and kinematic mounts to allow for the very precise alignment required to minimise system aberrations. When aligning the imaging system, the camera is mounted first, with its tilt and position adjusted such that the sensor is perpendicular to and centred on the incident beam (using a series of pinholes to which the incident beam is aligned). We can then use the camera to confirm the alignment of the objective lens. The objective can be roughly aligned using a power meter and two pinholes - one before the lens to align lens position and a second after the lens to align tilt. After this rough alignment, the back reflection of the lens can be used to adjust tilt, and the transmission through a

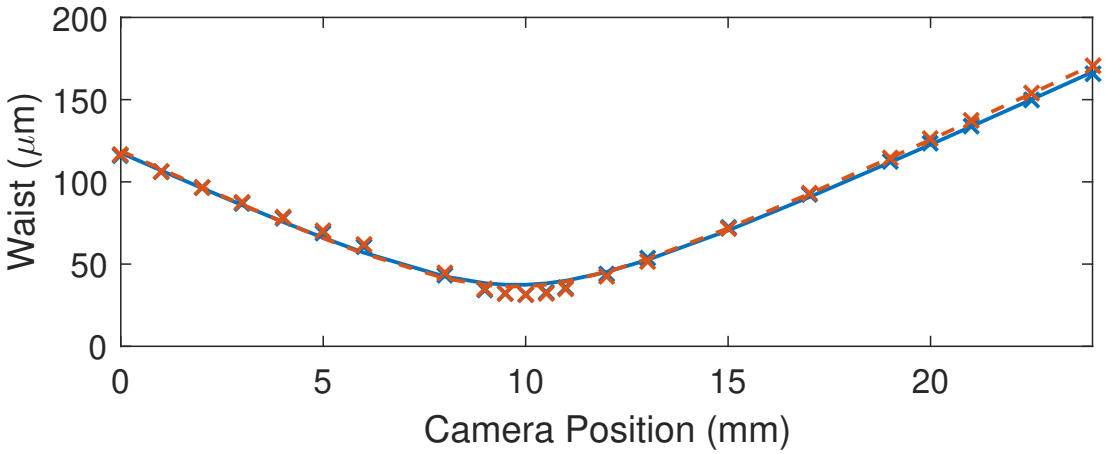

Figure 6.3: The M^2 measurement for the incident beam (calculated to be close to 1 in both directions), using a 100 mm focal length lens. The blue (red) crosses show the width of the beam in the horizontal (vertical) x (y) direction, the corresponding lines (solid blue and dashed red respectively) show Gaussian propagation fits to these data points.

pinhole close to the camera can be used to optimise position. At this point, the diffraction patterns from all pinholes should be centred on the sensor as was the case before insertion of the lens. Despite very careful alignment at this stage additional lens and zone plate adjustment may be needed: the tilt of the objective can be minutely adjusted to optimise the smoothness of ring patterns later in the acquisition procedure.

The camera used for measurements is a Cinogy CMOS1201 which is a modification of the IDS UI-1540LE-M camera. Due to the wavelength used for the zone plates (1071 nm), most cameras are unsuitable either due to negligible quantum efficiency at that wavelength or fringing and woodgraining occurring as a result of etaloning within the camera. As the sensor coverglass of the Cinogy beam profiler has been removed (a process which has a high risk of sensor damage), it is less affected by etaloning than other cameras available to us. Side by side comparisons of the Cinogy beam profiler the UI-1540LE-M-NO (which has the filter removed), and the UI-3240LE-NIR-GL (a similar IDS camera with a boosted NIR response and glass filter) confirm that the sensor glass is the most dominant contributor to fringing. We have attempted to mitigate the etaloning by clever alignment and by attaching a glass wedge to the sensor glass with index matching gel, but these approaches have not yielded any positive results.

Before we can begin imaging the zone plate patterns in this set-up we must calibrate it in order to determine the magnification and hence resolution of the system. To

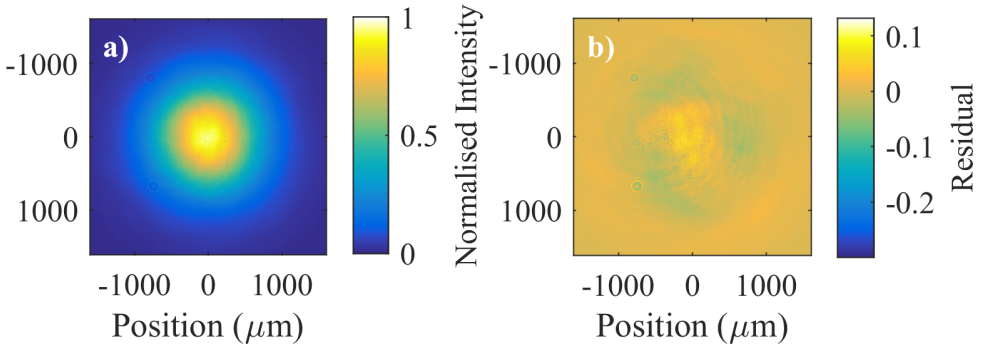

Figure 6.4: The incident beam used to illuminate the zone plate is shown in a. Fitting to a two-dimensional Gaussian gives a $1/e^2$ waist of w_x, w_y = 1048 µm, 1073 µm (quoted to 4 s.f.). The residuals for this fit are shown in b.

do this we use a 1951 USAF resolution test target (Thorlabs R1DS1P) mounted on the same translation stage as the zone plate will be. We then use the largest feature which can fit on the sensor to calculate the pixel size. This method yields an image pixel size of (0.5207 ± 0.0005) µm. This method can also be used to calculate the actual magnification of the system and so the correct position of the camera with respect to the objective can be determined by matching this calculated value to the stated magnification of the objective. Despite careful calibration at this stage, we find that this measurement becomes inaccurate when imaging the zone plate potentials (this is likely to be due to the different optical thickness of the two elements), this is confirmed by imaging the zone plates without a magnifying lens. Therefore, we recalibrate resolution later in the analysis process. This is outlined further in Sec. 6.2.3. In the future, this calibration will be completed using time-of-flight imaging of atoms falling under gravity.

The zone plate is mounted in a standard prism mount and attached to a three dimensional translation stage, giving us five degrees of freedom in alignment. This means that we can align the zone plate to be perpendicular to the incident beam and scan the imaging plane through the focus of the pattern. In order to align the zone plate, we first use xy translation to approximately centre the incident beam on the chosen kinoform. We then use the back reflection to align the tilt of the plate with respect to the input beam. Once these parameters are approximately aligned, we can adjust the z-position of the zone plate to bring the pattern into focus on the camera or to scan through the focus and obtained a map of intensity. The transverse position and tilt of the zone

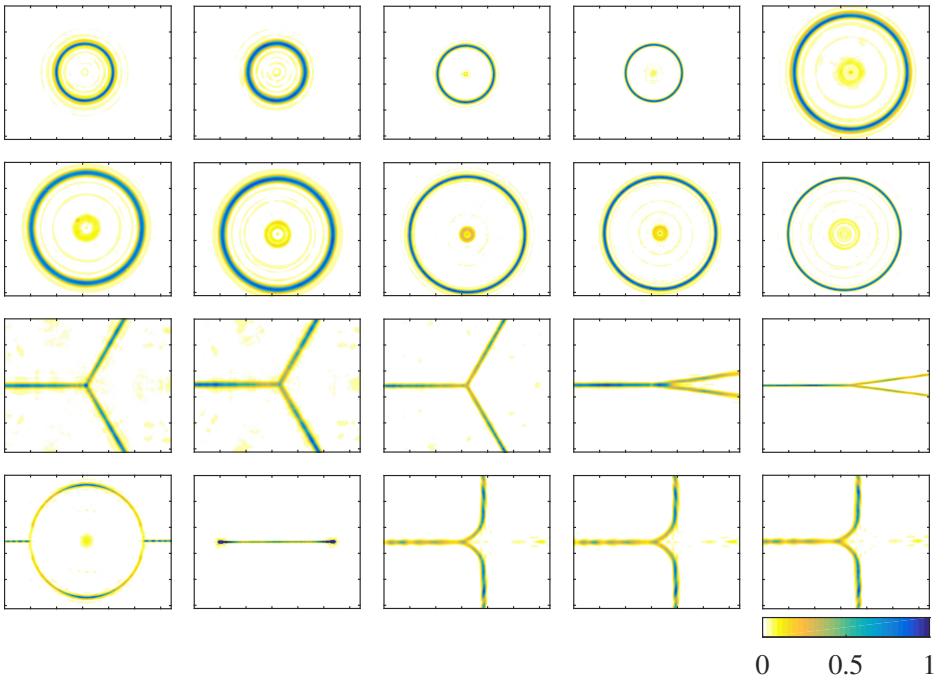

Figure 6.5: Raw data experimental images of zone plate patterns excluding single foci. Acquisition conditions are discussed in the text. Each plot is 1280×1024 pixels (or 6.6560 mm$\times$5.3248 mm). The colour map represents normalised intensity.

plate can then be iteratively adjusted to generate the most central and smooth image recorded on the beam profiler.

6.2.2 Results

Following the methods detailed above, we image each of the potentials produced by the zone plates. The focus patterns are reproduced exactly but are unlikely to be used for atom trapping purposes, having been manufactured for optical benchmarking Therefore their results are not presented here. We show the raw data for each of the complex patterns in Fig. 6.5, with the ordering following that shown in Tab. 5.1. For each of these images, data is captured at the focus of the electric field and with the maximum camera exposure possible without over-exposure. An exception to this is the line, which is over-exposed so that detail in the middle of the line can be seen, as discontinuity at the ends of the line create very bright spots which overwhelm the rest of the pattern. Each of the plots show an area of 1280×1024 pixels (of 5.2 µm), and has been magnified 10 times by the objective lens in the system before imaging.

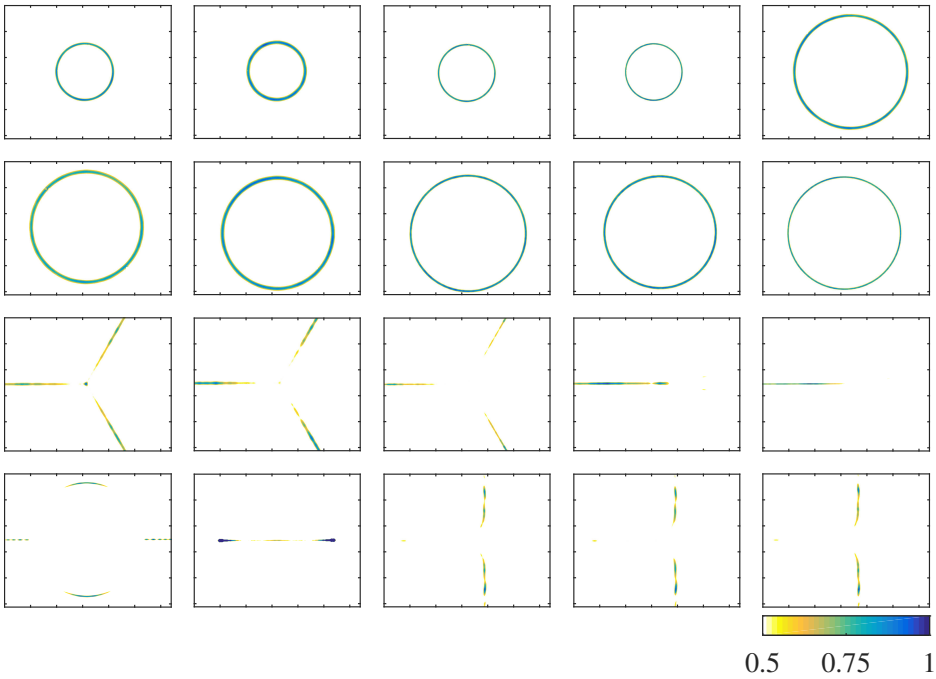

Figure 6.6: Raw data experimental images of zone plate patterns (excluding single foci) with colour bar rescaled so only show the top 50% of the intensity. Acquisition conditions are discussed in the text. Each plot is 1280×1024 pixels (or 6.656 mm$\times$5.3248 mm). The colour map represents normalised intensity.

The patterns shown in Fig. 6.5 show that general shapes of the potentials are reproduced, even for the complex case of the 'ring-track' (the bottom left image). However it is obvious that many of the potentials do not have the smooth maxima that would be required to operate successfully as a waveguide. We can more easily see this roughness in the potentials by looking at the top 50 % of the potential as is shown in Fig. 6.6 through the rescaling of the colour map such that it begins at $I_{\max}/2$. In this rescaled plot, we see that the rings look very smooth, but all the other, less symmetric patterns have significant intensity variations along the bottoms of the traps, where the atoms are meant to reside. For example, the addition of the input/output coupler to a ring to make a ring track creates a discontinuity at the junction between the lines and the ring and removes the circular symmetry present in one of the ordinary ring traps. For the beam splitters, we see that the curved beam splitters (final 3 patterns) and the narrower Y-junctions (last two patterns on the 3rd line from the top) do not successfully produce all the ports of the splitter even far from the junction, with the input port being much less intense than the output ports of the curved beam splitter and the opposite being

true of the narrow Y-junction. This compares to the symmetric Y-junction where each of the ports is equally separated by $2\pi/3$; here we see the input/output waveguides are well defined and self-similar. Even here we see that there is an intensity gradient centred on the junction meaning that atoms would not be able to travel toward the junction, although there are some simple techniques which could potentially be used to make the Y-junction useful for atomtronics, such as introducing a compensatory beam overlapping the potential.

In order to establish the suitability of our holograms for atom trapping and guiding, we need to characterise the potentials in terms of geometry and smoothness. In general, in the quasi-1D systems such as rings and straight waveguides, trap geometry will determine the trap confinement and depth, whereas the smoothness of the pattern will affect the coherence and propagation of any atoms or matter-waves placed within it. In more complex patterns, such as beam splitters, geometry is expected to contribute to heating as atoms travel through sections such as corners [105]. In the following sections, we will focus on the analysis of the ring traps as they are both the most useful (e.g. for guided interferometry) and the most promising selection of patterns due to their apparent smoothness.

6.2.3 Basic Characterisation

With the following analysis, we characterise rings using the following routine: first 'unfold' the ring, going from Cartesian to polar co-ordinates; then individually fit radial slices to a Gaussian; then finally fit the full 2-dimensional ring. Though conceptually simple, the process of fitting rings can be nuanced and computationally intensive due to the dimensionality of the system, meaning that each stage much be completed with care.

The 'unfolding' of the rings is completed using nearest neighbour interpolation (specifically using the MATLAB inbuilt function *scatteredInterpolant*) to transform from the Cartesian, camera co-ordinate system to a more intuitive polar co-ordinate system which allows us the view the ring in the frame of the atoms (i.e. as a line with periodic boundary conditions). Although this process yields good results, it is reliant on accurate determination of the centre of the rings – a non-trivial process in itself. The centre of the ring is initially estimated as the centre of mass of the image and improved iteratively by conversion to progressively larger polar co-ordinate systems where its centrality can be confirmed by plotting each radial intensity maximum against its an-

gular position. For perfect centre choice, this should be a straight line of zero gradient equal to the radius; otherwise it is a sinusoidal curve with amplitude equivalent to the centre offset and phase indicating the direction of the offset, which allows rapid iteration to zero offset. In the polar co-ordinate system, the radial resolution is kept as a single pixel, and the angular resolution is determined by calculating the angle which corresponds to a single camera pixel at a radial position of the radius. This means $dr = dx$ and $d\phi = 2\sin^{-1}(dr/r)$.

Once in polar co-ordinates, we can fit each radial slice (these slices each correspond to an individual angular position) to a Gaussian to obtain the value of the width, intensity, background and radius. The fits are carried out on the top 70 % of the intensity as this is the area which can be well approximated by a Gaussian. Here the initial parameters of the fit are estimated from a knife-edge type sum across the Gaussian (error function). We can then average the slice fit parameters and either use these numbers and their associated errors or use them as initial guess parameters for a global, 2-dimensional fit of the original Cartesian ring. The errors obtained are kept in terms of the standard deviation to allow for consistent comparison between data-sets.

Radial Trap Parameters

It is relatively easy to characterise the shape of potentials (in the plane of the focus) using the fitting procedures described above. On first observation we see well reproduced rings with no perceivable ellipticity. However, initial analysis indicated that the radii obtained did not match the designed radii (with each ring having a radius of approximately 10 % higher than expected), suggesting that either the rings are not reproduced accurately or that the resolution of the system is not calculated appropriately using the test target. By imaging a selection of the rings without any magnification (this could only be done for the longer focal length zone plates due to spatial constraints), as is shown in Fig. 6.7, we were able to measure the radius of the rings independently of magnification. In these images, the radii of the rings matched the designed radius, allowing us to use the radius to recalibrate the rings imaged using the objective lens. This recalibration process gives us a mean resolution of (0.464 ± 0.007) µm compared to (0.5207 ± 0.0005) µm calculated with the test target. We believe that the discrepancy between these two values is due to difficulties in the positioning of the test target with respect to the imaging system (both in terms of physical position and the relative angle of the pattern) and to the difference in optical thickness of the test target and the

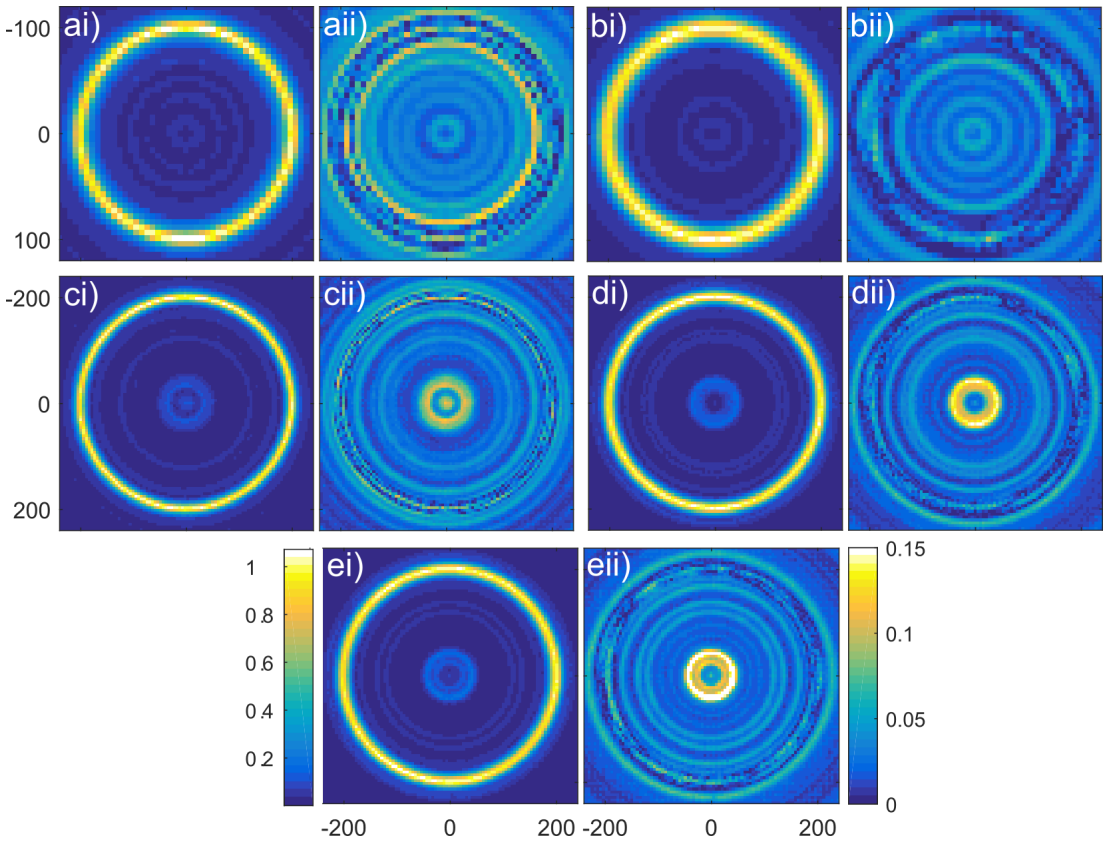

Figure 6.7: Experimental imaging of 18.185 mm focal length rings without any magnification. Rings are (a-e) (radius/width): 100 µm/5 µm; 100 µm/10 µm; 200 µm/5 µm; 200 µm/10 µm; 200 µm/15 µm. For each ring, (i) shows the raw image of the ring, and (ii) shows the residuals of the fits as described in the text, the respective colour scales are shown by e.

zone plate.

The trap parameters obtained for magnified rings potentials with resolution calibrated by the radius are shown in Tab. 6.1, with the images of all rings and their respective fitted residuals shown in Fig. 6.8. We obtained the measured trap parameters shown in Tab. 6.1 by taking the mean and standard deviation of the slice fits for each ring (rather than the global fit, as this approach allows for sensible error estimation – the best fit parameters are very similar).

When comparing the designed and measured trap width, it is immediately obvious that the focal length of the kinoform (and so the numerical aperture) greatly influence the trap width, meaning that a width of 5 µm is not obtainable with a 18.185 mm focal length. We can naïvely estimate the diffraction limit of the system using Eq. 2.4 and

estimating the diameter of the lens to be between the diameter of the ring (which corresponds to the case where wavefronts do not overlap at the centre of the rings) and the diameter of the kinoform. Using this back of the envelope calculation gives a diffraction limited ring width of between 100 µm and 10 µm for a 100 µm radius 18.185 mm focal length ring. The smaller estimate (for NA corresponding to the whole kinoform rather than a subsection) is of the order of the ring widths achieved, suggesting that the rings are diffraction limited. However, this does not explain why the same widths ((14.8 ± 0.2) µm and (14.9 ± 0.2) µm) are observed for two rings of different designed widths (10 µm and 15 µm respectively – the 4^{th} and 5^{th} lines of Tab. 6.1). To determine the actual diffraction limit and whether our system is diffraction limited we need to examine the relationship between the designed and observed widths, the focal length and the radius of the ring. The data shown in Tab. 6.1 suggest that the observed ring width is influenced by all the other parameters listed. Initial exploration suggests that the diffraction limit may be close to 15 µm, but it will be explored further in Chap. 7.

From the fit residuals shown in Figs. 6.8 and 6.7 we can gain a qualitative impression of the smoothness of the traps that the rings provide. In the region of the trap bottom, the magnitude of the residuals are all below 10 % and the majority of the errors lie outside of the trapping region. The residuals themselves are neither smooth nor regular in both the radial and azimuthal directions. In some places, we see a checkerboard effect related to the readout of the camera, in others we see dust on the sensor

Design			Observed	
Focal Length (mm)	Radius (µm)	Width (µm)	Radius (µm)	Width (µm)
18.185	100	5	100 ± 1	9.1 ± 0.1
	100	10	100 ± 1	14.1 ± 0.2
	200	5	199 ± 3	11.9 ± 0.2
	200	10	203 ± 3	14.8 ± 0.2
	200	15	205 ± 3	14.9 ± 0.2
10	100	5	100 ± 1	7.0 ± 0.1
	200	5	199 ± 3	8.8 ± 0.2
	200	10	195 ± 3	9.0 ± 0.2
7	100	5	102 ± 1	5.77 ± 0.09
	200	5	197 ± 3	6.15 ± 0.09

Table 6.1: Parameters corresponding to the rings designed and manufactured. The errors quoted correspond to the fitted standard deviation.

(though this does not affect the quantitative roughness calculated later). In some places the residuals seem to 'pulse' irregularly, this can be seen most clearly in aii). It is practically impossible to disentangle the origin of the errors between those that are from the kinoform design and those that are artefacts of the imaging system. Though in prin-

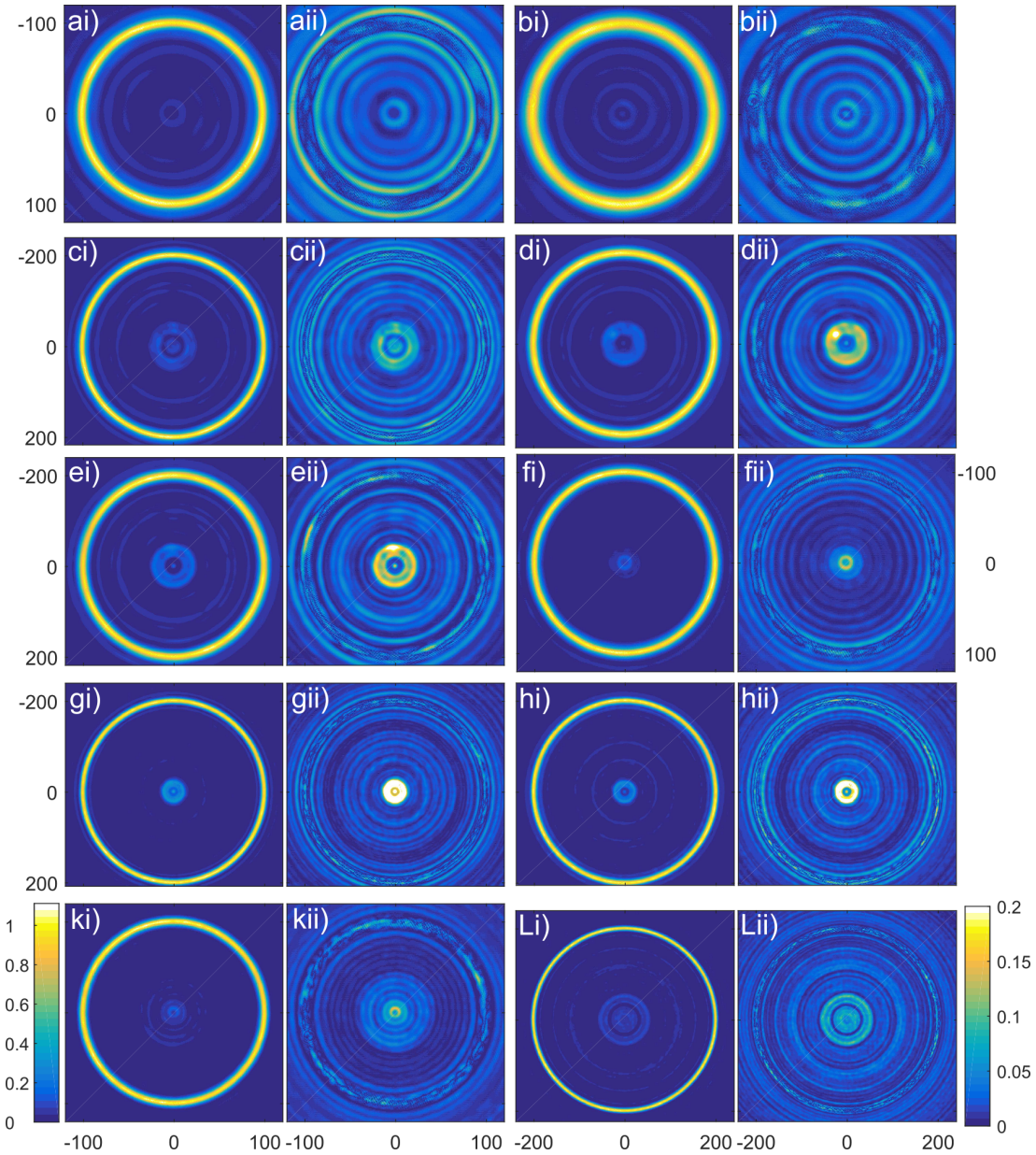

Figure 6.8: Experimental imaging of all rings using a 10× magnification microscope objective. Rings are shown in the same order as in Tab. 6.1, following the ordering (a-h, k, L). For each ring, (i) shows the raw image of the ring, and (ii) shows the residuals of the fits as described in the text.

ciple one could begin to study this if we had full control of the phase and intensity of the incident field. We have, in part been able to isolate and minimise the imperfections caused by the incident beam through alignment and collimation. Due to the relative size of the roughness around the ring compared to the total intensity, it is very hard to minimise the residuals by careful alignment, though this has been carried out as much as possible.

The influence of incident beam imperfections has been characterised and then minimised. The characterisation was completed by rotating the incident beam with a Dove prism and monitoring the location of imperfections in the ring. Despite alignment issues, we were able to show that the roughness tends to move with the incident beam as it is rotated, meaning that the quality of the incident beam is important for the zone plates. We were then able to improve the M^2 of the beam to close to 1, with a circularly symmetric profile (as demonstrated in Figs. 6.3 and 6.4), and so improve the rings.

Axial Trap Parameters

In order to determine trapping parameters in the direction of beam propagation (axially), we can map out the average radial profile of the potential as one scans through the focal plane (with this scanning achieved by moving the zone plate). This process yields maps of the propagation as shown in Fig. 6.9 for a 100 µm radius, 5 µm width ring, with a focal length of 18.185 mm, and in Fig. 6.10 for a ring of the same parameters except for a increased width of 10 µm. By taking the maximum of each radial

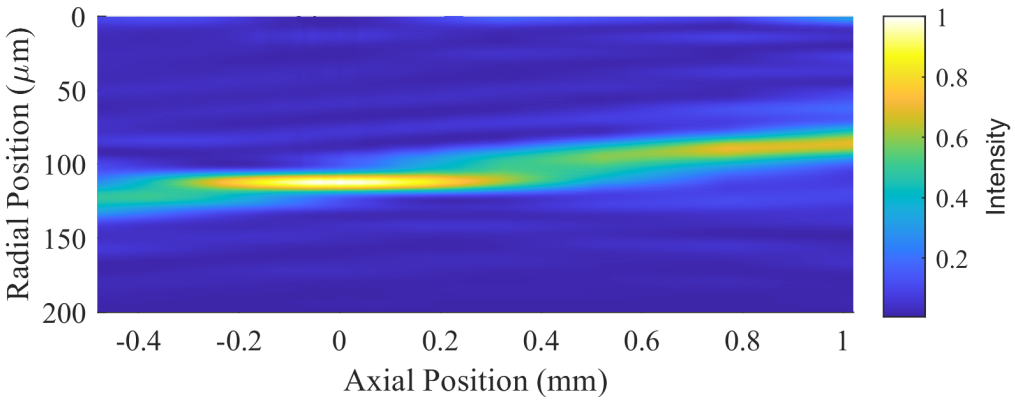

Figure 6.9: Propagation of the radial profile of a 100 µm radius, 5 µm width ring, with a focal length of 18.185 mm through its focus (the focal plane is located at axial position 0).

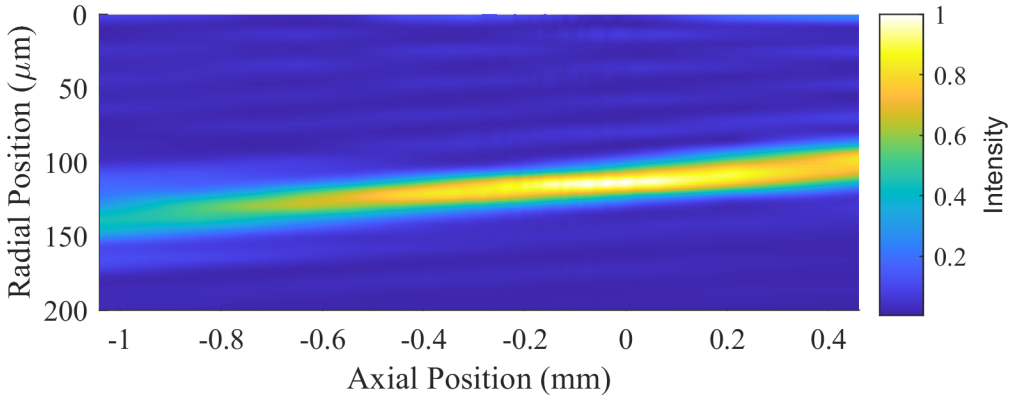

Figure 6.10: Propagation of the radial profile of a 100 µm radius, 10 µm width ring, with a focal length of 18.185 mm through its focus (the focal plane is located at axial position 0).

slice shown in the maps, we can plot out the intensity variation and change in width with position. This information is shown in Figs. 6.11 and 6.12 for the 5 µm and 10 µm rings respectively, with subplot (a) showing width variation, and (b) showing intensity information (the peak intensity of each slice).

As one can see from both the map and the plotted data, close to the focus of the beam (i.e. close to the trap bottom) the ring focuses in a similar way to an ordinary focused Gaussian, whereas, further from the focus, additional components can be seen which derive from the binary and diffractive nature of the zone plate. The most obvious of these diffraction effects are the appearance of 'shoulders' on either side of the focus (radially). The shape and behaviour of the foci are reproduced in the theoretical modelling shown in Sec. 7.1 (Figs. 7.1 and 7.2), including the diagonal nature of the focussing.

From a) in Figs. 6.11 and 6.12 we can calculate the $1/e^2$ waists as (8.76 ± 0.06) µm and (13.6 ± 0.1) µm respectively. This then allows us to fit the Rayleigh length using the fit in b) as (417 ± 3) µm and (980 ± 20) µm respectively (this is fitted by setting the waist and allowing z_R to vary). Alternatively, if we calculate the Rayleigh length using the definition $w(z_R) = \sqrt{2}w_0$, we obtain 170 µm and 740 µm respectively. These values are of a similar order of magnitude but are different due to the varying dominance of diffractive patterns in propagation. The values yield an axial trap frequency below 50 Hz if illuminated by a 10 W laser considering the efficiency information which is discussed later in this section. Comparing these values to those calculated in Sec. 5.1.1,

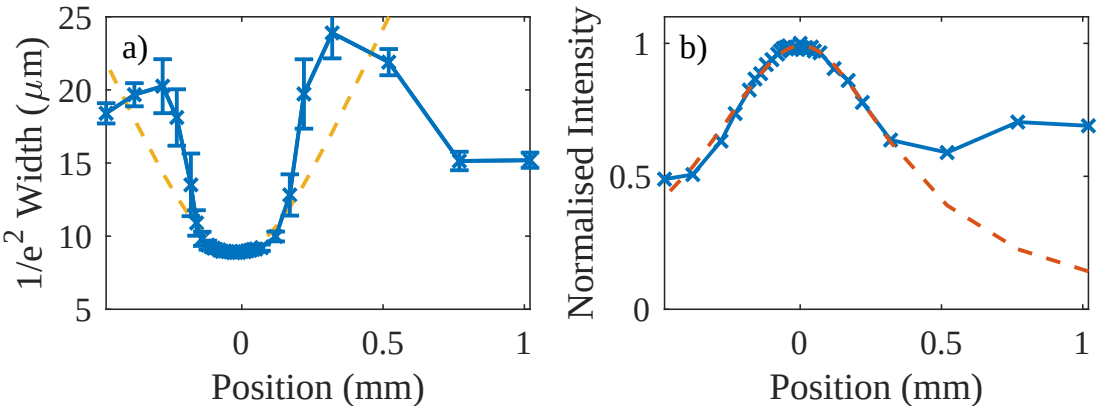

Figure 6.11: Propagation of the radial profile of a 100 µm radius, 5 µm width ring, with a focal length of 18.185 mm. (a) shows the variation in 1/e^2 width of the focusing beam, with data shown in blue and a fit to Eq. 2.3 in the yellow dashed line (only the data showing this trend close to the centre is fitted). (b) shows the peak intensity of each radial slice, with data shown again in blue, and a dashed red line showing a fit to Eq. 2.2 using the waist calculated in a.

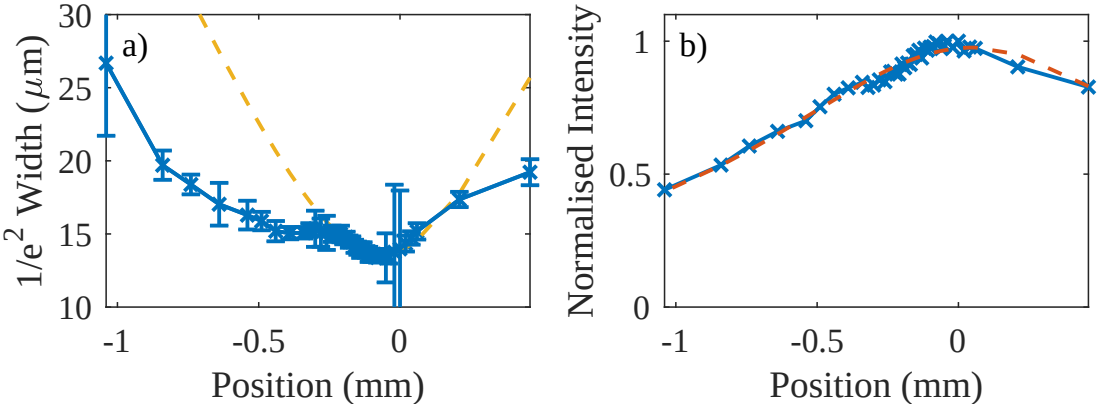

Figure 6.12: Propagation of the radial profile of a 100 µm radius, 10 µm width ring, with a focal length of 18.185 mm. (a) shows the variation in 1/e^2 width of the focusing beam, with data shown in blue and a fit to Eq. 2.3 in the yellow dashed line (only the data showing this trend close to the centre is fitted). (b) shows the peak intensity of each radial slice, with data shown again in blue, and a dashed red line showing a fit to Eq. 2.2 using the waist calculated in a.

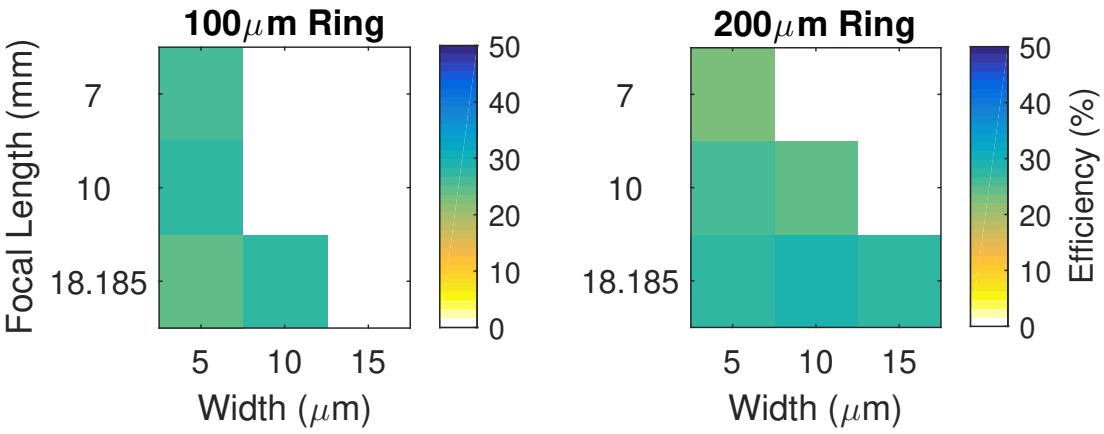

Figure 6.13: Efficiency of power transfer from the incident beam into an area of interest determined by the ring parameters. This is for rings imaged using the $\times 10$ magnification objective lens.

we can see that the potentials could not support against gravity if the plane of the ring was horizontal. We would thus propose to combine the traps with either a magnetic levitation field [18,30,31], or a light sheet [66]. The difference in axial Rayleigh length for these two rings suggests that the design width has a greater influence on the trap parameters in this direction than in the radial direction.

It is interesting to note that a repeated, nodal pattern, similar to that seen in the Talbot effect [31], can be observed close to the centre of the ring in Figs. 6.10 and 6.9. This is thought to occur because the zone plate effectively works as a grating in this area.

Ring Efficiency

Finally, we can measure the efficiency of the zone plates at directing incident light into the ring potentials. This is done by calibrating the camera's response to intensity at various exposures and then recording the exposure of each image and the power of the incident beam for each individual data point. For ease of analysis this meta-data was placed in the filenames. Then we determine the power contained within an area of interest on the image of a potential by integrating the measured intensity across this area. For rings, the area of interest is chosen to be where the intensity of an ring is non-zero. This is defined by an ideal ring of the same parameters as the measured ring.

The calculated efficiencies for all the magnified rings are shown in Fig. 6.13, the equivalent information for a system without magnification is shown in Fig. 6.14. As

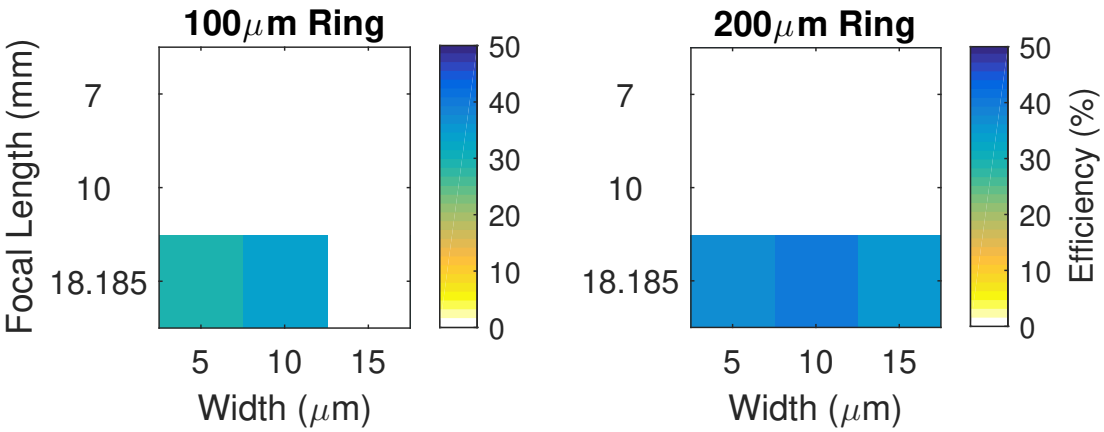

Figure 6.14: Efficiency of power transfer from the incident beam into an area of interest determined by the ring parameters. This is for rings imaged without any magnification, therefore only long focal length patterns could be practically measured.

can be easily seen by comparing the above figures, the addition of the objective lens reduces the efficiency of the system, as would be expected considering the imperfect alignment and wavelength mismatch between the design of the lens and illumination beam. Thus, the efficiency measured when using the lens can be used as a lower limit. We have a typical efficiency of 30%, which is likely to be closer to 40% when used in a cold atom system (i.e. a system without magnification). The absolute maximum efficiency that can be achieved in a binary diffractive optics system is 50 %, which is limited by the presence of a virtual focus. Higher efficiencies are obtainable using blazed and multi-level diffractive optics [275, 276, 278].

6.2.4 Roughness Characterisation

When using these traps as waveguides, the coherence time and dynamics of the atom cloud will be affected by the roughness of the bottom of the trap. In order to understand the various forms of roughness we need to analyse both the magnitude of the roughness compared to trap depth and the length scales of this roughness. There are two ways to approach this which are outlined below.

A simpler method of measuring trap 'goodness' uses the root mean squared (RMS) error between an ideal trap and the observed trap. This is an established method used in SLM holography as an optimisation parameter for design algorithms [99, 111, 112, 260] or to compare design methods [123]. It is discussed in the previous chapter. For our traps, we calculate the RMS error of the top 10 % of the potential, this is shown in

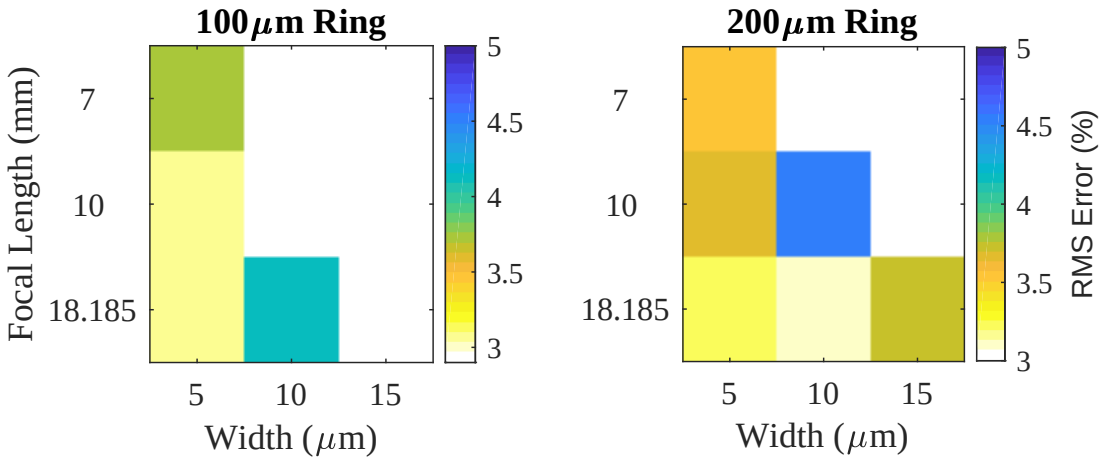

Figure 6.15: RMS error between measurements and the top 10% of an ideal ring of the same width, radius and average depth. This calculation is for rings imaged using the $\times 10$ magnification objective lens.

Fig. 6.15. We calculate the 'ideal' ring through the fitting routines detailed previously, rather than comparing it to the designed pattern.

The RMS errors presented in Figs. 6.15 and 6.16 give an upper bound on the RMS error, suggesting that all rings have an RMS error below 5 % (and could be below 3 %), which is compatible with atom guiding. The RMS errors in the non-magnified system are similar. As discussed in the previous section, we are unable to disentangle imaging aberrations and kinoform aberrations as possible sources of the RMS error.

A more thorough and complex method of analysis is through Fourier analysis of azimuthal potentials. The methods used to calculate the azimuthal potential and obtain trap parameters are detailed in Sec. 6.2.3. By analysing the variation of these parameters, we can isolate the information most important to the atoms.

All of the rings analysed using this method are shown in Appendix. A, with two examples (a 100 µm radius, 5 µm width ring with focal length 18.185 mm, and the equivalent 200 µm radius ring) shown in this chapter within Fig. 6.17. In this figure, on the first line we can see the 'unfolded' ring on a normalised intensity scale. Below this, the variation in trap depth (left axis, in blue) and trap width (right axis, in red) is shown as a percentage variation from the mean. No errors are shown on this plot as the errors obtained from the slice fitting routine are smaller than the slice-to-slice variation in obtained parameters. The dominant frequency components of these trap

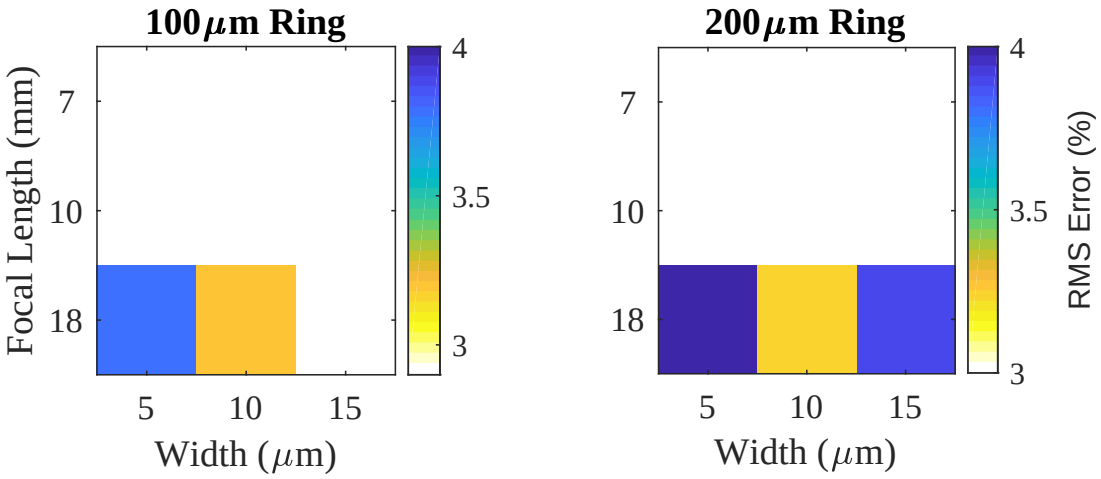

Figure 6.16: RMS error between measurements and the top 10% of an ideal ring of the same width, radius and average depth. This is for rings imaged without any magnification, therefore only long focal length patterns could be practically measured.

parameters are then shown on the bottom line, this is shown as a bar chart of dominant frequency components so that relevant lengths scales can be highlighted. The first eight harmonics are labelled numerically (the 1st harmonic corresponds to variation over the whole circumference, the second is over half the circumference, and so on), with the final two boxes labelled as 'A' for the length scales larger than the trap width, and 'B' for lengths scales smaller than the trap width. For the 'A' and 'B' bars, the bar chart shows the mean amplitude of components in this length range.

In the ring examples shown in this chapter and in the appendix, we can see that the trap parameters vary by between 5 % and 10 % from their mean value, this is a promising result as it is close to the 5 % to 10 % variation limit suggested in previous literature [65, 99, 112] and so they are expected to be suitable for atom trapping if the trap depth is scaled appropriately to match the chemical potential (further details can be found in Secs. 5.1.1 and 6.2.5). From the Fourier transform information, we can see that dominant length scales in the trap depth variation are on the order of the ring circumference (i.e. low frequency), with much lower contributions at length scales of the order of the trap width and even lower contributions at even higher frequencies. The low frequency components may affect the expansion dynamics causing uneven speed around the two arms of an interferometer but are expected to be easy to correct for with the use of an SLM. Many of these defects may be artefacts of the imaging system as they vary with alignment or artefacts of the 'unwrapping' process. This means that our

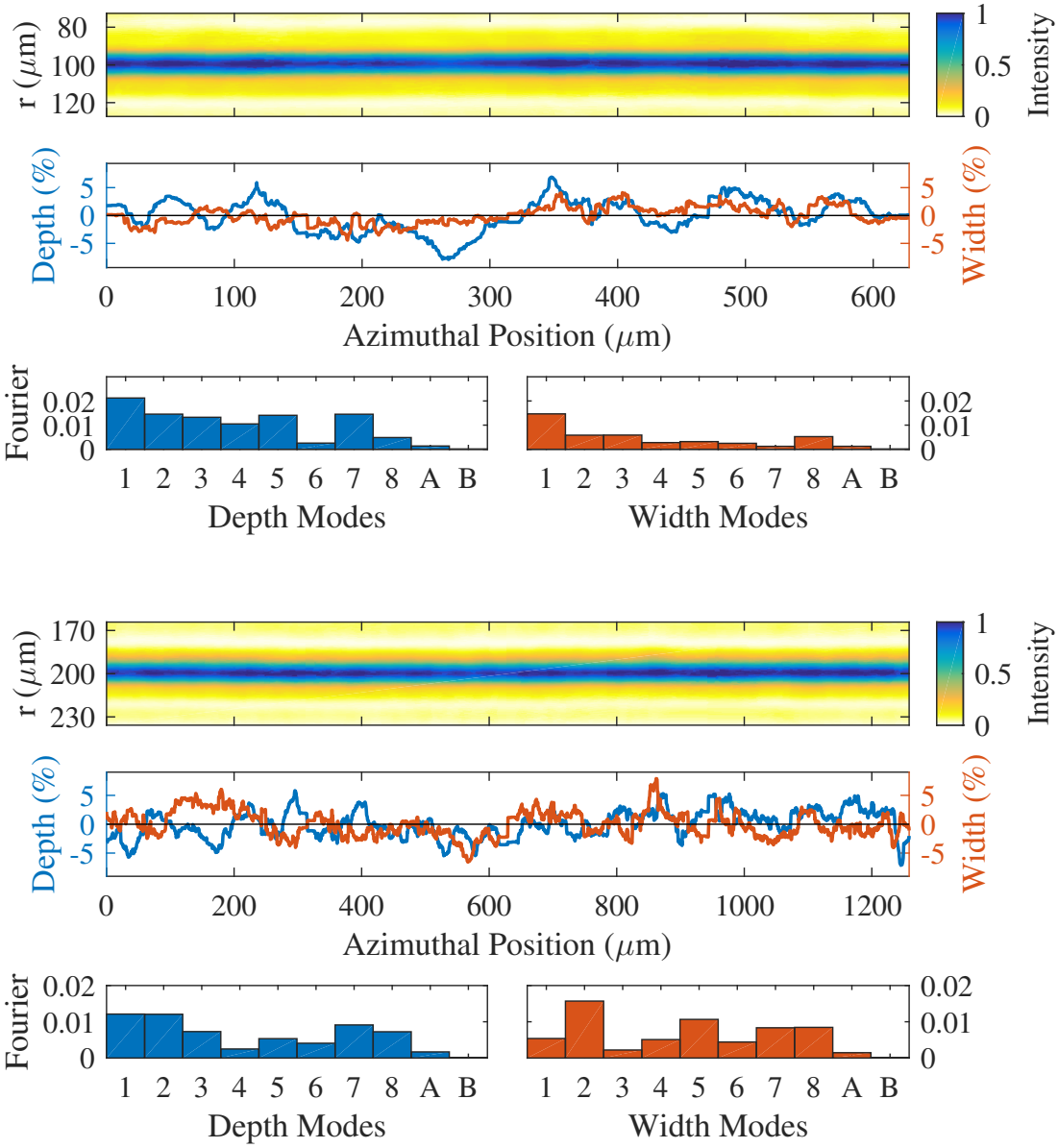

Figure 6.17: Analysis of variation in ring parameters for a 100 µm radius, 5 µm width ring with focal length 18.185 mm focal length, and the equivalent 200 µm radius ring. For each ring, the first line of data shows the unfolded ring, the second is the variation in trap depth (blue, left axis) and width (red, right axis) as a percentage of the average value, finally a bar chart of the dominant frequency components of trap depth and width is shown. More details are given in the text.

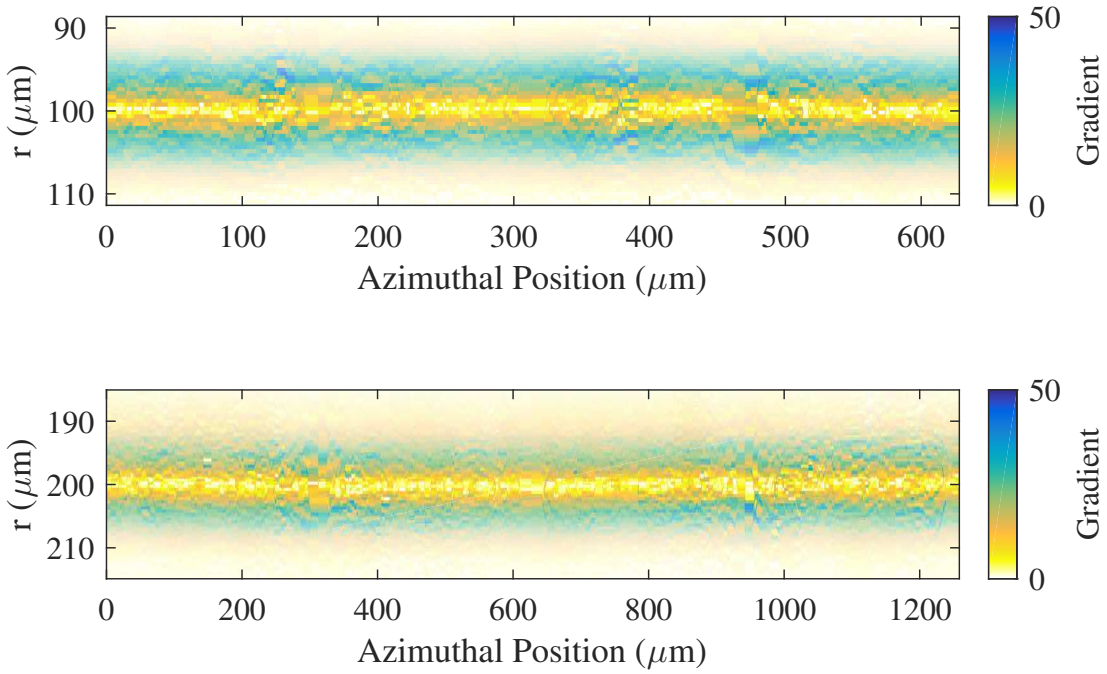

Figure 6.18: Map of gradient magnitude of the normalised intensity around the unfolded rings for a 100 µm radius, 5 µm width ring with focal length 18.185 mm, and the equivalent 200 µm radius ring. We note that the force experienced by the atoms is directly proportional to this gradient.

measurements constitute a worst-case scenario.

We can also show the roughness as a force by presenting the gradient of the measured intensity. This is shown in Fig. 6.18 for the same rings as presented in the Fourier analysis (with analysis for all rings being shown in the appendix in Fig. A.2). Here the gradient presented is the gradient of the normalised intensity as shown in the Fourier analysis, and thus demonstrates the relative force. The transparency of the gradient plot indicates the potential landscape. We can see that, close to the centre of the trap, the radial force felt by the atoms is close to zero with small fluctuations around the ring. However, we also notice some dislocations in the angular direction (if one isolates the angular contribution ($dU/d\phi$) to the gradient, these points show as vertical lines), these are thought to arise due to imperfections in the 'unfolding' routine used but it has not yet been possible to confirm this.

Design			Observed		Depth (μK)			ν_r (kHz)		
f (mm)	r (μm)	w (μm)	r (μm)	w (μm)	10 W	5 W	2 W	10 W	5 W	2 W
18.185	100	5	100	9.1	65.5	32.7	13.1	5.0	3.6	2.3
	100	10	100	14.1	42.3	21.1	8.5	2.0	1.4	0.9
	200	5	199	11.9	25.2	12.6	5.0	3.1	2.2	1.4
	200	10	203	14.8	19.8	9.9	4.0	1.4	1.0	0.6
	200	15	205	14.9	19.5	9.8	3.9	0.9	0.6	0.4
10	100	5	100	7.0	85.2	42.6	17.0	5.7	4.1	2.6
	200	5	199	8.8	34.0	17.0	6.8	3.6	2.6	1.6
	200	10	195	9.0	34.0	17.0	6.8	1.8	1.3	0.8
7	100	5	102	5.77	101.3	50.7	20.3	6.3	4.4	2.8
	200	5	197	6.15	49.2	24.6	9.8	4.4	3.1	2.0

Table 6.2: Trap parameters estimated from the measured ring dimensions (see table 6.1 for errors on the measured parameters). An efficiency of 30 % is used.

6.2.5 Expected Atom Behaviour in a Fresnel Hologram

From the characterisation detailed above we can use trap parameters and efficiency to estimate the trap frequency and depth of a ring achievable with various laser powers (2 W, 5 W and 10 W), using Eq. 2.32. The trapping parameters for the rings tested in this generation are shown in Tab. 6.2. An efficiency of 30 % is used as this is the lower bound established through observations (see Fig. 6.13).

In the ring potentials we expected scattering rates of the order 10^{-1} photons/s for illumination with 5 W. This is estimated using Eq. 2.29, with I_0 calculated using 30 % power efficiency and Eq. 7.6. The scattering rate scales as $1/(w_0 r_0)$.

6.3 Combination with a Spatial Light Modulator

Following simulated investigations into the possibility of hybrid FZP-SLM systems in Sec. 5.5, here we present preliminary results from the experimental implementation of such a system.

The optical layout used for the tests is shown in Fig. 6.19, with the SLM being accessed by flip-mirrors so that the original, basic zone plate imaging set up is undisturbed. We use a modified version of the optical set-up shown in [268] and the same algorithms for producing the incident beams generated by the SLM. The technique has been tested extensively within this and other publications.

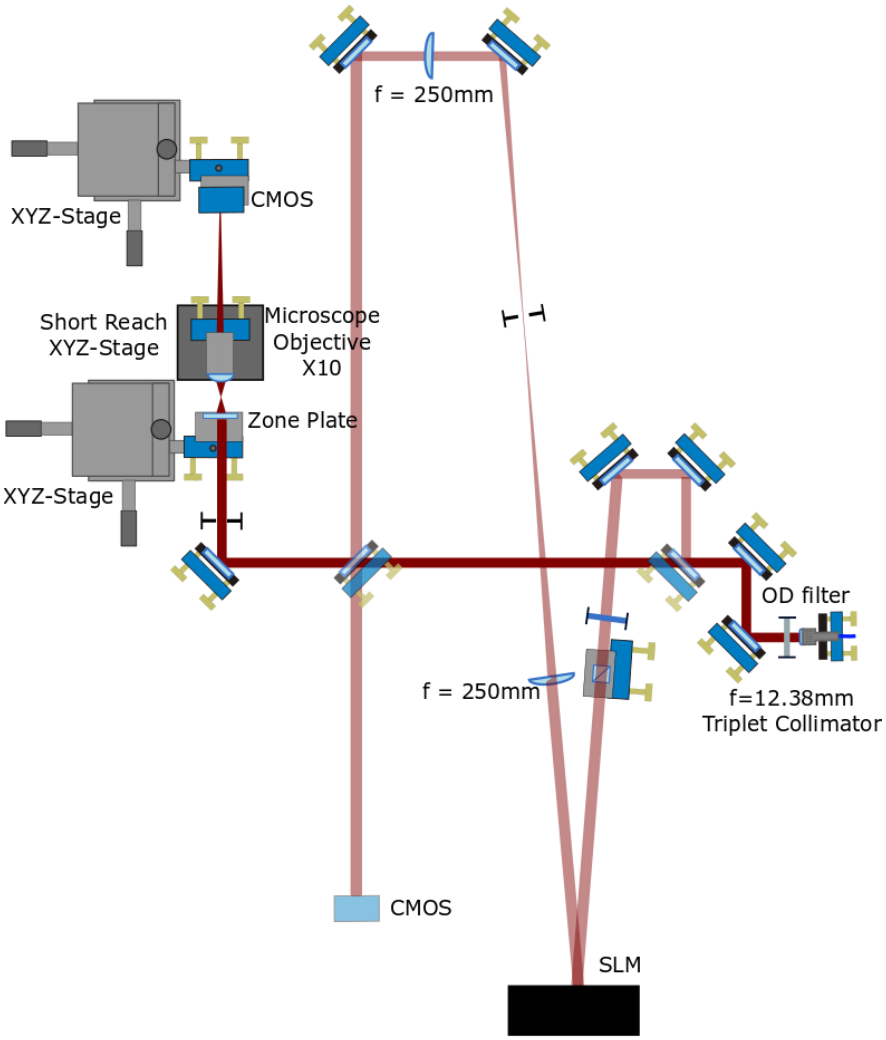

Figure 6.19: A schematic of the optical layout used to apply an SLM generated incident beam to a kinoform and then image it. Flip mirrors (shown as semi-transparent mirrors in the schematic) are used to switch between the hybrid and standard system and to include imaging of the SLM-modified beam without changing the system's alignment. Not to scale.

The optical system is modified to include an SLM by deflecting the beam from the main path with a flip mirror, then a series of mirrors align the beam with the SLM. Before reaching the SLM, the light's polarisation is cleaned and rotated (with a polarising beam splitter and a half waveplate) such that the correct orientation (horizontal) is incident on the active area of the SLM. The beam reflected off the SLM is passed through a 1-to-1 telescope formed by two 250 mm lenses with a pinhole at the focus (i.e. Fourier plane) to filter out additional diffraction orders. The light from the SLM is then incident on the zone plate a few Rayleigh lengths from the image plane of the SLM, meaning that less higher order noise should be present in the illuminating beams than if the zone plate was in the imaging plane [268]. The SLM used is a Hamamatsu X13138-03, which is a liquid crystal on silicon (LCOS) SLM. The screen has 1280×1024 pixels of size 12.5 µm, giving an effective area of 16 mm$\times$12.8 mm. We use the deformation correction pattern supplied by the manufacturers.

In order to demonstrate that we can use incident beams tailored by an SLM to modify the generated potentials, we applied a range of LG and HG modes to the 100 µm radius, 10 µm width, 18.185 mm focal length ring. The results of this are shown in Figs. 6.20 (for the full (normalised) intensity range) and 6.21 (showing the top 25 % of the intensity distribution). The patterns applied are as follows from (a-g): LG($\ell = 1, p = 0$) with a 400 µm waist, LG($\ell = 1, p = 0$) with a 500 µm waist, LG($\ell = 1, p = 0$) with a 700 µm waist, LG($\ell = 1, p = 0$) with a 900 µm waist, LG($\ell = 1, p = 0$) with a 1 mm waist, 300 µm waist Ferris wheel [120, 268] (the same superposition state used in Ref. [268]), and HG($m = 1, n = 1$) with a 600 µm waist. These waists were chosen so as to span the interval of $r_{LG}/r_{ring} = 2$ to 8 (where r_{LG} is the radius of the LG mode, see Eq. 2.7). Fig. 6.21e) shows the onset of the double ring features seen in Fig. 5.11 when the LG beam was larger than the ring radius (e.g. in first kinoform in Fig. 5.11 illuminated with an LG beam of $\ell = 1$ and $r_0/R = 10$).

We find that the use of an LG beam as an illuminator does not significantly modify the profile of the ring until the radius of the LG beam (Eq. 2.7) is significantly bigger than the radius of the ring (d and e in Figs. 6.20 and 6.21) at which point a faint double ring structure appears (this is most easily seen with the modified colour map in Fig. 6.21). The behaviour at smaller radius was expected as LG modes ($p = 0$) are similar in shape to ideal illumination. We note that these rings display significantly more roughness than the Gaussian illuminated rings, this is likely to be due to imperfect LG

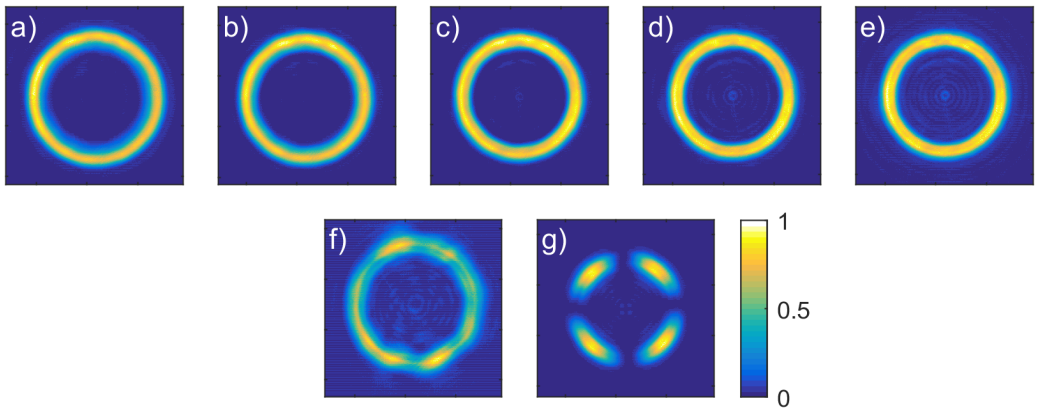

Figure 6.20: Images of the potentials resulting from the use of tailored incident potentials. Each pattern is normalised by its maximum value and is the central 900×900 pixels. The incident beams from a-g) are: 400 µm radius LG10, 500 µm radius LG10, 700 µm radius LG10, 900 µm radius LG10, 1 mm radius LG10, 300 µm radius Ferris wheel [120, 268], and 600 µm radius HG11.

mode creation with the SLM and the reduce amount of system optimisation completed. As expected, the Ferris wheel pattern (f) does not immediately translate into the ring structure. This is likely to be due to the larger radial width of the Ferris wheel (w.r.t. the other LG modes) and its complexity along with poor incident beam creation as we are using a small area of the SLM for experimental simplicity. The application of an HG$(m = 1, n = 1)$ beam (g) also shows some double-ring type structure, but more importantly, it allows us to examine the angular mapping of a modified incident beam. By rotating the HG beam (with the SLM), we can observe the lobes of the pattern also rotating with the same angular dependence, showing a 1-to-1 mapping in that sense.

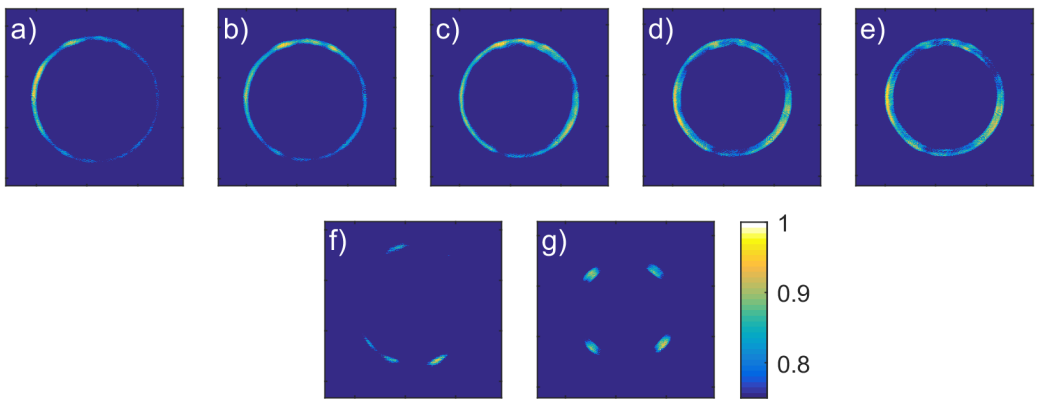

Figure 6.21: The same ring images as in Fig. 6.20 but with a modified colour map, showing the top 25 % of the intensity. This allows the emerging double ring structure to be seen more clearly in d) and e).

Chapter 7

Designing Second Generation Zone Plates

In this chapter, we present the theoretical and numerical details necessary to inform the design of the next generation of zone plates. This extends the numerical simulations presented in Chap. 5 using the lessons learnt from the optical characterisation in Chap. 6.

We begin, in Sec. 7.1, by numerically recreating some of the experimental results present in Chap. 6, concentrating on how trapping parameters change with design parameters (particularly the trap frequency/width in both the radial and axial directions). This allows us to determine which parameters we should change for a second generation of patterns.

Following this, we propose a different method for zone plate simulation which should allow us to simulate bigger areas with better resolution when considering limits to computing power. Sec. 7.2 begins by considering the role of evanescent waves in our simulations (an understanding of this is necessary to be able to design kinoforms with sub-wavelength resolution). We then discuss the use of Hankel transforms to model propagation in a cylindrically symmetric co-ordinate system in Sec. 7.2.2. This reduces the memory requirements of our design algorithm by reducing the 2D Cartesian system to a 1D cylindrical system.

At this point we can turn our attention to the decision of which potentials we would want to create with a new set of zone plates.

We propose a dark ring potential in Sec. 7.3 which would operate using light which is blue-detuned from the atomic transition, enabling trapping at a minimum of intensity, and so reducing photon scattering (see Sec. 2.2.8 for information about the benefits of blue-detuned dipole traps).

Finally, in Sec. 7.4, we build a numerical theoretical description for determining the best ring parameters to use considering the use of a Gaussian illumination beam.

7.1 Understanding Experimental Results

Within Chap. 6 (particularly Sec. 6.2.3), we discussed some ways in which the zone plates deviate from the design parameters, namely the mismatch between designed width and the achieved width. Using our existing simulation algorithms, we are able to produce a theoretical map of ring propagation – a numerical version of Figs. 6.9 and 6.10. These simulated maps are shown in Figs. 7.1 and 7.2 (the figures for all rings are shown in Fig. A.3). From the simulated intensity maps, we can estimate an expected ring width and radius. This is shown in Tab. 7.1.

From these figures and the table of simulated parameters, we can see the following:

- Experimental (Tab. 6.1) and simulated (Tab. 7.1) radial widths generally agree within experimental errors. The experimentally measured ring widths are slightly larger than their simulated equivalents. This is to be expected considering the experimental set-up constitutes a real-world scenario. For example, in the simulations, the kinoforms are illuminated with a perfect Gaussian beam of flat phase;

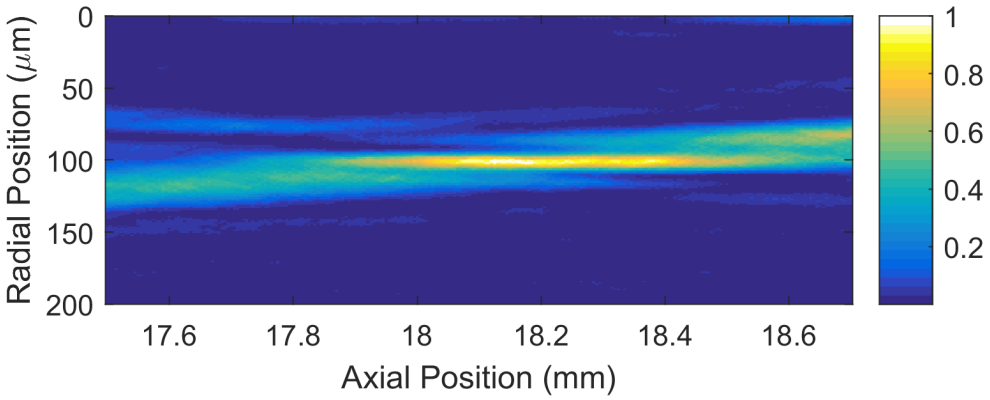

Figure 7.1: Simulated propagation of the radial profile of a 100 µm radius, 5 µm width ring, with a focal length of 18.185 mm through its focus.

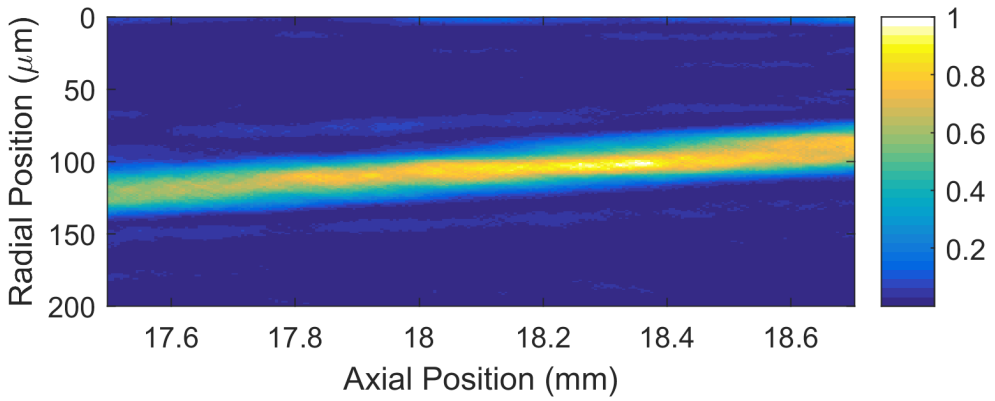

Figure 7.2: Propagation of the radial profile of a 100 µm radius, 10 µm width ring, with a focal length of 18.185 mm through its focus.

whereas, in the physical experiments, one cannot produce a completely collimated Gaussian beam and optics within the set-up will always introduce some sort of aberrations. Both data-sets show the same behaviour in comparison with the designed width.

- Experimental and simulation radii agree well.
- The position of the focal plane in the simulated data does not match the design. It was not possible to measure the position of the focal plane experimentally to a sufficient level of precision to compare these results. We note that we experimentally determine the position of the focal plane by the point of highest intensity.
- The wider the designed ring, the longer the simulated focal length appears to be, regardless of the measured simulation/experimental ring width. This is most clearly seen for the three 200 µm radius, 18.185 mm focal length rings, where ring widths of 5 µm, 10 µm and 15 µm yield focal lengths of 18.23 mm, 18.33 mm and 18.52 mm respectively. This is despite both the 10 µm and 15 µm widths having the same observed widths (14.8 µm experimentally and 13.5 µm numerically)

The resultant parameters of the rings are a balancing act between maintaining tighter axial focussing, achieving the desired focal length, and producing a ring of similar parameters to those desired. The ring radius and focal position have an obvious effect on the nature of the resultant potential, but the effects of the width are less

Design			Simulation		
Focal Length (mm)	Radius (μm)	Width (μm)	Radius (μm)	Width (μm)	f (mm)
18.185	100	5	101	7.5	18.170
	100	10	100	13.8	18.360
	200	5	201	8.7	18.230
	200	10	201	13.5	18.325
	200	15	203	13.5	18.515
10	100	5	100	6.1	10.060
	200	5	198	7.3	10.105
	200	10	199	7.3	10.220
7	100	5	100	5.2	7.030
	200	5	198	5.4	7.065

Table 7.1: Simulated parameters corresponding to the rings designed and manufactured. No errors are included for the width and radius as the data is simulated, however the error on focal plane position is estimated as 5 μm, which corresponds to a single step size in the axial direction.

easy to describe. Above a threshold width (which we assume to be equivalent to a diffraction limit, which is discussed in Sec. 6.2.3), the design width acts to increase the focal length of the ring rather than to change the width of the resultant potential. The higher the width, the looser the trap in the axial direction and the longer the focal length appears to be. Below the threshold width, the smaller design width acts to make the resultant width smaller but does not necessarily create a width matching that designed. At this point focal lengths are comparable with the designed value and the pattern has a tighter axial focus.

We could summarise by saying that, at large widths, the focal length of the pattern defines the actual width, whereas at small designed widths, a combination of the design width and focal length sets the actual ring width. This leads us to believe that the numerical aperture is defined by both the designed width and designed focal length.

7.2 Improving the Simulation Algorithm

To produce better zone plates, we want to be able to simulate with smaller pixel sizes (and with bigger areas to minimise aliasing originating from the finite simulation area). Decreasing the pixel size causes us two problems: very large arrays (the biggest array storable with 8 GB of RAM is $2^{12} \times 2^{12}$); and the handling of complex wave-vectors

(evanescent waves). In this section, we will discuss solutions to both of these problems.

7.2.1 Evanescent Waves

In order to simulate zone plates with pixel or feature size smaller than a wavelength, we need to be able to handle evanescent waves with our simulations.

An evanescent wave has a complex wave-vector. In the literature, this is typically encountered when light propagates through an medium in which the refractive index is complex or for light incident on a surface at an angle greater than the critical angle [279]. In both these cases, the wave can be considered as a combination of a propagating beam and an exponentially decaying, evanescent term. For the case of light incident on a surface, the propagating term travels along the interface, whereas the evanescent term is the electric field within the medium – i.e. it doesn't propagate in the medium.

In our vacuum propagation scenario, when the component of the wave-vector in the propagation direction (k_z) is complex, that part of the beam behaves as an evanescent wave. If we recall the equations for calculating propagation, Eq. 5.3, the propagation term (in k-space) is:

$$e^{ik_z z} = e^{i\sqrt{k^2-k_x^2-k_y^2}\,z} = e^{i\sqrt{k^2-k_r^2}\,z}\,, \tag{7.1}$$

for propagation of the beam by distance z in Cartesian or cylindrical co-ordinates. As one can easily see, k_z becomes imaginary when $k^2 < (k_x^2 + k_y^2)$ or equivalently $k < k_r$ (assuming that k, k_x, and k_y are real). The fast exponential decay of these evanescent waves means that they do not carry energy and so we can in effect remove them from our simulations by calculating only the real portion of k_z, and setting any complex components to zero. This approach works if we assume that our propagation distances are in the far-field.

7.2.2 Propagation of Cylindrically Symmetric Electric Fields

When creating and simulating zone plates, our computation power is limited by the size of the array which can be stored in the computer's RAM (and computation time). However, as we are now only considering potentials with cylindrical symmetry, we can significantly reduce the information stored by working in cylindrical co-ordinates,

allowing us to describe a ring using a vector of positions r rather than an array of positions x and y. This change of basis requires a modification of transforms and propagation techniques; the use of a Hankel transform rather than a Fourier Transform.

Hankel transforms and the quasi-discrete Hankel transform (the equivalent of the fast Fourier transform (FFT) that we use in Cartesian co-ordinates) has been treated in detail in literature [280–282]. They are the result of changing from the Cartesian co-ordinate system of the Fourier transform, to cylindrically symmetric co-ordinates, where $r^2 = x^2 + y^2$ and the pattern is independent of θ where $x = r\cos(\theta)$, $y = r\sin(\theta)$. As the function we're transforming (a ring or another cylindrically symmetric function) is not dependent on the angle, we can immediately integrate over it, resulting in the following equations for transforming between the electric field $E(r)$ and the angular spectrum $\mathcal{A}(k_r)$:

$$\mathcal{A}(k_r) = 2\pi \int_0^\infty E(r) J_0(2\pi k_r r) r dr \ , \tag{7.2}$$

$$E(r) = 2\pi \int_0^\infty \mathcal{A}(k_r) J_0(2\pi k_r r) k_r dk_r \ , \tag{7.3}$$

where J_0 is the 0-th order Bessel function of the first kind. These integrals are difficult to calculate due to the behaviour of Bessel functions and so are commonly computed through a quasi-discrete method as laid out in Ref. [280] and implemented in Ref. [281]. This approach simplifies the calculation by turning it from an integral over all space into matrix multiplication which uses an $N \times N$ transformation matrix to transform between position and spatial frequency N-dimensional bases. It effectively calculates the integral over the interval $0 \leq r \leq R_{\max}$, assuming that the electric field is zero outside of this interval.

Our simulations are based on MATLAB code sourced from Ref. [283] which uses the algorithm detailed in Ref. [281] with various modifications to improve computation speed and relevancy to our problems.

When using Hankel transforms ($\mathscr{H}$), Eq. 5.3 becomes:

$$\mathcal{E}^{(z)} = \mathscr{H}^{-1}\left[\mathcal{H}(z)\mathcal{A}^{(0)}\right] = \mathscr{H}^{-1}\left[e^{ik_z z}\mathscr{H}\left[\mathcal{E}^{(0)}\right]\right] \ , \tag{7.4}$$

where $k_z = \sqrt{k^2 - k_r^2}$ for $k > k_r$ and 0 otherwise. A comparison of this propagation method to Fourier propagation (Eq. 5.3) and the analytic solution for a Gaussian beam

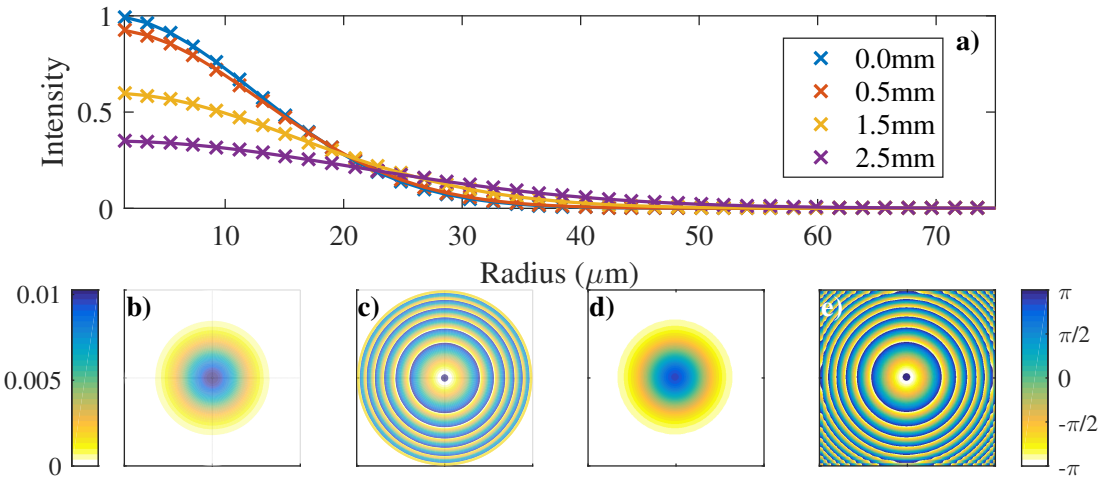

Figure 7.3: a) shows a comparison of the analytic result (lines) and the results of a Hankel transform calculation (crosses) of the propagation of a 25 µm $1/e^2$ waist Gaussian at a variety of distances. b) and c) show the intensity and phase of the same beam at a distance of 18 mm propagated using the Hankel transform. d) and e) show the same results calculated in Cartesian co-ordinates with Fourier transforms. The colour bar on the left shows intensity (W m^{-2}) for a beam with initial peak intensity of 1 W m^{-2}. Each plot in b-e) has an area of 1 mm^2.

(Eq. 2.2) is shown in Fig. 7.3. We note that when creating this figure, the Hankel method was 40 times faster than the Fourier method. In terms of memory usage, we are still limited by the computer RAM available. However, due to circular symmetry, the largest array used to generate a zone plate of $N \times N$ pixels will now only be $N/2 \times N/2$ as we only need to consider $r > 0$ rather than the full $-x_{\max} \leq x \leq x_{\max}$, hence increasing the maximum possible simulation size four-fold (to 2^{14} pixels, at the limit of our computing power). We only need to store one of these large matrices (the transform matrix) rather than multiples of it as in the Cartesian algorithm.

We note that the energy conservation of the transformation is dependent on the transformation matrix being unitary (that is $\mathscr{T}^T = \mathscr{T}^{-1}$). In our simulation code, the matrix is always unitary to within a tolerance (the tolerance being $\Sigma\left|\mathscr{T}^T - \mathscr{T}^{-1}\right|$), with this tolerance increasing with increasing number of pixels, the tolerance for: $N = 2^{14}$ is 4.7218×10^{-4}, $N = 2^{13}$ is 4.2377×10^{-5}, $N = 2^{12}$ is 3.7925×10^{-6}, $N = 2^{11}$ is 3.2565×10^{-7}. This leads us to carrying out additional benchmarking the Hankel transforms by monitoring optical power loss during propagation for a variety of different pixel sizes. This is shown in Fig. 7.4. We find that more power is lost for larger pixel sizes, but that this loss is of the order of the double-precision accuracy of

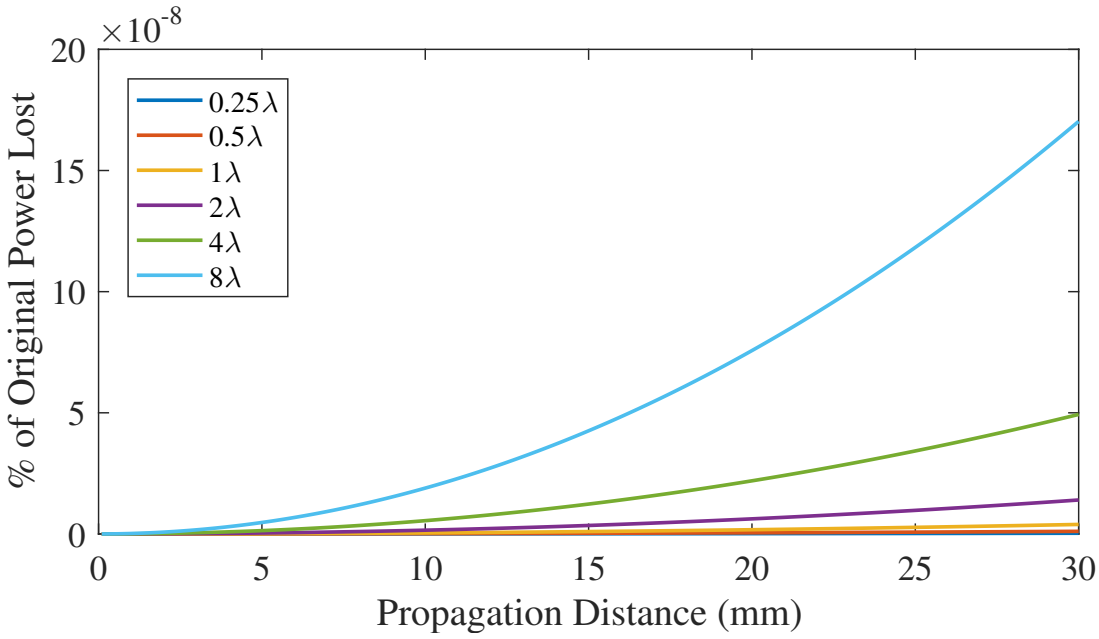

Figure 7.4: Power lost on propagation using the Hankel transform algorithm for different pixel sizes (with the legend showing the pixel sizes at multiples of the wavelength).

our MATLAB installation squared. We note that (for our particular installation) the accuracy of double-precision floats in MATLAB is limited to 2.2204×10^{-16} for values close to 1.

7.3 FZPs for Dark Rings

If we wish to create a dark ring potential, a ring in which atoms are trapped in a minimum of intensity, we must use blue-detuned light. This approach reduces photon scattering (and so increases trap lifetimes) as atoms are trapped in areas of low intensity. In this section, we will discuss a theoretical description of dark-ring potentials that we will use in the future for a second generation of zone plates.

In principle, a dark ring could be created using two concentric Gaussian rings, as used in previous chapters. However, here we would have a minimum of intensity rather than a zero of intensity. If we can create an electric field with a zero-crossing, this will give us a true zero of intensity by definition. Thus, we can write a potential for this shape by simply using the (normalised) derivative of the Gaussian rings used

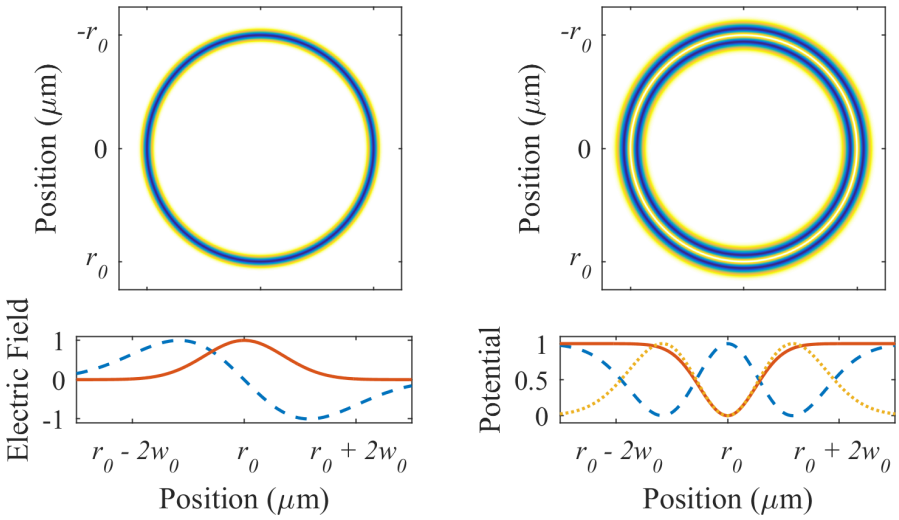

Figure 7.5: A comparison of dark and bright ring potentials. The top line shows the overall intensity distributions of two rings with equivalent widths and the same radii. Electric field close the radius of each ring is shown in the bottom left for light (solid red) and dark (dashed blue) rings. The equivalent potentials are shown on the bottom right, with a red-detuned light ring (solid red), red-detuned dark ring (dashed blue), and blue-detuned dark ring (dotted yellow).

previously:

$$E(r) = -E_0 \frac{\sqrt{2}(r - r_0)}{w_D} \exp\left(\frac{1}{2} - \frac{(r - r_0)^2}{w_D^2}\right), \tag{7.5}$$

where $w_D = w_0\sqrt{e}$ is the modified $1/e^2$ width. This modification allows direct comparison with light rings by generating rings with the same radial trapping angular frequency (i.e. that a dark ring with $w_D = w_0\sqrt{e}$ has the same radial trap frequency as a light ring with w_0). We note that the $\sqrt{2}$ factor at the front of Eq. 7.5 and the $1/2$ inside the exponential act to normalise electric field. The fields for dark and light rings are shown in Fig. 7.5, showing a zero-crossing in electric field for the dark ring.

To be able to draw useful comparisons between dark and light potentials, the trap parameters must be equivalent. We also must be able to make traps that are useful when using a reasonable illuminating power. To calculate the relevant trap depth and frequency, we must first calculate the maximum intensity ($I_0 = |E_0|^2$) in terms of the total power in a ring (P_0). For a light ring ($P_{0,\mathrm{light-ring}}$), integrating the intensity across

all space gives us:

$$P_{0,\mathrm{light-ring}} = \sqrt{2\pi^3} I_0 r_0 w_0 \ , \tag{7.6}$$

assuming that $r_0/w_0 >> 1$ such that the contributions to power from $\mathrm{erf}(\sqrt{2}r_0/w_0) \approx 1$ and $\exp(-2r_0^2/w_0^2) \approx 0$. Equivalently, and under the same assumptions (and using the same method), the total power in a dark ring $P_{0,\mathrm{dark-ring}}$ is given by,

$$P_{0,\mathrm{dark-ring}} = \sqrt{\frac{\pi^3}{2}} \mathrm{e} I_0 r_0 w_D \ , \tag{7.7}$$

We can then use Eq. 7.5, Eq. 7.6, Eq. 7.7, and Eq. 2.30 to determine the trap depth, as we did for a tightly focused Gaussian in Eq. 2.32:

$$U_{\text{dip,light-ring}}(r) = -\frac{\bar{U} P_{0,\mathrm{ring}}}{\sqrt{2\pi^3} r_0 w_0} \exp\left(-\frac{2(r-r_0)^2}{w_0^2}\right) \ , \tag{7.8}$$

$$U_{\text{dip,dark-ring}}(r) = \frac{4\bar{U} P_{0,\mathrm{dark-ring}} (r-r_0)^2}{\sqrt{2\pi^3} r_0 w_D^3} \exp\left(-\frac{2(r-r_0)^2}{w_0^2}\right) \ , \tag{7.9}$$

where $\bar{U}$ is the prefactor to $I(r)$ in Eq. 2.30. For both rings, the trap depth easily follows as the prefactors to the r dependent terms, ignoring the normalisation terms included in the dark ring electric field (Eq. 7.5):

$$U_{0,\mathrm{light}} = \frac{\bar{U} P_0}{\sqrt{2\pi^3} r_0 w_0} \ , \quad U_{0,\mathrm{dark}} = \frac{2\bar{U} P_0}{\mathrm{e}\sqrt{2\pi^3} r_0 w_D} \ . \tag{7.10}$$

Trap frequency can then be calculated by inserting Eq. 7.10 into Eq. 2.34. A light ring has the same relation between trap width/depth and trap frequency as a focussing Gaussian, but the dark ring has the following trap frequency:

$$\omega_r = \sqrt{\frac{4U_0 \mathrm{e}}{m w_0^2}} \ . \tag{7.11}$$

Clearly the trap depths (and frequencies) of a dark or light ring would be different if we used the same width and radius. However, we can set them to be the same, by solving the simultaneous equations and equating trap depth and frequency between the two types of rings. To create a dark ring equivalent to a light ring, we would require $w_D = w_0\sqrt{e}$ and $P_{0,\mathrm{dark-ring}} = P_{0,\mathrm{light-ring}}\sqrt{\mathrm{e}}/2$.

7.4 Selecting Ideal Zone Plate Parameters

In addition to improving our design algorithms and considering new potentials, we also want to create some patterns similar to existing rings, but with more well chosen parameters (focal length, trap width and ring radius). Carefully considering trap parameters may allow us to correct or better understand some problems outlined in Chap. 6 such as diffractive effects reducing the axial trap frequency and the mismatch of design and experimental potential width.

To do this we split the investigation into two parts. The first focusses on the focal length and how it changes the propagation behaviour, and the second investigates how well the design parameters are reproduced in the resulting potential.

7.4.1 Focal Length

In Tab. 1.2, Tab. 7.1 and the corresponding propagation maps in Figs. 6.9, 6.10, 7.1, and 7.2 we see that changing the focal length of the zone plate effects the radial and axial trap widths, and changes the qualitative shape of the focus.

To try to understand how and why this is happening, we'll approximate the system in different ways. First we approximate the ring as a circle of individual Gaussian foci which each propagate as typically expected. This gives us an intuitive, but very naïve way of picturing the system as overlapping wavefronts where phase 'information' is lost at the overlap. We add complexity to this model by comparing the ideal illumination intensity distribution to the actual illumination and consider the intensity 'information' loss by using non-ideal illumination. We then create a full theoretical description by considering the 'information' loss by calculating the full overlap (or correlation) integral for the ideal and experimental electric fields.

Avoiding Overlap - a ring approximated by many Gaussian spots

When we design zone plates, we take the desired electric field and propagate is back to where the zone plate will be located, and use the phase information here to create the zone plate. In Sec. 5.3, to intuitively understand some results, we imagined wavefronts emanating from waveguides like the magnetic field lines around a wire to describe phase fronts 'emanating' from a waveguide. This approach can be extended and made more physical by considering behaviour we already know about the propa-

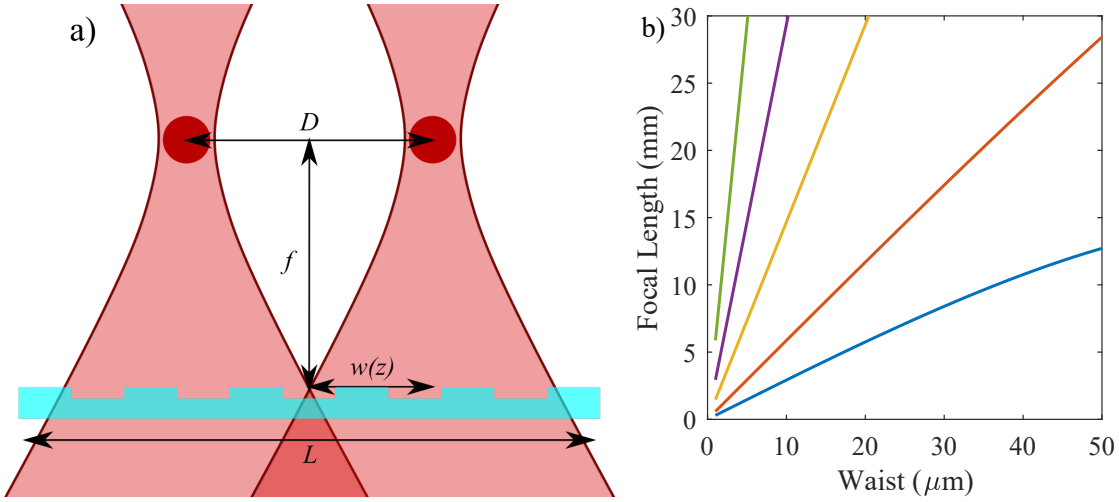

Figure 7.6: (a) The overlap of the wavefronts from each side of the ring determines the maximum focal length of zone plate which obeys Gaussian optics. (b) The maximum focal lengths for different potential waists are shown for rings of radius 100 µm (blue), 200 µm (red), 500 µm (yellow), 1 mm (purple), and 2 mm (green).

gation of light. We could approximate a ring-shaped waveguide as a line of individual Gaussian foci which superimpose with one another such that the propagation behaves according to Eqs. 2.2 and 2.3 in the radial direction, and is cylindrically symmetric. A 2D schematic of this for a ring with width w_0 and diameter $D = 2r_0$, is shown in Fig. 7.6.

By considering the size of the beam to be the $1/e^2$ radius ($w(z)$), the focal length at which light from either side of the ring begins to overlap is given by $w(f) = r_0 = D/2$. Rearranging this gives a maximum focal length (without overlap) in terms of the ring radius and $1/e^2$ waist:

$$f_{\max} = \frac{\pi w_0^2}{\lambda}\sqrt{\frac{r_0^2}{w_0^2} - 1}\,. \tag{7.12}$$

The dependence of this maximum focal length on the width of the ring is plotted for a variety of different radii in Fig. 7.6b. We can see that the 100 µm and 200 µm radius rings used in Chap. 6 have focal lengths much larger than this requirement. Since the zone plates have been shown to work well in this regime, it's clear that this extremely simplistic model doesn't accurately describe what is happening, this is unsurprising considering the assumptions made.

We also note that this method also allows us to define a minimum zone plate size (edge length L), such that the field from the ring is not larger than the plate. In

general, this means that the zone plate must have $L > D + 2w(f)$ or equivalently $L/2 > r_0 + w(f)$. At the the maximum focal length, defined above, this gives is $L > 4r_0$.

Approximating phase knowledge loss - a ring approximated by many Gaussian spots

In Sec. 5.3, we talked about the aberrations in patterns being due to information loss. We call this information loss as we are losing knowledge about the electric field when we illuminate with a Gaussian and when we round phase.

Using the approximation detailed above, if we consider the information lost through beam overlap to be proportional to the power contained in the overlapping region, we can attempt to quantify this information loss. In a simplistic approximation, the proportion of the power which crosses the centre of zone plate can be assumed to be proportional to the knowledge lost. The integral defining the power contained between two points (r_a and r_b) on a 1D Gaussian centred on the origin is given by

$$\int_{r_a}^{r_b} I dr = I_0 \left(\frac{w_0}{w(z)}\right)^2 \frac{w(z)}{2}\sqrt{\frac{\pi}{2}}\left[erf\left(\frac{\sqrt{2}r}{w(z)}\right)\right]_{r_a}^{r_b}. \tag{7.13}$$

For the overlap region, we calculate $P_0 - \int_0^{L/2} I dr$ and divide this by the total power P_0. This is shown in Fig. 7.7 for the rings demonstrated in generation 1. We can see that the information loss plateaus at 50 % as we are assuming that the overlap does not reduce information outside of the radius of the ring. So, as long as the zone plate has $L > 4w(f)$, at least half of the information always remains. In reality, interference means that information is not completely 'lost' from light 'crossing' the centre line, but it does make the resulting diffraction less efficient and can lead to the centrally peaked aberration we see in the experimental rings produced.

Intensity Overlap

In the model that describes Fig. 7.7, the so-called information loss is imagined as being due to the washing out of phase information when beams overlap. It doesn't take into account the mismatch between the field used to illuminate the zone plates and the ideal illumination intensity.

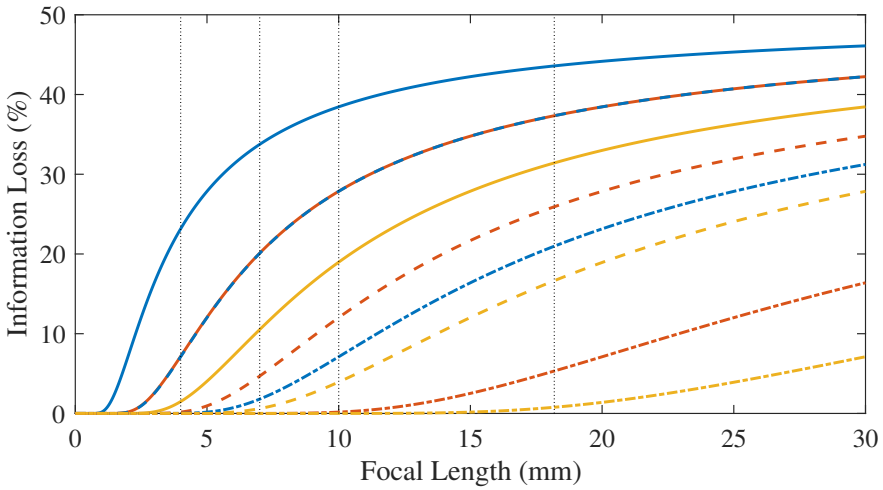

Figure 7.7: Information lost into the overlapping region as a function of focal length. This done for rings of varying widths: 5 µm blue, 10 µm red, and 15 µm yellow; and varying radii: 100 µm solid lines, 200 µm dashed lines, and 500 µm dashed-dot lines. The vertical dotted lines denoted the focal length utilised.

We can calculate this by calculating the overlap between the power normalised intensity distributions: $2\pi \int_0^\infty \min(\tilde{I}_{\text{ideal}}, \tilde{I}_{\text{illum.}}) r dr$, these results are shown in Fig. 7.8.

These results suggest that, for short focal lengths, a Gaussian isn't a good approximation for the ring's intensity distribution at the zone plate. However, as one would expect, the Gaussian becomes a better approximation at longer focal lengths. This improvement plateaus at certain focal length (which is shorter for smaller w_0/r_0). The reasoning for this plateauing is difficult to understand and may not be important once we include phase in our calculations, as is done the following section.

Electric Field Overlap

Figs. 7.7 and 7.8 give us a way to intuitively see the mechanisms for knowledge loss in the system, but to determine the most appropriate focal lengths, we need to combine these two methods.

We do this by computing the overlaps of electric fields, which can then be decomposed into real and complex parts to represent to the intensity and phase mismatch. The overlap power (P_{overlap}) of two power normalised electric fields, $\tilde{E}_1$ and $\tilde{E}_2$ is given by

$$P_{\text{overlap}} = 2\pi \int_0^\infty \tilde{E}_1^* \tilde{E}_2 r dr \, . \tag{7.14}$$

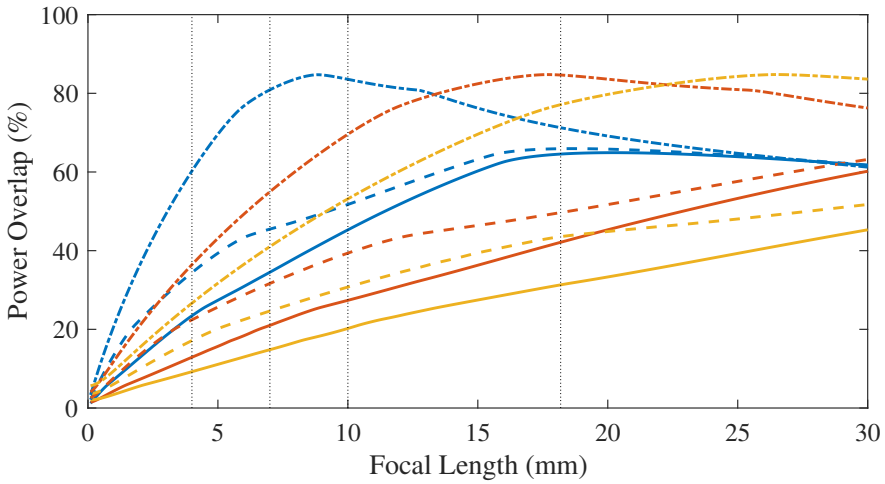

Figure 7.8: The mismatch between the illumination intensity distribution and the ideal intensity distribution as a function of focal length. This done for rings of varying widths: 5 µm blue, 10 µm red, and 15 µm yellow; and varying radii: 100 µm solid lines, 200 µm dashed lines, and 500 µm dashed-dot lines. The vertical dotted lines denoted the focal length utilised.

Before calculation of the integral, we normalise each electric field by power, such that we only examine the similarity of the shapes rather than considering the actual efficiency of the hologram. We can use this integral to compare two sets of electric fields, the input beams and the output beams. The overlap of the input beams, is the overlap between the illumination field multiplied by the phase contribution of the zone plate, and the ideal field (as calculated by back-propagating the ring). This could be represented by $E_{\text{illum.}} \exp(-i\phi_{\text{ZP}})$ and E_{ideal}. The overlap of the output beams, is the overlap between the target potential and the simulated expected potential ($E_{\text{targ.}}$ and $E_{\text{sim.}}$). We find that the input and output overlaps are the same. This is unsurprising as there is no additional field modification down stream of the zone plate. The input overlap is shown in Fig. 7.9, with the equivalent for a higher (10-bit) depth zone plate shown in Fig. 7.10.

The first thing we notice in the overlap plots is that, in the case of a binary zone plate, we see regular oscillations that disappear when the bit-depth of the zone plate is increased. On further investigation, we find that this disappearance is gradual. A Fourier transform of the oscillations is shown in Fig. 7.11. The oscillations occur with a dominant frequency (period) of 833.3 m^{-1} (1.2 mm). The frequency components are independent of trap parameters and the period of the oscillations are not obviously

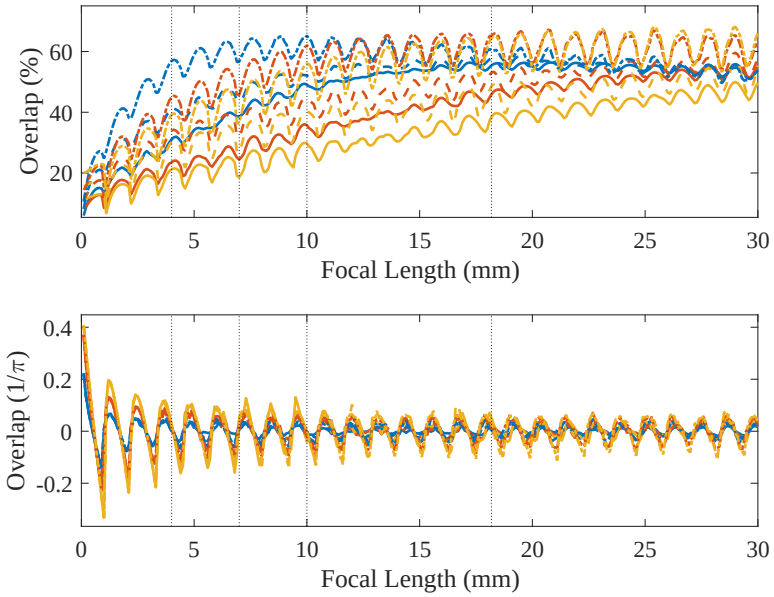

Figure 7.9: Overlap between the ideal and actual electric fields in the plane of a binary zone plate plotted as a function of focal length. The overlap is split into intensity (top) and phase components (bottom plot oscillating about zero). This done for rings of varying widths: 5 µm blue, 10 µm red, and 15 µm yellow; and varying radii: 100 µm solid lines, 200 µm dashed lines, and 500 µm dashed-dot lines. The vertical dotted lines denoted the focal length utilised in Gen1.

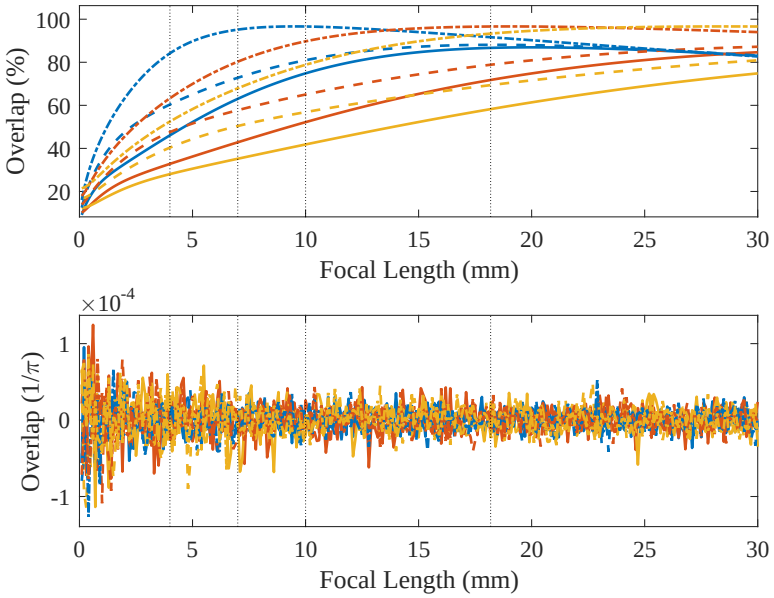

Figure 7.10: Overlap between the ideal and actual electric fields in the plane of the zone plate plotted as a function of focal length for a zone plate with 10-bit phase resolution. The colours and styles are as previously described.

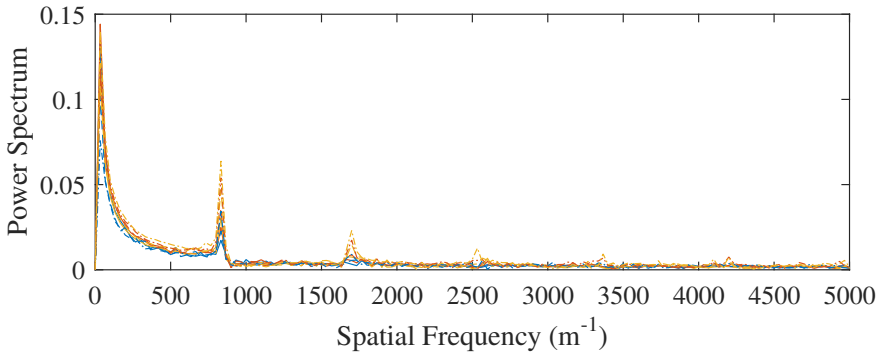

Figure 7.11: Fourier analysis of oscillations in overlap as focal length is increased. This done for rings of varying widths: 5 µm blue, 10 µm red, and 15 µm yellow; and varying radii: 100 µm solid lines, 200 µm dashed lines, and 500 µm dashed-dot lines.

related to the simulation size (8 mm) or wavelength. This leads us to believe that its origin relates to the phase rounding process, but as of yet we are unsure of its exact source. This may explain some of the aliasing between adjacent pixels in the RMS error plots of Figs. 5.5 and 5.6.

The general trend of the overlap is consistent between the binary and 10-bit phase depth scenarios, meaning that we can assume it results from intensity mismatch and possibly long scale phase mismatch. Overall trends are most clearly seen in the high phase depth plot, with the overlap either peaking at a medium focal length (as is the case for the 5 µm width rings) or slowly increasing before plateauing for the larger width rings. These general trends mean that we wouldn't expect to gain a significant amount of information by choosing focal lengths more carefully, but we should examine the effect of focal length on the accuracy of the top of the trap in order to determine usefulness for atom traps. This is shown in Fig. 7.12.

In the case of examining the shape overlap of electric fields located in the brightest 20% of the target pattern (Fig. 7.12), we first notice that the oscillation for binary patterns are less pronounced. When comparing the general trends in overlap between Fig. 7.10 and Fig. 7.12 we see that, rather than the smooth plateauing seen when looking at the full field overlap, we see a rapid increase in overlap at small focal length, which then drops for medium focal lengths and increases to a plateaued value at longer focal lengths (typically plateauing either above or at the same value as the original peak). The rate of change of overlap, location of the initial peak and the distance over which the overlap plateaus is mainly dependent on trap width but is also influenced to

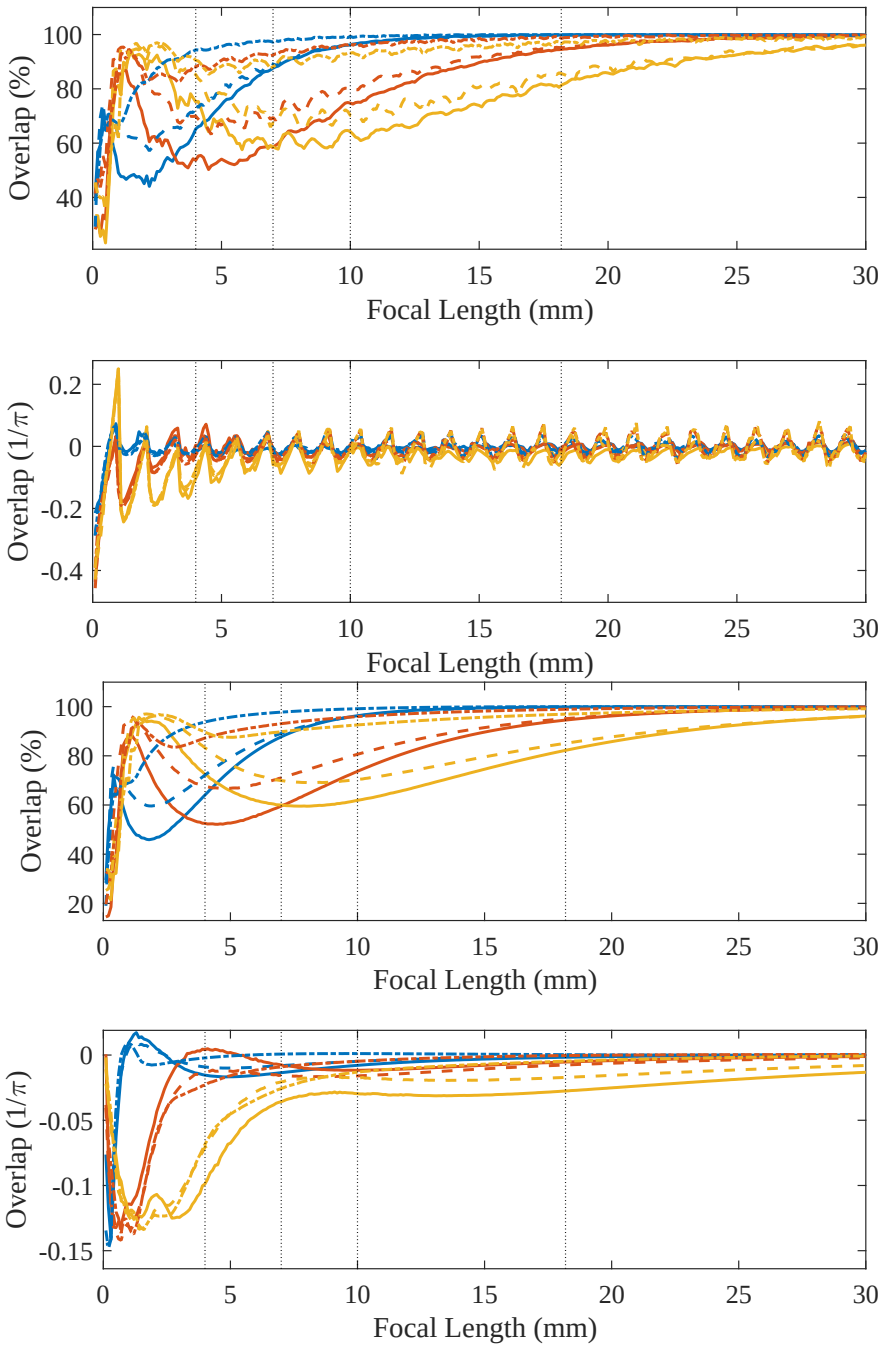

Figure 7.12: Overlap between the brightest 20% of the ideal and actual electric fields in the plane of the potential plotted as a function of focal length for a zone plate with binary (10-bit) phase resolution at the top (bottom). The overlap is split into intensity (top) and phase components (bottom plot oscillating about zero). This done for rings of varying widths: 5 µm blue, 10 µm red, and 15 µm yellow; and varying radii: 100 µm solid lines, 200 µm dashed lines, and 500 µm dashed-dot lines. The vertical dotted lines denoted the focal length utilised in Gen1.

a lesser extent by the radius of the ring. The initial peaks in overlap percentage are of similar values to the ideal maximum focal length in linear propagation predicted in Fig. 7.6, suggesting that these initial peaks are the ideal focal length for propagation without extra diffractive features (i.e. propagation that most resembles an ordinary focussing Gaussian). These diffractive features (such as the 'shoulders' seen in experimental results in Chap. 6) become more dominant at focal lengths in the plateaued region. To summarise these trends, we can see that our choice of a focal length of 18.185 mm sits at a point where narrow rings are expected to be well reproduced in terms of shape.

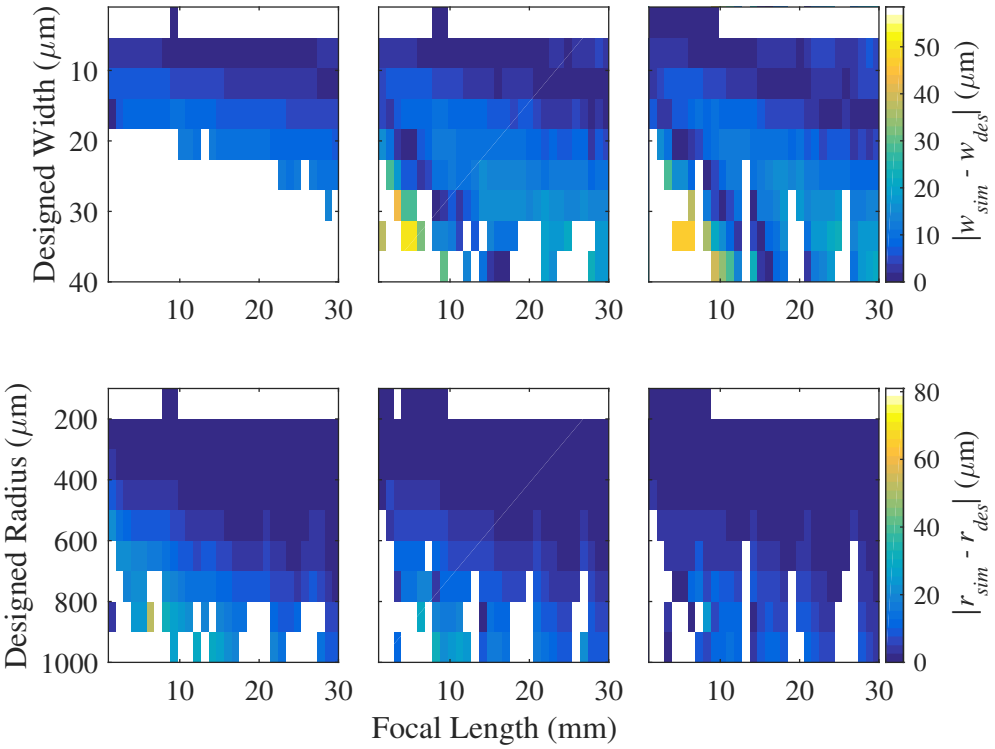

Figure 7.13: The absolute difference between the design (r_{des} and w_{des}) and predicted (r_{sim} and w_{sim}) trap parameters presented as a function of focal length and designed trap width (1st row) or designed trap radius (2nd row) for radii (widths) 100 µm, 200 µm and 500 µm (5 µm, 10 µm and 15 µm) in the columns from left to right. Here we simulate a zone plate with binary phase.

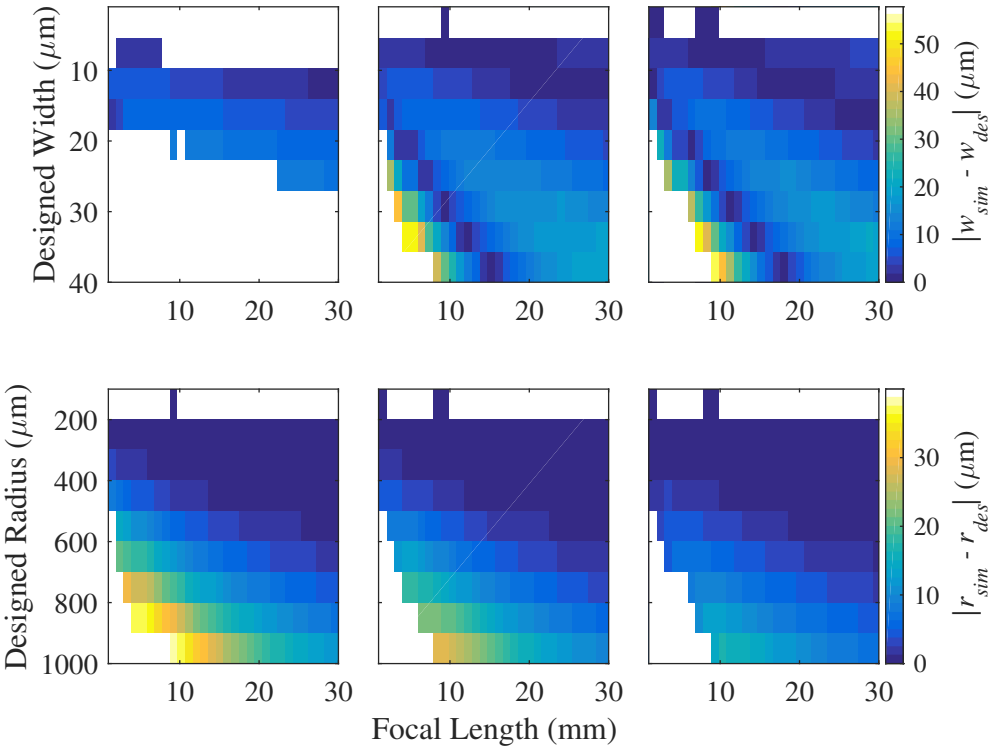

Figure 7.14: The absolute difference between the design (r_{des} and w_{des}) and predicted (r_{sim} and w_{sim}) trap parameters presented as a function of focal length and trap width (1st row) or trap radius (2nd row) for radii (widths) 100 µm, 200 µm and 500 µm (5 µm, 10 µm and 15 µm) in the columns from left to right. Here we simulate a zone plate with 10-bit phase.

7.4.2 Parameter Reproduction

We can simulate the expected output patterns for the zone plates designed to the same parameters as shown in Figs. 7.7 and 7.8 for illumination with a 1 mm $1/e^2$ waist Gaussian. These can then be fitted to a Gaussian ring (as done in the analysis of Chap. 6) in order to determine the difference between input and output parameters when designing different rings at different focal lengths. The results of this process are shown in Figs. 7.13 and 7.14.

In Figs. 7.13 and 7.14, we can see that, in the case of $w_0 \ll r_0$, the ability of a zone plate to produce a ring of a particular radius is independent of the focal length of the zone plate. This can be seen in the areas close to zero in the upper right corner of the plots of focal length against radius (bottom rows of both figures). On the other hand,

the ability to reproduce a width is clearly very dependent on the choice of focal length.

We see that for a 10-bit zone plate, the mismatch is minimised for a focal length of the order of a few Rayleigh lengths, and again at longer focal lengths. The benefits of choosing a longer focal length are particularly strong for a binary zone plate as the initial minima (seen as a dark stripe in the top line of Fig. 7.13 compared to white areas in Fig. 7.13) is often obscured by poor shape matching (the missing data corresponds to points which could not be fitted).

It is of note that, for shorter focal lengths, the simulation does not yield reliable and consistently characterisable rings (as shown by missing data corresponding to nan results in the fitting algorithm). This could occur for a combination of reasons. Firstly, at short focal lengths, the numerical aperture of the system is such that a very narrow focus is produced (of only a few simulation pixels in size), meaning that the peak is hard to fit. This observation is backed up by noting that the simulated width is much smaller than the designed width at smaller focal lengths. Secondly, in order to reproduce the target pattern, there needs to be sufficient distance for light to diffract/interfere such that the illumination intensity changes from a Gaussian beam to the ring shape desired. We can also see this as poor intensity overlap, as was seen in Figs. 7.9, 7.10, and 7.12

We can also see that we should be able to create a much larger radius rings (here we have shown up to 500 µm radius) at realistic focal lengths. Wider rings should also be possible if the focal length of the ring is carefully chosen (we can see this in the dark diagonal stripe in the bottom left of the width plots of Figs. 7.13 and 7.14. We expect it to be easier to load atoms into the wider traps and note that existing successful ring traps (Sec. 1.4.2) are much wider than those tested in Chap. 6.

7.4.3 Summary of Parameter Choice

In summary, the investigations above show that the choice of focal length depends mainly on the desired trap width and the axial confinement required. In reality, experimental practicality is likely to be a more dominant factor in choices, as we can select a kinoform based on the simulated output width.

If one wants to operate outside of a vacuum chamber (so with a long focal length), then the longer the focal length the better. For narrow width traps, the regime of linear propagation is too small to be practical and may be too close to the zone plate for use with non-ideal illumination. Therefore one should use a longer focal length. If linear

propagation of the ring is required (rather than it only occurring close to the focus), then one should use the maximum ideal focal length detailed in Fig. 7.6. A value close to this maximum ideal focal length should be used for all patterns if the focal length obtained is practical.

We expect to be able to produce wider width rings successfully. Though this will need fine-tuned selection of zone plate parameters to ensure suitable reproduction. For these wider rings, we have simulated that the choice of focal length is much more important than for narrow widths (Figs. 7.13 and 7.14).

Sec. 7.1 shows that, if tight axial confinement is required, then one should aim to use a narrow ring width and as short a focal length as is practical. This would also yield tight radial confinement, so is not necessarily compatible with typical BEC sizes. Therefore, we expect a light sheet or other axial confinement tool to be used with the next generation of zone plates generated rings.

Chapter 8

Conclusion and Outlook

8.1 Summary

In chapter 1 we began by introducing the motivations of the work within this thesis: improving inertial sensing via the use of a compact atom interferometer. Atom interferometers have the potential to revolutionise inertial measurements by offering high per particle sensitivity in a system with far greater stability than existing light interferometers. This is a hard problem, particularly with a view towards creating a compact sensor which would be practical for field use. One way to reduce the size of an atom interferometry experiment is to guide the atoms. We propose and investigate Fresnel holography as a method to produced ring-shaped optical waveguides.

8.1.1 Building a BEC Machine

The biggest step towards creating an atom interferometer is building a cold atom or BEC machine. The theory of the cooling and control techniques needed to create one of these machines was presented in chapter 2. In chapter 3, the current progress towards designing and building this new experiment was detailed. At the time of writing, we have successfully created a 2D+ MOT which loads a 3D MOT.

A thorough understanding of BEC behaviour is crucial to creating a BEC-based atom interferometer and to successfully designing a waveguide. In chapter 4 this behaviour was theoretically described, beginning generally with the Gross-Pitaevskii equation, before applying the Thomas-Fermi limit to approximate a BEC in a harmonic

potential. This theory was then utilised for scenarios relevant to our experiment, such as behaviour in ring potentials and how density measurements can be used to calculate temperature and infer the existence of phase fluctuations. This chapter ended with the presentation of investigations from an existing BEC experiment, where I started my PhD. We observed density fluctuations which result from phase fluctuations in a quasi-1D BEC. We have not yet been able to explain the strongly periodic nature of the fluctuations observed using existing fluctuation models.

8.1.2 Fresnel Zone Plate Holographic Waveguides

The second half of the thesis dealt with holographic waveguides intended for use in conjunction with the ultracold atom experiment.

The theory pertaining to Fresnel zone plates was presented in chapter 5 alongside the comparative simulations contained within Ref. [123]. Our numerical simulations compared Fresnel zone plates (binary phase depth and wavelength pixel size) to typical SLM kinoforms (8-bit phase and a typical pixel size of 12 µm). This effectively determines whether spatial or phase resolution is more important for kinoforms when operated in a lensless Fresnel regime.

We confirmed that spatial resolution is much more critical than bit-depth, particularly in situations where Gaussian or plane-wave illumination is used rather than a tailored beam intensity profile. We note that a small increase of bit-depth for a zone plate would improve the holograms significantly. FZPs consistently showed an improved root mean square error compared to an SLM style kinoform, with this advantage increasing for more complex target intensity distributions. The simulations also demonstrated 3D mapping of the focus of these patterns, showing the potential for (weak) axial trapping.

Significantly extending upon published results [123], we also demonstrated that one could theoretically produce rings with phase winding, by either illuminating a ring zone plate with an LG beam, or by other tailoring of the incident electric field.

Twenty four Fresnel zone plates, in a variety of geometries, were manufactured and optically tested in chapter 6. We used a variety of rings and other atomtronic-type potentials (such as Y-junctions), with the ring potentials showing the most promising

results.

The rings were then analysed to determine their trapping parameters and the smoothness of the trap. The rings were reproduced without observable ellipticity, and radii corresponding to the design parameters. Imperfect illumination (a 1 mm $1/e^2$ radius Gaussian) and numerical aperture limits the widths of the rings produced, though these are of an order expected when estimating the numerical aperture of the system.

We were able to make benchmarking measurements of the quality (smoothness) of the rings. All rings had a root mean squared error of between 3 % and 5 %, corresponding to an upper limit on the roughness we expect to be experienced by atoms in the potential. This is expected to be compatible with atom trapping and guiding. Trap parameters ($1/e^2$ radius, trap depth and radii of the rings) varied by a maximum of 10 % peak-to-peak, with the dominant variation occurring in the first few azimuthal modes, meaning that they are slowly varying. The benchmarking is limited by aberrations inherent to the imaging system and by the analysis algorithms involved in converting from Cartesian to polar co-ordinates.

The illuminating electric field was modulated using a SLM as an experimental proof-of-principle demonstration of a hybrid SLM-FZP system.

In chapter 7 we detailed the theoretical considerations for designing a second generation of zone plate kinoforms. Here we further investigated the axial propagation of our existing kinoforms through numerical simulations. This confirmed our observations about the limits on ring width related to numerical aperture.

We then improved our design and simulation algorithm by extending it to sub-wavelength pixel sizes and larger simulation areas. This required an understanding of the role of evanescent waves for this type of kinoform. For cylindrically symmetric target distributions such as rings, the use of a Hankel transform was demonstrated to reduce the computation power required for kinoform design.

A dark ring, which in an experiment would utilise blue-detuned light to trap atoms in intensity minima, was investigated theoretically and the corresponding trap parameters were calculated. The numerical analysis will allow these potentials to be directly compared to bright rings (red-detuned) in future experiments.

In the final section, we explored the parameter space of rings that are producible using Fresnel zone plate kinoforms. Here we concluded that, for the narrow ring widths used in the first FZPs, long focal lengths reproduce the designed width most accurately,

though a narrow range of small focal length could also reproduce these rings well. We also showed that wider rings would be possible if the focal length is carefully selected. This increases the range of possible applications of these kinoforms by allowing us to obtain a range of radial trap frequencies.

8.2 Outlook

The future of the experiment is very promising. We hope to reach BEC within the next months. Work pertaining to the use of zone plates for atom trapping is ongoing. Current work is focussed on methods to operate a zone plate potentials and imaging co-axially; this is likely to require relaying of the potentials with a low-aberration lens.

Once BEC is reached, work will turn to loading atoms into the ring potentials and studying the trapping parameters. We can then implement interferometry beams equivalent to those used in Refs. [8–10].

It is hoped that a second generation of kinoforms will be manufactured shortly. We plan to expand on our capabilities by generating larger radius rings, larger width rings, and kinoforms suitable for creating blue-detuned dark rings (using a different wavelength).

Bibliography

[1] K. U. Schreiber and J.-P. R. Wells, *Invited Review Article: Large ring lasers for rotation sensing*, Review of Scientific Instruments **84**, 041101 (2013).

[2] B. Barrett *et al.*, *The Sagnac effect: 20 years of development in matter-wave interferometry*, Comptes Rendus Physique **15**, 875 (2014).

[3] G. Sagnac, *L'éther lumineux démontré par l'effet du vent relatif d'éther dans un interféromètre en rotation uniforme*, Comptes rendus de l'Académie des Sciences **157**, 708 (1913).

[4] R. Anderson, H. R. Bilger, and G. E. Stedman, *"Sagnac" effect: A century of Earth-rotated interferometers*, American Journal of Physics **62**, 975 (1994).

[5] D. Döring *et al.*, *Quantum-projection-noise-limited interferometry with coherent atoms in a Ramsey-type setup*, Physical Review A **81**, 043633 (2010).

[6] A. D. Cronin and D. E. Pritchard, *Optics and interferometry with atoms and molecules*, Reviews of Modern Physics **81**, 1051 (2009).

[7] A. Dinkelaker, *Smooth inductively coupled ring trap for cold atom optics*, Phd thesis, University of Strathclyde, 2013.

[8] B. I. Robertson, *High Contrast Measurements with a Bose-Einstein Condensate Atom Interferometer*, Phd thesis, University of Strathclyde, 2016.

[9] B. I. Robertson *et al.*, *Detection of applied and ambient forces with a matter-wave magnetic gradiometer*, Physical Review A **96**, 053622 (2017).

[10] A. R. Mackellar, *Atom Interferometry with Bose-Einstein Condensates and Degenerate Fermi Gases*, Phd thesis, University of Strathclyde, 2017.

[11] A. Einstein, *Über einen die Erzeugung und Verwandlung des Lichtes betreffenden heuristischen Gesichtspunkt*, Annalen der Physik **322**, 132 (1905).

[12] L. De Broglie, *Waves and Quanta*, Nature **112**, 540 (1923).

[13] T. Young, *The Bakerian Lecture: On the Theory of Light and Colours*, Philosophical Transactions of the Royal Society of London **92**, 12 (1802).

[14] C. J. Davisson and L. H. Germer, *Reflection of Electrons by a Crystal of Nickel*, Proceedings of the National Academy of Sciences **14**, 317 (1928).

[15] O. Carnal and J. Mlynek, *Youngs double-slit experiment with atoms: A simple atom interferometer*, Physical Review Letters **66**, 2689 (1991).

[16] F. Shimizu, K. Shimizu, and H. Takuma, *Double-slit interference with ultracold metastable neon atoms*, Physical Review A **46**, R17 (1992).

[17] M. R. Andrews, *Observation of Interference Between Two Bose Condensates*, Science **275**, 637 (1997).

[18] M. E. Zawadzki, P. F. Griffin, E. Riis, and a. S. Arnold, *Spatial interference from well-separated split condensates*, Physical Review A **81**, 043608 (2010).

[19] M. Zawadzki, *Bose – Einstein condensate manipulation and interferometry*, Phd thesis, University of Strathclyde, 2010.

[20] C. H. Carson, *High Contrast Interferometry and Finite Temperature Coherence of Bose-Einstein Condensates*, Phd thesis, University of Strathclyde, 2015.

[21] B. Brezger *et al.*, *Matter-Wave Interferometer for Large Molecules*, Physical Review Letters **88**, 100404 (2002).

[22] S. Gerlich *et al.*, *Quantum interference of large organic molecules*, Nature Communications **2**, 263 (2011).

[23] C. S. Adams and E. Riis, *Laser cooling and trapping of neutral atoms*, Progress in Quantum Electronics **21**, 1 (1997).

[24] V. Bagnato, D. Pritchard, and D. Kleppner, *Bose-Einstein condensation in an external potential*, Physical Review A **35**, 2343 (1987).

[25] S. N. Bose, *Plancks Gesetz und Lichtquantenhypothese*, Zeitschrift für Physik **26**, 178 (1924).

[26] A. Einstein, *Quantentheorie des einatomigen idealen Gases*, Akademie der Wissenshaften (1924).

[27] M. H. Anderson, J. R. Ensher, M. R. Matthews, C. E. Wieman, and E. A. Cornell, *Observation of Bose-Einstein Condensation in a Dilute Atomic Vapor*, Science **269**, 198 (1995).

[28] K. B. Davis *et al.*, *Bose-Einstein Condensation in a Gas of Sodium Atoms*, Physical Review Letters **75**, 3969 (1995).

[29] A. S. Arnold and E. Riis, *Bose-Einstein condensates in 'giant' toroidal magnetic traps*, Journal of Modern Optics **49**, 959 (2002).

[30] A. S. Arnold, C. S. Garvie, and E. Riis, *Large magnetic storage ring for Bose-Einstein condensates*, Physical Review A **73**, 041606 (2006).

[31] Y. Zhai *et al.*, *Talbot-enhanced, maximum-visibility imaging of condensate interference*, Optica **5**, 80 (2018).

[32] T. L. Gustavson, P. Bouyer, and M. a. Kasevich, *Precision Rotation Measurements with an Atom Interferometer Gyroscope*, Physical Review Letters **78**, 2046 (1997).

[33] D. S. Durfee, Y. K. Shaham, and M. A. Kasevich, *Long-Term Stability of an Area-Reversible Atom-Interferometer Sagnac Gyroscope*, Physical Review Letters **97**, 240801 (2006).

[34] B. Plotkin-Swing, D. Gochnauer, K. McAlpine, A. O. Jamison, and S. Gupta, *Three-path atom interferometry with large momentum separation*, arXiv:1712.06738 (2017).

[35] O. Garcia, B. Deissler, K. J. Hughes, J. M. Reeves, and C. A. Sackett, *Bose-Einstein-condensate interferometer with macroscopic arm separation*, Physical Review A **74**, 031601 (2006).

[36] A. Peters, K. Y. Chung, and S. Chu, *High-precision gravity measurements using atom interferometry*, Metrologia **38**, 25 (2001).

[37] J. M. McGuirk, G. T. Foster, J. B. Fixler, M. J. Snadden, and M. A. Kasevich, *Sensitive absolute-gravity gradiometry using atom interferometry*, Physical Review A **65**, 033608 (2002).

[38] J. B. Fixler, G. T. Foster, J. M. McGuirk, and M. A. Kasevich, *Atom Interferometer Measurement of the Newtonian Constant of Gravity*, Science **315**, 74 (2007).

[39] R. Battesti *et al.*, *Bloch Oscillations of Ultracold Atoms: A Tool for a Metrological Determination of h/m*, Physical Review Letters **92**, 253001 (2004).

[40] P. Cladé *et al.*, *Determination of the Fine Structure Constant Based on Bloch Oscillations of Ultracold Atoms in a Vertical Optical Lattice*, Physical Review Letters **96**, 033001 (2006).

[41] S. Gupta, K. Dieckmann, Z. Hadzibabic, and D. E. Pritchard, *Contrast Interferometry using Bose-Einstein Condensates to Measure h/m and α*, Physical Review Letters **89**, 140401 (2002).

[42] C. Burrage, E. J. Copeland, and E. Hinds, *Probing dark energy with atom interferometry*, Journal of Cosmology and Astroparticle Physics **2015**, 042 (2015).

[43] H. Müntinga *et al.*, *Interferometry with Bose-Einstein Condensates in Microgravity*, Physical Review Letters **110**, 093602 (2013).

[44] S. Kulas *et al.*, *Miniaturized Lab System for Future Cold Atom Experiments in Microgravity*, Microgravity Science and Technology **29**, 37 (2017).

[45] D. K. L. Oi *et al.*, *Nanosatellites for quantum science and technology*, Contemporary Physics **58**, 25 (2017).

[46] K. U. Schreiber, T. Klügel, J. P. Wells, R. B. Hurst, and A. Gebauer, *How to detect the Chandler and the annual wobble of the earth with a large ring laser gyroscope*, Physical Review Letters **107**, 1 (2011).

[47] N. Beverini *et al.*, *High-Accuracy Ring Laser Gyroscopes: Earth Rotation Rate and Relativistic Effects*, Journal of Physics: Conference Series **723** (2016).

[48] T. L. Gustavson, A. Landragin, and M. A. Kasevich, *Rotation sensing with a dual atom-interferometer Sagnac gyroscope*, Classical and Quantum Gravity **17**, 2385 (2000).

[49] Honeywell International Inc., *GG1320AN Digital Laser Gyro*, 2016.

[50] L-3 Space and Navigation, *CIRUS-A Strategic Grade Inertial Measurement Unit*, 2015.

[51] S. M. Dickerson, J. M. Hogan, A. Sugarbaker, D. M. Johnson, and M. A. Kasevich, *Multiaxis inertial sensing with long-time point source atom interferometry*, Physical Review Letters **111**, 1 (2013).

[52] A. V. Rakholia, H. J. McGuinness, and G. W. Biedermann, *Dual-Axis High-Data-Rate Atom Interferometer via Cold Ensemble Exchange*, Physical Review Applied **2**, 054012 (2014).

[53] I. Dutta *et al.*, *Continuous Cold-Atom Inertial Sensor with 1nrad/sec Rotation Stability*, Physical Review Letters **116**, 183003 (2016).

[54] G. E. Marti, R. Olf, and D. M. Stamper-Kurn, *Collective excitation interferometry with a toroidal Bose-Einstein condensate*, Physical Review A **91**, 013602 (2015).

[55] H. Wang and T. Williams, *Strategic inertial navigation systems - high-accuracy inertially stabilized platforms for hostile environments*, IEEE Control Systems Magazine **28**, 65 (2008).

[56] Y. B. Kale and P. F. Griffin, *Private Communication*, 2018.

[57] J. H. T. Burke and C. A. Sackett, *Scalable Bose-Einstein-condensate Sagnac interferometer in a linear trap*, Physical Review A **80** (2009).

[58] E. Andersson *et al.*, *Multimode Interferometer for Guided Matter Waves*, Physical Review Letters **88**, 100401 (2002).

[59] P. L. Halkyard, M. P. A. Jones, and S. A. Gardiner, *Rotational response of two-component Bose-Einstein condensates in ring traps*, Physical Review A **81**, 061602 (2010).

[60] Y.-J. Wang *et al.*, *Atom Michelson Interferometer on a Chip Using a Bose-Einstein Condensate*, Physical Review Letters **94**, 090405 (2005).

[61] J. D. Pritchard, a. N. Dinkelaker, a. S. Arnold, P. F. Griffin, and E. Riis, *Demonstration of an inductively coupled ring trap for cold atoms*, New Journal of Physics **14**, 103047 (2012).

[62] L. Amico, G. Birkl, M. Boshier, and L.-C. Kwek, *Focus on atomtronics-enabled quantum technologies*, New Journal of Physics **19**, 020201 (2017).

[63] C. Ryu *et al.*, *Observation of Persistent Flow of a Bose-Einstein Condensate in a Toroidal Trap*, Physical Review Letters **99**, 260401 (2007).

[64] S. Moulder, S. Beattie, R. P. Smith, N. Tammuz, and Z. Hadzibabic, *Quantized supercurrent decay in an annular Bose-Einstein condensate*, Physical Review A **86**, 013629 (2012).

[65] K. C. Wright, R. B. Blakestad, C. J. Lobb, W. D. Phillips, and G. K. Campbell, *Driving Phase Slips in a Superfluid Atom Circuit with a Rotating Weak Link*, Physical Review Letters **110**, 025302 (2013).

[66] S. Eckel *et al.*, *Hysteresis in a quantized superfluid 'atomtronic' circuit*, Nature **506**, 200 (2014).

[67] A. Ramanathan *et al.*, *Superflow in a Toroidal Bose-Einstein Condensate: An Atom Circuit with a Tunable Weak Link*, Physical Review Letters **106**, 130401 (2011).

[68] A. Kumar *et al.*, *Minimally destructive, Doppler measurement of a quantized flow in a ring-shaped Bose–Einstein condensate*, New Journal of Physics **18**, 025001 (2016).

[69] A. Kumar, S. Eckel, F. Jendrzejewski, and G. K. Campbell, *Temperature-induced decay of persistent currents in a superfluid ultracold gas*, Physical Review A **95**, 021602 (2017).

[70] S. Beattie, S. Moulder, R. J. Fletcher, and Z. Hadzibabic, *Persistent Currents in Spinor Condensates*, Physical Review Letters **110**, 025301 (2013).

[71] A. Kumar *et al.*, *Producing superfluid circulation states using phase imprinting*, Physical Review A **97**, 043615 (2018).

[72] M. Aidelsburger *et al.*, *Relaxation Dynamics in the Merging of N Independent Condensates*, Physical Review Letters **119**, 190403 (2017).

[73] M. A. Cazalilla, R. Citro, T. Giamarchi, E. Orignac, and M. Rigol, *One dimensional bosons: From condensed matter systems to ultracold gases*, Reviews of Modern Physics **83**, 1405 (2011).

[74] S. Eckel, A. Kumar, T. Jacobson, I. B. Spielman, and G. K. Campbell, *A Rapidly Expanding Bose-Einstein Condensate: An Expanding Universe in the Lab*, Physical Review X **8**, 021021 (2018).

[75] J. L. O'Brien, A. Furusawa, and J. Vučković, *Photonic quantum technologies*, Nature Photonics **3**, 687 (2009).

[76] F. Brennecke *et al.*, *Real-time observation of fluctuations at the driven-dissipative Dicke phase transition*, Proceedings of the National Academy of Sciences **110**, 11763 (2013).

[77] P. F. Griffin, E. Riis, and A. S. Arnold, *Smooth inductively coupled ring trap for atoms*, Physical Review A **77**, 051402 (2008).

[78] D. Cassettari, B. Hessmo, R. Folman, T. Maier, and J. Schmiedmayer, *Beam splitter for guided atoms.*, Physical Review Letters **85**, 5483 (2000).

[79] D. Müller *et al.*, *Waveguide atom beam splitter for laser-cooled neutral atoms.*, Optics letters **25**, 1382 (2000).

[80] S. Gupta, K. W. Murch, K. L. Moore, T. P. Purdy, and D. M. Stamper-Kurn, *Bose-Einstein Condensation in a Circular Waveguide*, Physical Review Letters **95**, 143201 (2005).

[81] J. H. T. Burke, B. Deissler, K. J. Hughes, and C. A. Sackett, *Confinement effects in a guided-wave atom interferometer with millimeter-scale arm separation*, Physical Review A **78**, 1 (2008).

[82] E. Bentine *et al.*, *Species-selective confinement of atoms dressed with multiple radiofrequencies*, Journal of Physics B: Atomic, Molecular and Optical Physics **50**, 094002 (2017).

[83] B. E. Sherlock, M. Gildemeister, E. Owen, E. Nugent, and C. J. Foot, *Time-averaged adiabatic ring potential for ultracold atoms*, Physical Review A **83**, 043408 (2011).

[84] O. Morizot, Y. Colombe, V. Lorent, H. Perrin, and B. M. Garraway, *Ring trap for ultracold atoms*, Physical Review A **74**, 023617 (2006).

[85] I. Lesanovsky and W. von Klitzing, *Time-Averaged Adiabatic Potentials: Versatile Matter-Wave Guides and Atom Traps*, Physical Review Letters **99**, 083001 (2007).

[86] P. Navez *et al.*, *Matter-wave interferometers using TAAP rings*, New Journal of Physics **18**, 075014 (2016).

[87] M. Vangeleyn, B. M. Garraway, H. Perrin, and A. S. Arnold, *Inductive dressed ring traps for ultracold atoms*, Journal of Physics B: Atomic, Molecular and Optical Physics **47**, 071001 (2014).

[88] O. Zobay and B. Garraway, *Two-Dimensional Atom Trapping in Field-Induced Adiabatic Potentials*, Physical Review Letters **86**, 1195 (2001).

[89] Y. Colombe *et al.*, *Ultracold atoms confined in rf-induced two-dimensional trapping potentials*, Europhysics Letters (EPL) **67**, 593 (2004).

[90] A. S. Arnold, *Adaptable-radius, time-orbiting magnetic ring trap for Bose–Einstein condensates*, Journal of Physics B: Atomic, Molecular and Optical Physics **37**, L29 (2004).

[91] M. J. Renn *et al.*, *Laser-guided atoms in hollow-core optical fibers*, Physical Review Letters **75**, 3253 (1995).

[92] M. J. Renn, E. A. Donley, E. A. Cornell, C. E. Wieman, and D. Z. Anderson, *Evanescent-wave guiding of atoms in hollow optical fibers*, Physical Review A **53**, R648 (1996).

[93] O. Houde, D. Kadio, and L. Pruvost, *Cold Atom Beam Splitter Realized with Two Crossing Dipole Guides*, Physical Review Letters **85**, 5543 (2000).

[94] G. L. Gattobigio, A. Couvert, G. Reinaudi, B. Georgeot, and D. Guéry-Odelin, *Optically Guided Beam Splitter for Propagating Matter Waves*, Physical Review Letters **109**, 030403 (2012).

[95] D. Schneble, M. Hasuo, T. Anker, T. Pfau, and J. Mlynek, *Integrated atom-optical circuit with continuous-wave operation*, Journal of the Optical Society of America B **20**, 648 (2003).

[96] W. Guerin *et al.*, *Guided Quasicontinuous Atom Laser*, Physical Review Letters **97**, 200402 (2006).

[97] G. D. McDonald *et al.*, *Optically guided linear Mach-Zehnder atom interferometer*, Physical Review A **87**, 013632 (2013).

[98] L. Corman *et al.*, *Quench-Induced Supercurrents in an Annular Bose Gas*, Physical Review Letters **113**, 135302 (2014).

[99] A. L. Gaunt and Z. Hadzibabic, *Robust Digital Holography For Ultracold Atom Trapping*, Scientific Reports **2**, 721 (2012).

[100] A. L. Gaunt, T. F. Schmidutz, I. Gotlibovych, R. P. Smith, and Z. Hadzibabic, *Bose-Einstein Condensation of Atoms in a Uniform Potential*, Physical Review Letters **110**, 200406 (2013).

[101] A. Turpin *et al.*, *Blue-detuned optical ring trap for Bose-Einstein condensates based on conical refraction*, Optics Express **23**, 1638 (2015).

[102] T. A. Bell *et al.*, *Bose–Einstein condensation in large time-averaged optical ring potentials*, New Journal of Physics **18**, 035003 (2016).

[103] T. A. Bell *et al.*, *Phase and micromotion of Bose-Einstein condensates in a time-averaged ring trap*, arXiv:1802.05488 , 1 (2018).

[104] C. Ryu, P. W. Blackburn, a. a. Blinova, and M. G. Boshier, *Experimental Realization of Josephson Junctions for an Atom SQUID*, Physical Review Letters **111**, 205301 (2013).

[105] C Ryu and M. G. Boshier, *Integrated coherent matter wave circuits*, New Journal of Physics **17**, 092002 (2015).

[106] K. Henderson, C. Ryu, C. MacCormick, and M. G. Boshier, *Experimental demonstration of painting arbitrary and dynamic potentials for Bose-Einstein condensates*, New Journal of Physics **11**, 1 (2009).

[107] D. Trypogeorgos, T. Harte, A. Bonnin, and C. Foot, *Precise shaping of laser light by an acousto-optic deflector*, Optics Express **21**, 24837 (2013).

[108] R. Dumke *et al.*, *Interferometer-type structures for guided atoms*, in *2003 European Quantum Electronics Conference. EQEC 2003 (IEEE Cat No.03TH8665)*, p. 273, IEEE, 2003.

[109] S. Bergamini *et al.*, *Holographic generation of microtrap arrays for single atoms by use of a programmable phase modulator*, Journal of the Optical Society of America B **21**, 1889 (2004).

[110] G. Gauthier *et al.*, *Direct imaging of a digital-micromirror device for configurable microscopic optical potentials*, Optica **3**, 1136 (2016).

[111] G. D. Bruce, J. Mayoh, G. Smirne, L. Torralbo-Campo, and D. Cassettari, *A smooth, holographically generated ring trap for the investigation of superfluidity in ultracold atoms*, Physica Scripta **T143**, 014008 (2011).

[112] G. D. Bruce *et al.*, *Feedback-enhanced algorithm for aberration correction of holographic atom traps*, Journal of Physics B: Atomic, Molecular and Optical Physics **48**, 115303 (2015).

[113] F. K. Fatemi, M. Bashkansky, and Z. Dutton, *Dynamic high-speed spatial manipulation of cold atoms using acousto-optic and spatial light modulation.*, Optics express **15**, 3589 (2007).

[114] J. G. Lee and W. T. Hill, *Spatial shaping for generating arbitrary optical dipole traps for ultracold degenerate gases*, Review of Scientific Instruments **85**, 103106 (2014).

[115] T. A. Haase, D. H. White, D. J. Brown, I. Herrera, and M. D. Hoogerland, *A versatile apparatus for two-dimensional atomtronic quantum simulation*, Review of Scientific Instruments **88**, 113102 (2017).

[116] D. Barredo, S. de Léséleuc, V. Lienhard, T. Lahaye, and A. Browaeys, *An atom-by-atom assembler of defect-free arbitrary two-dimensional atomic arrays*, Science **354**, 1021 (2016).

[117] D. Barredo, V. Lienhard, S. de Léséleuc, T. Lahaye, and A. Browaeys, *Synthetic three-dimensional atomic structures assembled atom by atom*, arXiv:1712.02727 (2017).

[118] H. Rubinstein-Dunlop and A. Forbes, *Roadmap on Structured Light*, Journal of Optics **19** (2017).

[119] D. Stuart and A. Kuhn, *Single-atom trapping and transport in DMD-controlled optical tweezers*, New Journal of Physics **20**, 023013 (2018).

[120] S. Franke-Arnold *et al.*, *Optical ferris wheel for ultracold atoms*, Optics Express **15**, 8619 (2007).

[121] W. H. Heathcote, E. Nugent, B. T. Sheard, and C. J. Foot, *A ring trap for ultracold atoms in an RF-dressed state*, New Journal of Physics **10**, 043012 (2008).

[122] C. De Rossi, *Gaz de Bose en dimension deux: modes collectifs, super uidité et piège annulaire*, Phd thesis, Université Paris 13, 2016.

[123] V. A. Henderson, P. F. Griffin, E. Riis, and A. S. Arnold, *Comparative simulations of Fresnel holography methods for atomic waveguides*, New Journal of Physics **18**, 025007 (2016).

[124] G. Lochead, *Excited state spatial distributions in a cold strontium gas*, Phd thesis, Durham University, 2012.

[125] A. D. Bounds *et al.*, *Rydberg-Dressed Magneto-optical Trap*, Physical Review Letters **120**, 183401 (2018).

[126] D. P. Sadler *et al.*, *Radiation trapping in a dense cold Rydberg gas*, Physical Review A **95**, 013839 (2017).

[127] T. G. Tiecke, S. D. Gensemer, A. Ludewig, and J. T. M. Walraven, *High-flux two-dimensional magneto-optical-trap source for cold lithium atoms*, Physical Review A **80**, 013409 (2009).

[128] M. Padgett and L. Allen, *The Poynting vector in Laguerre-Gaussian laser modes*, Optics Communications **121**, 36 (1995).

[129] F. Gori, G. Guattari, and C. Padovani, *Bessel-Gauss beams*, Optics Communications **64**, 491 (1987).

[130] X. Chu *et al.*, *Generating a Bessel-Gaussian beam for the application in optical engineering*, Scientific Reports **5**, 18665 (2016).

[131] V. Garcés-Chávez, D. McGloin, H. Melville, W. Sibbett, and K. Dholakia, *Simultaneous micromanipulation in multiple planes using a self-reconstructing light beam*, Nature **419**, 145 (2002).

[132] G. Milne, G. D. M. Jeffries, and D. T. Chiu, *Tunable generation of Bessel beams with a fluidic axicon*, Applied Physics Letters **92**, 261101 (2008).

[133] N. Chattrapiban, E. A. Rogers, D. Cofield, W. T. Hill, III, and R. Roy, *Generation of nondiffracting Bessel beams by use of a spatial light modulator*, Optics Letters **28**, 2183 (2003).

[134] E. Courtade, O. Houde, J.-F. Clément, P. Verkerk, and D. Hennequin, *Dark optical lattice of ring traps for cold atoms*, Physical Review A **74**, 031403 (2006).

[135] T. W. Hänsch and A. L. Schawlow, *Cooling of gases by laser radiation*, Optics Communications **13**, 68 (1975).

[136] W. D. Phillips and H. Metcalf, *Laser Deceleration of an Atomic Beam*, Physical Review Letters **48**, 596 (1982).

[137] S. Chu, L. Hollberg, J. E. Bjorkholm, A. Cable, and A. Ashkin, *Three-dimensional viscous confinement and cooling of atoms by resonance radiation pressure*, Physical Review Letters **55**, 48 (1985).

[138] S. Chu, J. E. Bjorkholm, A. Ashkin, and A. Cable, *Experimental Observation of Optically Trapped Atoms*, Physical Review Letters **57**, 314 (1986).

[139] C. J. Foot, *Atomic physics* (Oxford University Press, 2005).

[140] D. Boiron, C. Triché, D. R. Meacher, P. Verkerk, and G. Grynberg, *Three-dimensional cooling of cesium atoms in four-beam gray optical molasses*, Physical Review A **52**, R3425 (1995).

[141] K. N. Jarvis, J. A. Devlin, T. E. Wall, B. E. Sauer, and M. R. Tarbutt, *Blue-Detuned Magneto-Optical Trap*, Physical Review Letters **120**, 083201 (2018).

[142] W. Gerlach and O. Stern, *Der experimentelle Nachweis der Richtungsquantelung im Magnetfeld*, Zeitschrift für Physik **9**, 349 (1922).

[143] W. Gerlach and O. Stern, *Das magnetische Moment des Silberatoms*, Zeitschrift für Physik **9**, 353 (1922).

[144] W. Gerlach and O. Stern, *Der experimentelle Nachweis des magnetischen Moments des Silberatoms*, Zeitschrift für Physik **8**, 110 (1922).

[145] D. J. Griffiths, *Introduction to Electrodynamics*, 3rd ed. (Prentic Hall, 1999).

[146] A. L. Migdall, J. V. Prodan, W. D. Phillips, T. H. Bergeman, and H. J. Metcalf, *First Observation of Magnetically Trapped Neutral Atoms*, Physical Review Letters **54**, 2596 (1985).

[147] D. M. Brink and C. V. Sukumar, *Majorana spin-flip transitions in a magnetic trap*, Physical Review A **74**, 035401 (2006).

[148] E. Majorana, *Atomi orientati in campo magnetico variabile*, Il Nuovo Cimento **9**, 43 (1932).

[149] P. O. Schmidt *et al.*, *Continuous loading of cold atoms into a Ioffe Pritchard magnetic trap*, Journal of Optics B: Quantum and Semiclassical Optics **5**, S170 (2003).

[150] H. Ott, J. Fortagh, G. Schlotterbeck, A. Grossmann, and C. Zimmermann, *Bose-Einstein Condensation in a Surface Microtrap*, Physical Review Letters **87**, 230401 (2001).

[151] D. S. Naik and C. Raman, *Optically plugged quadrupole trap for Bose-Einstein condensates*, Physical Review A **71**, 033617 (2005).

[152] W. Petrich, M. H. Anderson, J. R. Ensher, and E. A. Cornell, *Stable, Tightly Confining Magnetic Trap for Evaporative Cooling of Neutral Atoms*, Physical Review Letters **74**, 3352 (1995).

[153] B. M. Garraway and H. Perrin, *Recent developments in trapping and manipulation of atoms with adiabatic potentials*, Journal of Physics B: Atomic, Molecular and Optical Physics **49**, 172001 (2016).

[154] D. E. Pritchard, *Cooling Neutral Atoms in a Magnetic Trap for Precision Spectroscopy*, Physical Review Letters **51**, 1336 (1983).

[155] A. Arnold, *Preparation and Manipulation of an Rb Bose-Einstein Condensate*, Phd thesis, University of Sussex, 1999.

[156] E. L. Raab, M. Prentiss, A. Cable, S. Chu, and D. E. Pritchard, *Trapping of Neutral Sodium Atoms with Radiation Pressure*, Physical Review Letters **59**, 2631 (1987).

[157] H. J. Metcalf and P. van der Straten, *Laser Cooling and Trapping*Graduate Texts in Contemporary Physics (Springer New York, 1999).

[158] K. Lindquist, M. Stephens, and C. Wieman, *Experimental and theoretical study of the vapor-cell Zeeman optical trap*, Physical Review A **46**, 4082 (1992).

[159] S. Gensemer, V. Sanchez-Villicana, K. Tan, T. Grove, and P. Gould, *Trap-loss collisions of Rb85 and Rb87: Dependence on trap parameters*, Physical Review A **56**, 4055 (1997).

[160] M. Haw *et al.*, *Magneto-optical trap loading rate dependence on trap depth and vapor density*, Journal of the Optical Society of America B **29**, 475 (2012).

[161] T. Arpornthip, C. A. Sackett, and K. J. Hughes, *Vacuum-pressure measurement using a magneto-optical trap*, Physical Review A **85**, 033420 (2012).

[162] J. P. McGilligan, P. F. Griffin, E. Riis, and a. S. Arnold, *Phase-space properties of magneto-optical traps utilising micro-fabricated gratings*, Optics Express **23**, 8948 (2015).

[163] C. J. Myatt, N. R. Newbury, R. W. Ghrist, S. Loutzenhiser, and C. E. Wieman, *Multiply loaded magneto-optical trap.*, Optics letters **21**, 290 (1996).

[164] Z. T. Lu *et al.*, *Low-velocity intense source of atoms from a magneto-optical trap*, Physical Review Letters **77**, 3331 (1996).

[165] S. Chaudhuri, S. Roy, and C. S. Unnikrishnan, *Realization of an intense cold Rb atomic beam based on a two-dimensional magneto-optical trap: Experiments and comparison with simulations*, Physical Review A **74**, 1 (2006).

[166] J. Schoser *et al.*, *Intense source of cold Rb atoms from a pure two-dimensional magneto-optical trap*, Physical Review A **66**, 023410 (2002).

[167] K. Dieckmann, R. J. C. Spreeuw, M. Weidemüller, and J. T. M. Walraven, *Two-dimensional magneto-optical trap as a source of slow atoms*, Physical Review A **58**, 3891 (1998).

[168] A. Di Carli, C. Colquhoun, and E. Haller, *Private Communication*, 2017.

[169] K. I. Lee, J. A. Kim, H. R. Noh, and W. Jhe, *Single-beam atom trap in a pyramidal and conical hollow mirror*, Optics Letters **21**, 1177 (1996).

[170] M. Vangeleyn, P. F. Griffin, E. Riis, and A. S. Arnold, *Single-laser, one beam, tetrahedral magneto-optical trap*, Optics Express **17**, 13601 (2009).

[171] M. Vangeleyn, P. F. Griffin, E. Riis, and A. S. Arnold, *Laser cooling with a single laser beam and a planar diffractor*, Optics Letters **35**, 3453 (2010).

[172] C. C. Nshii *et al.*, *A surface-patterned chip as a strong source of ultracold atoms for quantum technologies*, Nature Nanotechnology **8**, 321 (2013).

[173] J. P. Cotter *et al.*, *Design and fabrication of diffractive atom chips for laser cooling and trapping*, Applied Physics B **122**, 172 (2016).

[174] J. P. McGilligan, P. F. Griffin, E. Riis, and A. S. Arnold, *Diffraction-grating characterization for cold-atom experiments*, Journal of the Optical Society of America B **33**, 1271 (2016), 1601.07431.

[175] J. P. McGilligan *et al.*, *Grating chips for quantum technologies*, Scientific Reports **7**, 384 (2017).

[176] J. P. Mcgilligan, *Micro-fabricated Diffractive Optics for Quantum Sensors and Atomic Clocks*, Phd, University of Strathclyde, 2017.

[177] J. P. McGilligan, R. Elvin, P. F. Griffin, E. Riis, and A. S. Arnold, *Utilising diffractive optics towards a compact, cold atom clock*, in *2016 European Frequency and Time Forum (EFTF)*, pp. 1–2, IEEE, 2016.

[178] E. Imhof *et al.*, *Two-dimensional grating magneto-optical trap*, Physical Review A **96**, 033636 (2017).

[179] O. Burrow and P. F. Griffin, *Private communication*, 2017.

[180] Y. Castin, H. Wallis, and J. Dalibard, *Limit of Doppler cooling*, Journal of the Optical Society of America B **6**, 2046 (1989).

[181] J. Dalibard and C. Cohen-Tannoudji, *Laser cooling below the Doppler limit by polarization gradients: simple theoretical models*, Journal of the Optical Society of America B **6**, 2023 (1989).

[182] D. A. Steck, *Rubidium 87 D Line Data*, available online at http://steck.us/alkalidata (2015).

[183] P. D. Lett *et al.*, *Observation of atoms laser cooled below the doppler limit*, Physical Review Letters **61**, 169 (1988).

[184] Y. Shevy, D. S. Weiss, P. J. Ungar, and S. Chu, *Bimodal speed distributions in laser-cooled atoms*, Physical Review Letters **62**, 1118 (1989).

[185] P. J. Ungar, D. S. Weiss, E. Riis, and S. Chu, *Optical molasses and multilevel atoms: theory*, Journal of the Optical Society of America B **6**, 2058 (1989).

[186] P. D. Lett *et al.*, *Optical molasses*, Journal of the Optical Society of America B **6**, 2084 (1989).

[187] D. S. Weiss, E. Riis, Y. Shevy, P. J. Ungar, and S. Chu, *Optical molasses and multilevel atoms: experiment*, Journal of the Optical Society of America B **6**, 2072 (1989).

[188] C. G. Townsend *et al.*, *Phase-space density in the magneto-optical trap*, Physical Review A **52**, 1423 (1995).

[189] M. T. DePue, S. Lukman Winoto, D. Han, and D. S. Weiss, *Transient compression of a MOT and high intensity fluorescent imaging of optically thick clouds of atoms*, Optics Communications **180**, 73 (2000).

[190] D. Boiron *et al.*, *Laser cooling of cesium atoms in gray optical molasses down to 1.1 μK*, Physical Review A **53**, R3734 (1996).

[191] D. Rio Fernandes *et al.*, *Sub-Doppler laser cooling of fermionic 40 K atoms in three-dimensional gray optical molasses*, Europhysics Letters **100**, 63001 (2012).

[192] A. T. Grier *et al.*, *Λ-enhanced sub-Doppler cooling of lithium atoms in D1 gray molasses*, Physical Review A **87**, 063411 (2013).

[193] G. Salomon *et al.*, *Gray-molasses cooling of 39 K to a high phase-space density*, EPL (Europhysics Letters) **104**, 63002 (2013).

[194] G. D. Bruce *et al.*, *Sub-Doppler laser cooling of 40 K with Raman gray molasses on the D2 line*, Journal of Physics B: Atomic, Molecular and Optical Physics **50**, 095002 (2017).

[195] S. Rosi *et al.*, *Λ-enhanced grey molasses on the D2 transition of Rubidium-87 atoms*, Scientific Reports **8**, 1301 (2018).

[196] W. Petrich, M. H. Anderson, J. R. Ensher, and E. A. Cornell, *Behavior of atoms in a compressed magneto-optical trap*, Journal of the Optical Society of America B **11**, 1332 (1994).

[197] W. Ketterle, K. B. Davis, M. A. Joffe, A. Martin, and D. E. Pritchard, *High densities of cold atoms in a dark spontaneous-force optical trap*, Physical Review Letters **70**, 2253 (1993).

[198] A. G. Sinclair, E. Riis, and M. J. Snadden, *Improved trapping in a vapor-cell magneto-optical trap with multiple laser frequencies*, Journal of the Optical Society of America B **11**, 2333 (1994).

[199] M. H. Anderson, W. Petrich, J. R. Ensher, and E. A. Cornell, *Reduction of light-assisted collisional loss rate from a low-pressure vapor-cell trap*, Physical Review A **50**, 3597 (1994).

[200] C. G. Townsend *et al.*, *High-density trapping of cesium atoms in a dark magneto-optical trap*, Physical Review A **53**, 1702 (1996).

[201] N. Radwell, G. Walker, and S. Franke-Arnold, *Cold-atom densities of more than 10^{12} cm^{-3} in a holographically shaped dark spontaneous-force*, Physical Review A **88**, 043409 (2013).

[202] C. Corder, B. Arnold, and H. Metcalf, *Laser Cooling without Spontaneous Emission*, Physical Review Letters **114**, 043002 (2015).

[203] R. Grimm, M. Weidemüller, and Y. B. Ovchinnikov, *Optical Dipole Traps for Neutral Atoms*, Advances in Atomic, Molecular and Optical Physics **42**, 95 (2000).

[204] J. Dalibard and C. Cohen-Tannoudji, *Dressed-atom approach to atomic motion in laser light: the dipole force revisited*, Journal of the Optical Society of America B **2**, 1707 (1985).

[205] W. Ketterle and N. V. Druten, *Evaporative Cooling of Trapped Atoms*, in *Advances In Atomic, Molecular, and Optical Physics*, volume 37, pp. 181–236, Elsevier, 1996.

[206] W. Ketterle, D. S. Durfee, and D. M. Stamper-Kurn, *Making, probing and understanding Bose-Einstein condensates*, Proceedings of the 1998 Enrico Fermi summer school on Bose-Einstein condensation in Varenna, Italy. (1999), arXiv:9904034.

[207] A. Kuhn, H. Perrin, W. Hänsel, and C. Salomon, *Three Dimensional Raman Cooling using Velocity Selective Rapid Adiabatic Passage*, in *in OSA TOPS on Ultracold Atoms and BEC*, volume 7, p. 58, Optical Society of America, 1997.

[208] M. D. Barrett, J. A. Sauer, and M. S. Chapman, *All-Optical Formation of an Atomic Bose-Einstein Condensate*, Physical Review Letters **87**, 010404 (2001).

[209] S. Kumar *et al.*, *Simple and Fast Production of Bose–Einstein Condensate in a 1 μm Cross-Beam Dipole Trap*, Journal of the Physical Society of Japan **81**, 084004 (2012).

[210] K. Yamashita, K. Hanasaki, A. Ando, M. Takahama, and T. Kinoshita, *All-optical production of a large Bose-Einstein condensate in a double compressible crossed dipole trap*, Physical Review A **95**, 013609 (2017).

[211] J.-F. Clément *et al.*, *All-optical runaway evaporation to Bose-Einstein condensation*, Physical Review A **79**, 061406 (2009).

[212] A. B. Deb, T. McKellar, and N. Kjærgaard, *Optical runaway evaporation for the parallel production of multiple Bose-Einstein condensates*, Physical Review A **90**, 051401 (2014).

[213] Y.-J. Lin, A. R. Perry, R. L. Compton, I. B. Spielman, and J. V. Porto, *Rapid production of 87Rb Bose-Einstein condensates in a combined magnetic and optical potential*, Physical Review A **79**, 063631 (2009).

[214] A. L. Gaunt, T. F. Schmidutz, I. Gotlibovych, R. P. Smith, and Z. Hadzibabic, *Bose-Einstein Condensation of Atoms in a Uniform Potential*, Physical Review Letters **110**, 200406 (2013).

[215] S. Stellmer, B. Pasquiou, R. Grimm, and F. Schreck, *Laser Cooling to Quantum Degeneracy*, Physical Review Letters **110**, 263003 (2013).

[216] L. Hu, N. Poli, L. Salvi, and G. M. Tino, *Atom Interferometry with the Sr Optical Clock Transition*, Physical Review Letters **119**, 263601 (2017).

[217] O. J. Luiten, M. W. Reynolds, and J. T. M. Walraven, *Kinetic theory of the evaporative cooling of a trapped gas*, Physical Review A **53**, 381 (1996).

[218] J. Rudolph *et al.*, *A high-flux BEC source for mobile atom interferometers*, New Journal of Physics **17**, 065001 (2015).

[219] M. Gajdacz *et al.*, *Non-destructive Faraday imaging of dynamically controlled ultracold atoms*, Review of Scientific Instruments **84**, 083105 (2013).

[220] M. Gajdacz *et al.*, *Preparation of Ultracold Atom Clouds at the Shot Noise Level*, Physical Review Letters **117**, 073604 (2016).

[221] M. R. Andrews *et al.*, *Direct, Nondestructive Observation of a Bose Condensate*, Science **273**, 84 (1996).

[222] J. Ye, S. Swartz, P. Jungner, and J. L. Hall, *Hyperfine structure and absolute frequency of the 87Rb 5P3/2 state*, Optics Letters **21**, 1280 (1996).

[223] S. Bize *et al.*, *High-accuracy measurement of the 87 Rb ground-state hyperfine splitting in an atomic fountain*, Europhysics Letters (EPL) **45**, 558 (1999).

[224] C. E. Wieman and L. Hollberg, *Using diode lasers for atomic physics*, Review of Scientific Instruments **62**, 1 (1991).

[225] L. Ricci *et al.*, *A compact grating-stabilized diode laser system for atomic physics*, Optics Communications **117**, 541 (1995).

[226] A. S. Arnold, J. S. Wilson, and M. G. Boshier, *A simple extended-cavity diode laser*, Review of Scientific Instruments **69**, 1236 (1998).

[227] Newport Corporation, *TA-7600-Series Tapered Amplifier Model Manual*, 2013.

[228] S. T. Seidel, *Eine Quelle für die Interferometrie mit Bose-Einstein-Kondensaten auf Höhenforschungsraketen*, Phd thesis, Gottfried Wilhelm Leibniz Universität Hannover, 2014.

[229] H. Busche, *Efficient loading of a magneto-optical trap for experiments with dense ultracold Rydberg gases*, Master thesis, Heidelberg, 2011.

[230] B. Höltkemeier, *2D MOT as a source of a cold atom target*, PhD thesis, University of Heidelberg, 2011.

[231] P. Cheinet *et al.*, *Compact laser system for atom interferometry*, Applied Physics B **84**, 643 (2006).

[232] J. Ramirez-Serrano, N. Yu, J. M. Kohel, J. R. Kellogg, and L. Maleki, *Multistage two-dimensional magneto-optical trap as a compact cold atom beam source*, Optics Letters **31**, 682 (2006).

[233] D. M. Farkas *et al.*, *A compact, transportable, microchip-based system for high repetition rate production of Bose-Einstein condensates*, Applied Physics Letters **96**, 093102 (2010).

[234] D. M. Farkas, K. M. Hudek, S. Du, and D. Z. Anderson, *Efficient direct evaporative cooling in an atom-chip magnetic trap*, Physical Review A **87**, 053417 (2013).

[235] M. Horikoshi and K. Nakagawa, *Atom chip based fast production of Bose–Einstein condensate*, Applied Physics B **82**, 363 (2006).

[236] T. Kinoshita, T. Wenger, and D. S. Weiss, *All-optical Bose-Einstein condensation using a compressible crossed dipole trap*, Physical Review A **71**, 011602 (2005).

[237] R. Roy, A. Green, R. Bowler, and S. Gupta, *Rapid cooling to quantum degeneracy in dynamically shaped atom traps*, Physical Review A **93**, 043403 (2016).

[238] J. F. Annett, *Superconductivity, Superfluids and Condensates (Oxford Master Series in Physics)* (OUP Oxford, 2004).

[239] C. J. Pethick and H. Smith, *Bose Einstein Condensation in Dilute Gases* (Cambridge University Press, Cambridge, 2008).

[240] M. Naraschewski and D. M. Stamper-Kurn, *Analytical description of a trapped semi-ideal Bose gas at finite temperature*, Physical Review A **58**, 2423 (1998).

[241] L. Salasnich, A. Parola, and L. Reatto, *Bosons in a Toroidal Trap: Ground State and Vortices*, Physical Review A **59**, 15 (1999).

[242] A. Roy and D. Angom, *Finite temperature expansion dynamics of Bose-Einstein condensates in ring traps*, Physics Letters A **381**, 2483 (2017).

[243] J. L. Helm, T. P. Billam, A. Rakonjac, S. L. Cornish, and S. A. Gardiner, *Spin-Orbit-Coupled Interferometry with Ring-Trapped Bose-Einstein Condensates*, Physical Review Letters **120**, 063201 (2018).

[244] F. Dalfovo, S. Giorgini, L. P. Pitaevskii, and S. Stringari, *Theory of Bose-Einstein condensation in trapped gases*, Reviews of Modern Physics **71**, 463 (1999).

[245] G. Baym and C. J. Pethick, *Ground-State Properties of Magnetically Trapped Bose-Condensed Rubidium Gas*, Physical Review Letters **76**, 6 (1996).

[246] R. Srinivasan, *Vortices in Bose-Einstein condensates: A review of the experimental results*, Pramana **66**, 3 (2006).

[247] N. Murray *et al.*, *Probing the circulation of ring-shaped Bose-Einstein condensates*, Physical Review A **88**, 053615 (2013).

[248] F. Jendrzejewski *et al.*, *Resistive Flow in a Weakly Interacting Bose-Einstein Condensate*, Physical Review Letters **113**, 045305 (2014).

[249] L. Mathey *et al.*, *Phase fluctuations in anisotropic Bose-Einstein condensates: From cigars to rings*, Physical Review A **82**, 033607 (2010).

[250] S. Dettmer *et al.*, *Observation of Phase Fluctuations in Elongated Bose-Einstein Condensates*, Physical Review Letters **87**, 160406 (2001).

[251] I. Shvarchuck *et al.*, *Bose-Einstein Condensation into Nonequilibrium States Studied by Condensate Focusing*, Physical Review Letters **89**, 270404 (2002).

[252] S. Richard *et al.*, *Momentum Spectroscopy of 1D Phase Fluctuations in Bose-Einstein Condensates*, Physical Review Letters **91**, 010405 (2003).

[253] D. Petrov, G. Shlyapnikov, and J. Walraven, *Phase-Fluctuating 3D Bose-Einstein Condensates in Elongated Traps*, Physical Review Letters **87**, 050404 (2001).

[254] Y. Kagan, E. L. Surkov, and G. V. Shlyapnikov, *Evolution of a Bose-condensed gas under variations of the confining potential*, Physical Review A **54**, R1753 (1996).

[255] Y. Castin and R. Dum, *Bose-Einstein Condensates in Time Dependent Traps*, Physical Review Letters **77**, 5315 (1996).

[256] S. Manz *et al.*, *Two-point density correlations of quasicondensates in free expansion*, Physical Review A **81**, 031610 (2010).

[257] A. Imambekov *et al.*, *Density ripples in expanding low-dimensional gases as a probe of correlations*, Physical Review A **80**, 033604 (2009).

[258] P. Engels, C. Atherton, and M. a. Hoefer, *Observation of Faraday Waves in a Bose-Einstein Condensate*, Physical Review Letters **98**, 095301 (2007).

[259] E. M. Wright, J. Arlt, and K. Dholakia, *Toroidal optical dipole traps for atomic Bose-Einstein condensates using Laguerre-Gaussian beams*, Physical Review A **63**, 013608 (2000).

[260] M. Pasienski and B. DeMarco, *A high-accuracy algorithm for designing arbitrary holographic atom traps*, Optics Express **16**, 2176 (2008).

[261] L.-C. Ha, L. W. Clark, C. V. Parker, B. M. Anderson, and C. Chin, *Roton-Maxon Excitation Spectrum of Bose Condensates in a Shaken Optical Lattice*, Physical Review Letters **114**, 055301 (2015).

[262] C. Muldoon *et al.*, *Control and manipulation of cold atoms in optical tweezers*, New Journal of Physics **14**, 073051 (2012).

[263] F. Nogrette *et al.*, *Single-Atom Trapping in Holographic 2D Arrays of Microtraps with Arbitrary Geometries*, Physical Review X **4**, 021034 (2014).

[264] L. Amico, A. Osterloh, and F. Cataliotti, *Quantum Many Particle Systems in Ring-Shaped Optical Lattices*, Physical Review Letters **95**, 063201 (2005).

[265] A. S. Arnold, *Extending dark optical trapping geometries*, Optics Letters **37**, 2505 (2012).

[266] J. Fortágh, H. Ott, S. Kraft, A. Günther, and C. Zimmermann, *Surface effects in magnetic microtraps*, Physical Review A **66**, 041604 (2002).

[267] E. Hecht, *Optics*, 4th ed. (Pearson, 2013).

[268] T. W. Clark, R. F. Offer, S. Franke-Arnold, A. S. Arnold, and N. Radwell, *Comparison of beam generation techniques using a phase only spatial light modulator*, Optics Express **24**, 6249 (2016).

[269] E. Schonbrun, C. Rinzler, and K. B. Crozier, *Microfabricated water immersion zone plate optical tweezer*, Applied Physics Letters **92**, 2007 (2008).

[270] G. Thalhammer, R. Steiger, S. Bernet, and M. Ritsch-Marte, *Optical macro-tweezers: trapping of highly motile micro-organisms*, Journal of Optics **13**, 044024 (2011).

[271] T. Harte, G. D. Bruce, J. Keeling, and D. Cassettari, *Conjugate gradient minimisation approach to generating holographic traps for ultracold atoms*, Optics Express **22**, 26548 (2014).

[272] A. McDonald, G. McConnell, D. C. Cox, E. Riis, and P. F. Griffin, *3D mapping of intensity field about the focus of a micrometer–scale parabolic mirror*, Optics Express **23**, 2375 (2015).

[273] L. Novotny and B. Hecht, *Principles of Nano-Optics* (, 2012).

[274] Hamamatsu, *LCOS-SLM (Liquid Crystal on Silicon - Spatial Light Modulator)*, p. 1 (2012).

[275] J. Kedmi and I. Grossinger, *Diffractive optical element*, 1990.

[276] I. Grossinger and J. Kedmi, *Diffractive optical element*, 1993.

[277] T. Kitoh, N. Takato, M. Yasu, and M. Kawachi, *Bending loss reduction in silica-based waveguides by using lateral offsets*, Journal of Lightwave Technology **13**, 555 (1995).

[278] S. Katz, N. Kaplan, and I. Grossinger, *Diffractive Optical Elements: Minimizing Zero Order*, 2018.

[279] M. Milosevic, *On the Nature of the Evanescent Wave*, Applied Spectroscopy **67**, 126 (2013).

[280] L. Yu *et al.*, *Quasi-discrete Hankel transform*, Optics Letters **23**, 409 (1998).

[281] M. Guizar-Sicairos and J. C. Gutiérrez-Vega, *Computation of quasi-discrete Hankel transforms of integer order for propagating optical wave fields*, Journal of the Optical Society of America A **21**, 53 (2004).

[282] K. Li and C. Jacobsen, *Rapid calculation of paraxial wave propagation for cylindrically symmetric optics*, Journal of the Optical Society of America A **32**, 2074 (2015).

[283] Adam Wyatt, *Hankel Transform (Matlab File Exchange "15623")*, 2009.

Appendix A

Additional Zone Plate Data

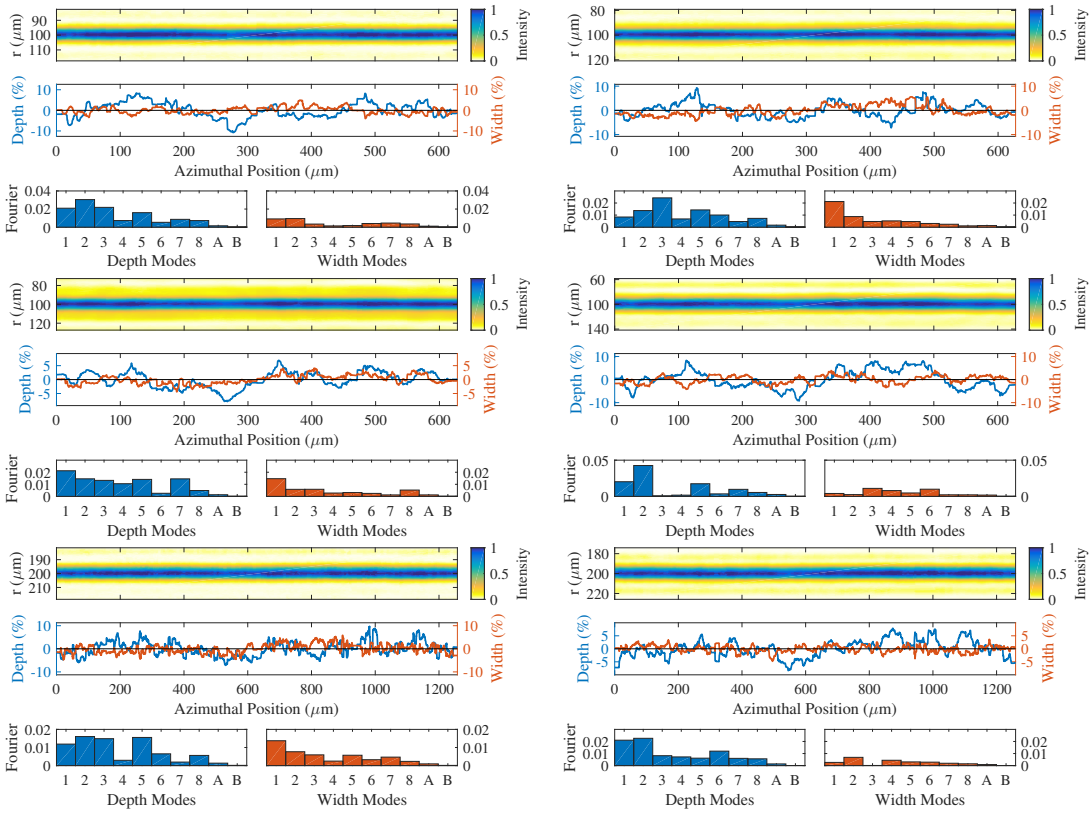

Figure A.1: Fourier roughness analysis for all rings. See Fig. 6.17 and Sec. 6.2.4 for further details.

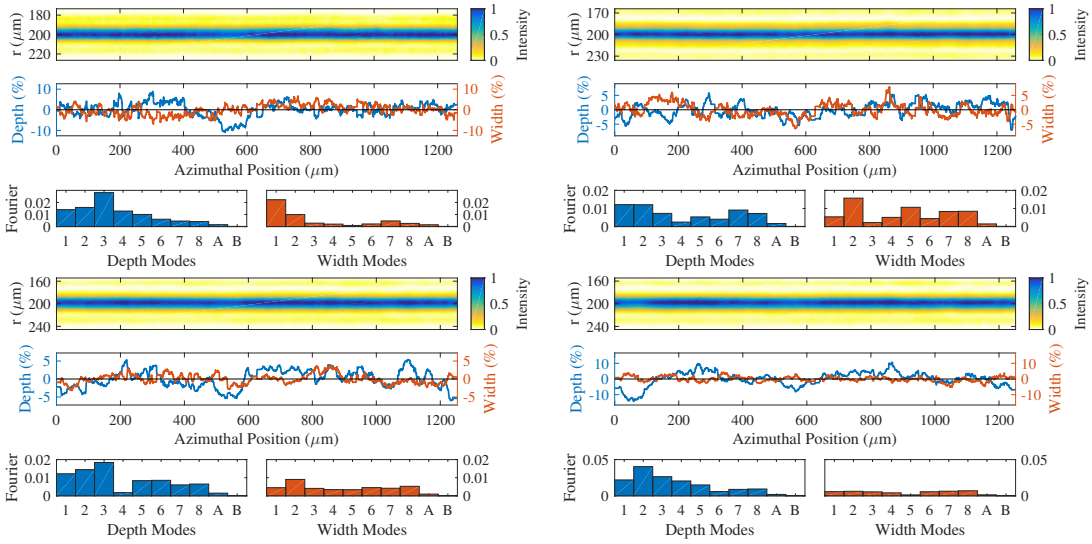

Figure A.1: A continuation of the above figure

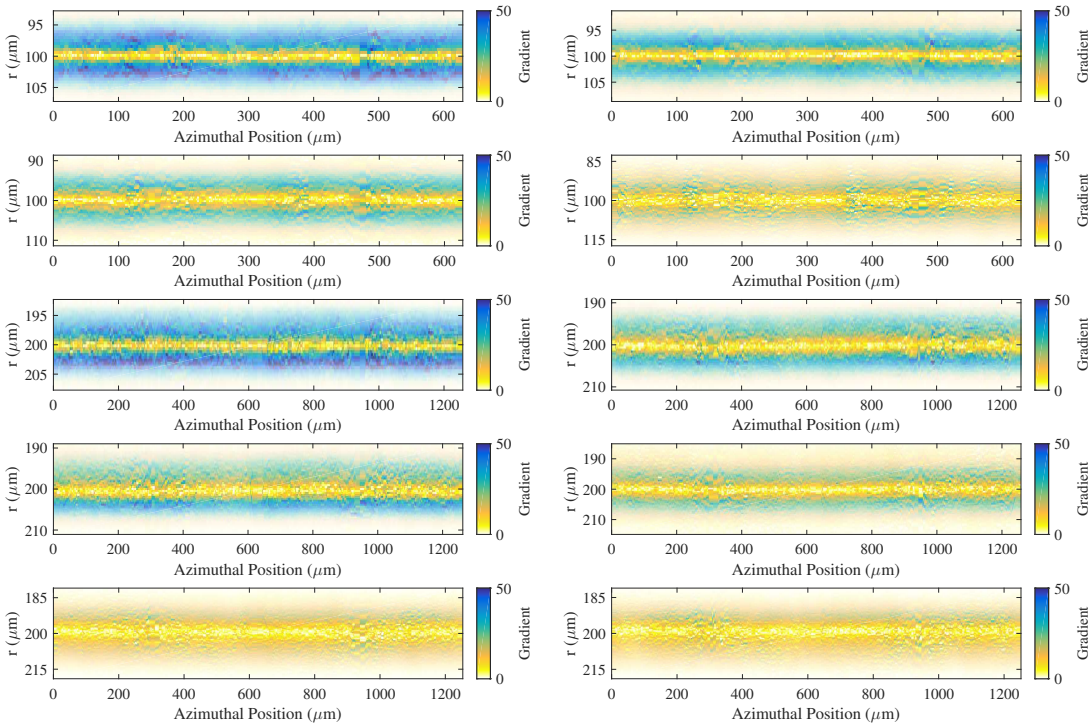

Figure A.2: All the azimuthal force plots, see Fig. 6.18 and Sec. 6.2.4.

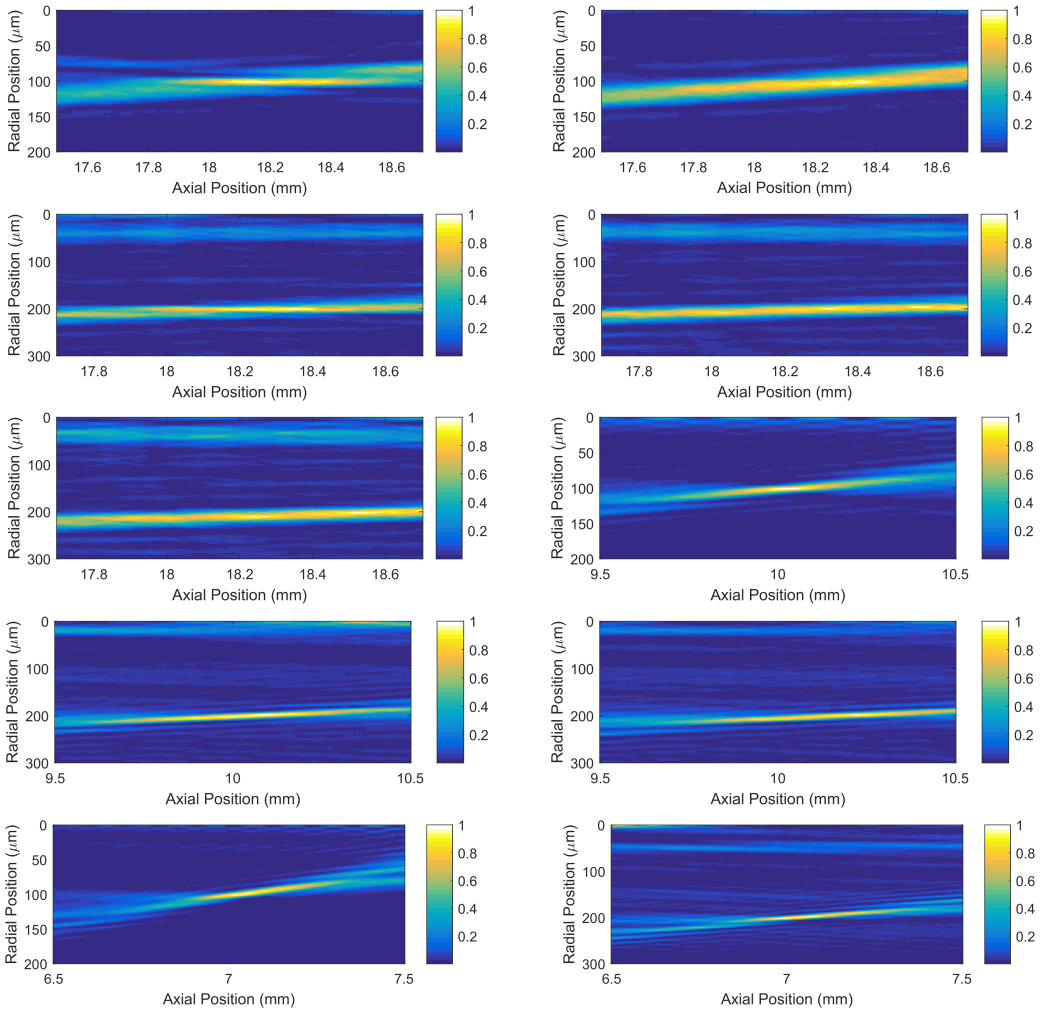

Figure A.3: Simulated propagation of all the rings, displayed in the same order as ring parameter tables.

Appendix B

Knitting Pattern for a Kinoform Shawl

As a knitter, the Fresnel zone plate kinoforms are an exciting candidate for a quirky stripe pattern on a shawl. As a result of this, I designed (and am close to finishing) a semi circular π-shawl which approximates the kinoform for a ring with a radius equal to half the radius of the shawl. The stripe pattern was calculated using MATLAB and optimised for aesthetics. The main and contract colours (MC and CC respectively) were inspired by the *parula* colourmap used in figures within this thesis, but with yellow replaced with a more tonal grey.

The following instructions are not for a beginner as familiarity with shawl knitting is assumed. One should begin with a garter tab, then begin in stocking stitch with 3 stitch garter border either side. Tab. B.1 details the locations of colour changes and increase rows, with all intermediate rows being stocking stitch. The increase rows are K3, kfb until 3 stitches before end, K3, or the equivalent in the wrongside. One could use the increase rows as a log base 2 axis by replacing kfb with *k1, yo*. The original schematic is shown in Fig. B.1. Photos and further details of the finished item can be found on Ravelry.

Row	Colour	Instruction	Number of Stitches (excluding border)
1	MC	begin	3
2	MC	inc.	6
5	CC	inc. and change colour	12
9	MC	change colour	12
10	MC	inc.	24
13	CC	change colour	24
18	MC	change colour	24
19	MC	inc.	48
23	CC	change colour	48
28	MC	change colour	48
34	CC	change colour	48
36	CC	inc.	96
41	MC	change colour	96
50	CC	change colour	96
60	MC	change colour	96
69	MC	inc.	192
112	CC	change colour	192
122	MC	change colour	192
131	CC	change colour	192
134	CC	inc.	384
138	MC	change colour	384
144	CC	change colour	384
149	MC	change colour	384
154	CC	change colour	384
159	MC	change colour	384
163	CC	change colour	384
167	MC	change colour	384
171	CC	change colour	384
175	MC	change colour and start edging	384

Table B.1: A zone plate knitting pattern

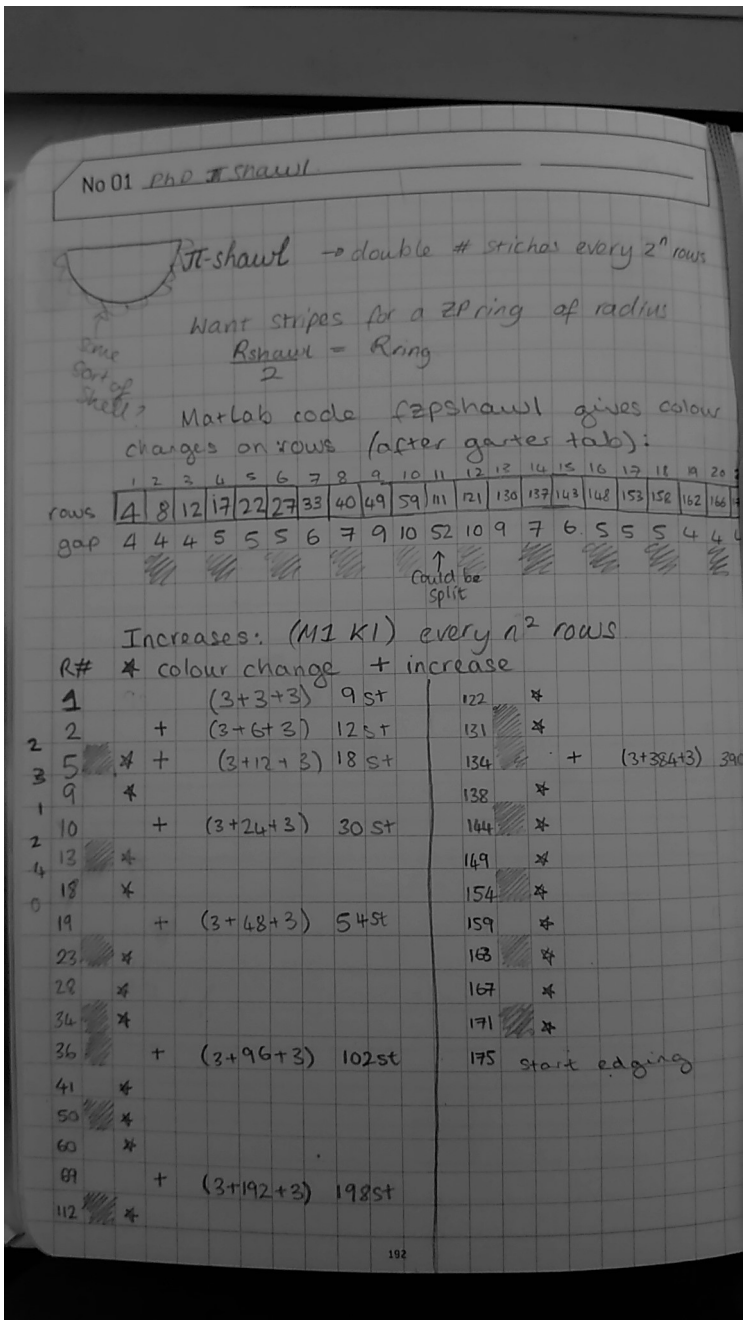

Figure B.1: A sketched pattern for the shawl. This is the pattern version which has been followed to make the shawl.